THE OPTIMIZATION OF VIBRATION DATA ANALYSIS FOR THE DETECTION AND DIAGNOSIS OF INCIPIENT FAULTS IN ROLLER BEARINGS

IBRAHIM A. M. REHAB

A thesis submitted to the University of Huddersfield in partial
fulfilment of the requirements for the degree of

Doctor of Philosophy

The University of Huddersfield

School of Computing and Engineering

Mechanical Engineering Department

December 2016

COPYRIGHT STATMENT

ABSTRACT

The rolling element bearing is a key component of many machines. Accurate and timely diagnosis of its faults is critical for proactive predictive maintenance. The research described in this thesis focuses on the development of techniques for detecting and diagnosing incipient bearing faults. These techniques are based on improved dynamic models and enhanced signal processing algorithms.

Various common fault detection techniques for rolling element bearings are reviewed in this work and a detailed experimental investigation is described for several selected methods. Envelope analysis is widely used to obtain the bearing defect harmonics from the spectrum of the envelope of a vibration signal. This enables the detection and diagnosis of faults, and has shown good results in identifying incipient faults occurring on the different parts of a bearing. However, a critical step in implementing envelope analysis is to determine the frequency band that contains the signal component corresponding to the bearing fault (the one with highest signal to noise ratio). The choice of filter band is conventionally made via manual inspection of the spectrum to identify the resonant frequency where the largest change has occurred. In this work, a spectral kurtosis (SK) method is enhanced to enable determination of the optimum envelope analysis parameters, including the filter band and centre frequency, through a short time Fourier transform (STFT). The results show that the maximum amplitude of the kurtogram indicates the optimal parameters of band pass filter that allows both outer race and inner race faults to be determined from the optimised envelope spectrum. A performance evaluation is carried out on the kurtogram and the fast kurtogram, based on a simulated impact signal masked by different noise levels. This shows that as the signal to noise ratio (SNR) reaches as low as -5dB the STFT-based kurtogram is more effective at identifying periodic components due to bearing faults, and is less influenced by irregular noise pulses than the wavelet based fast kurtogram.

A study of the accuracy of rolling-bearing diagnostic features in detecting bearing wear processes and monitoring fault sizes is presented for a range of radial clearances. Subsequently, a nonlinear dynamic model of a deep groove ball bearing with five degrees

of freedom is developed. The model incorporates local defects and clearance increments in order to gain the insight into the bearing dynamics. Simulation results indicate that the vibrations at fault characteristic frequencies exhibit significant variability for increasing clearances. An increased vibration level is detected at the bearing characteristic frequency for an outer race fault, whereas a decreased vibration level is found for an inner race fault. Outcomes of laboratory experiments on several bearing clearance grades, with different local defects, are used herein for model validation purposes.

The experimental validation indicates that the envelope spectrum is not accurate enough to quantify the rolling element bearing fault severity adequately. To improve the results, a new method has been developed by combining a conventional bispectrum (CB) and modulation signal bispectrum (MSB) with envelope analysis. This suppresses the inevitable noise in the envelope signal, and hence provides more accurate diagnostic features. Both the simulation and the experimental results show that MSB extracts small changes from a faulty bearing more reliably, enabling more accurate and reliable fault severity diagnosis. Moreover, the vibration amplitudes at the fault characteristic frequencies exhibit significant changes with increasing clearance. However, the vibration amplitude tends to increase with the severity of an outer race fault and decrease with the severity of an inner race fault. It is therefore necessary to take these effects into account when diagnosing the size of a defect.

DECLARATION

I hereby declare that I am the sole author of this thesis.

No portion of the work referred to in this thesis has been submitted in support of an application for another degree or qualification at this or any other university or other institute of learning.

Ibrahim Rehab

DEDICATION

بسم الله الرحمن الرحيم

فَلله الَّذِين آمَنُوا وَكُمْ الَّذِينَ أوتوا العِلمَ دَرجات

صدق الله العظيم
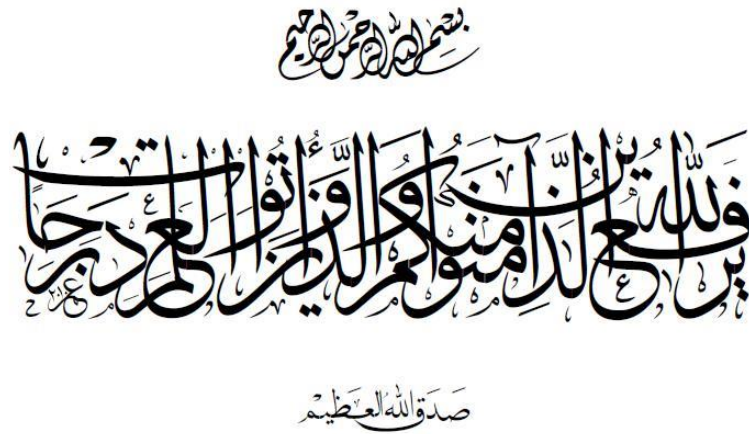
The road to success comes through hard work, determination, sacrifice and guidance of elders, especially those very close to the heart.

My humble effort I dedicate to my sweet and loving

Father, Mother, Wife and Children,

whose affection, love, encouragement and prayers day and night enable me to achieve much success and honour.

ACKNOWLEDGEMENT

I am deeply indebted and would like to express my sincere gratitude to **Prof. Andrew Ball** and **Dr. Fengshou Gu** for their Supervision of this work. They have been a strong source of inspiration throughout my PhD research. I have benefited greatly from their invaluable guidance and motivation.

LIST OF CONTENTS

LIST OF FIGURES

LIST OF TABLES

LIST OF ABBREVIATIONS

CM	Condition Monitoring
PM	Predictive Maintenance
CBM	Condition-Based Maintenance
PHM	Prognostics and Health Management
RMS	Root Mean Square
PV	Peak Value
CF	Crest Factor
IF	Impulse Factor
FFT	Fast Fourier Transform
BPFI	Ball Pass Inner Race Frequency
BPFO	Ball Pass Frequency Outer Race
FCF	Fundamental Cage Frequency
STFT	Short-time Fourier Transform
WVD	Wigner-Ville Distribution
WT	Wavelet Transform
AR	Autoregressive
SK	Spectral Kurtosis
AM	Amplitude Modulation
FM	Frequency Modulation
HOS	Higher Order Spectra
PS	Power Spectrum
CB	Conventional Bispectrum
MSB	Modulation Signal Bispectrum
MSB-SE	Modulation Signal Bispectrum Based Sideband Estimator
ABMA	American Bearing Manufacturers Association
MMF	Magnetomotive Force
DOF	Degrees of Freedom
rpm	Revaluation Pre Minute
cps	Cycle Per Second

Hz	Hertz
HT	Hilbert Transform
DFT	Discrete Fourier Transform
QPC	Quadratic Phase Coupling
AC	Alternative Current
EDM	Electrical Discharge Machining
SNR	Signal to Noise Ratio

LIST OF NOTATIONS

$x(t)$	Vibration signal
$x_f(t)$	Basic impulse series
$x_q(t)$	Modulation effect due to non-uniform load distribution
$x_{bs}(t)$	Bearing induced vibrations
$x_s(t)$	Vibration induced by the machine
$n(t)$	Gaussian white-noise sequence
y_{max}	Maximum amplitude of the signal
M_s	Total mass of shaft with inner race
M_h	Total mass of housing with outer race
M_r	Mass of sensor
K_s	Linear stiffness of shaft
K_h	Linear stiffness of housing
K_r	Linear stiffness of sensor
C_s	Equivalent viscous damping of shaft
C_h	Equivalent viscous damping of housing
C_r	Equivalent viscous damping of sensor
K	Nonlinear contact stiffness
F	Radial load applied to the bearing
δ	Contact defection in radial direction
ϕ_i	Ball angle position
X_s, Y_s	Shaft displacement along X and Y axes
$\dot{X}_s, \dot{Y}_s$	Shaft velocity along X and Y axes

$\ddot{X}_s, \ddot{Y}_s$	Shaft acceleration along X and Y axes
X_h, Y_h	Housing displacement along X and Y axes
$\dot{X}_h, \dot{Y}_h$	Housing velocity along X and Y axes
$\ddot{X}_h, \ddot{Y}_h$	Housing acceleration along X and Y axes
X_r	Sensor displacement along X axes
$\dot{X}_r$	Sensor velocity along X axes
$\ddot{X}_r$	Sensor acceleration along X axes
$\sum \rho$	Curvature sum
δ^*	Dimensionless curvature difference
Q	Hertzian contact force
Q_ϕ	Hertzian contact force at any angular position
Q_{max}	Maximum Hertzian contact force
F_s	Shaft rotational frequency
d_i	Inner race diameter
d_o	Outer race diameter
d_m	Pitch diameter
D	Ball diameter
d_s	Shaft diameter
N_b	Ball number
α	Contact angle
P_d	Internal radial clearance
c	Radial clearance at any angle
δ_{max}	Maximum radial deflection
δ_ϕ	Radial deflection at any rolling element angular position
ω_c	Cage angular velocity

ω_s Shaft angular velocity

LIST OF PUBLICATIONS

1- Rehab, I, Tian, X, Gu, F and Ball, A. (2014) '*The fault detection and severity diagnosis of rolling element bearings using modulation signal bispectrum'. In: Eleventh International Conference on Condition Monitoring and Machinery Failure Prevention Technologies, 10th - 12th June 2014,* Manchester, UK

2- Gu F, Tian X, Chen Z, Wang T, Rehab I and Ball, A. (2014) *'Fault severity diagnosis of rolling element bearings based on kurtogram and envelope analysis'. In: Proceedings of the International conference on advances in civil, Structural and Mechanical Engineering:* Institute of Research Engineers and Doctors. ISBN 978-981-07-8859-9

3- Rehab, I, Tian, X, Gu, F and Ball, A. (2013) *'Roller element bearing fault detection and diagnosis based on an optimised envelope analysis'. In: Proceedings of Computing and Engineering Annual Researchers' Conference 2013: CEARC'13.* Huddersfield: University of Huddersfield. pp. 176-181. ISBN 9781862181212

4- Rehab, I., Tian, X., Ball, A. and Gu, F. (2015) '*A study of diagnostic signatures of a deep groove ball bearing based on a nonlinear dynamic mode'*. In: Proceedings of the 21st International Conference on Automation and Computing (ICAC). : IEEE. . ISBN 978-0-9926801-0-7

5- Tian, X., Abdallaa, G., Rehab, I., Gu, F. and Ball, A. (2015) 'diagnosis of combination faults in a planetary gearbox using a modulation signal bispectrum based sideband estimator'. In: Proceedings of the 21st International Conference on Automation and Computing (ICAC): IEEE. ISBN 978-0-9926801-0-7

6- Tian, X., Gu, F., Rehab, I., Abdalla, G. and Ball, A. (2015) '*A robust fault detection method of rolling bearings using modulation signal bispectrum analysis'.* In: 28th International Congress of Condition Monitoring and Diagnostic Engineering Management (COMADEM 2015), 1st - 4th December 2015, Buenos Aires, Argentina

7- Rehab, I., Tian, X., Ruiliang, Z, Gu, F. and Ball, A. (2016) ' *A study of the diadnostic amplitude of rolling bearing under increasing radial clearance using modulation signal bispectrum'*. In: 29th International Congress of Condition Monitoring and

Diagnostic Engineering Management (COMADEM 2016), 20th – 22nd August 2016, Empark Grand Hotel, Xi'an, China

8- Rehab, I., Tian, X., Niaoqing H., Tianxiao Y., Ruiliang, Z., Gu, F. and Ball, A. (2016) '*A study of two bispectral features from envelope signals for bearing fault diagnosis*'. In: 1st International Conference on Maintenance Engineering (IncoME-I 2016), 30th – 31st August 2016, The University of Manchester, UK

CHAPTER ONE

INTRODUCTION

This chapter provides a general overview of condition monitoring, in particular bearing condition monitoring and diagnosis. This includes the monitoring of acoustic emissions, temperature, electric motor current, wear debris, and vibration. Focus is placed on vibration measurement because (a) it is the monitoring method most commonly used by industry, and (b) it is used for the rolling element bearings employed in this project. The summary of previous bearing fault diagnosis research provides the motivation for this research and enables the overall aim and objectives to be defined.

1.1 Background

The process of determining the operating characteristics (health and state) of a machine is known as condition monitoring (CM). It is used to predict the maintenance needs prior to any serious deterioration or breakdown of the machine. It involves identifying the life cycle of individual parts or a whole system. This can require the development of special purpose equipment in order to acquire and analyse data so that trends can be predicted. The CM process consists of either periodic or continuous data acquisition, followed by subsequent data analysis, interpretation and fault diagnosis. Predictive Maintenance (PM) is a widely accepted maintenance philosophy, also known as Condition-Based Maintenance (CBM), of which Condition Monitoring is an integral component. The PM philosophy is a strategy for prompting discussion, and is based on the scheduling of maintenance activities only when a potential functional failure is detected. This early detection is designed to avoid unexpected catastrophic failures. CBM can enhance the safety and operational effectiveness via the research and development of new technologies for the reliable and accurate prediction of the remaining useful life of in-service equipment. The CBM can also be described as Prognostics and Health Management (PHM). Figure 1-1 shows the three main elements of CBM. These elements are interconnected with each other such that none of them could be achieved effectively without the presence of others [1]. CM optimises the readiness of equipment whilst reducing the maintenance and staffing requirements. Common CM techniques include the analysis of vibration, oil, wear particles, ultrasonics, thermographics, and motor current signature analysis [1-3].
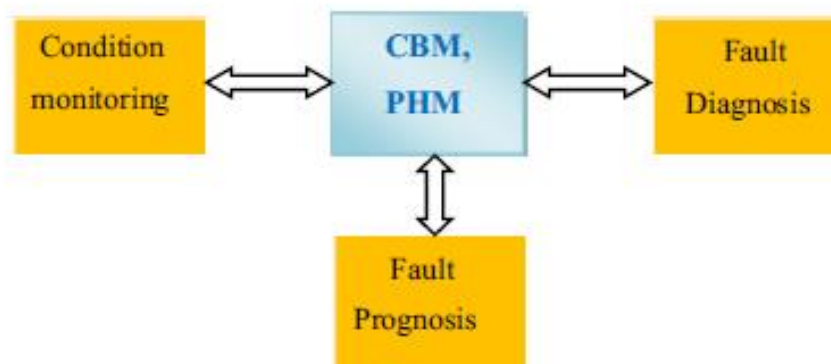
Figure 1-1 Components of condition based maintenance [1]

Two different approaches may be used for performing maintenance. Unplanned maintenance, often known as failure maintenance, occurs when a machine is operated without maintenance until it breaks down. Planned maintenance is characterized by the periodic stopping of machines for maintenance in order to lower the number of unplanned stops [3-5]. Various advantages are offered by Condition Monitoring, including:

- ✓ Reduced maintenance cost due to the minimisation of unnecessary machine services.
- ✓ Advanced information on the nature of the fault being repaired. Advance preparations can be made so that the duration of each intervention is minimised, thus minimising production loss.
- ✓ Condition Monitoring is used to derive advanced information on the severity of the fault under repair. In this manner, the possible duration of the intervention can be determined early so that disruption to the production process is minimised.
- ✓ Eliminating or reducing the severity of catastrophic failure.

The strong advantages of the CM approach have recently led to the development of a wide array of tools and techniques for the monitoring of machinery condition [2-5].

For all dynamic systems, their condition changes over time, and therefore their signature signals also change. These signal changes can provide information on the presence. As a result, a growing emphasis is being placed on the application of signal processing techniques for separating significant trends from random variations. They can also be used to provide an early diagnosis, which is of great value when the part crucially important to the production process, or when it is important to a safety procedure.

1.2 Bearing Condition Monitoring Techniques

Bearings are important to any processing or manufacturing plant that uses rotating equipment. Bearings can fail due to a range of problems: such as a machine running unbalanced, misalignment, critical speed, an incorrectly fitted bearing, incorrect grease, no grease, etc. Bearings are often replaced without determining the origin of the failure, and hence failure may occur again. It has been extensively documented that most vibration-based machinery problems are caused by misalignment or unbalance, often leading to bearing failure [4, 5].

The railway industry, for example, regularly suffers damage to equipment and wayside structures as a result of derailment that occurs when wheel bearings fail. To minimize this, several wayside inspection techniques have been developed to detect defective bearings before they fail. Any improvement in the ability to reliably detect and diagnose bearing faults can reduce the potential for derailment due to bearing failure, thus increasing railway safety [6].

Implementing key element of any effective diagnosis technology is the ability for early detection of faults without machine disassembly. This is crucial for condition monitoring, predictive maintenance and quality inspection, and it enables the remaining useful life of the machine to be estimated. There are various methods that can be used for diagnosing bearing defects. These methods are generally classified as for example (i) acoustic measurements, (ii) current and temperature monitoring, (iii) wear debris detection, and (iv) vibration analysis [7]. These will be detailed below.

- **Acoustic Measurement**

Acoustic emissions monitoring is the most effective acoustic-based method of gauging bearing health. Sound waves are formed in a solid material under mechanical or thermal stress, as a result of a transient impulse that is generated by a rapid release of strain energy. Measurements of a machine's acoustic emissions can also be used to detect defects in the bearings. The accuracy of acoustic methods typically depends upon the quality of the sound pressure and sound intensity data.

- **Temperature Monitoring**

Defective bearings produce greater friction and can hence generate excessive heat in the rotating components. The simplest method for fault detection in rotary machines is therefore to monitor the temperature of a bearing's housing or lubricant.

- **Electrical Motor Current Monitoring**

A machine's operating conditions may be monitored via analysis of the motor current spectrum. Changes in the measured electrical background noise are indicative of changes in the mechanical properties of the machine and its components. Fault signatures can hence be detected by intelligent signal processing of the measured motor current.

- **Wear Debris Analysis**

In wear debris analysis, any metallic particles present in the lubricant are detected by sensitive electrical sensors. Spectrographic analysis of the various metallic elements present in the lubricant can enable the location of the fault to be identified.

- **Vibration Measurement**

Abnormal vibration is often the first effect of rotary component failure to be detected in rotary machines. Vibration analysis is therefore widely used in industry. Any defect type will generate a vibration signal indicative of a fault when a damaged area interacts with a rolling surface. Vibration analysis can therefore be used to detect and diagnose all types of fault, whether they be localised or distributed. The vibration measurement method has a number of other advantages, including accurate results, low-cost sensors, straightforward setup, specific damage location information, and comparable damage rates.

1.3   Vibration based Condition Monitoring

Vibration analysis is a very popular tool for monitoring the condition of rotating machinery. It is able to identify common faults including imbalance, misalignment, looseness, rubbing, bent shaft, cracked shaft, gear faults, motor faults and blade/impellor defects. While these faults are the most common, they are primarily detected in high speed machinery (> 600 rpm). In fact for low speed machinery there is only limited information on faults that can occur, except for those generated by defective rolling element bearings [8, 9].

Even bearings with no faults generate some vibration. It is therefore important to study the base-line behaviour of a bearing so that abnormalities can be detected in the vibration signature of a damaged bearing. In roller element bearings the main source of vibration is variation in compliance. This is caused by the number of load carrying elements and the continuously changing position. Various models representing the periodic vibration of bearings have been proposed based on this phenomenon [10-13]

Vibrations are linked directly to a machine's periodically moving components, such as rotating shafts and its natural frequencies, which can provide essential fault diagnosis

information. The source of a vibration is directly indicated by the frequency and amplitude of a measured signal [4, 8]. Consequently, vibration analysis has been widely used in condition monitoring and fault diagnosis of machines. The analysis itself may take place in the time domain, frequency domain, or the time-frequency domain.

1.4 Review of Bearing Fault Diagnosis via Vibration Analysis

Much previous research into the diagnosis and prognosis of bearings is based on signal processing techniques for vibration characteristics. Generally, a localised or distributed defect is deliberately created on a bearing by grinding, drilling, acid etching, over speeding or overloading. A vibration signal is then measured, usually using accelerometers. Various signal processing techniques may then be used to extract the fault sensitive features that can be used as monitoring indices. The signal processing methods reported in the literature are categorised into time domain, frequency domain, and time-frequency domain methods. Such techniques are not completely independent, and they are often complementary to one other.

1.4.1 Bearing Failure

Many events can give rise to bearing defects. These include poor lubrication, poor maintenance, over-speed, overload, misalignment, imbalance, incorrect application, and high temperatures, among others [14]. Tandon et al. [15] gave an overview of several different failure modes for rolling element bearings. Bearing defects are usually grouped into two classes: distributed defects and localised defects. Distributed defects are usually caused by manufacturing errors. These can include surface roughness, waviness, off-size rolling elements, and misaligned races. Localised defects are caused by fatigue damage on the rolling surfaces [15]. These can appear as pits, cracks and spalls. The present research will focus only on localised defects, which usually originate as subsurface cracks, as will be described in more detail in Chapter two.

1.4.2 Signal Processing Techniques for Bearing Condition Monitoring

In order to reliably monitor the condition of rolling element bearings and to diagnose faults, fault features must be effectively extracted from vibration signals masked by background noise. Much research has been conducted which focusses on the development of bearing fault detection techniques for and vibration-based diagnosis. These techniques,

some of which are described briefly below, may be classified into (i) time domain, (ii) frequency domain, (iii) time–frequency domain, and (iv) higher-order spectral analysis. Signals encountered within a machine can generally be classed as being either stationary or non-stationary. Stationary signals analysis has traditionally been based on accepted spectral techniques such as the Fourier transform, which can be used to identify the dominant frequency components within the signal. For non-stationary signals, especially any that contain a transient component, the ability of the Fourier transform to identify frequency components is limited [5].

1.4.2.1 Time Domain Analysis

Direct analysis of vibration signals in the time domain is one of the cheapest and simplest approaches to detection and diagnosis. This analysis may be carried out via a visual examination of particular portions of the time domain waveform, or by examining the statistical properties of vibration signal in the time domain. Previous research has proposed various time domain approaches for detecting the presence of bearing damage. Those commonly used are (i) root mean square (RMS), (ii) crest factor and (iv) kurtosis. This are calculated in respect to the bearing condition. The RMS value is a good indicator of the level of energy in the vibration signal. The crest factor is the ratio of a waveform's peak value with its RMS value. The crest factor of a pure sine wave is $\sqrt{2}$ times larger than the RMS value, and can be larger still for any signal influenced by many factors, such as faulty bearing signals. These parameters are extracted, and used as key features in bearing fault detection algorithm(s) [15, 16].

Kurtosis quantifies the 'peakedness' of a distribution, i.e. whether data is more peaked or more flat in relation to a normal distribution (and by how much). Normally distributed data has a kurtosis value of 3. Data sets with high kurtosis have a stronger peak, which declines rapidly with heavy tails. Kurtosis reacts sensitively to the vibrations induced by bearing defects, and has been shown to be an effective indicator for rolling element bearing diagnostics [17-19]. A normal, undamaged bearing should have a kurtosis value close to 3. If the value is greater than 3, this indicates a defect may be present. However, when damage is significantly advanced, the kurtosis value may drop to below 3, and remain close to the value expected of an undamaged bearing [16, 20]. This scenario is the biggest problem with using the kurtosis value for fault detection.

The crest factor and the kurtosis do not account for the magnitude of the vibration signal, being only measures of the peakedness of the vibration signal. During the beginning stages of bearing damage, kurtosis and crest factor increase as the spikiness of the vibration increases. However, as the damage increases, the vibration signal becomes more randomised, so that the crest factor and kurtosis value drop close to more normal levels. Therefore, the kurtosis and crest factor are limited in their ability to detect bearing defects in the later stages of development. This is the primary problem associated with a statistical approach, and strongly limits the potential of these measures to be used for bearing prognosis [21].

Heng and Nor [22] recorded sound pressure and vibration signals from a rolling element bearing and calculated the crest factor, kurtosis and skewness in order to detect defects. They concluded that bearing defects can be detected by statistical methods. Additionally, they showed that the statistical parameters are affected by the shaft speed. This is because the vibration excites the fixing ring that holds the test bearing in position, and the bearing housing components are sensitive to this vibration.

1.4.2.2   Frequency Domain Analysis

In the frequency domain approach the dominant frequency components of the vibration signals and their amplitudes are used for trending purposes. When a fault occurs in any component of the rolling element bearing (inner race, outer race, or rolling elements), peaks in the vibration spectrum increase at the frequencies corresponding to that particular bearing defect, as well as at harmonic frequencies associated with the defective component(s). Sidebands are also produced in the neighbourhood of each peak, the spacing of which depends upon the cycle of the rotating shaft. The amplitudes of the power spectrum peaks generally increase as the bearing damage increases [21, 23].

Vibrational impulses are produced when a rolling element passes over a defect. The bearing system responds to such impulses at its natural frequency. This response reduces quickly over time, due to the heavy damping of the system. The excitation and response process occurs every time a rolling element passes over the defect, so the fundamental frequency observed in the response waveforms is governed by the rate at which elements roll over the specific defect. Several previous studies have examined the identification of

bearing defects based on the detection of these frequencies within the spectrum [15, 24-27].

A Fast Fourier Transform (FFT) is fundamental spectral analysis technique used in many fields of science and engineering. In particular, it can be used to analyse the vibration of machinery components. An FFT transforms time domain signals into the frequency domain. This can enable spectral features to be detected, for diagnosis of the machine's condition. When local faults exist within the bearing, the amplitude of vibration at such characteristic fault frequencies and at their harmonics can increase significantly [5]. Several studies have shown the potential for successful identification of those fundamentally important frequencies. Li et al. [28-30] described the application of a FFT for detecting bearing looseness and other faults in the rolling elements, inner race or outer race. This was done both via simulation and physical experimentation. An on-line monitoring system was designed by Wang [31], which was based on a FFT and other methods. Blair [32] also used an FFT in a diagnostic package.

However, FFTs suffer from their own limitations. The spectral peaks caused by bearing defects generally apparent in the low-frequency end of the spectrum, around 0-2 kHz and usually also at the associated harmonics. Therefore, the frequencies associated with bearing defects are in the same low frequency range as the vibrations normally induced by operation of the machine (for example due to misalignment and imbalance) as well as random vibrations. Hence, unless the defect is sufficiently large, it can be difficult to distinguish the spectral peaks in the presence of strong environmental noise. This is the main limitation of the traditional FFT-based methods.

The vibration signals produced by bearings generally contain an amplitude modulation, which gives rise to sidebands in the frequency spectrum. Modulation of the bearing tones can occur in a number of ways. One example is via a small crack forming on the inner race. This defect will effectively move into and out of the load zone at frequency at which the shaft rotates (f_s). When the defect enters the load zone, it causes high vibrations at the Ball Pass Inner Race Frequency *(BPIF),* but when it is out of the load zone is causes very little vibration at that frequency. This means that the amplitude of the *BPIF* vibration is modulated, and the sidebands of the *BPIF* are spaced by f_s. If a rolling element becomes damaged, then the roller also moves into and out of the load zone. However, this occurs at the Fundamental Cage Frequency *(FCF),* and not at f_s. This is due to the rolling

elements rotating around in the bearing at a frequency of *FCF*. In contrast to these behaviours, a defect formed in the stationary outer race is permanently within the load zone, so no modulation should occur.

Thus, defect detection based on characteristic defect frequencies in the spectrum presents the potential to measure bearing conditions. However, the direct identification of the sidebands and characteristic defect frequencies is difficult when there is a high background noise or when other factors interfere, as can often happen. Therefore, spectral analysis is not sufficient for bearing condition monitoring under many realistic scenarios; more robust, reliable methods must be adopted in order to accurately detect bearing integrity [11, 33].

Envelope detection is the most commonly used technique to improve signal-to-noise ratio (SNR) and thus enhance the spectral analysis of signals. This helps in the identification of bearing defects because it can extract the characteristic defect frequencies within a vibration signal recorded from a defective bearing [15].

Envelope analysis is a form of amplitude demodulation. It is another popular technique for analysing the frequency content of bearing vibrations. McFadden et al. [11] conducted a review of the rolling bearing monitoring using envelope analysis, providing a basis for ongoing research. It was reported that an envelope spectrum only contains individual, discrete components for very simple examples, such as an axial or radial bearing with a defect in the outer race. In this case it is possible to determine the bearing condition by passing the envelope signal through a bank of narrow bandpass filters tuned to the characteristic defect frequencies of the bearing, and then through a bank of level sensing circuits.

Molitor et al. [34] presented a method for the early identification of defects in car bearings. Similarly, Cline et al. [35] showed a promising analysis of the roller bearings on a freight car. The researchers in [36-38] also provided a robust demonstration of the efficiency of envelope analysis for bearing fault detection. However, Rubini [39] showed that the sensitivity of envelope analysis is governed by the selection of filtering band, and was thus unable to detect incipient faults. A key issue with envelope analysis (and other frequency domain approaches) is the need for bearing defect frequencies to already be known [40]. An additional problem is the increased difficulty in vibration spectrum

analysis if the signal-to-noise ratio is low, or if the complexity of the system generates a large number of dominant frequency components.

For roller bearings, the envelope analysis method provides an effective approach to fault diagnosis. Sawalhi et al. [41] and Yu et al. [42] described a fundamental limitation of envelope analysis. This is that the band pass filter's central frequency (structural resonance) and the filter's bandwidth are determined from experience when forming an envelope signal. This causes the process to be highly subjective, which can greatly influence the results.

Recently, ''spectral kurtosis'' has been examined as a method of optimising the extraction of bearing signals from background noise. Antoni et al. [43] introduced the concept of a Kurtogram, which shows the spectral kurtosis as a function of frequency. From this, optimal band pass filters can be designed in order to overcome the limitation of envelope analysis. The results showed that the maximum of the Kurtogram indicates the optimal parameters (central frequency and band width) for the band pass filter.

1.4.2.3   Time-Frequency Analysis Techniques

Time–frequency domain techniques utilise information from both the time and frequency domain. This allows transient features such as impacts to be investigated. A fundamental limitation of frequency domain approaches is that they are unable to handle non-stationary waveforms, which are a common signal type when machinery develops a fault [5]. Often a particular frequency of interest may appear at any time and for any period of time. Sometimes it can be beneficial to determine the frequency and time intervals of these particular components. Time-frequency analysis presents the energy or power of a signal as a function of both time and frequency, and can enable a more accurate diagnosis [5, 44]. Several time–frequency domain techniques have been developed. These include the short-time Fourier transform (STFT), the wavelet transform (WT), and the Wigner-Ville distribution (WVD) [45, 46].

Gabor (1946) considered the short time Fourier transform (STFT). In STFT the whole signal is divided into short time segments, and a Fourier transform is applied to each segment. The limitation of STFT is that the resolution is constant with the same length of window [5, 16]. The Wigner-Ville Distribution is a combination of an FFT and an auto-correlation function. The Wigner-Ville distribution produces a higher resolution than the

STFT, but it suffers from an interference term that is formed by the transformation itself [47-49]. This can lead to a negative energy level and spectrum aliasing, making the results difficult to interpret.

One alternative, wavelet analysis, has gained significant interests recently due to its ability to provide multi-resolution in both the time and frequency domains. The wavelet transform is extremely sensitive to transient phenomena, making it ideal for identifying the periodic shocks induced by a faulty bearing. Wavelet analysis was used as a pre-processing techniques in several previous studies [17, 50, 51]. A denoising method, based on wavelet analysis [52, 53], was shown to be highly applicable for the rolling element bearings. The method can improve the calculation efficiency, reducing the amount of data manipulation [54]. Wavelet analysis has also been used for early fault detection [19, 55, 56]. It can be used to identify bearing damage after the damage appears [39]. Additionally, it is insensitive to the operating conditions of the bearing, the load and the speed [57].

1.4.2.4 Spectral Kurtosis and the Kurtogram

Spectral kurtosis (SK) is based on higher-order statistics. It calculates the kurtosis at each frequency in a time-frequency analysis frame, for example from a short time Fourier transforms (STFT). Usually, high values are taken in the area of the resonance frequencies of the transients. It is ideally close to zero for Gaussian noise and stationary harmonic components. The benefit of SK stems from its ability to detect transients in a signal and to locate the central resonance frequency corresponding to the transients. This can then be used to filter the fault signal, demodulating it in order for the signal envelope to be extracted [43, 58, 59].

Envelope analysis of vibration signals is considered to be the most common way of monitoring bearing faults. However, envelope analysis required complex operations such as FFTs and digital filters. Successful implementation of envelope analysis depends upon the proper selection of the central frequency and bandwidth of the band pass filter. Even if appropriate parameters are initially selected, they may become invalid in an unpredictably changing environment. Thus, demodulation using a bandpass filter with constant parameters may not detect faults effectively in a bearing running under varying conditions and/or over a wide range of speeds [11, 60].

A number of techniques have been proposed to address this issue. Most recently, Antoni [59] performed a thorough analysis of spectral kurtosis. A spectral kurtosis was proposed that was derived from the short time Fourier transform, and was used to detect faults in gears and rolling element bearings [43]. To reduce the computation time and provide fast on-line fault detection, a 1/3 binary tree kurtogram estimator was proposed [61]. Sawalhi et al. [33] examined the capability of spectral kurtosis as an analysis tool for rolling element bearings. They combined it with (i) an autoregression (AR) based liner prediction filtering and (ii) minimum entropy deconvolution [62]. The results indicate that this method can dramatically sharpen the impulses and thereby increase the value of the kurtosis. Antoni and Randall [43] provided a warning that spectral kurtosis may be impractical because it is unrealistic to examining all window lengths used in STFT based SK techniques to find the optimal central frequency and bandwidth of the filter. An additional problem is that the kurtogram uses a fixed tiling pattern regardless of the signal being analysed. Barszcz and Jabionski [63] proposed a novel method known as a Protugram, which enables an optimal bandpass filter to be configured based on a calculation of the kurtosis of the amplitude of the spectrum envelope. It was shown to work in the case of low signal to noise ratio. An SK method that could adaptively determine the bandwidth and central frequency of the filter was proposed by Wang and Liang [64]. It functioned by margining right extended windows in order to maximise the kurtosis of the filtered signal.

1.4.2.5 Higher Order Spectral Analysis

Higher order spectra are useful tools for signal processing. They offer significant benefits over conventional spectral analysis methods due to higher order spectra having the properties of phase information retention, nonlinear system identification, and Gaussian noise elimination [65, 66]. Higher order spectrum techniques have been used for condition monitoring applications [67, 68]. It is clear from these studies multi-dimensional higher order spectra can yield more useful information for diagnostic purposes than conventional two-dimensional spectral measures. A defect in a bearing results in high phase correlation among the harmonics of one or more of the characteristic defect frequencies [69].

Higher-order spectra describe the degree of phase correlation between different frequencies within a signal. Large values of phase correlation between the harmonics of

any defect frequency can indicate that a defect is present within the bearing. McCormick and Nandi [70] discussed the application of bi-spectral and tri-spectral analysis for condition monitoring. Li et al. [71] used bi-coherence spectra to identify the features that indicate the bearing condition.

Bicoherence spectra have been applied to rolling element bearings for the automatic detection and diagnosis of localised defects by detecting features that can indicate the bearing condition [69]. McCormick et al. [69] examined the features that best describe the phase correlation between the first three harmonics of the characteristic bearing fault frequencies. Local bearing defects have been detected using bicoherence theory, with the results validated experimentally. The method was hence shown to be effective in detecting and diagnosing incipient bearing defects.

The potential of bispectral and trispectral analysis for condition monitoring has been examined by McCormick [69]. Higher-order spectral analysis was applied to machine vibrations in order to determine the useful diagnostic features. Experimental work was conducted using a small test rig with imposed bearing faults. The bispectrum and trispectrum of the recorded vibration signal were used to train a neural network classifier that would determine the bearing condition. The technique was then compared with simpler statistical methods and power spectral extraction algorithms. A more detailed investigation of the signals' HoS was undertaken to identify the practical features that can be easily estimated to provide swift, robust, reliable bearing diagnostics.

An earlier study [72] used the motor current of a reciprocating compressor for fault diagnosis. It was revealed that the random noise could be suppressed by a new data processing method known as a modulation signal bispectrum (MSB). MSB is an extension of the conventional bispectrum (CB), and is predominantly used for characterising modulation signals. It has been shown to provide an improved diagnosis compared to the power spectrum (PS). MSB is therefore an effective method of detecting and quantifying the sidebands in current signals due to its noise suppression capabilities.

Following the successful use of MSB for reciprocating compressors, the method has been further improved [73-78]. The influence of the carrier-magnitude at the fundamental supply is removed in the MSB slices of interest, meaning faster MSB analysis and accurate sideband estimation. This has produced impressive detection and diagnosis

results for a range of faults within multi stage gearboxes, electrical motors and roller bearings [73-78].

Rehab et al. [76] used MSB to extract fault features from envelope signals. MSB was selected due to its ability to suppress noise and reliably diagnose bearing fault severity. Tian et al. [77] presented a novel diagnosis method for combined faults inside planetary gearboxes. A modulation signal bispectrum based sideband estimator (MSB-SE) was used, as it allowed effective enhancement of the various sidebands and hence provided accurate diagnostic information. The same authors proposed a novel MSB detector, which was developed for accurately diagnosing bearing faults while overcoming the filter band optimisation problem experienced with traditional narrowband envelope analysis. This is compared with optimal envelope analysis using the fast Kurtogram [78].

It should be noted that the newer investigations mentioned above rely heavily on the magnitude information of MSB in order to perform fault diagnosis. The use of MSB coherence has not yet been explored in the diagnosis process. It may contain more useful information for detection and diagnosis of more complex ball bearing signals that are corrupted by the inventible wear/radial clearance grades and random noise. Moreover, this new method could be applied to a range of bearing faults with varying fault severity and under different clearance grades.

1.4.3   Model-Based Techniques

Modelling (simulation) of the vibration signals produced by bearing defects is a significant and effective tool in bearing diagnostics and prognostics. It produces signals with well-defined characteristics rather than waiting for such signals to arise randomly. Simulation can also enable an improved understanding of the generation mechanisms for fault symptoms, particularly when they involve non-linear interactions. Simulations of bearing faults can be used to characterise the performance of bearing diagnostic techniques under the influence of noise masking.

Much research has focused on the development of signal processing techniques for accurately detecting and isolating bearing faults. Conversely, very few studies have presented a mathematical (physics-based) model, allowing faults to be simulated under a range of operating conditions instead of either waiting for them to occur naturally or seeding them in laboratory testing.

Various mathematical models have been developed for the study of dynamic effects on roller bearings. McFadden and Smith [79] developed a model to describe the vibrations produced in a rolling element bearing under constant radial load with a single point defect on the inner race. Purohit et al. [79] studied the axial and radial vibrations from a rigid shaft supported ball bearing. Nonlinear springs are used to represent the contacts between the balls and the races in the analytical formulation. The spring stiffness is obtained using Hertzian elastic contact deformation theory. Culita et al. [80] proposed the McFadden-Smith vibration model. This was one of the first valid models of the bearing vibration generated by individual point defects. It was shown that the defect is encoded by the vibration model in a more natural and more accurate manner than was achieved in previous models. A significant contribution was made by Sassi et al. [81], who developed a numerical model based on the assumption that the dynamic bearing behavior could be represented by a coupled three-degrees-of-freedom system. Upadhyan et al. [82] examined the dynamic behavior of a high speed unbalanced rotor supported on roller bearings with damping. The non-linearity of the rotor bearing system was said to be a result of Hertzian contact, the unbalanced rotor effect and the radial internal clearance. An analytical model was presented by Patil et al. [83] for predicting the effect of localised defects on the vibrations of ball bearings. The contacts between the races and the ball are considered to be non-linear springs in their formulation. Patel et al. [13] studied the vibrations in a dynamic model of deep groove ball bearings which had single and multiple defects on the surfaces of both the inner and outer races. The mass of the shaft, housing, races, and balls were considered in their model. Results output by the model were validated against experimental results recorded for both defective and healthy deep groove ball bearings. Dougdag et al. [84] verified experimentally a simplified model of a ball bearing with nonlinear stiffness in both static and dynamic modes. They also tested the capabilities of the model to accurately simulate fault effects. The resulting defect simulations and model behavior for both static and dynamic modes were compared against the experimental results. Patel et al. [85] presented a theoretical and experimental study of the vibration in dynamically loaded deep groove ball bearings with localised circular defects. The mass of the shaft, housing, raceways and ball were all incorporated into the proposed mathematical model. Coupled solutions of the governing equations of motion were achieved via the Runge-Kutta method.

It is generally accepted that bearings undergo various types of wear during their lifetimes, which can lead to increased clearances and therefore high vibration levels [86]. This enhanced vibration can be used as an indicator of the remaining bearing life. However, the exact mechanisms behind how the increased clearance can effect on the vibration, and hence the diagnostic performance, were not found. The present study therefore focuses on the modelling of bearing vibration response for different levels of clearance, and quantifies the dependence of some common diagnostic features on the radial clearance. Additional experimental verification was also carried out for different clearance values with typical bearing faults.

1.4.4 Rolling Element Bearing Contact Fatigue and Wear Fundamentals

In a perfectly sealed rolling bearing running at a sensible speed and load, properly aligned and well lubricated, minimal wear should occur because under loaded conditions distortion at the ball/raceway interference means there is a small element sliding taking place. However, in most practical applications, wear and fatigue are the main factors establishing bearing life [86, 87].

Studies conducted with 100,000 bearings used in a range of vehicles, machinery, and manufacturing processes have identified the life-limiting wear level of the bearings [6]. The wear was run across at the cage sliding surfaces, at the contact surfaces between the rolling elements and the raceways, and on the lips and faces of the roller bearings. The initial phase of wear included rolling path becoming rougher, and a dull sign. The cause of the measured bearing wear was mainly friction against foreign objects that get into the bearing through inadequate or worn seals. However, wear debris from bearing surfaces and also from the related machine elements also played a role. Corrosion, resulting from condensation during temperature changes or water contamination was another cause, of bearing wear [88].

Any wear that occurs on the rolling bearing surfaces effectively increases the clearance, meaning that the heat generation, vibration and noise will increase [88-90]. Extensive research has focussed on measuring the internal radial clearance as a function of wear level during the time in service [6]. An expression was derived to describe the limiting radial wear factor f_v. This was proposed as a standard for comparing different sized bearings according to the following:

$$f_v = \frac{V}{e_0} = \frac{V}{0.46d^{2/3}}$$

(1-1)

In this equation V is the total wear required for bearing failure, measured in micrometres, in which reflects the increased internal radial clearance of an unmounted bearing. e_0 is a size factor calculated from the bore diameter of the bearing, d (mm), as $e_0 = 0.46\,d^{2/3}$.

Fatigue is generated in rolling element bearings by the repeated stressing of a finite volume of material [91]. Types of fatigue failure can include peeling, flaking, pitting and spalling. They all result in material being removed from the rollers and both the inner and outer races.
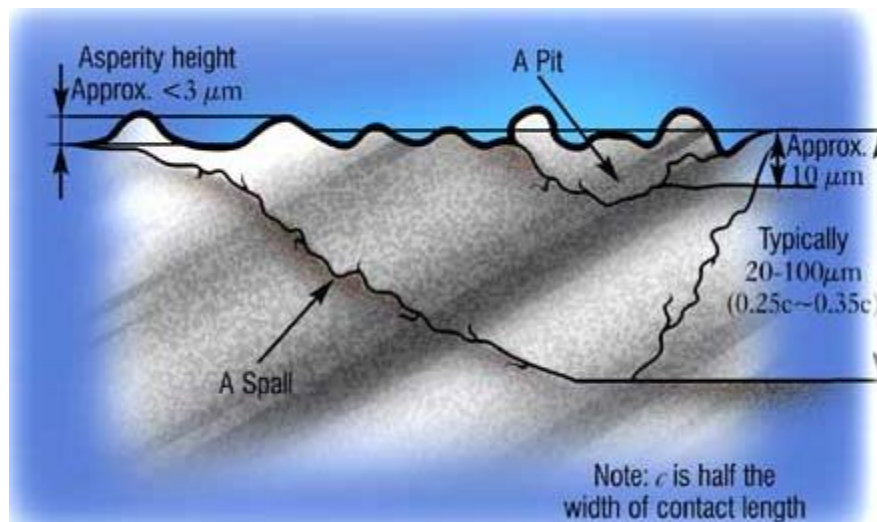
Figure 1-2 Pitting and spalling [92]

Three types of fatigue generally exist: fatigue pitting, fatigue spalling, and surface distress [92]. Surface distress establishes as a smooth surface due to plastic deformation occurring within the asperity region (usually less than 10 μm) [92]. Pitting presents as shallow craters in the contact surfaces, with a maximum depth equal to the work-hardened layer thickness (approximately 10 μm, see Figure 1-2) [92]. Spalling produces deeper cavities in the contact surfaces, with depth from 20 μm to 100 μm. Spalling and pitting are used indiscriminately in most of the literature. In some studies, spalling and pitting are used to distinguish the severity of the surface contact fatigue [92].

The life of a rolling element bearings is commonly measured by either (i) the number of million revolutions of the inner race (if outer race is stationary) until the first spall occurs,

or (ii) the number of hours of operation at reasonable angular speed before the first spalling occurs [93].

The standard issued by the American Bearing Manufacturers Association (ABMA) specifies that the first evidence of the failure criterion is caused by bearing fatigue. Timken Company laboratories defined the fatigue criterion as being when the spalling or pitting covered an area of 0.01 in^2 [93]. Timken also state that the useful life of a bearing can be considerably extended beyond the fatigue criterion. Fatigue life prediction algorithms have been developed as early as the 1940s. They provide a crucial method for estimating the survival time of bearings. The inventive work of Lundberg and Palmgren [6, 94] produced a model of bearing survival probability for the case of a dynamic load rating and an equivalent load.

In estimating the fatigue life and dynamic capacity of a bearing, Lundberg's model accounted for the size of the bearing, the number of rows, the number of rolling elements in each row, conformity between the races and the rolling element and the contact angle under load. Life adjustment factors were used to account for the lubricant properties, material properties, operating temperature and operating speeds.

The Weibull distribution function [95] was used to develop the theoretical basis of the model. The Weibull distribution builds on the theory that the fatigue lives of a group of homogenous bearings are linked according to Equation (1-2)

$$\ln \ln \left(\frac{1}{S} \right) = e \ln \left(\frac{L}{A} \right) \qquad (1\text{-}2)$$

Here S is the probability of survival ($0 < S < 1$), L is the fatigue life ($0 < L < \infty$) and e and A are constants.

Bearing fatigue lives from Equation (1-2) can be plotted on a Weibull plot (log log vs log) so that they form a straight line. This allows the service life at any reliability to be estimated. The most interesting fatigue lives are $L10$ ($S = 0.9$) and L50 ($S = 0.5$) [89, 91].

Zaretsky et al (2000). [96] provided a useful summary of life prediction methods for rolling element bearings, covering the past, present, and future work. In addition to summarising the life prediction formulae of Lundberg and Palmgren, Loannides and

Harris, and Zaretsky, the paper compares them against each other and also the ISO standards [97]. The standard formula for life rating is given by:

$$L_n = a_1 a_2 a_3 \left(\frac{C}{P} \right)^p$$

(1-3)

L_n is the rolling contact fatigue life (in revolutions $\times 10^6$) corresponding to the reliability level (100_n). a_1, a_2, and a_3 are the reliability factor, material factor, and lubrication factor respectively. C is the basic load rating of the bearing, and P is the equivalent load applied to the bearing. The exponent p takes a value of 3 for ball bearings, and of 10/3 for roller bearings. The life calculation from Equation (1-3) originates from the fatigue life theory developed by Lundberg and Palmgren. Nonetheless, the true life period of a bearing can vary significantly from the expectation due to the complexity of real life operating conditions. Therefore, rather than relying upon the statistical life estimates from laboratory tests, considerable attention is given to online condition monitoring systems that use real-time vibration analysis [21]

1.5   Research Motivation

So far, vibration-based condition monitoring of rolling element bearings has been examined only from a signal processing point of view. Little focus has been given to the use of mathematical (physical) models in understanding the effect that a fault can have on the vibrational behaviour of a bearing. The first step toward a successful implementation of bearing health monitoring is to establish a base-line dynamic model of the bearing. Robust techniques for fault diagnosis and prognosis can then be proposed based on variable load and speed conditions.

The nonlinear dynamics of rolling element bearings are studied in this thesis. The different categories of rolling element vibration are investigated via a comprehensive numerical study, and the characteristics under different internal radial clearance values are investigated. The effect of damage on the vibration signature of a bearing is then investigated. Experimental validation is then carried out to support the numerical results.

Faults in rotating machines generate a series of impacts during the early stages of operation, leading to transient vibration signals. These signals often exhibit a repetitive,

impulse-like nature due to the repetition of the fault motion as the mechanical components rotate. A range of techniques have been developed to capture the mechanical signatures of bearing faults. The main difficulty encountered is the severe corruption of the vibration signal due to high levels of background noise. This includes all other vibration sources within the overall system under inspection. The problem can hence be framed as the detection of transient signals amongst strong additive noise.

1.6   Overall Aim and Objectives

The main aim of this research is to investigate bearing dynamics and develop a nonlinear dynamic model and advanced data analysis techniques for accurate and reliable fault severity diagnosis in bearing faults under a range of clearance grades due to inevitable wear.

Objective 1: To research and describe machine condition monitoring techniques used for fault detection and diagnosis in rolling element bearings.

Objective 2: To carry out a comprehensive literature review covering the most commonly used vibration analysis techniques. This is to include fault detection methods for simple/premature rolling element bearings, such as (i) time domain, (ii) frequency domain and (iii) envelope analysis, (iv) kurtogram based short time Fourier transform, as well as advanced signal processing techniques such as higher order spectra.

Objective 3: To carry out an extensive literature review on topics related to the model based technique used for rolling element bearing.

Objective 4: To review the rolling element bearing fundamentals, theory, types, components, failure modes, friction and wear.

Objective 5: To review several conventional vibration analysis techniques that could be applied to the detection and diagnosis of rolling element bearing faults.

Objective 6: To develop an accurate dynamic nonlinear model that will provide a better understanding of the vibrations induced by rolling element bearing systems. Examine different fault types under different clearance values. Use this to characterise changes in the vibration signature arising from clearance increases, enabling more reliable diagnostic results.

Objective 7: To evaluate and discuss the outputs of the nonlinear model using time domain analysis, frequency domain analysis and envelope analysis for three different bearing conditions under two different clearance values.

Objective 8: To design and build an appropriate bearing test rig facility in which to allow the localised faults to be introduced into rolling element bearings, enabling the subsequent system behaviour to be characterised.

Objective 9: To study the influence of the envelope analysis parameters on resulting vibration signal of the motor bearing based on fixed bandpass and optimal bandpass filters parameters.

Objective 10: To accurately evaluate the performance of the kurtogram and fast kurtogram based on a simulated impact signal.

Objective 11: To analyse and discuss the bearing vibration signals recorded from the accelerometer when the bearing is subjected to localised defects and varying clearance values using the time domain, frequency domain and envelope analysis.

Objective 12: To accurately estimate the performance of higher order spectrum analysis (power spectrum, conventional bispectrum and modulation signal bispectrum) based on the statistical significance of the estimated spectra when combined with envelope analysis for different bearing conditions.

Objective 13: To apply the higher order spectrum analysis techniques to the envelopes of bearing vibration signals when the bearings are subjected to the different clearance values.

1.7   Thesis Organization

<u>Chapter 2</u>

This chapter gives a full review of the condition monitoring of rolling element bearings. This includes bearing theory, rolling element bearing types and their components, friction and wear, and bearing failure modes and causes.

<u>Chapter 3</u>

This chapter begins with an introduction to the vibration analysis techniques commonly used for bearing condition analysis followed by a literature survey covering the most popular techniques for diagnosis and fault detection of bearings. This begins with the well-established methods of time domain analysis, frequency domain analysis and envelope spectra. It goes on to review the use of kurtogram in selecting an optimal bandpass filter based on the short time Fourier transform to enhance the signal to noise ratio of the envelope analysis. Finally, higher-order spectra are introduced in this chapter due to their ability to suppress background noise and thus improve the rolling bearing fault detection and diagnosis

Chapter 4

This chapter explains the nonlinear dynamic model of roller bearings that can simulate vibration signals. The model considers the inner race-shaft and outer race-housing as lumped masses coupled by a nonlinear spring. This is formalised by the Hertzian contact deformation between the balls and races. This chapter also studies the internal radial clearances which become larger due to wear and localised defects.

Chapter 5

The results from the simulation of the nonlinear dynamic model described in Chapter four are presented in this chapter. First, a standard eigen method is used to conventionally calibrate the model parameters (including resonance frequencies and damping ratios). The solution of the nonlinear equation is obtained via the Runge-Kutta method, implemented in MATLAB, for different local bearing faults, clearance increments and radial loads.

Chapter 6

This chapter begins by describing the experimental test rig used to carry out the investigation, test rig components, and finished by discussing the fault seeding and data collection procedure.

Chapter 7

This chapter provides a detailed investigation of the kurtogram based short time Fourier transform method, as described in Chapter Three of this thesis. The investigation here is conducted by examining three bearing conditions: normal, inner race fault and outer race

fault. A comparison of these methods is conducted to determine the effect of optimal bandpass filter in the bearing vibration signal. Furthermore, performance evaluation of the kurtogram and fast kurtogram based on simulated impact signal is conducted.

Chapter 8

This chapter presents a detailed investigation of the time domain, frequency domain and envelope spectra methods described in Chapter Three. Two clearance grades and four bearing conditions were studied: normal, small inner race fault, large inner race fault and small outer race fault. The effect of clearance on the vibration signal is shown via a comparison of these methods.

Chapter 9

A detailed investigation of higher-order spectr is presented here, including the power spectrum, conventional bispectrum and modulation signal bispectrum, as described in Chapter Three. First an estimation is produced of the performance of higher order spectra. This is based on the statistical significance of the estimated spectra for two selected case studies: (i) a simulated time signal with known spectral content and then estimate the higher order spectral amplitudes output by the Mote Carlo estimator, (ii) the vibration signal of a tapered roller bearing undergoing a fatigue test were analysed using the aforementioned methods.

 Chapter 10

This chapter presents the conclusions of this research, and recommends some aspects for further study.

CHAPTER TWO

ROLLING ELEMENT BEARINGS AND THEIR MODES OF FAILURE

This chapter aims to provide a review of the state-of-the-art of different rolling element bearing types, their constituent components and the underlying theory of operation for each type. In addition, typical bearing failure modes caused by improper installation or lack of maintenance are discussed in this chapter. Moreover, how friction and wear can influence the radial clearance is explained too.

2.1   Introduction

Over the past few decades, the continuous advancements in materials and manufacturing
techniques has allowed for a significant improvement in rolling-element bearings. These
bearings are imperative for the development of modern machinery. These machines are
designed to operate at increased rotational speeds and loads, leading to a reduction in the
overall size of the machine. Thus, the incorporated rolling-element bearings are required
to provide a better reliability and a longer lifetime, even when exposed to higher
operational speeds [5, 15]. Rolling-element bearings are machine elements that allow for
the rotary motion of shafts in simple devices (e.g. AC induction motors), as well as in
many complicated engineering mechanisms (e.g. turbine engines). Rolling bearings are
referred to as anti-friction bearings because of their low friction value. Moreover, rolling-
element bearings are able to run at lower friction comparing to that in sliding bearings,
making them a suitable candidate for high-speed shaft operations that demand outstanding
endurance [8, 27].

In rotating machineries, rolling-bearing elements are one of the most critical components.
They are the most commonly wearing parts and a large majority of system failures arise
from faulty bearing operations. As a result, advanced technologies are necessitated to
effectively monitor the health status of the bearings under operation. This is especially
true when bearing faults result in machine downtime and substantial monetary loss or
even human casualties. By estimating the bearing health whilst in operation and
providing appropriate warnings in advance, it is possible to reduce the risk of unexpected
failures [4, 7, 98]. Thus, proper bearing condition monitoring is a necessity and must be
integral to modern machineries.

There are a number of mechanisms that lead to a rolling-bearing failure. The most
common defects are caused by material fatigue as a function of running time. This
particular defect type usually begins with small cracks that are formed under the surface
of bearing elements. During operation, these cracks propagate to the surface due to cyclic
loads and may result in surface pitting and spilling. Other factors of bearing failure
include overheating, misalignment errors, corrosion and poor lubrication, all of which
make the bearings under operation subject to incipient faults. If undetected, these small
faults will give rise to bad performance and may lead to failure of the machine [98]. In
the vast majority of cases, the bearing behaviour requires no more than subjective

supervision by the operating staff. Some useful indicators of bearing damage include vibration and high operating temperatures, as well as elevated levels of audible noise. However, advanced condition monitoring techniques can be incorporated to provide a more robust diagnosis of the bearing faults [6].

To facilitate a clear understanding of the state-of-the-art of the condition monitoring schemes, the construction and operation of different bearing types are considered and the induced fault signatures into machine vibration will be discussed in the remaining sections of this chapter.

2.2 Bearing Theory

Bearing designs can be categorically summarised into two types; sliding bearings and rolling bearings. Sliding bearings are further split into linear and journal bearings. Whereas linear bearings offer high degrees of precision, the journal types can tolerate axial shaft displacements within certain limits. Those bearings that transfer loads using rolling elements are denoted "rolling bearings". Depending on the type of the incorporated rolling elements, rolling bearings can be divided into sub-categories of "ball bearings" and "roller bearings". As illustrated in Figure 2-1a, the balls in a ball bearing transfer the load over a very small surface-point that is in contact with the raceway. The load-carrying capacity of these bearings is comparatively lower than that achieved by a roller bearing, where the rollers transfer the load via a line contact (see Figure 2-1b) with the raceways.

(a)   (b)
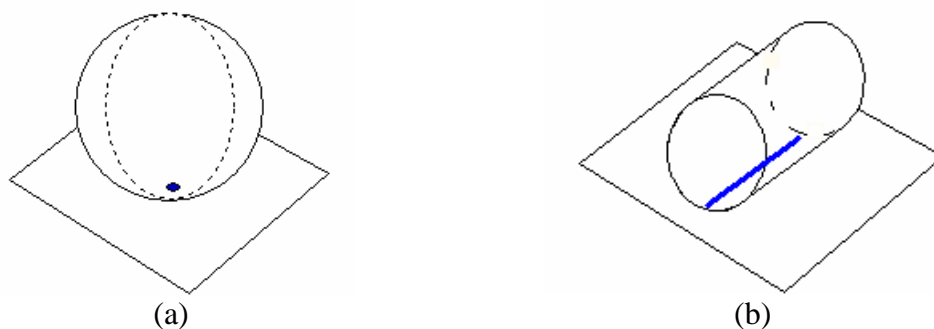
Figure 2-1 Type of contacts (a) point contact (b) line contact

One of the influential factors that make rolling-element bearings so popular for most types of machinery is their very low internal friction of the lubricant at high speeds due to churning and shear forces within the lubricant. In a plain bearing design, as shown in

Figure 2-2(a), the shaft slides in a housing or bushing that is separated by a relatively good lubrication film, whilst in a rolling-element bearing (see Figure 2-2b), the inner ring rolls over the rolling elements that are placed in between the inner and the outer rings. Under the same load conditions, the friction generated in a plain bearing is greater than that of a rolling bearing [86]. Furthermore, as can be seen in Figure 2-2(c), the friction in a plain bearing varies with respect to varying rotational speeds, whereas, for the rolling type, the bearing friction is practically a constant.
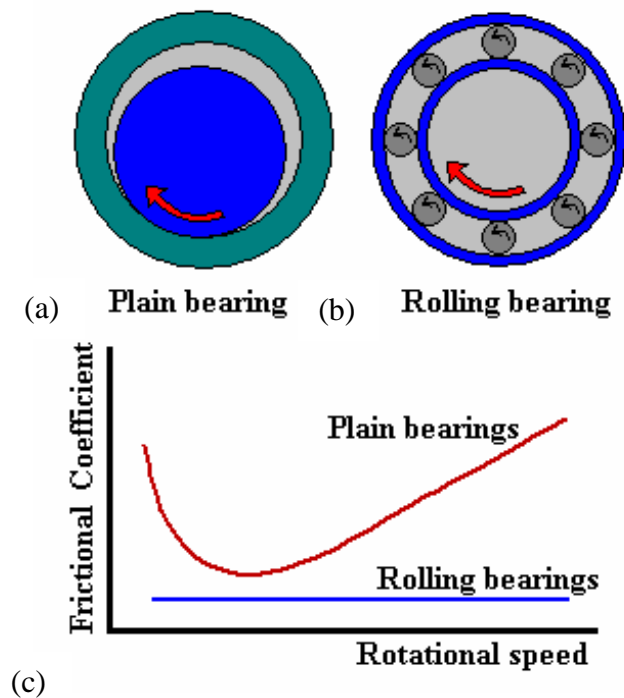
Figure 2-2 Frictional behaviour of (a) plain and (b) rolling bearings, showing (c) frictional coefficients as a function of rotational speed

2.3   Roller Element Bearing Type

The rolling-element bearings can be categorised into two main groups of ball and roller bearings, based on the shape of the rolling elements. Ball bearings are usually used in light- to moderately heavily-loaded applications and are well-suited for high-speed operations. On the other hand, roller bearings are able to support comparatively heavier loads; therefore, roller bearings are more favoured for applications such as in turbine engine main-shafts, transmission and gearbox with high loading capacities. Rolling-element bearings can be further classified into radial and thrust bearings, based on the

direction of applied load. Table 2-1 provides a list of different types of rolling-element bearings. Since most rolling bearing types, either radial or axial, can carry both radial and axial loads, it is difficult to distinguish between the two types. However, those bearings with a contact angle of $\alpha \le 45$ (shown in Figure 2-3) are considered radial and their load ratings are specified radially. In contrary, bearings with contact angles of $\alpha > 45°$ are considered axial bearings and are rated by their axial load capacity.

Table 2-1 Bearing Type [99]

Rolling Bearings	Ball Bearings	Radial ball bearings	Single-row deep-grove bearings Maximum capacity type ball bearings Single-row angular-contact ball bearing Duplex angular-contact ball bearings Duplex row angular-contact ball bearing Four-point-contact ball bearings Self-aligning ball bearings
		Axial-ball bearings	Single-direction axial ball bearings with flat back face Single-direction axial ball bearings with sealing ring Double-direction axial ball bearings with flat back face Double-direction axial ball bearings with sealing rings Double-direction angular-contact axial ball bearings
	Roller bearing	Radial roller bearings	Single-row cylindrical roller bearings Double-row cylindrical roller bearings Needle roller bearings Single-row tapered roller bearings Double-row tapered roller bearings Spherical roller bearings
		Axial-roller bearings	Cylindrical-roller axial bearings Needle-roller axial bearings Tapered-roller axial bearings Spherical-roller axial bearings
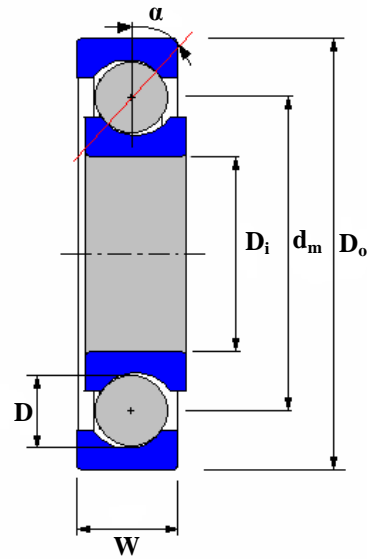
Figure 2-3 Bearing geometry

2.4 Roller Bearing Components

Roller bearings generally consist of four main basic parts. As illustrated in Figure 2-4, these parts include the rolling element, outer race, inner race and cage. Some bearings may also contain additional components such as guide rings and seals. The bearing load can be supported by the rolling elements and the inner and outer races, whilst the separation of adjacent rolling elements is provided by the cage. This separation allows for a non-metal-to-metal contact between two adjacent moving rolling element [100].
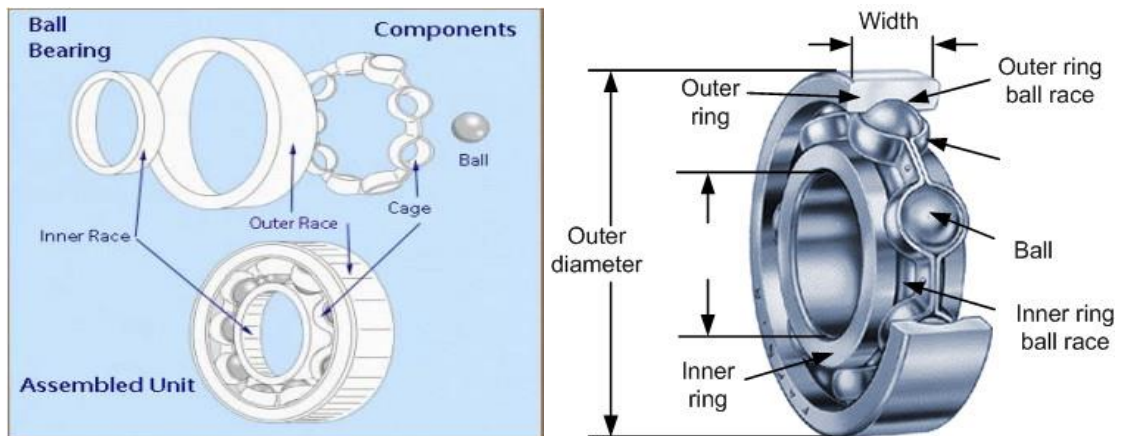
Figure 2-4 Rolling element bearing components [101]

2.4.1   Rolling Elements

As shown in Figure 2-5, the rolling elements may come in the form of balls, cylindrical rollers, spherical rollers, tapered rollers or needle rollers. These elements rotate against the inner and outer raceways and transmit the load imposed on the bearing via a small surface that is separated by a thin layer of lubricating film. The rolling elements are composed of carbon chromium steel, giving these elements the bearing steel name.

2.4.2   Outer Race

The outer race is mounted in the housing of the machine and in most cases is stationary. Depending on the shape of the rolling elements, the raceways, where the rolling elements run may come in different forms.

2.4.3   Inner Race

The inner race is mounted on the shaft of the machine and in most cases revolves at the same rotational speed as the shaft. The bore can be either cylindrical or tapered.

2.4.4   Cage

The cage allows for the separation of adjacent rolling elements to prevent metal-to-metal contact between them during operation, which can lead to poor lubrication conditions. With many bearing types, the cage is responsible for holding the bearing structure together during handling. Bearing cages are often made up of cold-rolled steel strips.

2.4.5   Seals

Seals are essential for reliable operations and help prolong the bearing's service life. They protect the bearing from contaminations and keep the lubricant inside the bearings.

2.4.6   Guide Race

Guide races are used in some spherical roller bearings that necessitate extremely high quality. The main function of the guide races, as the name suggests, is to guide the rollers to achieve a rotational movement that is parallel to the shaft, which allows for an even distribution of the load over the raceways.
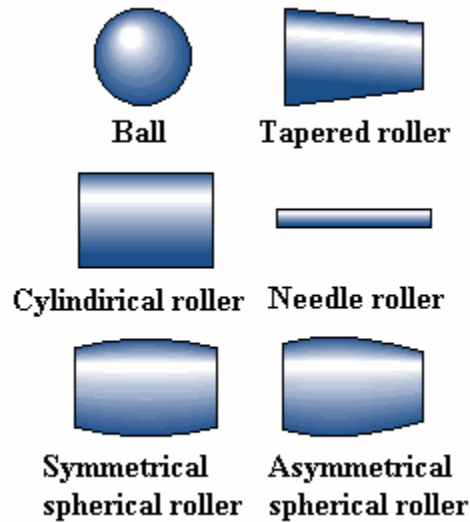
Figure 2-5 Types of rolling elements

2.5   Bearing Failure Modes and Their Causes

Healthy bearings are key to proper operation of most industrial machines as they are most likely to fail and cause machine downtime. This is due to the fact that all the applied forces to the machine during operation are usually transmitted through the bearings [14]. Therefore, rolling-element bearings have been the subject of extensive research over the past years with a view to improve their reliability. Most critical applications often involve a large number of bearings. Thus, system failure due to any individual bearings failing can dramatically increase. There are many reasons for early failures, such as excessive loading, inadequate lubrication, careless handling, ineffective sealing and/or insufficient internal bearing clearance due to tight fits. Each of the aforementioned deteriorating factors can eventually lead to the formation of a particular damage that is specific to the causing mechanism and can leave its own special imprint on the bearing.

The different types of the mechanical bearing failure and their frequencies of occurrences are listed in Table 2-2. Wear is the most common bearing failure factor, which is caused by lack of lubrication. Another particular failure in rolling-element bearings is caused by a chemical reaction that occurs between the oil and the surface of the bearing, generally from water or other corrosive materials present in the oil. Failure in rolling-element bearings can also be caused by dimensional discrepancies, which could be caused by manufacturing errors, improper handling or installation and severe overloading during service. Moreover, foreign objects carried by contaminated lubricant can become trapped

inside the bearing between the rolling elements and the raceway, leading to the failure of the bearing. In order to detect and treat these failure mechanisms at an early stage, it is imperative to understand the principal causes of these mechanisms and the diagnostic signatures [14, 102-104] they may entail.

Table 2-2 Bearing failure distribution [102]

Reason	Failure present (%)
Corrosion	35
Dimensional Discrepancies	29
Foreign Objects	24
Other	10
Fatigue	2

Those bearing failures that are not responsible for material fatigue are generally classified as premature failures. Most premature bearing failures occur as a result of faulty mounting, improper lubrication, contamination, unsuitable handling and improper maintenance [105]. Similar to previously mentioned failure mechanisms, each of these premature failures can result in a different bearing failure with its own characteristic damage. Such damage, also known as a primary damage, can lead to secondary failure inducing damages such as spalling and cracks. In practice, most failed bearings demonstrate a combination of both primary and secondary damages [106, 107]. The different types of bearing damages are summarised in Table 2-3 [108].

Table 2-3 Bearing damage types [108].

Damage Type		
Primary Damage	Secondary Damage	Other Damage
Wear	Spalling	Roll out
Indentations	Cracks	
Smearing	Cage damage	
Surface distress	Scoring	
Corrosion		
Electric current damage		

2.5.1   Primary Damage

2.5.1.1   Wear

Under normal circumstances, there is no noticeable wear induced in rolling bearings. However, wear can occur as a result of foreign objects penetrating into the bearing

structure or when the rolling elements are inadequately lubricated, see Figure 2-6 [14, 109]. Foreign materials can enter the bearing during poor maintenance practice or a worn seal, which can result in a premature wear of the bearing. Depending on the nature of the wear different corrective actions can be taken. If the wear is mild (i.e. involves very light surface bruising or denting), the bearing housing and rolling elements can be thoroughly cleared and properly adjusted, before going back into service again. Those bearings with excessive wear from penetration of foreign objects should be completely replaced. Similarly, abrasive wear can be caused by fine dust, metal, particles, grinding dust, or normal airborne dirt that is commonly present in a factory. Metal components in constant contact with each other can create fine metal particles in the lubricant. This can result in wear in the roller end and rib face, as well as in the roller body and races. Consequently, even a small amount of wear can change the bearing adjustment in the long run, which can cause bearing misalignment in extreme cases and thus failure. This can also have a detrimental effect on other components in the application. If the foreign material particles are fine enough, a polished or mirror-finish surface can occur [110].

Figure 2-6 Example of bearing wear caused by abrasive particles [111]

Adhesive wear occurs as result of the deformation, shearing and plucking away of material at points of adhesion as two surfaces slide over each other. These adhesion points arise at roughness peaks. The adhesive wear amount is largely proportional to the load and to the distance over which the surfaces have slid, and inversely proportional to the hardness of the surface on which wear occurs.

Lack of clearances due to ineffective seals and lubricants contaminated by worn particles from brass material cages can cause small indentations around the raceways and the

rolling elements. This particular wear is distinguished by its signatory dull and worn surfaces [101]. On the other hand, wear caused by inadequate lubrication often manifests itself as mirror-like worn surfaces and at late stages, a blue to brown discoloration of the lubricant follows. Lubricants that have gradually been used up or have lost their lubricating properties are the main reasons of this type of wear, which can often result in a temperature rise and subsequent bearing failure [112].

Wear caused by vibration, also known as false brinelling, can be characterised by the depressions that appear in the raceways. This particular wear type arises as a result of a small relative motion between the balls/rollers and the raceways, whilst the bearing is stationary. The signatory depression marks, also called flutings, appear in rectangular shapes for roller bearings and in circular forms for ball bearings. The bottoms of these depression marks may be either bright or dull and oxidised. Bearings imposed to vibrational wear are usually found in abandoned machines that have been out of service for a long period of time and are located close to the source of the vibration. When compared with ball bearings, roller bearings are more prone to vibration-related wears [107]. Misalignment is another factor of failure in bearings. This particular failure can be detected on the raceway of the non-rotating ring and is caused when a rolling-element wear path is not parallel to the edges of the raceway. Consequently, excess misalignment can cause an abnormal temperature rise and/or a heavy wear in the cage pockets. The most common causes of misalignment are bent shafts, burrs or dirt on the shaft, shaft threads not being square with the shaft seats and locking nuts with faces that are not perfectly square with respect to the thread axis.

2.5.1.2 Indentation

Indentations in the raceways and rolling elements may occur if the mounting pressure is applied to the wrong ring, or if the bearing is exposed to overloading whilst being at rest. The reader is referred to Figure 2-7 for an example of this type of wear. On the other hand, a dent caused by a faulty mounting or overload is called true brinelling. This defect is characterised by indentations that appear at intervals corresponding to the roller spacing in the raceways of both the inner and outer rings. The presence of these indentations in the raceways can increase the bearing noise and vibration, leading to a premature bearing failure. Common causes for this type of failure include imposing the wrong ring to mounting pressure, excessively hard drive-up on tapered seating and

overloading whilst stationary. Indentations can also occur when a sharp impact is encountered by the bearing during mounting or dismounting procedures.

Those indentations caused by foreign particles are termed contamination failure and are one of the leading causes of premature bearing failure. These defects are distinguished by small indentations that are distributed around the rolling elements and the raceways for both the inner and outer rings. Foreign particles, such as airborne dust, dirt, burrs, or any abrasive materials can enter the bearing and cause indentations when rolled into the raceways by the rolling elements. Indentations caused by larger metal chips or particles of dirt are identified as pitting and bruising. The depth and number of the indentations caused by these large particles determine whether the bearing must be replaced or not.

Figure 2-7 Bearing surface indentation [111]

2.5.1.3 Smearing

Smearing occurs when two inadequately and insufficiently lubricated surfaces (too little and/or too old) slide against each other whilst loaded, resulting in the transfer of material from one surface to another. This particular bearing defect may occur on the guiding faces of the flanges and/or on the ends of the rollers, when imposed to heavy axial loadings with inadequate lubrication in cylindrical and tapered roller bearings and in spherical roller bearings with guide flanges. The smeared surfaces usually have a torn appearance, as illustrated in Figure 2-8. When smearing occurs, the material is generally heated to a high temperature, which causes re-hardening to takes place. The re-hardening

process usually manifests itself as a localised stress concentration and may cause cracking or flaking [101]. In addition, a discolouration of the roller ends and flange faces are detected with smearing. A scored and discoloured area also appears at the start of the load zone in the raceways and on the surface of the rollers. This particular type of smearing is often caused by roller acceleration when the roller enters the load zone.

Figure 2-8 Bearing surface smearing [111]

In cylindrical roller bearings, transverse smearing marks (steaks) usually appear at intervals equal to the distance between the rollers in the raceways. This occurs when the ring is out of line with the roller and cage assembly on the other ring during the mounting operation. Smearing can also occur on the surface of the inner ring bore or on the surface of the outer ring, when heavily loaded rings are moved relative to the shaft or housing. In this case, scoring and discoloration on the affected area appears. Smearing can also occur in thrust-ball bearings, when imposed to light loading at very high rotational speeds, resulting in diagonal smear steaks in the raceways.

2.5.1.4 Surface Distress

When the lubricant film between the raceways and the rolling elements becomes too thin due to inadequate or improper lubrication, the peaks of the surface asperities can momentarily come into contact with each other. In this case, a small crack forms on the surfaces, as shown in Figure 2-9. This is known as surface distress, which is different to fatigue crack that initiates below the surface and develops into flaking. Initially, the damage caused by surface distress is not visible to the naked eye. However, the defect gradually turns into small shallow craters with crystalline-fracture surfaces, interfering with the smooth operation of the bearing.
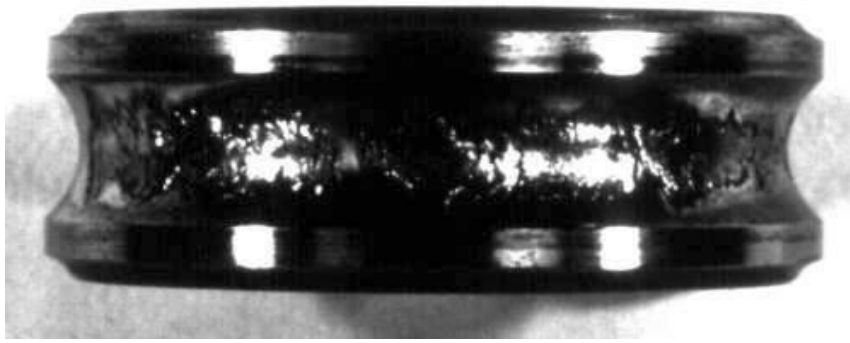
Figure 2-9 Example of surface distress in bearing surface [111]

2.5.1.5 Corrosion (rust)

Corrosion generally results in an increase in the bearing vibration, followed by wear, with subsequent increases in radial clearance or losses of preload. Corrosion or rust in bearings is developed as a result of water and/or corrosive materials (through a chemical attack) entering the bearing structure, which can have a detrimental effect on the lubricant properties. As the rust layer is further developed, the lubricant loses its chemical properties, leading to its failure as a protective barrier for the steel surfaces of the bearing elements. As illustrated in Figure 2-10, this process will soon develop into what is called a "deep-seated" rust. This type of rust is usually caused by the water, moisture or corrosive substance that sits on the bearing's exposed areas for a long period of time. The diagnostic signature of corrosion defects in an appearance of greyish black steaks across the raceways, coinciding with the rolling elements' spacing. When the deep-seated rust defect, also known as pits, occurs the bearing is no longer useable. This is due to the fact that pitting is a serious defect, which can further develop into premature spalling.

Also referred to as loose fit failure, fretting corrosion takes place as a result of a relative movement between the bearing ring and the shaft or housing, due to a loose fit. Consequently, this particular type of corrosion can lead to an unbalanced load distribution across the bearing rings, as induced by for example mechanical vibration in the shaft. With fretting corrosion, rusted areas can be visually inspected on the outside surface of the outer ring or in the bore of the inner ring. Moreover, the raceway path, as shown in Figure 2-10 can also be heavily marked at corresponding positions.

Figure 2-10 Deep-seated rust on the bearing surface [14, 111]

2.5.1.6 Electric Current Damage

Damage will occur when large electric currents conduct through the rolling elements in a rotating or non-rotating bearing to other parts. The process is similar to electric arc welding at the contact surfaces. The effect is a single burn or a line of small burns, called fluting, along the path crossed by the rollers in the raceways. The diagnostic feature of electrically-induced damages is the appearance of a dark brown or greyish black fluting or craters in the raceways and rollers. In Figure 2-11, an example of the trace of a localised burn on the raceway surface can be observed. In contrast to the raceways, the effect of electric damage on the rolling balls is a dark discoloration only. This type of damage is frequently seen in electric motors, but can be eliminated by applying a ceramic coating on the outside surface of the outer ring.

Figure 2-11 Electric pitting in bearing surface [107]

2.5.2   Secondary Damage

2.5.2.1   Spalling (flaking)

Spalling or flaking occurs as a result of normal fatigue, as shown in Figure 2-12. The criterion for fatigue damage largely depends on the nature of the application. In order to establish a rating system for bearing performance capabilities under spalling, in reference [101], the criterion for fatigue damage has been arbitrarily set as a small size of 0.01 inch^2 or 6.45 mm^2 in area. If these limits are exceeded at any time, the bearing is said to have reached its end of service life. Although, the bearing might still be able to continue its functionality well beyond this point.

Loud audible noises often serve as a good warning sign for a bearing spall condition at a certain stage, indicating bearing replacement is required. Several factors generally contribute to the development of a premature spalling. Some of which include, exceeding the maximum allowable load limit, preloading due to incorrect fits or excessive drive-up on a tapered seating, oval distortion owing to shaft or housing seating, and axial compression as a result of thermal expansion. Preloading is often caused by tight fits, excessive drive-up on a tapered seating, single-row angular-contact ball bearings or tapered roller bearings incorrectly adjusted to give excessive preload and great temperature mismatches between the inner and outer rings. Spalling due to preloading is indicated by heavy rolling-element wear paths in the bottom of the raceway around the inner and outer rings. This condition arises when the inner and outer rings engulf the rolling elements so tightly, exceeding the specified internal radial clearances. In such case, a rapid temperature rise is experienced, resulting in a severely marked path pattern in both inner and outer raceways. Preload spalling usually occurs in the most heavily loaded zone.

An oval shaft or bearing housing structure can cause flaking. The oval housing is a common defect in split housings and machine frames. As a result, a heavily marked spalling path pattern at two diametrically opposing sections of either bearing rings usually appears. Excessive loading is another common source of premature failure in bearings. It is identified by heavier ball wear paths, evidence of overheating, and a deeper spalling or fatigue area.

Spalling caused by axial compression, also known as reverse loading failure occurs when a bearing is incorrectly mounted. Excessive preloading of angular contact ball bearings and tapered roller bearings are the factors responsible for this type of spalling. As a result, a heavily marked path pattern appears on either side of both the inner and outer rings on deep-groove ball bearings. Also in self-aligning ball bearings and spherical roller bearings, severely marked raceway path patterns for one row of rolling elements can be observed. This is similar to the type of damage that results from preloading on single-row angular-contact ball bearings and tapered roller bearings.

Figure 2-12 Spalling or flaking in bearing surface [111]

Misalignment of bearings can also have a detrimental effect on the bearing's lifetime, depending on the amount of misalignment and operating conditions such as applied speeds and loads involved. If misalignment exceeds certain limits, high edge stresses and subsequent fatigue spalling takes place. This is due to the concentrated load in one area on the bearing races [23].

2.5.2.2 Cracks

Cracks may occur in bearing rings for various reasons. The most common one is lack of care, while the bearings are being mounted or dismounted. Rough treatments such as hammer blows may cause fine cracks to form, which in turn, result in chipping and/or breaking of the bearing rings under operation. Another factor accounting for ring cracking is excessive drive-up on a tapered seating or sleeve. The resulting tensile stresses built up in the rings, as shown in Figure 2-13, can aid the generation of cracks, when the bearing is put into service. Similarly, if the ring is struck with a hummer or hard chisel during mounting/dismounting process, cracks or broken pieces are likely to appear on one face of the bearing. Those cracks that intersect in the inner race and generally

longitudinally in the outer race are the diagnostic signatures of fretting corrosion defects, whilst cracks occurring at right angles to the direction of slide are generated by smearing defects.

Figure 2-13 Showing an example of a crack defect in the bearing surface [111]

2.5.2.3 Bearing Cage Damage

Cage breakage does not happen often. However, upon occurrence, it is often difficult to identify the cause of the failure since other components of the bearing will also be damaged too. However, there are certain identifiable causes of cage failure that include mechanical vibrations, excessive speeds, wear and blockage. An example of a bearing cage breakage is illustrated in Figure 2-14. Exposure to continuous vibrations can cause fatigue cracks to form in the cage material. Sooner or later these cracks will lead to cage fracture. On the hand, if the bearing is run at speeds beyond the cage specification, the cage becomes subjected to heavy forces of inertia, which can eventually lead to fractures [109].

Cage wear may be caused by insufficient lubrication or by abrasive particles. The basic function of rolling bearings is to avoid sliding friction. However, sliding in the contacts between the cage and other components of the bearing is inevitable. As a result, in cases where bearing lubrication is inadequate, the cage is the first component to be affected. Lack of lubrication can also cause peeling, an effect that produces a shallow frosted appearance on the surface, usually at a depth of less than 0.0001 inches [110]. The cage is always constructed from softer materials than the other bearing components, causing a relatively faster wear. Another cause of cage failure is fragments of flaked material or

other hard particles becoming wedged between the cage and a rolling element. When this happens, the rolling element is retained from rotating with respect to its own axis, leading to a cage failure.

Figure 2-14 Bearing cage damage [107]

2.5.2.4 Scoring (galling)

Insufficient lubrication between the rib face and the roller ends results in a metal-to-metal contact in these areas, which causes scoring. An example is shown in Figure 2-15. In a bearing assembly, scoring is easily noticeable on the roller ends. Scoring of the roller ends implies that the rib face is also scored. This particular type of bearing damage generally changes the geometry of the rib face and the roller ends.

Figure 2-15 Bearing scoring [111]

Continued operation of a scored bearing will entail some serious consequences, for example the rollers can skew under the cage bridges and become distorted and broken. Rollers may also become physically welded to the races and possibly the rib, stopping the bearing and severely damaging other expensive components. In such case, heat damage

becomes evident on the rib's outside diameter and the roller ends. Generally, heat damage changes the hardness of the bearing and is often associated with a dark blue spot or, in extreme cases, a black spot [110].

2.5.3   Other Damage

2.5.3.1   Rollout

When a bearing is highly overloaded, the applied stresses are employed deeply into the race. Moreover, if the race has had a hardened treatment, the stress levels may exceed the strength of the relatively soft core. In this case, a rollout, also called sub-case yielding or case crushing, defect occurs. Under such conditions, the core of the race will plastically deform only in the axial direction, since it is constrained in the radial direction by the housing. As the core expands axially it burdens the case, causing a circumferential fracture to the case. As shown in Figure 2-16, this type of damage exhibits circumferential cracks in the load zone.

Figure 2-16 Bearing rollout [111]

2.6   Friction and Wear of Rolling Element Bearing

The concepts of rolling element bearing friction are very important in terms of understanding the behaviour of machine elements. In rolling bearing friction resistance to motion arises from following typical sources [88, 113],

- Rolling friction that is generated at the raceway contacts as a result of elastic deformation under load.

- Sliding friction that is generated as a result of sliding contact of the cage with rolling elements and guiding surfaces, sliding from unequal curvatures in contact areas, sliding between the ends of rollers and ring flanges, and seal friction.

- Lubricant friction, which is generated as result of viscous shearing on raceway surfaces; rolling element, and cage.

- Rolling contact friction that results from elastic deformation between loaded rolling elements and their raceways.

Figure 2-17 depicts a microslip, which occurs in the rolling direction as the roller is depressed and the raceway stretches or deformation within the loaded rolling contact, which produce friction and cause the roller to go forward a distance minutely less than its circumference in one revolution.
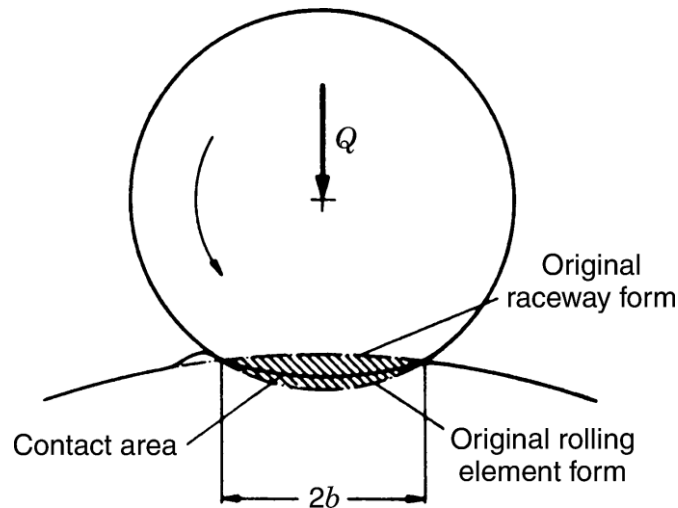
Figure 2-17 Rolling element and raceway deformation in the direction of rolling [88]

Additional sliding results in a ball bearing with the contact area in the raceways being curved transverse to the rolling direction (Figure 2-18). Since the rolling diameter varies throughout the contact zone, surface speed also varies. The middle portion of the ball slides opposite to the rolling direction, and the outer portion slides in the rolling direction. Frictional forces are balanced to result in pure rolling at points D and D'.

Insufficient lubrication between bearing surfaces often leads to wear as result of metal-to-metal contact. Wear rates are also increased usually as result of prompt speed changes, high speeds and load, and decreased seal effectiveness.

Wear will significantly increase the bearing internal clearance, vibration and noise, local surface stresses increase from raceway surface changes.
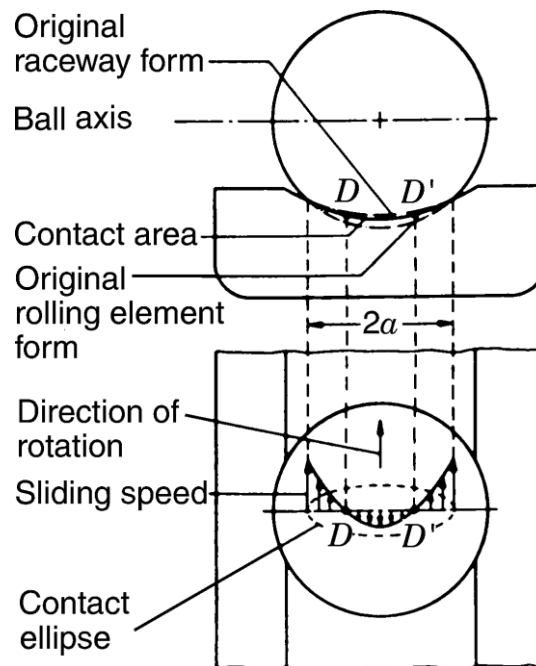
Figure 2-18 Sliding motion resulting from the curvature of the contact area [88]

2.7   Summary

In this Chapter, bearing theory (Section 2.2), rolling bearing type (Section 2.3) and roller bearing components (Section 2.4) were introduced. In addition, the rolling bearing failure model and their causes (Section 2.5) including primary and secondary damages were briefly explained. Moreover, rolling bearing friction and wear and how it influences the internal radial clearance was detailed too (Section 2.6).

CHAPTER THREE

VIBRATION ANALYSIS TECHNIQUES FOR ROLLING ELEMENT BEARINGS FAULT DETECTION AND DIAGNOSIS

This chapter provides an overview of rolling element bearing vibration analysis techniques and the vibration measurement methods that are used for the condition monitoring and defect detection of roller bearings. In addition, the dynamic responses of various roller bearings, arisen from local defects are also reviewed. It is shown that most common bearing defects can be characterised by the resulting peaks appearing in the obtained vibration spectra.

3.1   Introduction

All mechanical equipment in motion generates a specific vibration profile, which is a reflection of their operating conditions. Vibration analysis is a statistical tool that is widely applied in many engineering sectors, including in condition monitoring of mechanical components used in industrial machinery. In mechanical condition-monitoring systems, vibration analysis techniques form the basis of predictive maintenance and diagnostics [98]. There are many mechanical problems that can be directly associated with the features observed in the vibration profile of a system. Some examples of such mechanical problems include the presence of friction (rubbing), hydraulic forces, aerodynamic forces, electromagnetic forces, torque variations, defective bearings, damaged gears, loose components, bent (twisted) shafts, misalignment, eccentric component and imbalance in rotating parts [98, 114].

In literature, there has been a huge amount of research on vibration analysis techniques for bearing condition monitoring. In this case, the machine vibrations induce a cyclic excitation at specific intervals, which can be transmitted to adjacent components or adjoining structures, causing parts of the machine to resonate at different frequencies. These excitations can either be present during normal machine operation, or they can appear as a result of changes in the dynamic properties of the machine, such as a roller bearing failure. A change in the measured vibration signal can not only indicate a change in the machine's conditions, but can also be used to locate the source and cause of the vibration. When a machine is operating properly, the vibration level is small and constant. Faulty components usually cause significant changes in the machine's dynamics, leading to much higher vibration energy levels with intrinsic patterns. The amount of information contained in the measured vibration signals is huge [7] and thus, requires advanced techniques for processing.

Roller-element bearings produce impulses in the vibration signal, as local discontinuities in the material such as scratches or dents start to appear on different surfaces. The resulting vibration signal is modulated by the transmission paths (i.e. bearing structure) to the sensor. Therefore, the received signal will be covered in background noise. In the premature times of defect growth (e.g. fatigue), the impulse signal will generate an insignificant amplitude owing to the normal damping provided by, for instance the lubricants, will rapidly decline before the next excitation occurs. On the other hand, both

patterns of time and amplitude will occur in the signal, that allow for the identification of the bearing fault severity and the location.

Vibration monitoring of roller-element bearings has consistently produced good results, owing to the advancements in signal-processing techniques. For example, envelope analysis has been used for bearing fault detection for many years. In contrary to the previous works presented in literature, in this thesis, the modulation signal bispectrum technique is adopted for its reliability and improved signal-to-noise ratio.

3.2   Vibration Response due to Bearing Defects

Two approaches can be taken to study the vibration responses of different bearing defects. The first one is to run the bearing until failure, whilst monitoring the changes in their vibration response. Usually, accelerated failure tests include overloading, over-speeding or off lubricants. The second approach is to intentionally introduce defects into the bearing structure and compare the measured vibration responses under both healthy and faulty scenarios [15].

3.2.1   Dynamic Responses of Roller Bearings to Local Defects

Many dynamic models of rotating bearing elements have been developed in literature to represent the vibration responses of the ball bearings, raceways and rolling elements generated by defects [11, 13, 115]. A loaded healthy bearing undergoes many complex forces and moments. These include static and dynamic forces. The static forces can be due to any designed preloads, the loads (weights) of the shafts and other moving components. On the other hand, the dynamic forces include centrifugal forces acting towards the centre of rotational motion and frictional and traction forces due to fluid pressure build-up or the relative movement of surfaces in contact with each other.

For a typical bearing operation at constant speeds under a constant load, all the forces will be in quasi-equilibrium and thus, the sum of all forces will be negligible. However, when the rolling element encounters a local defect, a rapid elastic deformation occurs on the bearing elements, leading to generation of a transient force. These transient forces are detected by the resulting movements of the bearing components and are not normally simple, but can include impact and oscillatory contact between any two of the rollers, the raceways and the cage, as well as slippage between the cage and the roller elements.

Nevertheless, the periodic nature of the bearing movement will impose a periodicity on the signals generated. Therefore, a frequency domain analysis of the resulting signal can be used as a powerful tool for bearing defect detection [116, 117].

3.2.2   Bearing Fault Signatures and Machine Vibration

Vibration data is an excellent indicator for bearing faults. Every time a rolling element passes over a particular defect on the raceway, an impact is created between the rolling element and the raceway. This impact causes the bearing structure to be excited at its natural frequencies. All defects, whether distributed or local, will produce salient fault signatures in the machine vibration. Local defects produce predictable signatures referred to as, characteristic fault frequencies. Whilst distributed defects do not necessarily produce predictable frequency components [15].

3.2.3   Characteristic Frequencies of Bearing Faults

Rolling-element bearing, as presented in Figure 3-1, consists of an inner race, an outer race, rolling elements and a cage that holds the rolling elements in a given relative position. In order to identify the characteristics of the vibration responses due to faults, the bearing rings are assumed to be isolated continuous systems. It is further assumed that: (1) All rollers are equal in diameter; (2) There is a pure rolling contact between rollers, inner race and outer race; (3) There is no slipping between the shaft and the bearing; (4) Outer race is stationary and inner race rotates. The relative velocity between the rollers, inner race and outer race is zero. This is due to the pure rolling contact that exists between these components.

Race surface fatigue results in the appearance of spalls on the inner race, outer race or the rolling elements. If one of the races encounters a spall defect, it will almost impact with the rolling elements periodically. In this case, the fault signature is represented by successive impulses, with a repetition rate that is strongly dependent on the faulty component, geometric dimensions and the rotational speed. The period between every impact is different for all the listed bearing elements in Figure 3-1 and is a function of the bearing geometry, rotational speed and the load angle. For a fixed outer race bearing, the theoretical characteristic fault frequencies can be calculated using Equations (3-1) to (3-4). The reader is referred to reference [118] for a complete derivation of these equations.
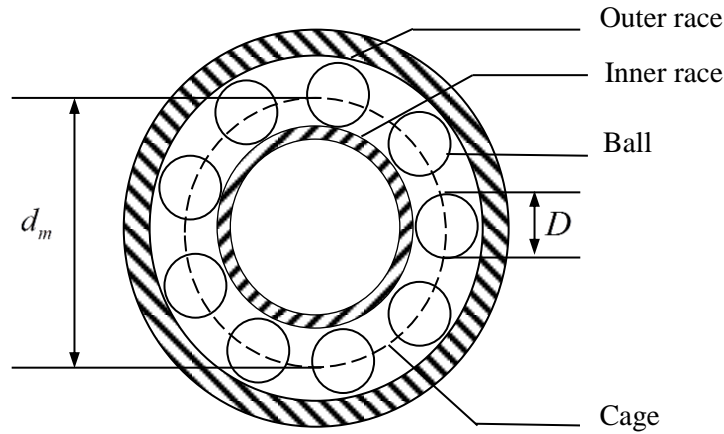
Figure 3-1 Roller element bearing components

The cage rotational frequency or the fundamental train frequency (FTF) is expressed by,

$$f_c = \frac{1}{2} F_s (1 - \frac{D}{d_m} \cos \alpha).$$

(3-1)

The outer race defect frequency (BPFO) is expressed as,

$$f_o = \frac{N}{2} F_s (1 - \frac{D}{d_m} \cos \alpha).$$

(3-2)

Similarly, the inner race defect frequency (BPFI) can be given as,

$$f_i = \frac{N}{2} F_s (1 + \frac{D}{d_m} \cos \alpha).$$

(3-3)

Finally, the ball spin frequency (PSF) is given by,

$$f_r = \frac{d_m F_s}{2D} (1 - \frac{D^2}{d_m^2} \cos^2 \alpha)$$

(3-4)

where, d_m is pitch circle diameter, D is ball diameter, α is contact angle, N is number of balls and F_s is the shaft rotational frequency in Hertz. In practice, there is always a slight amount of sliding and slippage, especially when a severely worn bearing is under dynamic loads. Therefore, practically measured vibration frequencies may differ slightly from those calculated theoretically using Equations (3-1) to (3-4) above.

The work of Robert et al. [118] shows that, there will always be some slippage due to the angle α varying with the position of the rolling elements in the bearing. The load angle on

each rolling element changes as the results of the change in the axial load. Essentially, each rolling element has a different effective rolling diameter at different speeds to another. However, the cage limits the deviation of the rolling elements from their mean position, causing some random slippage to occur. The resulting change in bearing frequencies is typically in the order of 1–2%, both as a deviation from the theoretically calculated values and as a random variation around the practically measured mean frequency [119].

In this research, the bearing type 6206ZZ (P206) is chosen for an experimental study on bearing fault detection and diagnosis, based on its widespread adoption in industrial machineries as well as its high capacity for carrying heavy loads. As measured in the laboratory, the adopted bearing type for testing has a the following parameter values; $N = 9$, $D = 9.53\ mm$ and $d_m = 46.4\ mm$. Knowing the shaft rotational frequency to be $F_s \cong 25\ Hz$ and taking α to be zero as there is no axial load, Equations (3-1) to (3-4) can be employed to calculate the fundamental fault frequencies, corresponding to the defects seeded individually into the different test bearings. Table 3-1 presents the theoretically calculated characteristic frequencies for the aforementioned parameter values.

Table 3-1 Calculated defect frequencies for bearing type 6206ZZ

Defect Position	Calculated Frequency (Hz)
Inner race	135.60
Outer race	89.40
Rolling elements	58.30
Cage	9.93

3.2.4 Rolling Element Bearing Vibration Signal

In the study performed by the authors in [120], the vibration signal $x(t)$ from a rolling-element bearing with a single-point fault is expressed as,

$$x(t) = x_f(t).x_q(t).x_{bs}(t) + x_s(t) + n(t) \tag{3-5}$$

where $x_f(t)$ is the basic impulse series produced by the fault as a result of repetitive impacts between different surfaces in the bearing (the repetition period is $T_f = 1/f$ and f is the characteristic frequency of the bearing fault); $x_q(t)$ is the modulation effect due

to non-uniform load distribution on the bearing and the cyclic variation of transmission path between the fault impact site and the transducer; $x_{bs}(t)$ is the bearing induced vibrations; $x_s(t)$ is the vibration induced by the machine; and $n(t)$ is a Gaussian white-noise.

The modulating effect $x_q(t)$ is partially induced due to the bearing geometry, but more significantly by the position of the vibration sensor relative to the fault location, where optimal sensor position may not be possible or perhaps undesirable. Failing to consider for the modulation effect, the efficacy of the signal model in real-life situations can be significantly changed. The signal $x_s(t)$ is an unwanted, structured, and predictable damped harmonic signal that is also considered to be a source of noise. Finally, the vibration component $n(t)$ is an unpredictable measurement noise that is present in any practical measurement system.

3.2.5 Amplitude Modulation

Amplitude modulation is the variation of the amplitude of one signal component as a result of the influence of another signal component. Thus, two different signals are involved at any time, where the higher frequency signal is called the modulated signal, and the lower frequency one is labelled the modulating signal.
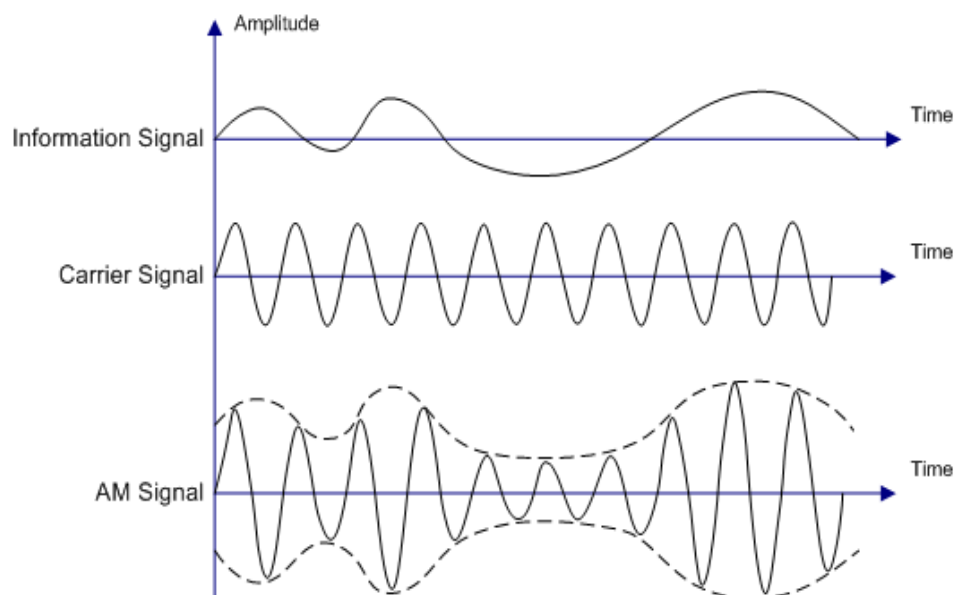
Figure 3-2 Example of signal amplitude modulation

The modulated signal always rides along the envelope of the higher frequency or carrier signal. In bearing defect-detection, an amplitude modulation occurs in the generated vibration signals. A serious impact is generated every time the rolling elements pass over the defect on the raceway in the load zone. Also, a vibration signal can be generated by the varying transmission path between the impact point and the measurement point. These impacts cause the bearing structure to be excited at one of the natural frequencies [24, 25].
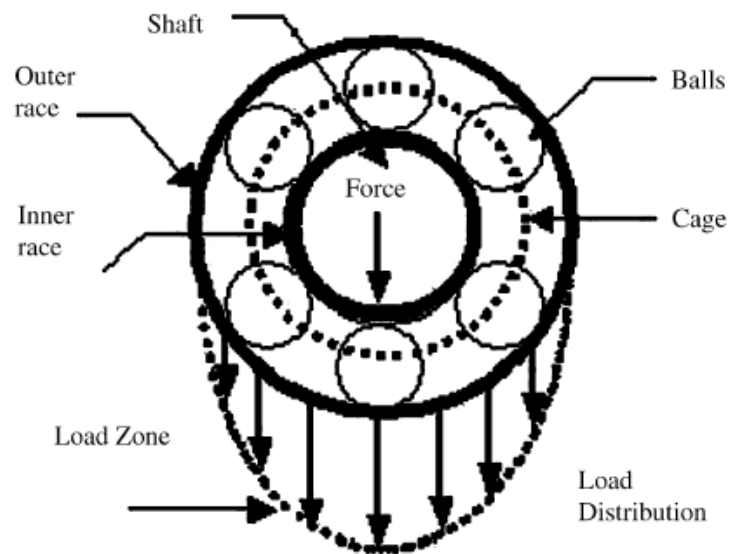
Figure 3-3 Rolling element bearing components and load distribution [33]

The amplitude-modulated vibration signals measured for bearings contain spectral sidebands. Detection of bearing defects by means of such sidebands allows for possible ways to predict the health condition of different bearings [11]. Modulation of bearing tones occurs in several ways. The work of Sawalhi et al. [33] shows that, if there is a small crack on the inner race, a signal excitation occurs every time the defect moves in and out of the load zone at the shaft rotating speed. When in the load zone, the defect gives rise to a vibration corresponding to the inner-race fault frequency, whilst, producing a very little vibration when the defect is outside the load zone. In contrary, if a rolling element is damaged, it will move in and out of the load zone, but at a frequency in accordance with the fundamental cage frequency, rather than with the shaft rotational frequency. This is because the rolling elements rotate around the bearing at the

fundamental cage frequency, a defect in the stationary outer race is always either inside or outside the load zone. Thus, no modulation occurs.
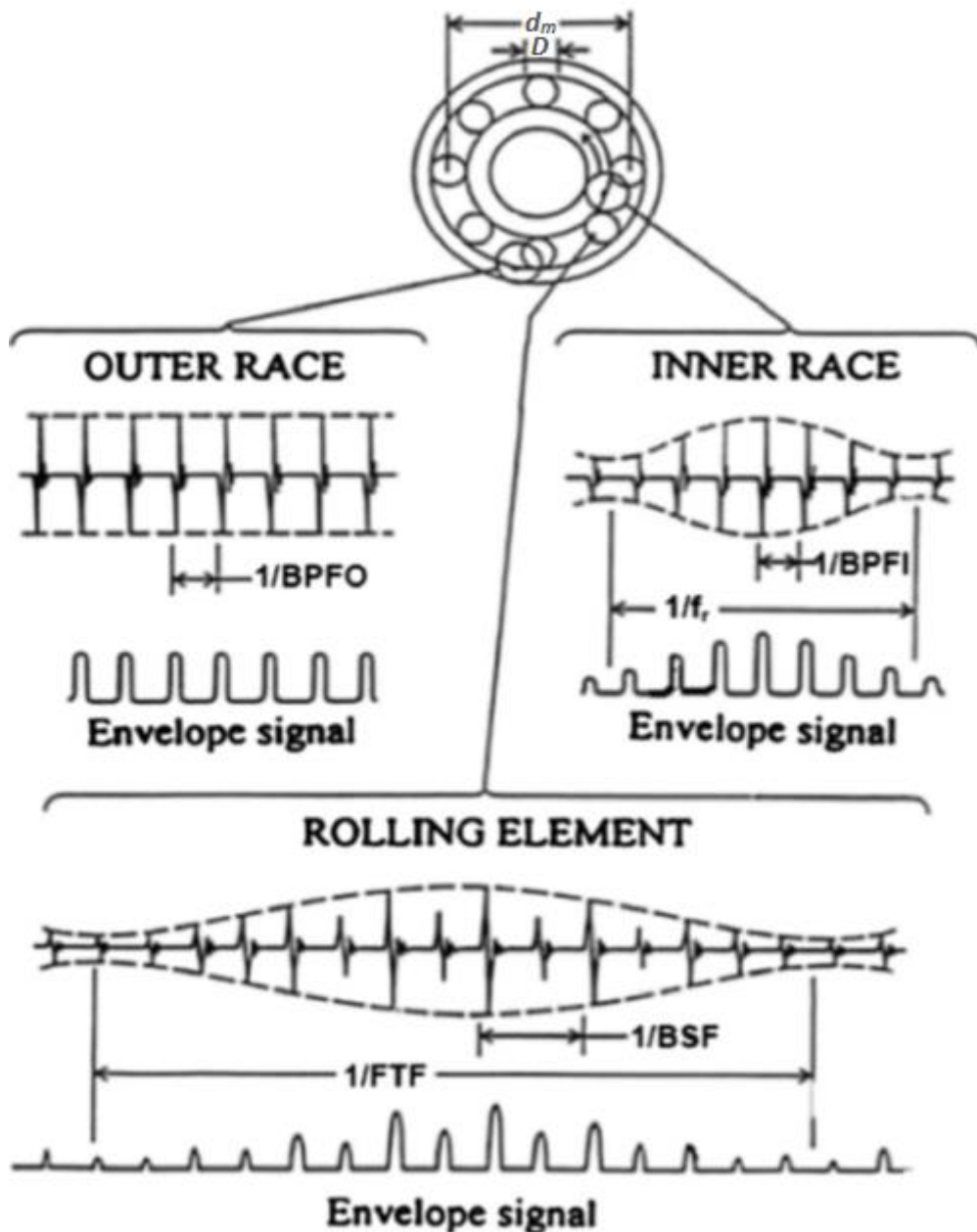
Figure 3-4 Typical envelope-signals generated from local faults in rolling element bearings (stationary outer race) [118]

3.2.6 Resonant Frequency

If the defect is at an early stage of development or the structural damping is significant, the characteristic fault-frequencies may not be directly extractable from the measured

machine vibration as a result of natural mechanical resonance. Thus, it is possible to extract useful information from these characteristic fault-frequencies within the bandwidth that include the natural resonance frequencies. This has led to some researchers to use the higher resonant frequencies for bearing condition monitoring and fault detection.

The natural resonant frequencies are frequency ranges, where structural damping tends toward zero. When a rolling element passes over a defect present in either the inner or outer raceways, the impact generates mechanical pressure waves that are transmitted throughout the machine elements. These pressure waves then excite the different machine parts at the resonant frequencies. The machine parts are comprised of the bearing, rotor, stator, sensors and any other coupled masses. The exact frequencies of resonance are almost impossible to theoretically predict. However, these frequencies can be easily determined through experimentation. A basic method for obtaining the resonant frequency for the machine elements is to strike it with a hammer whilst it is de-energised and measure the frequency response of the resulting vibration [24].

Although, resonance can occur at any frequency, for typical industrial machines most high frequency condition monitoring techniques are implemented in the range 1 kHz to 50 kHz, depending mainly on the structure of the casing [63]. Some researchers have derived formulas to calculate the specific resonant frequencies. However, these impractical equations are of only academic interest as they require parameters (e.g. angle of impact or amount of elastic deformation) that are impossible to measure and unreliable to estimate [121].

3.2.7 Miscellaneous Frequencies

Since the rotor of the rotating machine revolves with a periodic motion, defects in this component usually results in a vibration at the rotor's angular frequency and its integer multiples. This vibration is due to a number of factors including inherent asymmetries and minor imbalances. The vibration measured at the fundamental rotational frequency is very important with the amplitude of the corresponding harmonics being a function of structural damping. Another source of vibration is the inevitable magnetomotive force (MMF) harmonics that is produced by an electric machine under operation.

The MMF harmonics arise from, for example, supply voltage harmonics, inherent machine asymmetries and any faults present in the system. If these harmonics occur at frequencies where sufficient structural damping is available, the resultant vibration is minimal. However, research has shown that, when MMF harmonics often occur at or near a frequency of natural mechanical resonance, resulting in a significant vibration. These MMF harmonic components often occur with amplitudes and at frequencies comparable to typical characteristic fault-frequencies [24]. In addition to the aforementioned sources, many other frequency components can also be observed in a typical vibration spectrum. These include slip of the rotating elements, torsional vibration of the shaft, load imbalance and electrical noise [121].

3.3   Vibration Measurement

Vibration has been used to determine the mechanical condition of machinery for decades. Many researchers have attempted to investigate the relationships between the environmental and operational conditions with changes in the bearing vibration. The success of any monitoring program largely depends on the accuracy of the measurement methods employed. High accuracies can only be accomplished, if and only if the following conditions are met:

1. Instrumentation is properly calibrated;
2. Sensor mounting does not limit the vibration frequency and dynamic ranges of the sensor; and
3. Measurements are taken from the same locations [4].

Vibration accelerations are measured using so-called vibration transducers, also referred to as accelerometers. The piezo-electric accelerometer is thought to be the most popular transducer for vibration analysis in use today. They have features for instance light weight, good temperature resistance, a wider frequency response and higher sensitivity at higher frequencies than the velocity and displacement transducers. The acceleration signals acquired from these piezo-electric accelerometers are sometimes integrated, to produce velocity or even displacement, as required per application. These signals are then processed in different ways to highlight various aspects of the signal, which can then be used in the detection and diagnosis of the machine conditions [8].

3.4   Vibration Analysis Techniques

3.4.1   Theoretical Background

A vibration is a periodic motion or one that repeats itself after certain of interval. This interval is referred to as the period of motion (T). The inverse of the period $(f = 1/T)$ yields the frequency of the vibration in unit of cycle of second (cps) or (Hz) [98].

Vibration signal-analysis techniques or data processing have been used extensively in bearing-faults detection and diagnosis for many years, where useful information is extracted from raw data. This process is also referred to as feature extraction. Generally, once a signal is obtained, for example by an transducer, it is processed in the time domain, frequency domain or the joint time-frequency domain [5]. Note that, according to Nyquist-Shannon sampling theorem, the incoming signal should be sampled at least twice the highest frequency of interest $(f_s \geq f_{\max})$.

3.4.2   Time Domain Analysis

Most of the signals in practice are time-series waveforms. Time-domain analysis involves the statistical computation of certain characteristic features of time-series signals [4, 5, 44]. In literature, different time-domain methods have been proposed to detect the presence of bearing faults, based on some statistical parameters, for instance root-mean-square (RMS), peak value (PV), crest factor (CF), impulse factor (IF) and kurtosis. The probability density of acceleration for a healthy bearing follows a Gaussian distribution (bell shaped), whereas a damaged bearing results in non-Gaussian distribution with dominant tails. This is attributed to a relative increase in levels of acceleration [15, 114].

- **Root-Mean-Square (RMS)**

RMS calculated by obtaining the square-root of the average of the squared vibration levels and delivers as a good indicator of the amount of energy contained in the vibration signal. It works based on the measurement of the overall intensity of wide-band vibration. The RMS for a sine wave can be defined as 0.707 times the amplitude of the signal. It can track the global background noise level but it will not provide any evidence in which the bearing component is failing [16].

$$RMS = \sqrt{\frac{1}{N}\left[\sum_{i=1}^{N}(x_i)^2\right]} \qquad (3\text{-}6)$$

where x is the time signal amplitude, N is the number of samples or measurements and i is the sample index number.

- **Peak Value (PV)**

PV can be defined as the maximum vibration amplitude. For a sinusoidal signal $PV = \sqrt{2}\times RMS$.

$$PV = y_{max}(t) \qquad (3\text{-}7)$$

where y_{max} is the maximum amplitude of the signal.

- **Crest Factor (CF)**

CF can be defined as the ratio of the positive peak value of a waveform to its RMS level[122]. The greater the CF value, the more and sharper the peaks in the vibration signal will be, which can make repetitive impulses easier to detect. Nevertheless, peak values are very sensitive to random variations, requiring an averaging process [123] to avoid the effect of noise.

The RMS value increases, as the fault becomes more severe, but without certainly increases the peak value. This suggests that the CF value will rise to a peak after which it will fall. Therefore, the CF value might be engaged as an indicator to detect the bearing fault severity. Nevertheless, only CF values cannot be used for bearing faults detection. This is because even with averaging of the signal, CF values will differ over a wide range, based on operating conditions such as speed and load [16].

$$CF = \frac{Peak\ value}{RMS} \qquad (3\text{-}8)$$

Joining the calculated values of RMS, peak and CF could serve as a successful method for determination the presence of the bearing fault, but only if they can be compared with some baseline values for a healthy system running under the similar operating conditions.

Normalised values of RMS, peak and CF have been proposed [124] to allow for the detection of operating-condition dependent and non-defect induced vibrations.
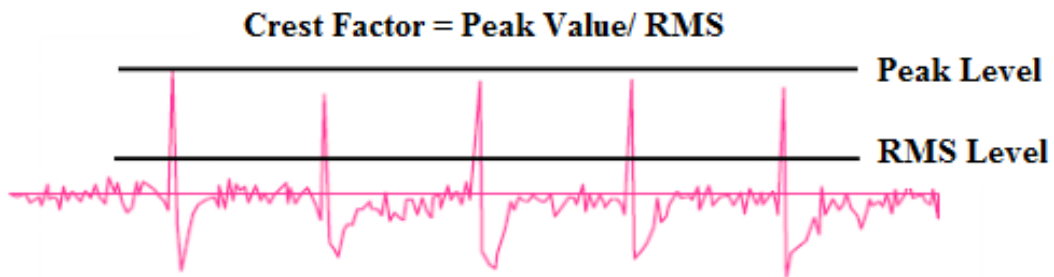
Figure 3-5 The levels of crest factor, peak value and RMS [16]

- **Impulse Factor (IF)**

The IF provides a measures the how sharp the probability density function of the amplitude distribution is. The presence of a few large spiky peaks in the measured machine vibration signal will yield a large IF value. Similarly, a flattish machine vibration signal will result in a low IF value [125].

$$IF = \frac{max\ x_i}{\sqrt{\frac{1}{N}\sum_{i=1}^{N}\left(x_i - \bar{x}\right)}} \tag{3-9}$$

where x is the time signal amplitude, N is the sample number, i is the sample index number and $\bar{x}$ denotes the mean value of the N samples.

- **Kurtosis**

The first and second moments of a sample distribution are the mean and standard deviation values of the distribution, respectively. The third moment is skewness and the fourth being kurtosis. For actual signals, the mean and skewness are typically close to zero, proposing a symmetrical amplitude distribution. However, as the moment-order of the event increases, so does the sensitivity of the impulses present in the signal.

Kurtosis is a measure of whether the bearing vibration data is peaked or flat relative to a normal distribution. That is, data sets with tall kurtosis tend to have a distinct peak characteristic, which decrease quicker with heavier tails. The sensitivity of kurtosis to pulses induced by bearing defects has been proven effective in several rolling-element

bearing diagnostics [17-19]. For a healthy bearing, the kurtosis value stated to be close to 3; thus any value larger than 3 can be used as a good indicator for defect presence. However, in practice, the kurtosis value might drop to fewer than 3, close to the value of an undamaged bearing, whilst the bearing defect has well developed [16, 20]. This is considered as a major drawback for kurtosis-based condition monitoring systems, which needs to be addressed.

The kurtosis for signal $x(t)$ is defined as:

$$Kurtosis = \frac{\frac{1}{N}\sum_{i=1}^{N}\left(x_i - \bar{x}\right)^4}{\left[\frac{1}{N}\sum_{i=1}^{N}\left(x_i - \bar{x}\right)^2\right]^2} - 3 \qquad (3\text{-}10)$$

where the signal consists of N samples of amplitudes and $\bar{x}$ is the mean value of the N samples. The value -3 is introduced to normalise the expression so that $Kurtosis = 0$ for the normal Gaussian distribution. It indicates that, the higher the kurtosis value the sharper the peak(s) and the longer the tails of the signal, and the lower the kurtosis value, the more rounded the peak(s) will be [15].

In [126], Alfredson et al. have chosen kurtosis as a compromise parameter between the insensitive lower-order moments and over-sensitive higher-order moments. It has been found that for healthy bearings, the distribution of amplitudes tends to follow a Gaussian or normal distribution with a kurtosis value of about zero. Whilst kurtosis is sensitive to incipient faults in bearings, it is insensitive to bearing operating conditions.

Kurtosis and CF are measures of the spikiness of the signal and are mainly based on the average magnitude of the signal. These two parameters have values of close to zero for healthy bearings and increase rapidly, upon the appearance of a fault representing fatigue spall. However, the relationship between kurtosis and CF with bearing damage growth is not linear. This is further explained by using an example scenario. In an inner-race fault, the early stage of a fatigue spall for instance, is probably to be sufficiently not more than the distance between two adjacent rolling elements. In this case, the bearing is liable to a periodic discrete impact whenever a rolling element passes over the defect on the raceways, resulting in a peak in the measured vibration signal. As the defect grows throughout the inner race, the vibration signal becomes less impulsive and more

continuous, resulting in random behaviours in the vibration signal. In this case, both kurtosis and CF values will start to decrease, which will eventually approach the baseline values obtained for healthy conditions. Consequently, these two measurements alone cannot always deliver accurate information on the severity of fault damage. Nevertheless, in serious-fault conditions, a significant increase in the overall vibration energy is reflected by high RMS values. Hence, by using a combination of kurtosis, CF and RMS, it is possible to create a robust set of statistical parameters for identification of bearing fault levels.

It has been found that, IF parameter delivers similar results to kurtosis. Moreover, IF is as sensitive to incipient fatigue spalling as CF and kurtosis are [126], an opinion which has been confirmed in [91]. However, kurtosis appears to be the greatest sensitive measurement to incipient bearing faults, but at the same time, it is the least robust with respect to operating conditions.

The statistical parameters for the vibration signal in the time domain can either be calculated directly without any frequency filtering, or the vibration signal can be passed via a high-pass filter first, in a try to minimise undesirable low-frequency background noise. Band-pass filtering methods also exist that allow for the reduction of unwanted signal noise outside a specified frequency band. The time-domain parameters are subsequently calculated for each band.

For most well-known bearing fault-detection techniques, the RMS value of the vibration signal in the time domain is often accompanied by other statistical parameters. Nonetheless, for the bearing initial defects detection, all the time-domain parameters, whether supported by frequency filtering or not, suffer from a common disadvantage. That is, the energy level of the signal must be at a certain level to be able to detect it, over the background noise generated by the other machine components.

3.4.3   Frequency Domain Analysis

The Fourier transform is the mainly the most common technique for converting a varying time-domain signal into the frequency domain. The resulting frequency spectrum is proved to be very consistent and reliable in the identification of certain machine faults [5].

Fast Fourier Transform (FFT) plays an important role in the analysis of the machine vibrations in the frequency domain. FFT can provide salient features, useful for the diagnosis of machine conditions. The main idea of spectrum analysis is that by considering either the whole spectrum or certain frequency components, some signatory features can be extracted from the signal [5].

The frequency spectrum obtained for a vibration signal represents the quantity of energy contained in the vibration signal as a function of frequency, and allows for an assessment of the contribution of individual machine components. For instance, when using time-domain analysis, the developed vibration signal from an early roller bearing fault will be buried amongst the background bearing noise. In contrast, in the frequency-domain analysis, a distinguishing feature peak in the spectrum is observable at the distinctive bearing fault frequency. The main challenge is to notice the presence of a premature bearing fault as early as possible to avoid complete failures.

Defects in roller-element bearings produce pulses with very short durations. These pulses excite the natural frequency (usually above 5 kHz) of the bearing elements and the housing structures. As a defect grows in a bearing component, peaks start to appear in the vibration spectrum at the bearing characteristic frequency and its harmonics. Moreover, around each peak, there are side-bands [15]. It is difficult to obtain conclusive results directly from the spectrum of a faulty bearing vibration signal, unless the defect is significantly large. This is due to the presence of noise or vibration from other mechanical or electrical sources [15, 127, 128]. This problem is usually overcome by the use of well-organized filtering and enveloping technique. However, a prior knowledge of the frequency band of interest is required, which may not be known beforehand.

Each time a rolling element moves over a damaged area under load, an impulsive waveform is generated. However, more often than not, the bearing faults cannot be directly identified by simple frequency-analysis of the complex vibration signals. This is due to the following reasons [64]:

- Wideband frequency content and short duration,
- Low energy levels at the early stages of fault evolution,
- Strong background noise,
- Interfering vibrations from other machine elements, and

- Quasi-periodical non-stationary characteristics due to the roller slippage.

3.4.4   Envelope Analysis

Frequency-domain studies show that the interaction between a rolling element and defect in a bearing produces high-level pulses of very short duration. Every time when the defect is struck by the rolling element, the bearing produces a response, which decays quickly due to damping. The energy of the generated pulse is spread over a wide frequency range at a low level. Normally, the impulse excites a resonance at a high frequency, which is quite different from those induced by other machine components. This means that the impulse energy within a certain narrow band around the resonant frequency, where there is a high signal-to-noise ratio, is more simply observed than at other frequency bands [34].

An excitation occurs each time when one of the rolling elements passes over the defect on the raceways. Therefore, the fundamental frequency of the response waveforms is the rate at which the element rolls over the defect. This is one of the characteristic frequencies described in this Chapter Section 3.2.3. For example, if the defect occurs on the inner race or a rolling element of the bearing, the resonant frequency of the bearing (carrier) is amplitude modulated by the characteristic fault frequency (modulator).

This type of modulation causes sidebands to appear, due to the movement of the defect on the inner race inside and outside the bearing load-zone once per revolution. While in the load zone, the defect produces a vibration at the ball pass frequency, but when it is out of the load zone, very little vibration is produced at this frequency. In addition, the resulting waveform, as demonstrated in Figure 3-2, contains important information on the modulating or the fault frequency.

Envelope analysis or demodulation analysis is a well-known technique used to detect and diagnose rolling-element bearing fault conditions [11]. This technique is derived by demodulating the high-resonant frequency created by the impacts that are caused by the interactions between the rolling element and the defects on the race way [119]. By conducting envelope analysis or amplitude demodulation of the resonance signal, the period of the excitation and thus the defect can be detected.

The envelope analysis technique is comprised of four steps, as shown in Figure 3-6. First, the row data is band-pass filtered to allow a certain frequency range through, with other

frequencies caused by imbalance, misalignment or background noise eliminated. Second, a half wave (or full wave) rectifier converts the bipolar band-passed signal into a unipolar one. Third, the peak-hold smoothing section is applied to remove the carrier frequency, by smoothing/filtering the fast transitions in the signal. And fourth, the signal is further low-pass filtered to remove high-frequency components, while low-frequency contents associated with bearing faults are retained [3, 16, 114, 129]. The remaining signal content will then only consist of the defect frequencies. The analogue rectification and smoothing before sampling is one of the many possible paths to envelope detection. Modern digital signal processing techniques tend to use Hilbert transform for robust envelope analysis [119].
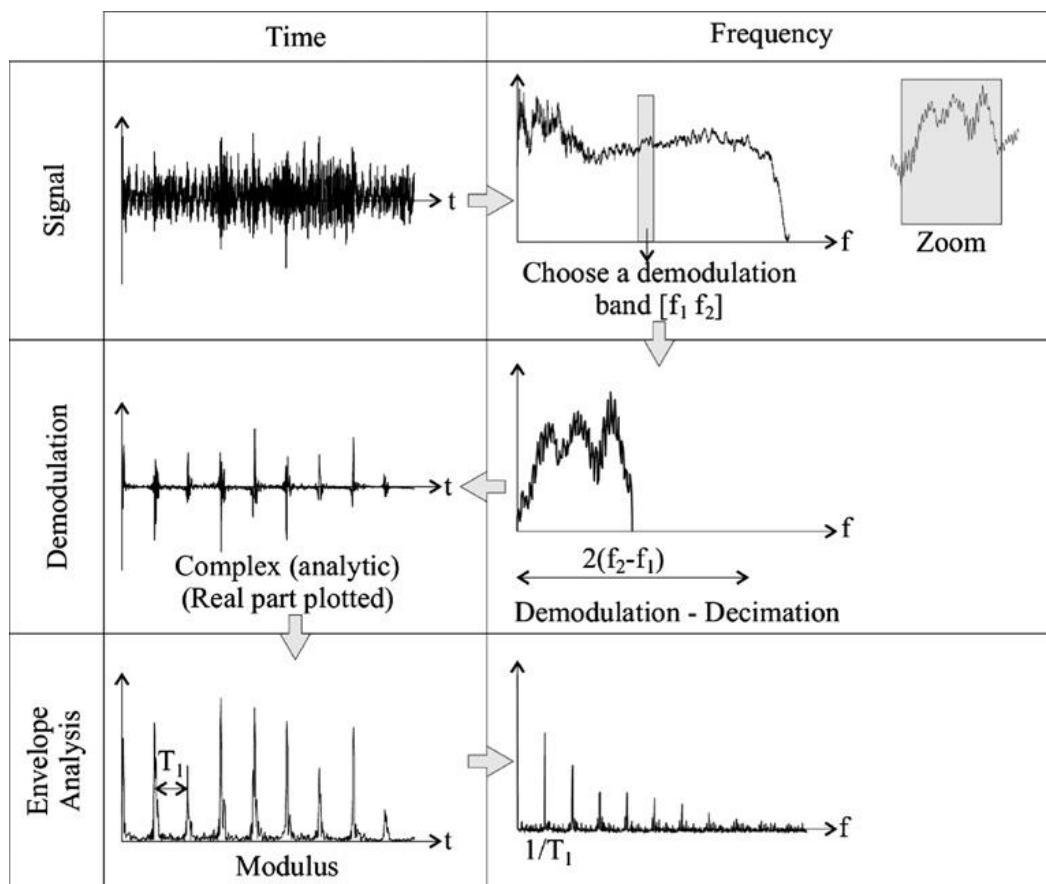
Figure 3-6 Envelop analysis procedure [118]

The envelope of the signal is calculated using Hilbert transformation. In this case, the acquired signal can be taken into account as a complex signal that consists of only the real part [130]. Equations (3-11) to (3-13) show the procedures required to compute the Hilbert transformation. The real part of the analytic signal x_a for x_{in} is the original data

x_{in}, whilst the imaginary part is the Hilbert transformation of x_{in} and is related to the original signal by a 90° phase shift. The envelope of the vibration signal is expressed by Equation (3-14). Equation (3-15) exhibits the amplitude spectrum of the envelope. By using the Hilbert transformation algorithm, the computing buffer can be reused, which is quite critical for a processor with limited storage.

$$X(k) = \sum_{n=0}^{N-1} x_{in}(n)e^{-j(2\pi/N)kn} \tag{3-11}$$

$$X_a(k) = \begin{cases} X(k), & k = 0, \dfrac{N}{2} \\ 2X(k), & 1 < k < \dfrac{N}{2} - 1 \\ 0, & \dfrac{N}{2} + 1 < k < N - 1 \end{cases} \tag{3-12}$$

$$x_a(n) = \frac{1}{N} \sum_{k=0}^{N-1} X_a(k)e^{j(2\pi/N)kn} \tag{3-13}$$

$$x_{env}(n) = \sqrt{x_a(n)x_a^*(n)} \tag{3-14}$$

$$X_{env}(k) = \left| \sum_{n=0}^{N-1} x_{env}(n)e^{-j(2\pi/N)kn} \right| \tag{3-15}$$

where x_{in} is the bearing vibration signal, X is the fast Fourier transform of x_{in}, X_a is the FFT of the analytic signal for x_{in}, x_a is the analytic signal for x_{in}, x_{env} is the analysed envelope and X_{env} is the envelope spectrum. Envelope detection takes advantages of the large amplitudes present in defect signals within certain frequency bands, to achieve high signal-to-noise ratios in the presence of low-frequency mechanical noise. Therefore, the envelope spectrum can provide clear peaks at the harmonics of the characteristic defect frequencies.

McFadden et al. [11] proposed that, the band-pass filter centre-frequency should be designated accordingly to match with the resonance frequency of the structure. The filter bandwidth should be at least two times the highest defect frequency. This will ensure that

the filter will pass the carrier frequency and at least one pair of the modulation sidebands. Although, Antoni et al. [43] found that the optimum band-pass filter parameters can be achieved by using a kurtogram.

3.4.4.1 Hilbert Transform

Hilbert transform can be defined as the relationship between the real and imaginary parts of the Fourier transform of a one-sided function [8]. It can be applied to nonlinear and non-stationary data analysis, especially for time- and frequency-domain energy representations. Hilbert transform yields much sharper results than those attained from any of the traditional analysis methods in the time frequency energy. Given a signal $x(t)$ in the time domain, the Hilbert transform is the convolution of $x(t)$ with the signal $1/\pi t$ and the result is a new signal also in the time domain. Hilbert transform can be expressed as,

$$\hat{x}(t) = \frac{1}{\pi t} \times x(t) = \frac{1}{\pi} \int_{-\infty}^{\infty} \frac{x(\tau)}{t - \tau} \, d\tau \tag{3-16}$$

where t and τ are the time and transformation parameters, respectively.

Hilbert transform is a multiplier operator that delivers an output with a 90° phase shift from the input. It can be achieved by first transforming the signal into the frequency domain, then shifting the phase of positive frequency components by $-\pi/2$ and of the negative components by $+\pi/2$. In the straightforward instance, if the input is a cosine wave, the Hilbert transform will produce a sine-wave output, without any modifications in the wave's amplitude. However, it should be noted that, if the input signal is modulated, the output will be the modulating signal or the so-called 'envelope of modulation'. In the case of the roller bearing with a fault in, say, the inner race, the output will be a series of pulses occurring at the roller passing frequency [8, 131].

3.4.5 Time-Frequency Analysis

One limitation of frequency domain is the lack of ability to handle non-stationary waveform signals, which are very common in faulty machine conditions [5]. In practice, as well as the frequency of a particular vibration, identifying the time intervals between which the pulses occur can also be beneficial. As a result, time-frequency techniques are

developed. This type of analysis considers the power or energy of the waveform signals as a two-dimensional function of both time and frequency, achieving a more accurate diagnosis of bearing faults [5, 44].

3.4.5.1   Short-Time Fourier Transfer

The short-time Fourier transformer (STFT) or spectrogram was developed by Gabor in 1946. He divided the whole signal into segments with short-time windows and then computed the Fourier transform for each segment. The STFT of a signal $x(t)$ can be defined using the weighting function $u(t) = g(t-\theta)e^{-j\omega t}$, with a window function $g(t)$, as opposed to $u(t) = e^{-j\omega t}$ in the ordinary Fourier transform [5, 16, 132] as,

$$STFT(j\omega,\tau) = \int_{-\infty}^{\infty} x(t)g(t-\tau)e^{-j\omega t}dt \qquad (3\text{-}17)$$

where, τ is some time shift.

The limitation of STFT is that it provides a constant resolution with the same window length for each segment.

3.4.6   Spectral Kurtosis

Since the early days of envelope analysis, there has been a discussion on how to choose the most suitable band for demodulation. Several claim that it is hard a task and some recommending the use of hammer-tap testing to find the bearing-housing resonances. This problem is now principally solved by the use of spectral kurtosis (SK) and the kurtogram to find the most impulsive bands.

SK was first used in the 1980's for detecting impulsive events in sonar signals [133]. It was based on the STFT algorithm and gave a measure of the impulsiveness of a signal, as a function of frequency. Since its proposal by Stewart et al. in the 1970's [128], kurtosis had long been used to assess the severity of machine faults. However, there was only a vague suggestion that clearer results might be achieved by using filtering in the frequency bands, and the concept of spectral kurtosis had not yet been fully developed. The application of SK to bearing fault detection was first outlined in [43, 59], where a very thorough study of the definition and calculation of the SK for this purpose was presented.

3.4.6.1   Calculation of the Spectral Kurtosis

The SK extends the concept of the kurtosis, which is a global value, to that of a function of frequency that indicates how the impulsiveness of a signal, if any, is distributed in the frequency domain. The principle is analogous in all respects to the power spectrum density (PSD), which decomposes the power of a signal with respect to frequency, except that fourth-order statistics are used instead of second-order. This makes SK a powerful tool for detecting the presence of transients in a signal, even when they are buried in strong additive noise. SK achieves this by indicating in which frequency bands the transients have taken place [118].

The key to fault diagnosis of a rolling-element bearing is to capture any special vibration signatures resulting from the fault. Acceleration signals measured on the casing mainly consist of two parts such that,

$$y(t) = n(t) \tag{3-18}$$

$$y(t) = x(t) + n(t) \tag{3-19}$$

where $y(t)$ is the monitored vibration signal, $x(t)$ is the faulty bearing signal and $n(t)$ is unknown background noise, including vibration signals generated by other components (e.g. rotor imbalance, looseness, spalls, cracks, etc.). The faulty bearing signal has some distinct features that include a wide frequency range, small energy and non-stationary characteristics.

The main idea is that the random mechanical noise follows a Gaussian distribution, that is the kurtosis of the signal is almost equal 3.0, while the presence of impact hidden in the vibration signal, changes the kurtosis to values more than 3.0 [134].

The spectral kurtosis of a signal $x(t)$ may be computed using the STFT $X(t, f)$, that is, the local Fourier transform at time t obtained by moving a window along the signal. When seen as a function of frequency, the squared magnitude $|X(t, f)|^2$—i.e. the spectrogram returns the power spectrum at time t and its further average over time, $\langle |X(t, f)|^2 \rangle$, the PSD as computed by the Welch method. On the other hand, if considered as a function of t, $X(t, f)$ may then be interpreted as the complex envelope

of signal $x(t)$ that is bandpass-filtered around frequency f, whose squared magnitude will indicate how energy is flowing at that particular frequency with respect to time. If that frequency band happens to carry any pulses, bursts of energy will appear in the spectrum. This may be simply detected by computing the kurtosis of the complex envelope $X(t, f)$ as follows [118],

$$K(f) = \frac{\left\langle |X(t,f)|^4 \right\rangle}{\left\langle |X(t,f)|^2 \right\rangle^2} - 2 \tag{3-20}$$

where $\langle . \rangle$ is the time-averaging operation and the offset of -2 is used to enforce $K(f) = 0$ in case $X(t, f)$ is a complex Gaussian signal, instead of 3 for a real signal.

As the fault signal $x(t)$ of the rolling element bearings give rise to series of short impulse as the rolling elements strikes defect on the race. However, It can be assumed that $x(t)$ has a transient nature, whereas $n(t)$ is stationary. Incipient faults in roller bearing (e.g. looseness, spelling, clearance and creaks) produce a series of repetitive short transient forces, which in turn excite some structural resonances. Therefore, a reasonably useful model for $x(t)$ is the generalised-shot-noise process [43, 135].

The interpretation of the spectral kurtosis is further illustrated in Figure 3-7, where a rolling-element bearing signal $x(t)$ is modelled as a series of impulse responses $g(t)$ excited by impulses X at times τ_k [43]. This is given as,

$$x(t) = \sum_k g(t - \tau_k) X(\tau_k) . \tag{3-21}$$

Statistical parameters in time domain are sensitive to the peakiness of a fault signal, which can only characterise the intensity of the signal. Spectral analysis fails to detect the presence of a fault signal, when the impacts of random fluctuations in X and τ_k are strong. The advantages of the kurtosis indicator are listed below [43]:

- Kurtosis takes high values in the presence of the fault signal $x(t)$;
- Kurtosis is ideally zero when the background noise $n(t)$ is well separated from the signal i.e. the signal-to-noise-ratio is significantly high; and

- Kurtosis is sometimes unable to capture the peakiness of the fault signal and hardly departs from the zero reference line, especially in poor signal-to-noise conditions, where it fails to detect the incipient faults.
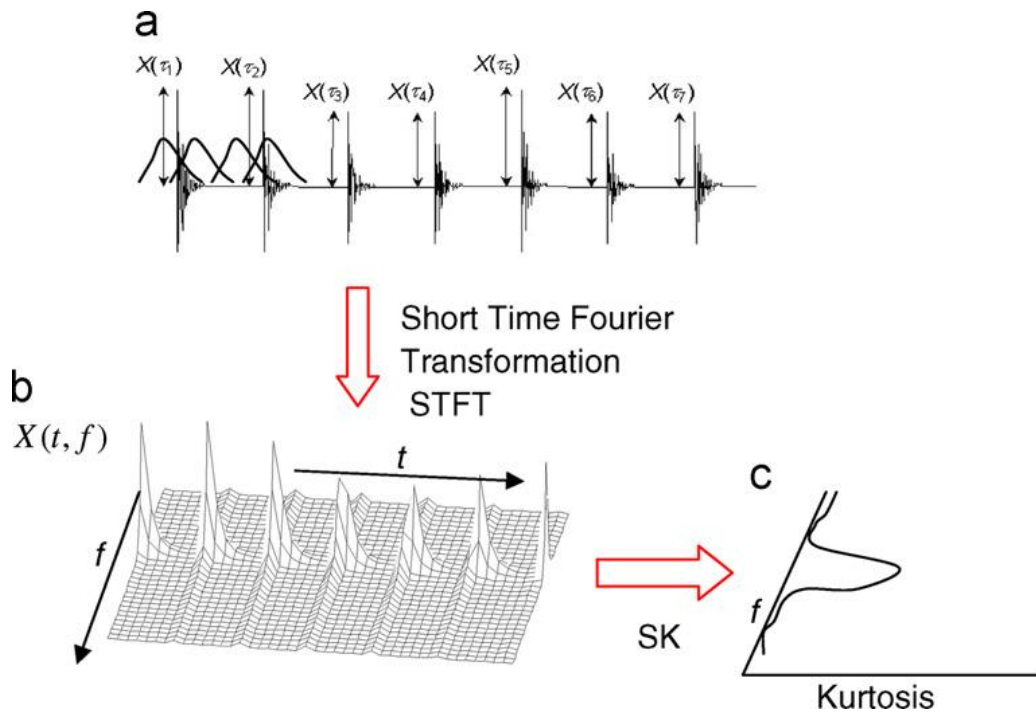
Figure 3-7 Spectral kurtosis of bearing fault signal: (a) time signal (b) STFT, and (c) SK as a function of frequency [118]

SK of STFT is largely dependent on the length of the window used. Antoni *et al.* [43] pointed some remarks with respect to the SK as the following:

- SK increases with sampling rate of the signal, and
- SK decreases with the window length of STFT.

The last remark suggests that a short window length will yield high SK values, which is more favourable. However, a too short window length will produce a SK with poor spectral resolution, causing some details to be lost. In practice, several window lengths should be tried before selecting a length that emphasises the transient characteristics of the fault signal.

3.4.6.2 The Kurtogram

The SK is large in frequency windows where the fault signal is dominant, and small where the spectrum is dominated by stationary signals. Antoni et al. (2006) [43] developed the kurtogram, a map indicating the optimum centre-frequency and bandwidth combination, by considering the following in his approach:

1. The band-pass filter has a good chance of selecting the frequency band, where the signal-to-noise ratio is maximum,
2. The band-pass filter has a better chance of selecting only the strongest impulsive source, in the case where several sources are present in the signal, and
3. The band-pass filter is a necessary pre-processing stage that is applied prior to carrying out an envelope demodulation of the signal [43].

The employed filter should maximise the signal-to-noise ratio, which did not necessarily guarantee that the impulse like nature of the fault was optimally recovered. In order to achieve this aim, the band-pass filter should be designed so that it maximises the envelope kurtosis of the filtered signal. Interestingly, this problem is similar to finding the frequency and the window-length, which also maximises the STFT-based SK over all possible choices. This statement is justified via the interpretation of the STFT by the filter bank, where the central frequency of a narrow-band filter is proportional to the inverse of the window length [43].

Furthermore in [43], Antoni et al. clarified the process of selecting the best window-length for the STFT analysis and thus, optimising the STFT-based SK. This was achieved by the use of the kurtogram. Hence, the optimal central-frequency and bandwidth of the best band-pass filter can be found as those values that jointly maximise the kurtogram.

3.4.6.3 Fast Kurtogram

All possible window widths of spectral kurtosis based on STFT should be tested using kurtogram to accurately yield the proper central frequency and bandwidth which is computationally expensive. Therefore, Antoni in [61] developed the fast kurtogram to fast compute and understand the results of spectral kurtosis based on the multirate filter-bank structure and quasi-analytic filters [136].

Figure 3-8 illustrates the main idea in this respect starting by calculating the largest bandwidths, that covers the whole signal spectrum and stopping at narrow bandwidth where sufficient independent time samples in $X(t, f)$ is taken inconsideration to calculate the time averages in Equation (3-20). It has been decomposed based on ''1/3-binarytree'', where each halved-bandwidth is further divided into 3 other bandwidths, this will produce a frequency resolution in the sequence of 1/2, 1/3, 1/4, 1/6, 1/8, 1/12, …,2^{-k-1}, with corresponding scale level of k=0, 1, 1.6, 2, 2.6,….[118]
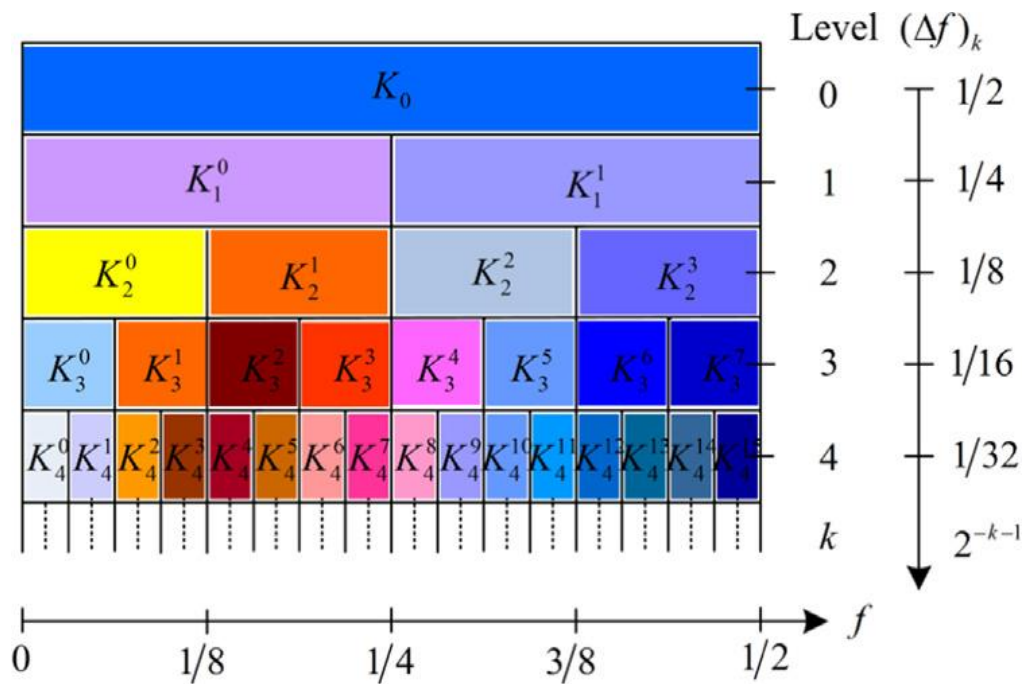
Figure 3-8 bandwidth and centre frequency for the 1/3-binary tree kurtogram [136].

3.4.7 Higher Order Spectra

The first- and second-order statistics, for example, mean, variance, autocorrelation and power spectrum, are accepted signal-processing implements and are used widely in data analysis problems. Specifically, second-order statistics can be used to describe Gaussian and linear processes. In reality, there are many circumstances where the processes deviate from Gaussianity and linearity. The generalised concept of higher order spectra was firstly introduced by Tukey and Brillinger in the early 1960's. latterly, these higher order spectra methods have been used in a large number of research outputs [137].

3.4.7.1   Power Spectrum (PS)

The discrete Fourier transform (DFT) $X(f)$ of a discrete-time signal $x(t)$ is defined as [138],

$$X(f) = DFT[x(t)] = \sum_{t=-\infty}^{\infty} x(t)e^{-j2\pi ft} \; . \tag{3-22}$$

The power spectrum (PS) method is mainly used to characterize the power distribution of a signal $x(t)$ in the frequency domain. In the same conditions, the amplitude of PS rises with the development of fault severity, serving as a good diagnosis indicator [139].

$$p(f) = E\left\langle X(f)X^{*}(f) \right\rangle \tag{3-23}$$

where $X(f)$ and its conjugate $X^{*}(f)$ are the Fourier transform of the sequence $x(t)$, and $E\langle . \rangle$ is the expectation operation, suggesting that a statistical averaging is needed in the spectrum estimation process [62]. Although PS can characterize the power levels of different frequency components, it also contains noise in the spectrum which will impact the accuracy of the fault diagnosis's outcome.

3.4.7.2   Conventional Bispectrum (CB)

The bispectrum analysis is a type of higher order spectra, which is used in a large number of researches since the 1980's [140]. Compared to PS analysis, bispectrum analysis has a number of distinctive properties for instance nonlinear system identification, phase information retention and Gaussian noise elimination. Bispectrum is often used to detect quadratic phase coupling (QPC), which occurs when two waves interact nonlinearly and generate a third wave with a frequency and phase equal to the sum (or difference) of the first two waves [72]. In case of bearing fault detection, the vibration signal is formed by the nonlinear combination of two components, namely, the shaft frequency and bearing fundamental frequency. Thus it is anticipated that bispectrum can give a more accurate representation of the vibration signal for fault diagnosis. The conventional bispectrum $B(f_c, f_x)$ can be defined in frequency domain as [141]

$$B(f_c, f_x) = E\left\langle X(f_c) X(f_x) X^*(f_c + f_x) \right\rangle \tag{3-24}$$

where $X^*(f)$ is the complex conjugate of $X(f)$ and $E\langle . \rangle$ is the statistical expectation operation. f_c, f_x and $f_c + f_x$ indicate three individual frequency components achieved from Fourier series integral. Note that, unlike the second-order measures, this third-order measure is a complex quantity, which contains both magnitude and phase information about the original time signal. If the frequency components at f_c, f_x and $f_c + f_x$ are independent of each other, then each frequency can be characterised by statistically-independent random phases that are distributed over $(-\pi, \pi)$. Upon the completion of statistical averaging denoted by the expectation operator $E\langle . \rangle$ in Equation (3-24), the bispectrum will tend towards the zero line. This is due to the random-phase mixing effect, allowing for the random noise to be suppressed significantly.

On the other hand, if the three spectral components f_c, f_x and $f_c + f_x$ are nonlinearly coupled to each other, the total phase of the three components will no longer be random at all, even though each of the individual phases are random. Consequently, in the bispectrum method, the statistical averaging of the time-series signal will not lead to a zero value. In particular, the phases have the following relationship,

$$\varphi(f_c) + \varphi(f_x) = \varphi(f_c + f_x). \tag{3-25}$$

This nonlinear coupling is indicated by a peak in the bispectrum at the bifrequency $B(f_c, f_x)$. To measure the degree of coupling between different components, a normalised form of the bispectrum or bicoherence is usually adopted, which can be expressed as.

$$b^2(f_c, f_x) = \frac{\left| B(f_c, f_x) \right|^2}{E\left\langle \left| X(f_c) X(f_x) \right|^2 \right\rangle E\left\langle \left| X(f_c + f_x) \right|^2 \right\rangle}. \tag{3-26}$$

The bicoherence is independent of the value of the triple product of DFT amplitudes and is confined to a range between 0 and 1. A bicoherence of close to 1 suggests that there is a nonlinear interaction between the frequency components, f_c, f_x and $f_c + f_x$. On the other hand, a value of near 0 implies an absence of interaction between the components.

The possible amplitudes in the latter case may suggest that the components are originated independently from a system. Therefore, based on the amplitude of bicoherence, those nonlinear interactions can be detected and the degrees of interaction between the coupled components can be measured.

3.4.7.3 Modulation Signal Bispectrum (MSB)

From spectrum features of points, Equation (3-24) only includes the presence of nonlinearity from the harmonically-related frequency components f_c, f_x and $f_c + f_x$. In other words, it overlooks the possibility of a nonlinear interaction between f_c and f_x, which can lead to the occurrence of $f_c - f_x$. As a result, the conventional bispectrum is not an adequate technique to describe AM-like signals such as bearing vibration signals.

To improve the performance of the conventional bispectrum in characterising the rolling bearing vibration signals, a modified bispectrum, named the modulated signal bispectrum (MSB) has been proposed in [25]. MSB has the ability to detect nonlinear components and suppress any random noise by detecting phase couplings in the modulated signals. The definition of MSB can be described by Equation (3-27) [62, 72].

$$B_{MS}(f_c, f_x) = E\left\langle X(f_c + f_x)X(f_c - f_x)X^*(f_c)X^*(f_c)\right\rangle \tag{3-27}$$

where $X^*(f)$ is the complex conjugate of $X(f)$ and $E\langle . \rangle$ is the statistical expectation operation. f_c, f_x and $f_c + f_x$ indicate the three individual frequency components achieved by the integral of the Fourier series. Similarly, the magnitude and phase of MSB can be expressed as Equations (3-28) and   (3-29), respectively.

$$A_{MS}(f_c, f_x) = E\left\langle \left|X(f_c + f_x)\right|\left|X(f_c - f_x)\right|\left|X^*(f_c)\right|\left|X^*(f_c)\right|\right\rangle \tag{3-28}$$

$$\varphi_{MS}(f_c, f_x) = \varphi(f_c + f_x) + \varphi(f_c - f_x) - \left|\varphi(f_c)\right| - \left|\varphi(f_c)\right|. \tag{3-29}$$

By considering both $(f_c - f_x)$ and $(f_c + f_x)$ simultaneously in Equation (3-27), MSB is able to measure the nonlinear effects of signal modulation. If $(f_c - f_x)$ and $(f_c + f_x)$ are both due to the nonlinear effect between $(f_c - f_x)$ and $(f_c + f_x)$, there will be a bispectral

peak at the bifrequency $B_{MS}(f_c, f_x)$. On the other hand, if these components are not coupled but have a random distribution, the magnitude of the MSB will be close to zero. This enables the wide-band noise in the bearing vibration signals to be suppressed effectively so that the discrete components can be identified more accurately.

To measure the degree of coupling between the three components, a modulation signal bicoherence (MSB$_C$) can be used, that is calculated by Equation (3-30).

$$b_{MS}^2(f_c, f_x) = \frac{\left|B_{MS}(f_c, f_x)\right|^2}{E\left\langle \left|X(f_c)X(f_c)X^*(f_c)X^*(f_c)\right|^2 \right\rangle E\left\langle \left|X(f_c+f_x)X(f_c-f_x)\right|^2 \right\rangle} \quad (3\text{-}30)$$

Based on MSB property of highlighting modulation effect, a MSB detector can be developed. Firstly, MSB amplitude array is averaged along the f_x direction according to Equation (3-31) to obtain an average spectrum at different f_c.

$$A_j = \frac{1}{N}\sum_i A_{ij} \quad (3\text{-}31)$$

where i and j are the index of f_x and f_c respectively. Then the carrier frequencies which have high amplitudes are selected as the candidates for feature extraction. Finally, the selected f_c slices are farther averaged to get the MSB detector as expressed by Equation (3-32).

$$MSBdt = \frac{1}{m}\sum_{j=k_1}^{K_m} A_{ij} \quad (3\text{-}32)$$

where $j = k_1,...k_m$ is the slice number that selected for calculating MSB detector.

From Equation (3-27), it can be deduced that for the case $f_x = 0$, the MSB can be reduced to the power spectrum described by Equation (3-33).

$$PS(f_c) = \sqrt{B_{MS}(0, f_c)} = \sqrt{E\left\langle X(f_c)X^*(f_c)X(f_c)X^*(f_c) \right\rangle} \quad . \quad (3\text{-}33)$$

The phase of power spectrum for any component is zero and thus, it is not possible to suppress random noise by averaging operation. Therefore, compared to the PS method, MSB can be employed as more effective means of random-noise suppression.

3.5 Summary

This chapter has reviewed the theoretical basis of the bearing vibration response due to localized defects (Section 3.2), vibration measurements (Section 3.3) and vibration analysis techniques (Section 3.4) to assist understanding the data and results presented in the following Chapters. A brief discussion of the state of the art signal processing techniques that are commonly used for rolling bearing fault detection and diagnosis including time domain analysis (Section 3.4.2), frequency domain analysis (Section 3.4.3), envelope analysis (Section 3.4.4), time-frequency analysis (section 3.4.5), spectral kurtosis which includes the kurtogram and fast kurtogram (Section 3.4.6), and higher order spectra (Section 3.4.7). Among them the spectral kurtogram provide outstanding performance in finding optimal bands for envelope analysis. However, it has little capability of suppressing inevitable noise which may be solved by using higher order spectra as they have high performance of random noise suppression and nonlinear characterisation.

CHAPTER FOUR

DYNAMIC MODEL OF A DEEP-GROOVE BALL BEARING

In this Chapter, a nonlinear dynamic model for deep-groove ball bearing is presented, which allows simulating the vibration signals under different conditions. The model is based on a five degrees of freedom (5-DOF) incorporating with various local defects and different degree of clearance increments. The inner race-shaft and outer race-housing are treated as two lumped masses, which are coupled together using a nonlinear spring formula based on the Hertzian contact deformation between the balls and races in order to highlight the localised effects due to bearing faults.

4.1   Introduction

Rolling-element bearings are widely used in rotary machinery. Bearing failure is considered as one of the main causes of breakdown in rotary machines and can cause loss of production and costly damage to the whole system. As a remedy, researchers have paid an increased amount of attention to timely monitoring and diagnosis of incipient faults.

There are two pathways to expanding the research carried out on rolling-bearing diagnosis and fault-detection: developing more advanced signal processing methods to enhance fault-related signal contents, and improving fault models to gain an in-depth understanding of vibration responses to different types of faults under various application scenarios [118, 142]. The effective signal processing methods require a full understanding of the vibration mechanisms. Therefore, in recent years, more and more studies have put their focus on modelling bearing vibrations, in parallel with a great deal of efforts on development of signal processing methods.

Simulation models play an important role in the development of diagnostic and prognostic techniques in real rolling-element bearings systems. Such models allow for the faults to be simulated under different operating conditions, instead of waiting for their natural occurrence, or alternatively having them seeded for laboratory testing. In a simulation model, not only the location, but also the size and type of a fault can be varied. Thus, the signals produced for a range of operating conditions, including random fluctuations, can be used for testing new diagnostic algorithms, which may only occur under certain conditions. Simulation studies also provide a better understanding of how fault symptoms are generated, in particular where nonlinearities are involved. Subsequently, this Chapter reports on a simulation model, developed for a deep-groove ball bearing, in which a range of internal radial clearances, as well as bearing faults studied.

4.2   Modelling of Rolling Bearings with Clearances and Defects

A typical rolling-element bearing is comprised of four main fundamental components; the outer race, the inner race, the cage and the rolling elements. The most important geometrical quantities are the number of rolling elements N_b, the element diameter D, the pitch diameter d_m, and the contact angle α. In order to describe the behaviour of

every bearing component, a simulation model with a large number of degrees of freedom (DOF) is required. In this work, the bearing is modelled as a 5- DOF system that provides the load-deflection relationships, whilst neglecting the mass and the inertia of the rolling elements. The first two orthogonal DOFs describe the inner race-shaft, the second set of orthogonal DOFs describes the outer race-house, and finally, the last remaining DOF is related to the sensor in the 'X' axis.

The proposed model is carefully crafted to include the following metrics; the nonlinearity in a rolling bearing, arising from the nonlinear forces between the different elements (Hertzian contact); the time-varying stiffness (load transmission dependency on the positioning of the supporting elements); and the clearance value between the rolling elements and the bearing races. This leads to an enhanced simulation response of the dynamics of the roller-element bearings.

4.2.1 Free Body Diagram

Figure 4-1 illustrates the free-body diagram for the shaft-house system. As can be seen, the model is mainly comprised of four DOFs, representing the motions of the shaft and the housing in the horizontal and vertical directions, respectively. And one DOF is used to represent the output of the vibration sensor in the vertical direction. To realise an efficient simulation, the proposed model is developed on the foundations of the following realistic assumptions and considerations:

- Balls are positioned equidistantly around the shaft and there is no interaction between them,
- Ball mass is relatively small in comparison to other bearing parts (refer to Table 5-1), and thus, assumed negligible;
- The bearing under study operates under isothermal conditions;
- Forces act in radial directions along both the X and Y axes;
- The inner-race mass includes the shaft's mass, whilst the outer-race mass incorporates the housing's mass;
- The sensor is considered as a mass-damping system and is positioned along the X axes;
- The shaft-housing under study is modelled using three masses (M_s, M_k and M_r), yielding a 5-DOF system;

- The interactions between the balls and raceways are considered as nonlinear Hertzian contact-deformations.
- Damping due to lubrication is neglected in this study.
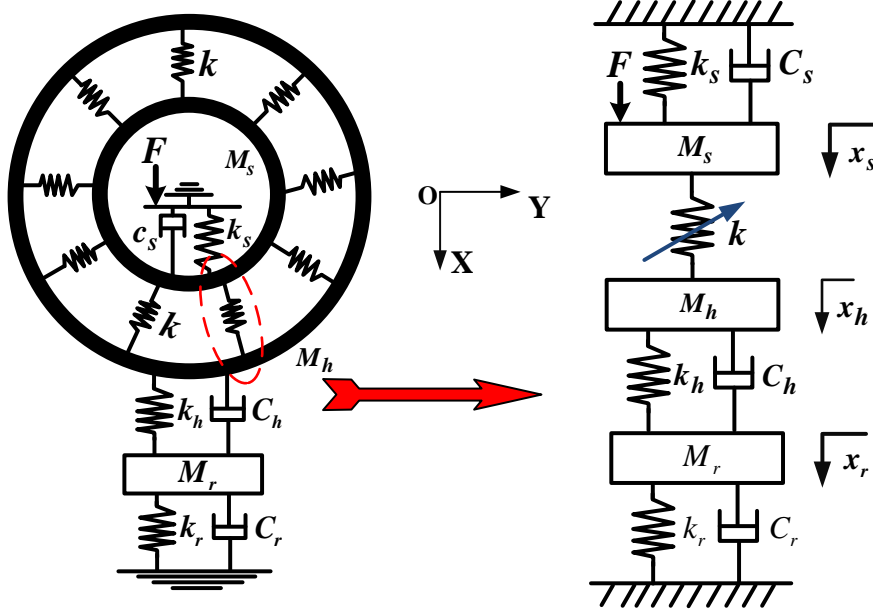
Figure 4-1 Free-body diagram of the shaft-housing system

4.2.2 Equation of Motion

Considering the modelling assumptions mentioned above, the governing equations for the mass of the shaft, housing and the sensor can be developed. Depending on the direction and coordinates of the motion, as shown in Figure 4-1, the governing equations are established in the X and Y directions as follows.

For the shaft:

$$M_s \ddot{X}_s + C_s \dot{X}_s + K_s X_s + \sum_{i=1}^{N_b} K [\delta]^{3/2} \cos \phi_i = F \tag{4-1}$$

$$M_s \ddot{Y}_s + C_s \dot{Y}_s + K_s Y_s + \sum_{i=1}^{N_b} K [\delta]^{3/2} \sin \phi_i = 0 \tag{4-2}$$

For the housing:

$$M_h \ddot{X}_h + C_h \dot{X}_h + K_h X_h - \sum_{i=1}^{N_b} K [\delta]^{3/2} \cos \phi_i = 0 \tag{4-3}$$

$$M_h \ddot{Y}_h + C_h \dot{Y}_h + K_h Y_h - \sum_{i=1}^{N_b} K[\delta]^{3/2} \sin \phi_i = 0 \tag{4-4}$$

For the sensor:

$$M_r \ddot{X}_r + C_r \dot{X}_r + K_r X_r - C_h \dot{X}_h - K_h X_h = 0 \tag{4-5}$$

where M_s, M_k and M_r denote the mass of shaft, housing and sensor, respectively; K_s, K_h and K_r, respectively, represent the stiffness of shaft, housing and sensor; C_s, C_h and C_r are the damping of shaft, housing and sensor, respectively; K represents the nonlinear stiffness, δ represents the nonlinear deformation and ϕ_i denotes the ball position. Equations (4-1) to (4-4) show that the vibration of a bearing is governed by a nonlinear process, in which the nonlinear deformation between the races and the balls are described by a time-varying stiffness.

4.2.3 Modelling the Effect of Bearing Clearances

4.2.3.1 Internal Clearance

Internal radial clearance is defined as the geometrical clearance between the inner race, outer race and ball. Whereas, radial clearance is the movement between the ball and the raceway, perpendicular with the bearing axis. The internal clearance has a significant effect on thermal, vibrational, noise and fatigue life of the bearing. In order to extend the bearing's lifetime and improve the machine's reliability, the internal clearance at operational conditions must be as close to zero as possible [89, 90]. As the bearing ages, the properties of the clearances vary due to the inevitable wear. Thus, for the purposes of fault-detection and diagnosis, it is important to have an appreciation for the effect of different clearances on the characteristic vibration features. Changes in the bearing internal clearance can directly affect the size of the stressed area of the rings (i.e. the load zone), as shown in Figure 4-2. The smaller the clearance (or the more the preload), the more the rolling elements will have to share the externally applied forces to the bearing shaft. However, preload may reduce the life of the bearing under operation due to the increased levels of fatigue stress in the rolling elements.

In order to measure the dimensions of a bearing's internal clearance, a slight measurement load is applied to its raceway. However, this results in a slight amount of elastic deformation to occur, causing the clearance measurement value (measured clearance) to be slightly larger than it actually is.
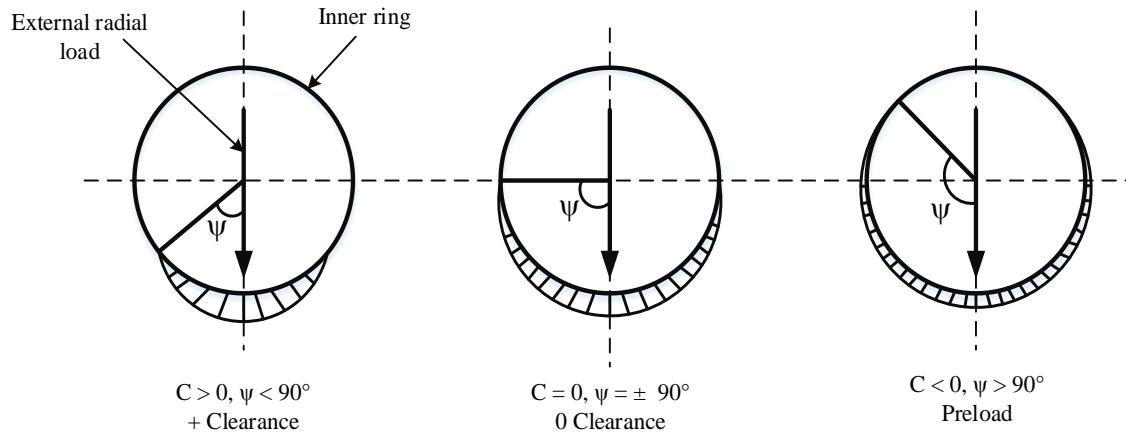
Figure 4-2 Rolling element load distribution for different amounts of clearance [143]

The angular-contact ball bearings are specifically designed to operate under radial and thrust loads. Moreover, the clearance built into the unloaded bearing angle of the radially loaded bearing. There are five clearance groups, namely, C2, C0 (Normal), C3, C4 and C5. The radial internal clearances for a radial-contact deep-groove ball beating 6206ZZ (UC206) are presented in Table 4-1 [89].

Table 4-1 Radial internal clearance for deep groove ball bearing 6206ZZ under no load [89]

Clearance values (μm)									
C2		C0		C3		C4		C5	
Min	Max	Min	Max	Min	Max	Min	Max	Min	Max
1	11	6	20	15	33	28	46	40	64

In order to demonstrate the effect of clearance on bearing vibration response, the nonlinear load deformation and its distribution along the rolling elements are examined according to the Hertzian theory. As stated in [89], the relationship between the load Q and the resulting deformation can be expressed as,

$$Q = K\delta^n \tag{4-6}$$

where K is the load deflection factor or constant for Hertzian contact elastic deformation, which depends upon material properties and geometry of the contact surfaces; δ is the radial deflection or contact deformation; and n is the load deflection exponent, where $n = 3/2$ for the ball bearing and $n = 10/9$ for the roller bearing [89]. As illustrated in Figure 4-3, the elastic deformation in rolling-element bearings takes place between both the inner and outer raceways and the rolling elements.
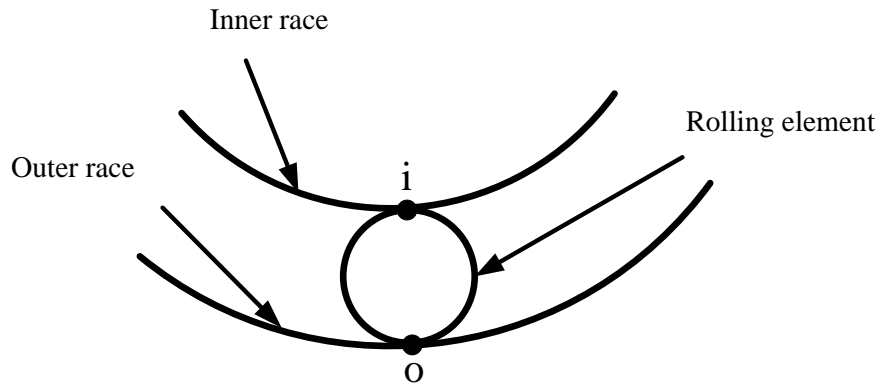
Figure 4-3 Contacts of a ball with the inner and outer raceways

The stiffness coefficients at the contact points formed by the races and the *ith* ball are evaluated using the following equation as [144, 145],

$$K_{i,o} = \frac{2\sqrt{2}\left(\dfrac{E}{1-\nu^2}\right)}{3\left(\sum \rho\right)^{1/2}} \left(\frac{1}{\delta^*}\right)^{3/2} \tag{4-7}$$

For steel ball-steel raceway contact,

$$K_{i,o} = 2.15 \times 10^5 \sum \rho^{-1/2} \left(\delta^*\right)^{-3/2} \tag{4-8}$$

where $K_{i,o}$ is the stiffness of the contact between the inner and outer raceways and the ball respectively; E is Young's modulus; ν is Poisson's ratio; $\sum \rho$ is the sum of the curvatures and is calculated using the radii of the curvature in a pair of principal planes, passing through the point of contact; and δ^* is a dimensionless contact deflection, which is obtained using the curvature differences (refer to Table 4-2).

According to the work carried out in [89], the total deflection between two raceways can be expressed as the sum of the corresponding approaches between the rolling elements and each raceway, given as,

$$K = \left[\frac{1}{\left(1/K_i\right)^{1/(3/2)} + \left(1/K_o\right)^{1/(3/2)}} \right]^{3/2}$$

(4-9)

Table 4-2 Dimensional contact parameters [143]

$F(\rho)$	a^*	b^*	δ^*
0	1	1	1
0.1075	1.0760	0.9318	0.9974
0.3204	1.2623	0.8114	0.9761
0.4795	1.4556	0.7278	0.9429
0.5916	1.6440	0.6687	0.9077
0.6716	1.8258	0.6245	0.8733
0.7332	2.011	0.5881	0.8394
0.7948	2.265	0.5480	0.7961
0.83495	2.494	0.5186	0.7602
0.87366	2.800	0.4863	0.7169
0.9099	3.233	0.4499	0.6636
0.93657	3.738	0.4199	0.6112
0.95738	4.395	0.3830	0.5551
0.97290	5.267	0.3490	0.4960
0.983797	6.448	0.3150	0.4352
0.990902	8.062	0.2814	0.3745
0.995112	10.222	0.2497	0.3176
0.997300	12.789	0.2232	0.2705
0.9981849	14.839	0.2072	0.2427
0.9989156	17.974	0.18822	0.2106
0.9994785	23.55	0.16442	0.17167
0.9998527	37.38	0.13050	0.11995
1	∞	0	0

Now, assuming the shaft and housing damping are hysteretic, the equivalent viscus damping coefficient is calculated as,

$$C_{s,h} = 2\varsigma\sqrt{K_{s,h} \times M_{s,h}}$$

(4-10)

where ς is the damping ratio, $K_{s,h}$ is the shaft and housing stiffness, and $M_{s,h}$ is the shaft and housing mass.

- **Curvature and Relative Curvature**

When two bodies are under a no-load condition and in revolution with different radii of curvature, they may become in contact with each other at a single point on a pair of principal planes. This is referred to as a 'point contact' condition [89]. The effective radii of curvature, r_i and r_o for the inner and outer ball-bearing races are respectively expressed as [90],

$$r_i = \left[\frac{2d_m}{D(d_m - D)} + \frac{2f_i - 1}{f_i D} \right]^{-1} \tag{4-11}$$

$$r_o = \left[\frac{2d_m}{D(d_m - D)} + \frac{2f_o - 1}{f_o D} \right]^{-1} \tag{4-12}$$

Where, f_i and f_o are the inner and outer race conformities respectively,

$$f_i = \frac{d_i / 2}{D} \tag{4-13}$$

$$f_o = \frac{d_o / 2}{D} \tag{4-14}$$

In Figure 4-4 body 'I' is the upper body, whilst 'II' is the lower body. The principal planes are denoted by 1 and 2. Therefore, the radius of curvature for body 'I' on plane 2 is denoted by r_{I2}. The relationship between the radius r of a curvature and the curvature itself can be defined as,

$$\rho = \frac{1}{r} \tag{4-15}$$

It should be noted that, despite the fact that the radius of curvature is always positive, the curvature itself can take either a positive or negative sign, such that, convex surfaces considered positive and concave surfaces as negative. To describe the contact between the mating surfaces of revolution, herein, the following definitions are adopted [143].

Curvature sum:

$$\sum \rho = \frac{1}{r_{I1}} + \frac{1}{r_{I2}} + \frac{1}{r_{II1}} + \frac{1}{r_{II2}} \tag{4-16}$$

Curvature difference:

$$F(\rho) = \frac{(\rho_{I1} - \rho_{I2}) + (\rho_{II1} - \rho_{II2})}{\sum \rho} \tag{4-17}$$

where, $F(\rho)$ always take a value between 0 and 1.

For ball-bearing inner-race contact:

$$r_{I1} = \frac{D}{2}, \ r_{I2} = \frac{D}{2}, \ r_{II1} = \frac{1}{2}d_i = \frac{1}{2}\left(\frac{d_m}{\cos\alpha} - D\right) \text{ and } r_{II2} = r_i \tag{4-18}$$

Therefore,

$$\rho_{I1} = \rho_{I2} = \frac{2}{D}, \ \rho_{II1} = \frac{2}{d_i} \text{ and } \rho_{II2} = -\frac{1}{r_i} \tag{4-19}$$
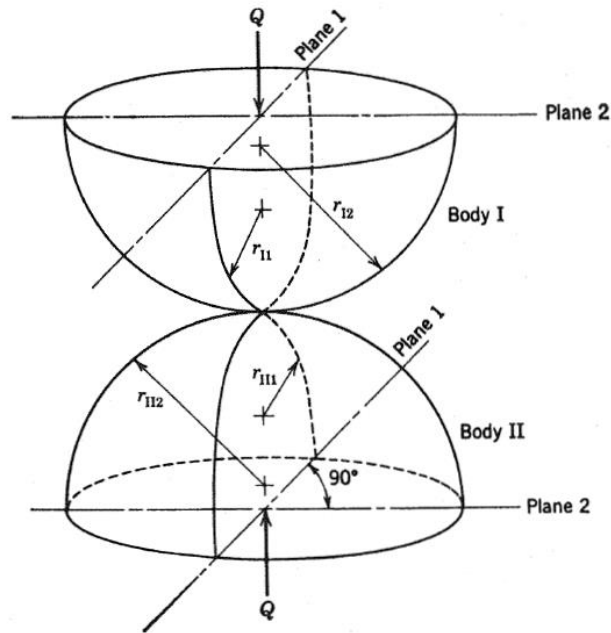
Figure 4-4 Geometry of contacting bodies [89]

For the ball-bearing outer race contact:

$$r_{I1} = r_{I2} = \frac{D}{2}, \ r_{II1} = \frac{1}{2}\left(\frac{d_m}{\cos\alpha} + D\right) = \frac{d_o}{2}, \text{ and } r_{II2} = r_o \tag{4-20}$$

Therefore,

$$\rho_{I1} = \rho_{I2} = \frac{2}{D}, \ \rho_{II1} = \frac{-2}{d_o} \ \text{and} \ \rho_{II2} = -\frac{1}{r_o} \tag{4-21}$$

4.2.3.2   Calculation of Load Distribution with Clearance

A rigidly supported rolling-element bearing that is subjected to a radial load is illustrated in Figure 4-5. Evidently, a uniform radial clearance of $\frac{P_d}{2}$ between the rolling element and the races can be observed for the concentric arrangement. In the case of a subjectively small radial load applied to the shaft, the inner race moves a distance of $\frac{P_d}{2}$, before creating contact between a rolling element located on the load line and the inner and outer races. Regardless of the angle, a radial clearance will still be present.

Now, assuming a relatively small P_d in comparison to the radius of the groove, the radial clearance c can be expressed with adequate accuracy by [146],

$$c = P_d/2(1 - \cos\phi) \tag{4-22}$$

On the load line, when $\phi = 0^o$ the clearance is zero, whereas for $\phi = 90^o$, the clearance retains its initial value of $\frac{P_d}{2}$.

The application of a load will elastically deform the balls. This will further reduce the clearance around an arc of the size 2ψ. Now, considering $\delta_{\max}$ as the interference or total compression on the load line, the corresponding radial deflection δ at any rolling element angular position ϕ can be expressed as [89, 146],

$$\delta_\phi = (\delta_{\max} + \frac{P_d}{2})\cos\phi - \frac{1}{2}P_d \tag{4-23}$$

where $\delta_{\max} + P_d/2$ represents the total radial displacement of the inner and outer races, relative to one another. Now, considering $\delta = \delta_{\max} + P_d/2$, Equation (4-23) can be simplified and re-written as,

$$\delta_\phi = \delta\cos\phi - \frac{1}{2}P_d \tag{4-24}$$

(a)   (b)   (c)
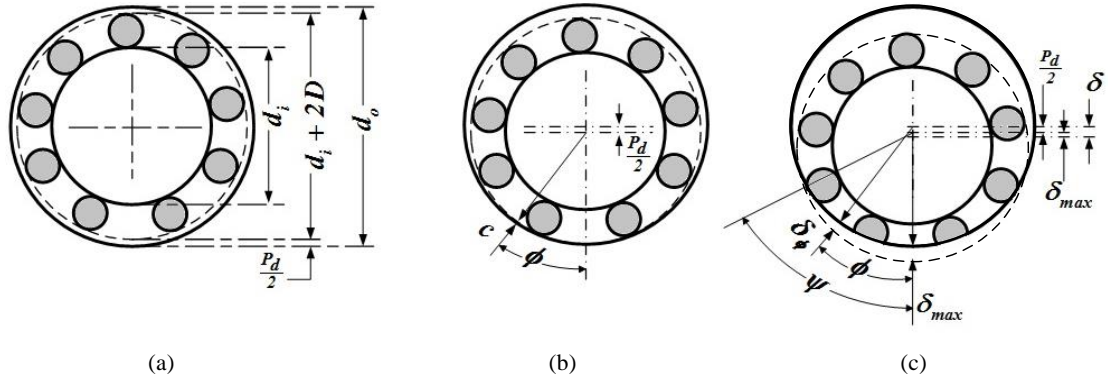
Figure 4-5 Radial deflection at a rolling element position. (a) concentric arrangement, (b) initial contact, (c) interference [89, 146]

It should be noted that, the angular positions ϕ_i of the rolling elements are given as a functions of time increment dt, the previous ball position ϕ_0 and the cage speed ω_c. Assuming no slippage, cage speed can be calculated from bearing geometry and shaft speed ω_s. Ultimately, the angular positions of the rolling elements are given as,

$$\phi_i = \frac{2\pi}{N_b}(i-1) + \omega_c t + \varphi_0, \ i = 1,...,N_b \tag{4-25}$$

The angular velocity ω_c of the cage can be expressed in terms of the shaft's speed ω_s as,

$$\omega_c = \left(1 - \frac{D}{d_m}\right)\frac{\omega_s}{2}, \ \omega_s = 2\pi f_s \tag{4-26}$$

where f_s is the shaft frequency. Similarly, the angular velocity of the balls can be expressed in terms of the shaft's angular velocity as,

$$\omega_b = \frac{D}{d_m}\frac{\omega_s}{2}\left(1 - \frac{D^2}{d_m^2}\right) \tag{4-27}$$

The radial deflection at any rolling-element angular position, in terms of maximum deformation, may be obtained by rearranging Equation (4-23) as,

$$\delta_\varphi = \delta_{max}\left[1 - \frac{1}{2\varepsilon}(1 - \cos\phi_i)\right] \tag{4-28}$$

where $\varepsilon = \dfrac{1}{2}\left(1 - \dfrac{P_d}{2\delta_r}\right)$

Therefore, the contact force at any angular position can be given as,

$$Q_\varphi = Q_{\max}\left[1 - \frac{1}{2\varepsilon}\left(1 - \cos\phi_i\right)\right]^{3/2} \tag{4-29}$$

For a ball bearing with a nominal-diameter clearance under a purely radial load, the maximum reaction force can be approximated as [143],

$$Q_{\max} = \frac{5F}{N_b \cos\alpha} \tag{4-30}$$

As can be seen in Figure 4-6, the overall applied radial load (F) is equal to the sum of the vertical components of the contact reactions caused by the rolling-element loads. Mathematically, this is expressed as,

$$F = \sum_{\phi=0}^{\phi=\pm\psi} Q_\varphi \cos\psi \tag{4-31}$$
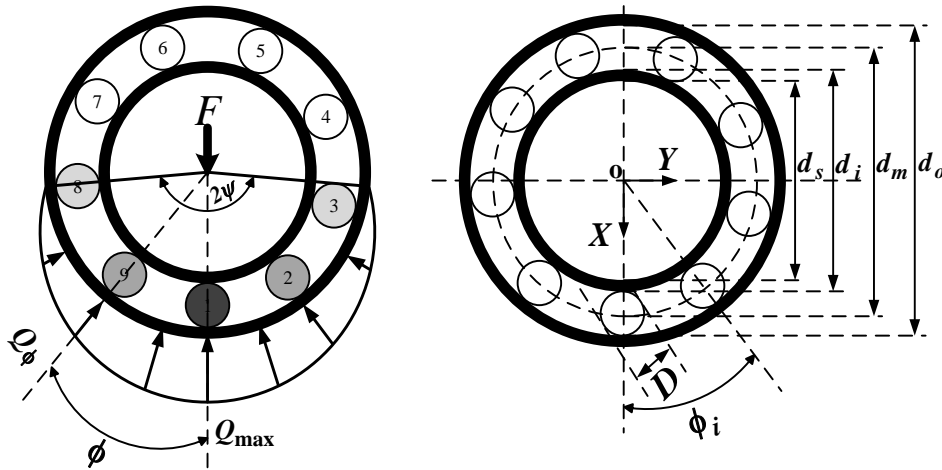
Figure 4-6 Load distributions in a ball bearing

4.2.3.3 Calculation of Restoring Force

The total restoring force is calculated by summing the restoring forces caused by each individual rolling element in the X and Y directions as,

$$F_X = \sum_{i=1}^{N_b} K\left[\delta\right]^{3/2} \cos\phi_i \tag{4-32}$$

$$F_Y = \sum_{i=1}^{N_b} K\left[\delta\right]^{3/2} \sin\phi_i \tag{4-33}$$

The overall contact deformation (or contact compression) δ for the *ith* ball can be expressed as a function of shaft displacement relative to the housing in the X and Y directions, ball position ϕ_i and the radial clearance c give as,

$$\delta = \left(X_s - X_h\right)\cos\phi_i + (Y_s - Y_h)\sin\phi_i - c \tag{4-34}$$

Since the Hertzian forces arise only when there is a contact deformation, the springs are required to act only in compression. This means that the respective spring force comes into play only when the instantaneous spring length is shorter than its unstressed length, yielding only a positive δ value. Otherwise, a separation between the ball and the race takes place, setting the restoring force back to zero [12]. Subsequently, the contact force Q at any ball position can be defined as,

$$Q = \begin{cases} K\delta^{3/2}, & \delta > 0 \\ 0, & \delta \leq 0 \end{cases} \tag{4-35}$$

At the time of impact between the rolling element and the defect, a short-duration pulse is generated causing an additional deflection. This is denoted by the term Δ, yielding a modified expression for δ given as,

$$\delta = \left(X_s - X_h\right)\cos\phi_i + \left(Y_s - Y_h\right)\sin\phi_i - c - \Delta \tag{4-36}$$

4.2.4   Modelling Localized Defects

Cracks on the inner and outer raceways are classified as localised defects. The study of such defects allows for a better understanding of the effect of different clearances on the bearing vibration response and the diagnostic features of interest. Therefore, this section aims to provide a mathematical simulation of the localised bearing defects.

4.2.4.1 Vibration Responses due to Different Sizes of Fault

The characteristic bearing frequency Equations reported in Chapter three Section 3.2.3 provide a theoretical estimate of the expected frequencies in the case of different bearing defects. The equations are derived based on the assumption that an ideal impulse will be produced whenever the defect is struck by a bearing element. Localised bearing faults, such as spalling and pitting, result in sharp impacts to be generated. In practice, these impacts excite the bearing's structural resonances, where the resulting vibration is measured by the transducer mounted externally on the machine's casing [147]. Due to the different geometrical properties of the contact between the localised defect and the bearing component in the contact zones, the contact-stiffness can change. This results in a repetition of impulsive impacts, producing small amplitudes of vibration in the high frequency bands [117].
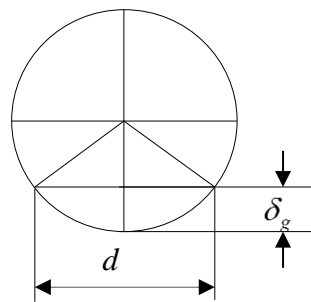
Figure 4-7 Schematic diagram of geometry deformation
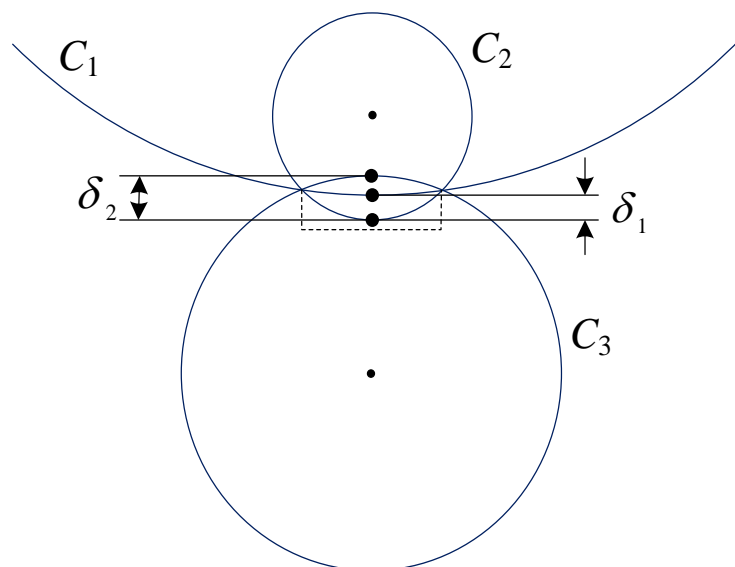
Figure 4-8 Geometry deformation for two kinds of contact

The contact deformation consists of both geometric and elastic deformations. Elastic deformation occurs along the contact surfaces of a bearing's rolling elements and the raceway surfaces, whilst under loading. Whereas geometric deformation is related to the defect's location and size.

The total deformation δ includes the geometry deformation δ_g and the elastic deformation δ_e, such that,

$$\delta = \delta_g + \delta_e \tag{4-37}$$

As can be seen in Figure 4-7, the chord height for a fault width of d, and a radius of r can be calculated as,

$$crd = r - \sqrt{r^2 - \left(\frac{d}{2}\right)^2} \tag{4-38}$$

There are two types of models that describe the contact between bearing components, as shown in Figure 4-8; first type describes the contact between a convex and a concave surface (C1 and C2), and the second type describe the contact between two convex surfaces (C2 and C3). Now, if the chord height for C1, C2 and C3 are defined as $crd1$, $crd2$ and $crd3$, the geometry deformation of a concave-convex contact δ_1 and that of a concave-concave contact δ_2 can be obtained by using Equation (4-39) and Equation (4-40), respectively.

$$\delta_1 = crd2 - crd1 \tag{4-39}$$

$$\delta_2 = crd2 + crd3 \tag{4-40}$$

Note that, a fault on the inner-race gives rise to a concave-concave contact, whereas a fault on the roller can result in both concave-concave and concave-convex contacts. The resulting vibration from an inner-race defect produces the highest response when the fault sizes are all the same on different races as shown in Equation (4-41). From the relationship it is easy to understand that geometry deformations on different components have a relationship.

$$\delta_{go} < \delta_{gr} < \delta_{gi} \qquad\qquad (4\text{-}41)$$

Considering the effect of elastic deformation, it is possible to understand the impulsive differences between different fault severities. As the fault severity increases, the load area decreases and the elastic deformation δ_e increases too. This results in a growth in the impulse height.

4.2.4.2   Vibration Responses due to Fault Location

The position of the defect on the raceway largely depends on the geometry of the inner and outer raceways. Figure 4-9 illustrates a defect of the same size on both the inner and outer raceways. It is apparent that the angular width of the inner-race defect θ_i is larger than that of the outer-race defect θ_o, as defined by Equation (4-42) and Equation (4-43), respectively. Therefore, the switch values and the periods of switching (W_{defect}) will not be the same for both races, which results in a deeper and longer contact for the inner-race defect, compared to the outer-race defect.

Angular width of the fault as sensed by the inner race is given by,

$$\theta_i = \frac{W_{defect}}{(d_i/2)} \qquad\qquad (4\text{-}42)$$

Angular width of the fault as sensed by the outer race is given by,

$$\theta_i = \frac{W_{defect}}{(d_o/2)} \qquad\qquad (4\text{-}43)$$
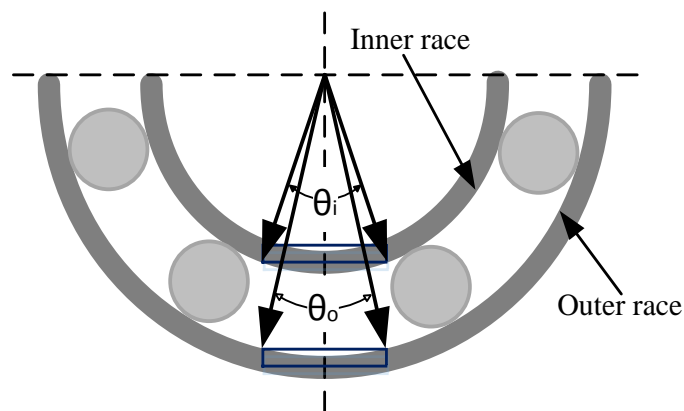
Figure 4-9 Defect angle on inner and outer raceways

4.2.4.3 Modeling Defect on the Inner Race

Figure 4-10 provides a typical inner-race defect. As can be noted, during operation, the inner race will rotate at the shaft' angular speed ω_s, implying that the location of the defect will not remain stationary. Thus, the resulting defect angle for the inner race α_{in} can be calculated as,

$$\alpha_{in} = \omega_s t \pm \left(W_{defect} / d_i \right) \tag{4-44}$$

where W_{defect} is the defect width and d_i is the inner race diameter. The rolling ball comes into contact with the defect either in the loaded zone or in the unloaded zone; thus, the deflection δ attained for every *ith* ball can vary. As the ball passes through the defect, an additional deflection Δ usually occurs (see Figure 4-10), which is mainly defined by the width of the defect and the radius of the rolling elements.

$$\Delta = (\frac{D}{2} - \frac{D}{2} \times \cos(0.5 \varphi_{ball})) \tag{4-45}$$

where φ_{ball} = width of the defect / radius of the ball.

The position of the *ith* ball in the defect zone is mathematically defined as,

$$\left(\omega_s t - W_{defect} / d_i \right) \leq \phi_i \leq \left(\omega_s t + W_{defect} / d_i \right) \tag{4-46}$$
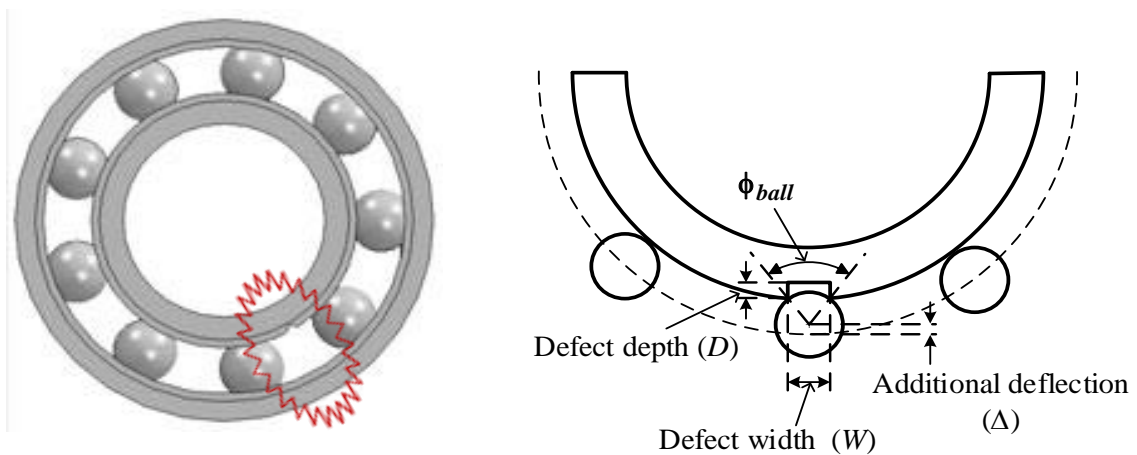
Figure 4-10 Additional deflection of ball due to defect on inner race

4.2.4.4   Modeling Defect on the Outer Race

An example of a defect occurring on the outer race is demonstrated in Figure 4-11. It is observable that the defect on the outer race is located at an angle α_{out} from the X axis. In contrast to the inner-race defects, the local defects on the outer race are normally found in the loaded region. Moreover, since the outer race is stationary, the position of the defect does not usually change. Similar to the inner-race defect, an additional deflection Δ is caused every time the ball passes over the defect.

The angular position of *ith* ball passing through the defect zone is mathematically defined by the following relation:

$$\left(\alpha_{out} - W_{defect} / d_o\right) \le \phi_i \le \left(\alpha_{out} + W_{defect} / d_o\right) \tag{4-47}$$
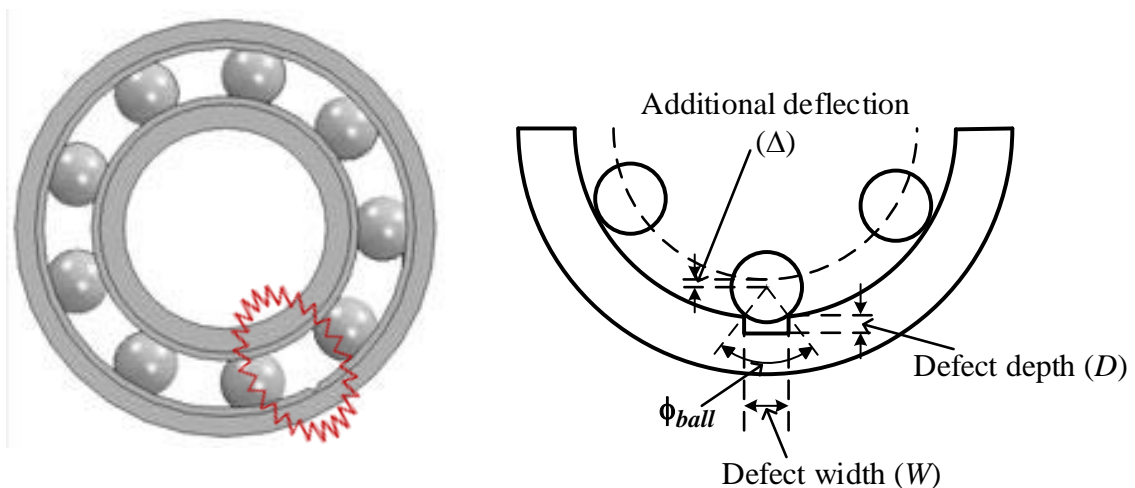
Figure 4-11 Additional deflection of ball due to defect on outer race

4.3   Summary

In this chapter, mathematical dynamic model of a deep-groove ball bearing has been developed. The study focused on the influence of internal radial clearance in the bearing vibration signature. 4-DOFs representing the shaft and housing and 1-DOF demonstrating the sensor are considered for the studied model (see Sections 4.2.1 and 4.2.2 for more details). The load-deflection relationship has been included as it is mainly influenced by the change in the internal radial clearance (see Section 4.2.3). Localised defects in both

inner-race and outer-race were mathematically included in this model, where the geometric deformation and the fault location are considered too (see Section 4.2.4).

CHAPTER FIVE

SIMULATION RESULTS OF DYNAMIC RESPONSES OF DEEP-GROOVE BALL BEARING

This Chapter investigates the simulation results based on the 5-DOF nonlinear model developed in the previous Chapter. Firstly, a linearised model is used to find system responses, which help to calibrate model parameters used. Subsequently nonlinear responses are obtained using ordinary differential equation solver (ode15s) under different fault conditions, different radial clearances and loads. This allows an in-depth understanding of vibration characteristics and paves ways to develop effective analysis methods.

5.1   Introduction

In order to gain an in-depth understanding of the mechanisms responsible for vibration in bearing transmission systems, dynamic models of rolling-element bearings are employed. By using such models, it is possible to capture the behavioural dynamic response of different bearing vibration signals, with respect to internal clearance increments caused by inevitable wear and localised defects (see Chapter four for more details). Finally, the results provided in this Chapter will be used to set the direction for measurement configuration, data processing selection and diagnosis rule development.

5.2   Predictive Behaviour of Diagnostic Features

5.2.1   Model Parameter Calibration

The physical model parameters, such as dimensions and the masses, are measured. The damping ratio and the stiffness of the model masses are, on the other hand, more difficult to calibrate. Therefore, a simplified linear version of the 5-DOF nonlinear model is developed by using the nonlinear contact stiffness value given in Equation (4-9). This linearisation step allows for the model parameters, including resonance frequencies and damping ratios to be conveniently identified using the standard eigen method.

By considering those linear factors in the system, the vibration can be described by a set of differential equations as,

$$[M]\{\ddot{q}\} + [C]\{\dot{q}\} + [K]\{q\} = f(t) \tag{5-1}$$

$$\{\dot{V}\} = [A]\{q\} \tag{5-2}$$

where [M] is the mass matrix, [C] is the damping matrix, [K] is the stiffness matrix, [A] is the system matrix and $\{q\}$ is the vibration response vector, consisting of displacement, velocity and acceleration of the system. By using the standard methods for linearisation, the frequency response under different parameter settings can be simulated. Moreover, it is possible to mimic the sensor's response to high-frequency natural vibrations associated with the inner and outer bearing races, and the sensor's own response under excitation. This is achieved by modifying the stiffness and damping coefficients.

Table 5-1 Geometric properties for simulation study

Description	Symbol	Unit	Value
Inner race diameter	d_i	mm	37.48
Outer race diameter	d_o	mm	56.45
Pitch diameter	d_m	mm	46.96
Ball diameter	D	mm	9.48
Number of balls	N_b	-	9

Table 5-2 Physical properties for simulation study

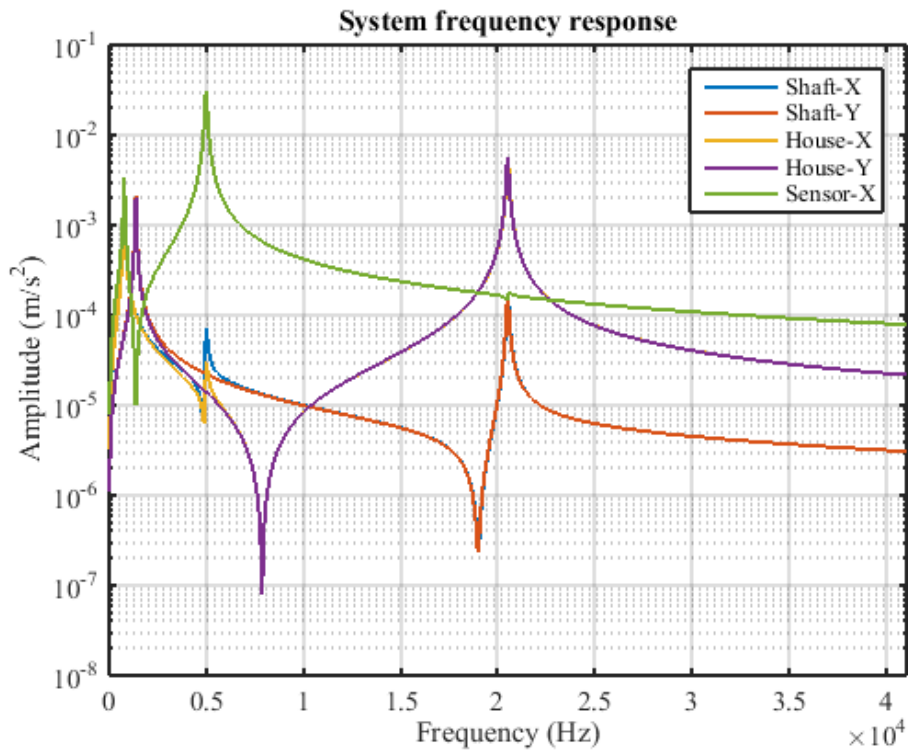| Description	Symbol	Unit	Value
Mass of outer race	M_o	g	59.84
Mass of inner race	M_i	g	32.40
Mass of sensor	M_r	g	35
Mass of ball	M_b	g	2.95
Mass of shaft	M_s	Kg	5.26
Mass of housing	M_h	Kg	1.0
Young's modulus	E	KN/mm^2	210
Poisson's ratio	v		0.3

Figure 5-1 Frequency response of the simulated ball bearing system

Figure 5-1 presents the simulation responses obtained using a refined set of parameters for a popular deep-groove ball bearing of the type 6206ZZ, with the specifications set in Table 5-1 and Table 5-2. It is observable that the sensor resonance frequency occurs at around 5 kHz. In order to maintain the stability of the nonlinear solutions at all times, small value of damping ratios (under damping) were used to represent a typical high resonance frequency. This will ensure a relatively sharp frequency response within the band of interest. Moreover, the frequency responses from the simulations match very well the measurement results obtained from the roller bearing installed in the lab. This implies that the key parameters used in the simulation model, (e.g. shaft and housing stiffness values and damping ratios) are set reasonably accurate. Therefore, the numerical procedures can be safely proceeded in order to obtain the nonlinear responses.

5.2.2 Non-linear Solution

Note that Equations (4-1) to (4-5) represent a second-order nonlinear differential model. To solve these nonlinear equations, they are first converted into two sets of first-order differential equations. Then, the ordinary differential equation solver 'ode15s' in MATLAB is then employed to solve the first-order differential equations for different faults and clearance conditions.

5.2.2.1 Effect of Variation of Radial Clearance

5.2.2.1.1 Initial Conditions

At the initialisation step, the displacements and velocities in X and Y directions are all set to zeroes. A shaft speed of 1500 rpm (25 Hz), with a radial load of 16 00 N is considered herein as the normal operating condition for the bearing under study. Moreover, two defects with widths of 0.2 and 0.4 mm on both inner and outer races are studied, which will be referred to as 'small' and 'large' faults, respectively.

The sequence of the calculation process is outlined in the flow chart presented in Figure 5-2. At each step in time, the governing equations of motions are solved using the ball position Equation (4-25) and the deflection relation Equation (4-36). Then, displacements in X and Y directions, and the corresponding velocities $\dot{X}$ and $\dot{Y}$ at time-step ($t + dt$) are calculated. Here, the time step (dt) is chosen as 0.2 μs for five cycles.
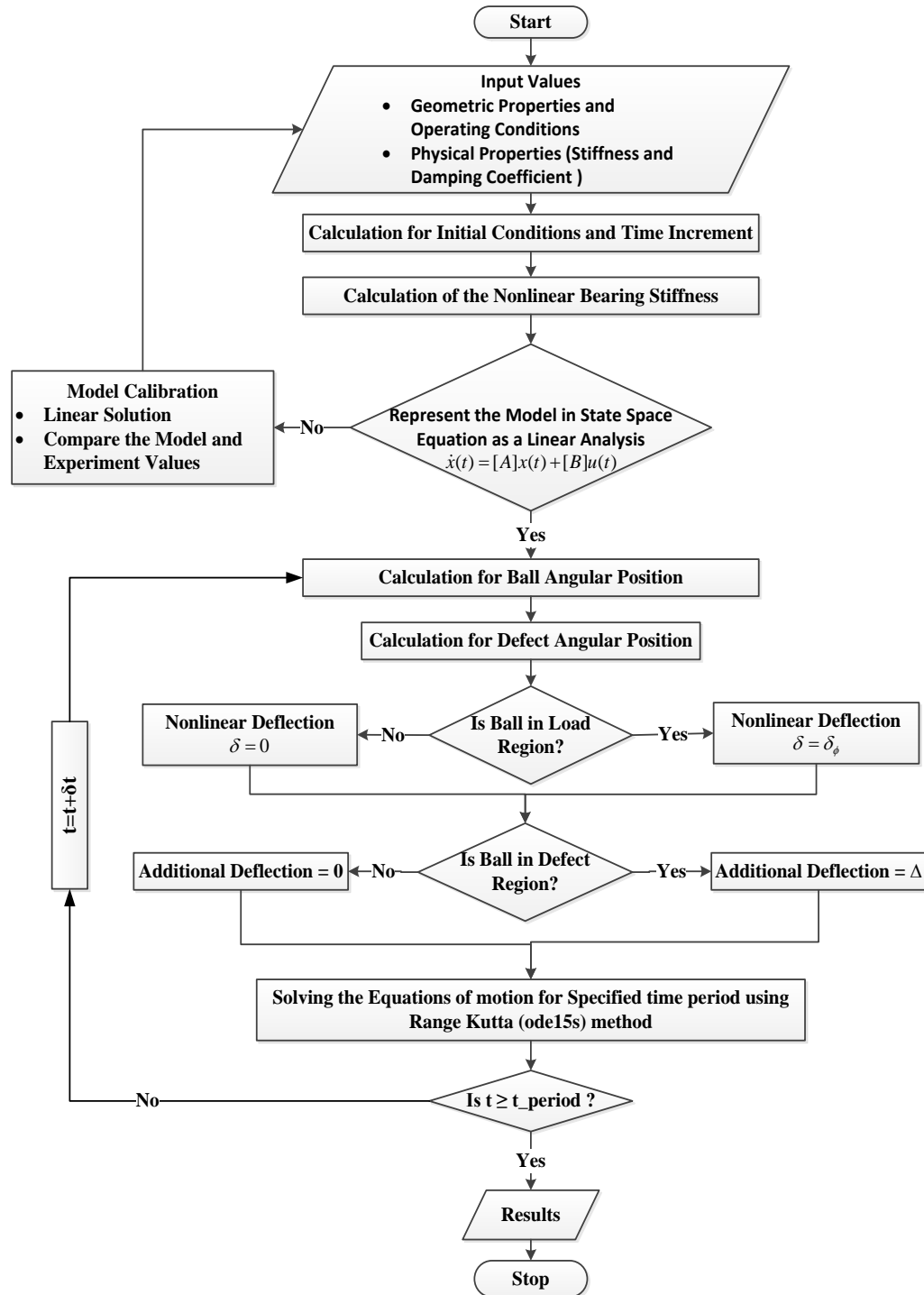
Figure 5-2. The flow chart of calculation process

5.2.2.1.2 Diagnosis of Outer Race Defect

Defects on the outer race usually appear in the loading zone and have a constant angular
position, i.e. the location of the defect is stationary. This means that, as the ball passes
over the defect every time, an impulse with the same amplitude is expected to appear.
The defect can also occur at the start of the loading zone, due to poor lubricant

conditions. Herein, two outer-race defect locations of 0 degrees and 320 degrees, with two defect widths of 0.2 and 0.4 mm are studied, under two incremental clearances of 15 and 45 μm.

1) Outer Race Defect at 0 Degree

Figure 5-3 presents the vibration acceleration of the sensor, simulated for a healthy bearing as the baseline and for a small and large defect cases, under clearance values of 15 and 45 μm. As can be seen, in the case of the baseline, as there is no defect on the races, a clear increase in the vibration acceleration is evident with clearance increments. Moreover, it can be seen that the amplitude of local (Hertzian deformation) becomes higher with increasing clearance. For the two defect cases, the impulses caused by the contact between the rolling elements and the defect repeat every 40 degrees. Moreover, an increase in both the impulse magnitude and duration with the defect size is observable.
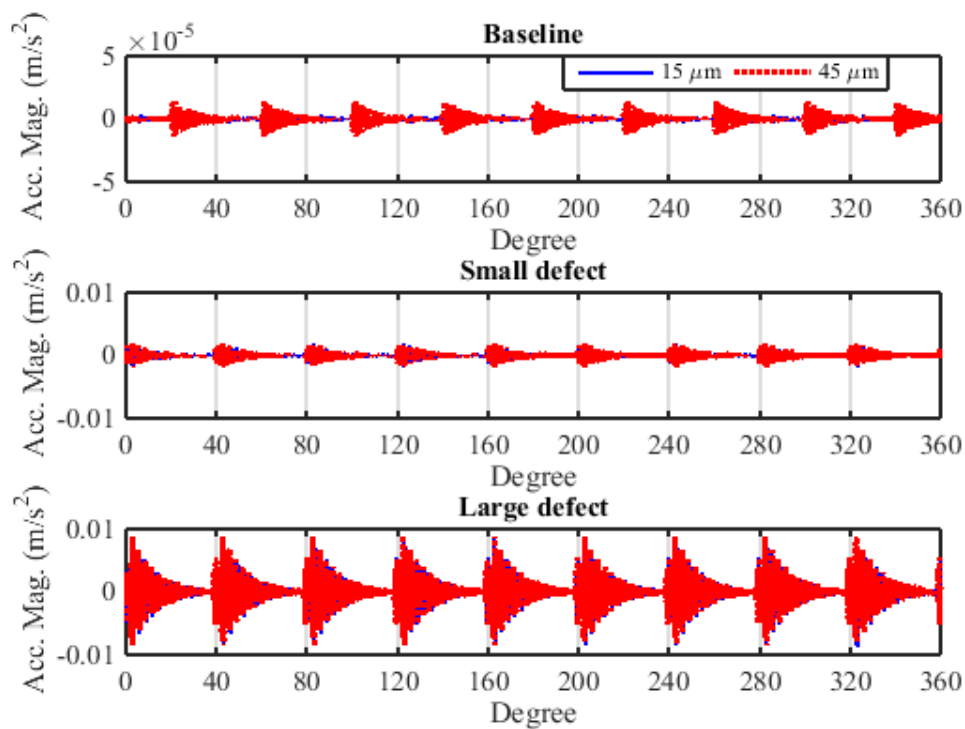
Figure 5-3 Vibration accelerations of baseline and outer-race defects

Figure 5-4 presents the frequency spectra obtained for the baseline and small and large defects. As can be seen, the band of resonance frequencies is concentrated at different areas. Nevertheless, the behavioural responses and excitation patterns for the three test

cases are shown to be similar. Moreover, the large defect case creates higher resonance amplitude than that observed for the smaller defect.
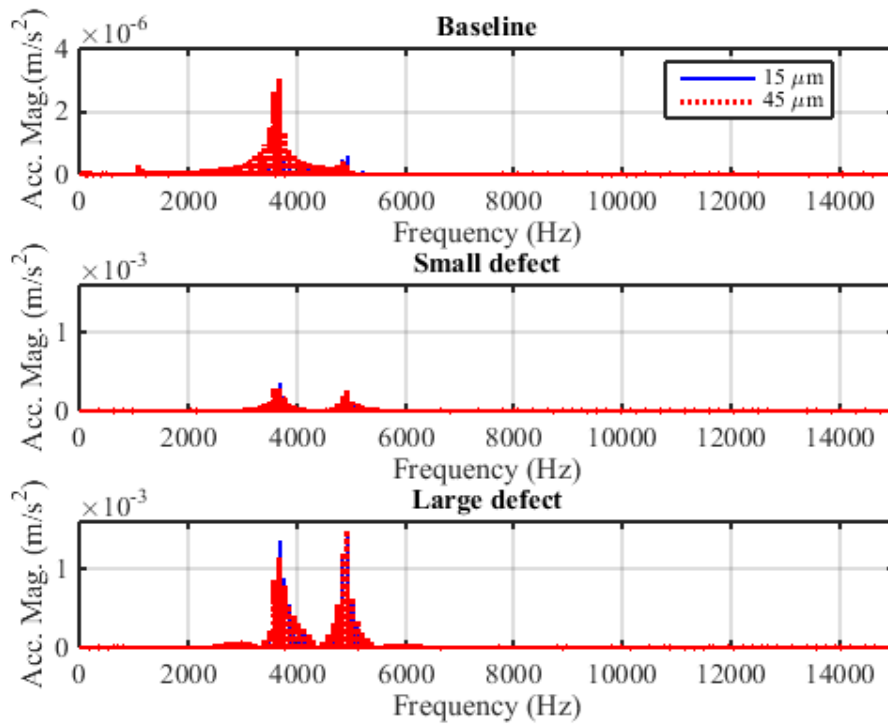
Figure 5-4 Acceleration spectra of baseline and outer-race defects
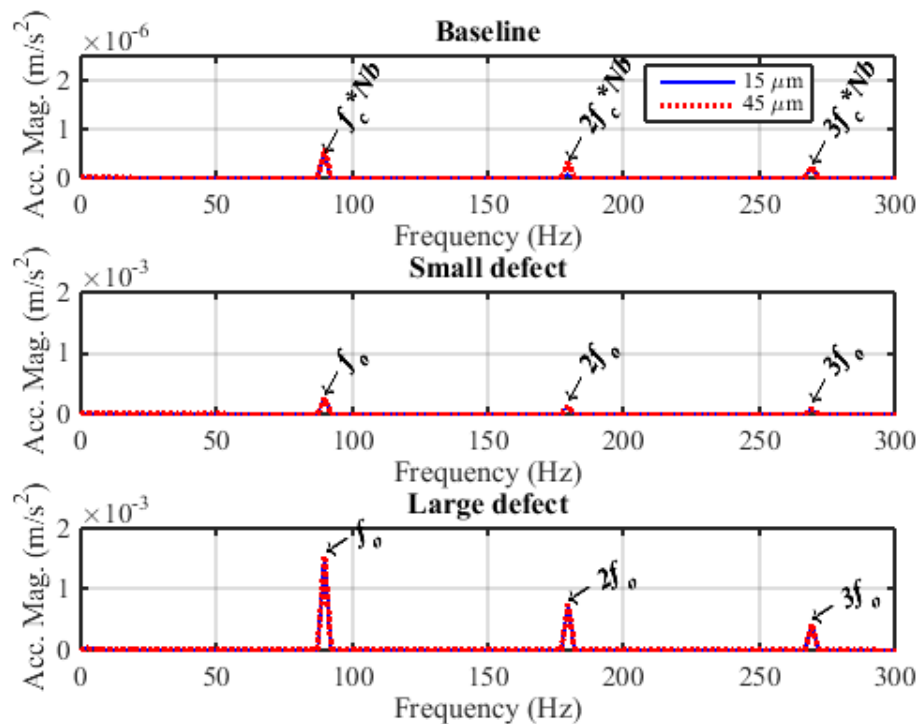
Figure 5-5 Envelope spectra for the baseline and the outer-race defects

Figure 5-5 presents the envelope spectra generated for the baseline and small and large defect cases. For the baseline, the loading frequency, which is equal to the cage frequency multiplied by the number of balls, is clearly observable. For the two defect cases, the ball-pass-frequency-outer-race (BPFO) is calculated at 89.8 Hz. The obtained fault feature-frequency and its harmonics are also apparent. Moreover, an increase in the defect acceleration magnitude can be seen, which is attributed to the defect size and the nonlinear deflection.
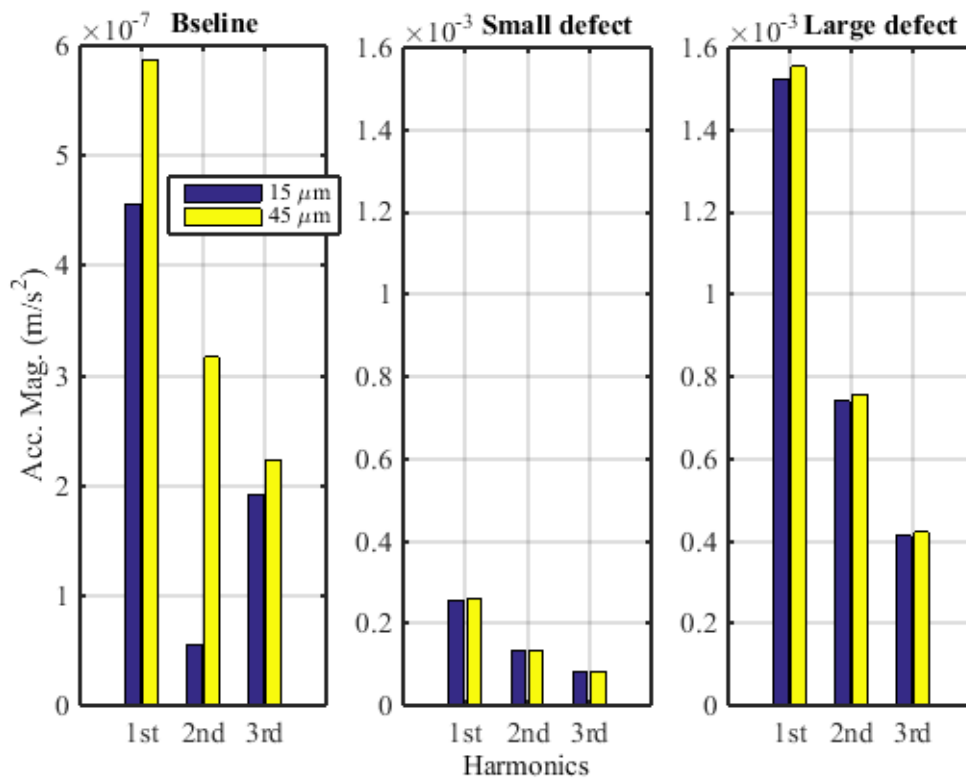
Figure 5-6 Baseline and outer-race acceleration amplitudes obtained for the fault characteristic-frequency

The acceleration amplitudes for the baseline, small defect and large defect cases are provided in Figure 5-6. As can be seen, for the baseline, the loading frequency amplitude is increased due to the large clearances. Similarly, for the defect cases, the BPFO magnitude and its harmonics are shown to have increased with increasing clearance values.

2) **Outer Race Defect at 320 Degrees**

In order to study the effect of changing defect position on the amplitude of the vibration acceleration, the defect's angular position is changed to 320 degrees, with two defect sizes of 0.2 and 0.4 mm, under a radial load of 1.6 kN. Figure 5-7 presents the vibration acceleration amplitudes for the two cases of small and large defects. In both cases, a decrease in the BPFO magnitude and its harmonics with increasing clearance values is evident.
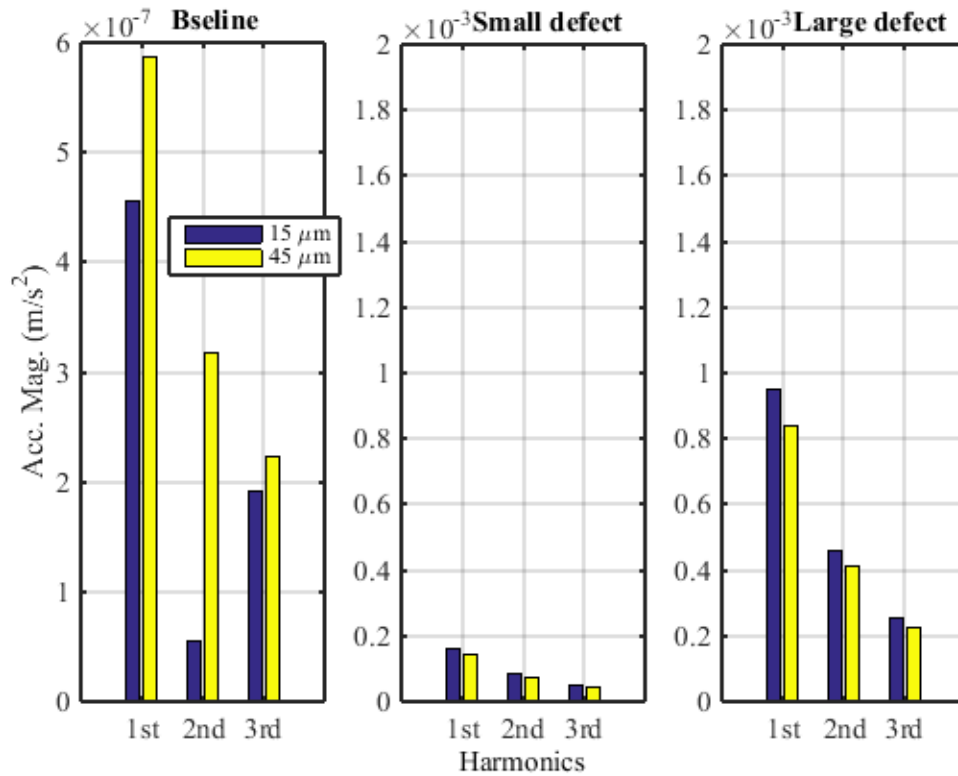
Figure 5-7 Baseline and outer-race acceleration amplitudes obtained for the fault characteristic-frequency

The vibration acceleration amplitudes obtained for different positions of outer-race defect present significant dissimilarities. For example, when the defect is at 0 degrees, the resulting vibration amplitude is a maximum. As the defect position is moved away from 0 degrees, the vibration amplitude is shown to decrease. This relationship can be observed more clearly in Figure 5-6 and Figure 5-7.

5.2.2.1.3 Diagnosis of Inner Race Defect

Since the position of the defect in an inner-race is no longer stationary, the resulting vibration signal is usually complicated due to the rotation of both defect and the balls.

Moreover, the amplitude of the inner-race defect is not constant. This is due to the varying load that is applied when the ball becomes in contact with the defect.

Figure 5-8 presents the vibration acceleration of the sensor obtained for the baseline and small and large defects under two different clearances. As expected for the baseline, where there is no defect on the races, an increase in the vibration acceleration amplitude with clearance increments is observable. This implies that, the amplitude of the local (Hertzian deformation) also increases with increasing clearance value. For the two defect cases, as the rolling ball approaches the defect, either in the loaded or unloaded zone, significant variations in the periodic vibration amplitudes can be seen.
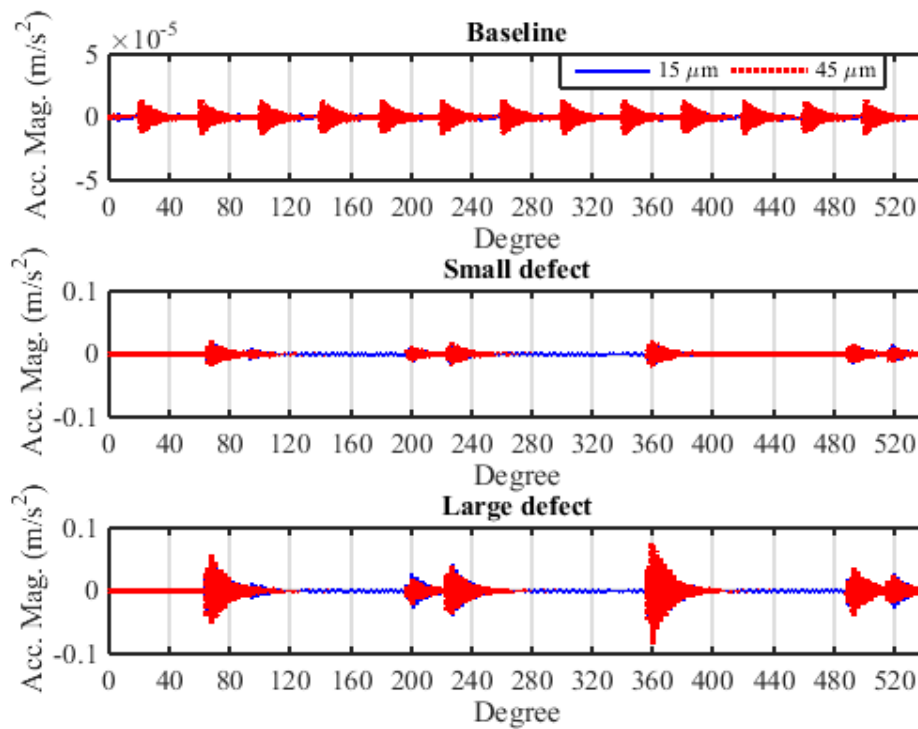
Figure 5-8 Vibration accelerations of baseline and inner-race defects

The frequency spectra of the sensor acceleration obtained for the baseline, small defect and the large defect cases are shown in Figure 5-9. For each case, the resonance frequency bands are shown to be concentrated at different areas; nevertheless, the observed behavioural responses and the excitation patterns for all three cases are quite similar. It is also observable that, the larger the defect size, the higher the resonance amplitude will be.
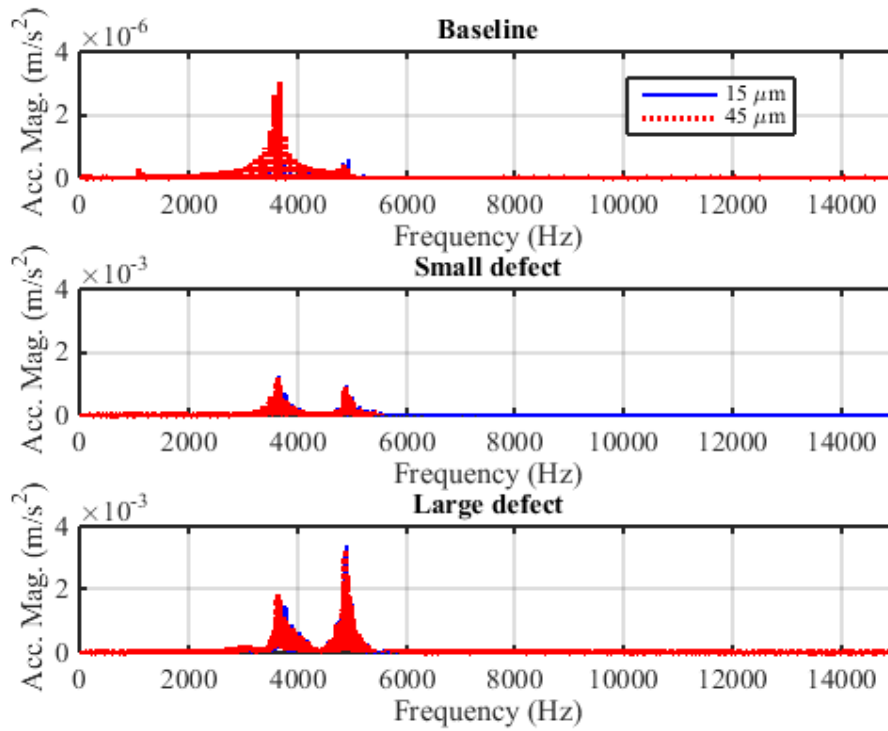
Figure 5-9 Baseline and inner-race acceleration spectrum
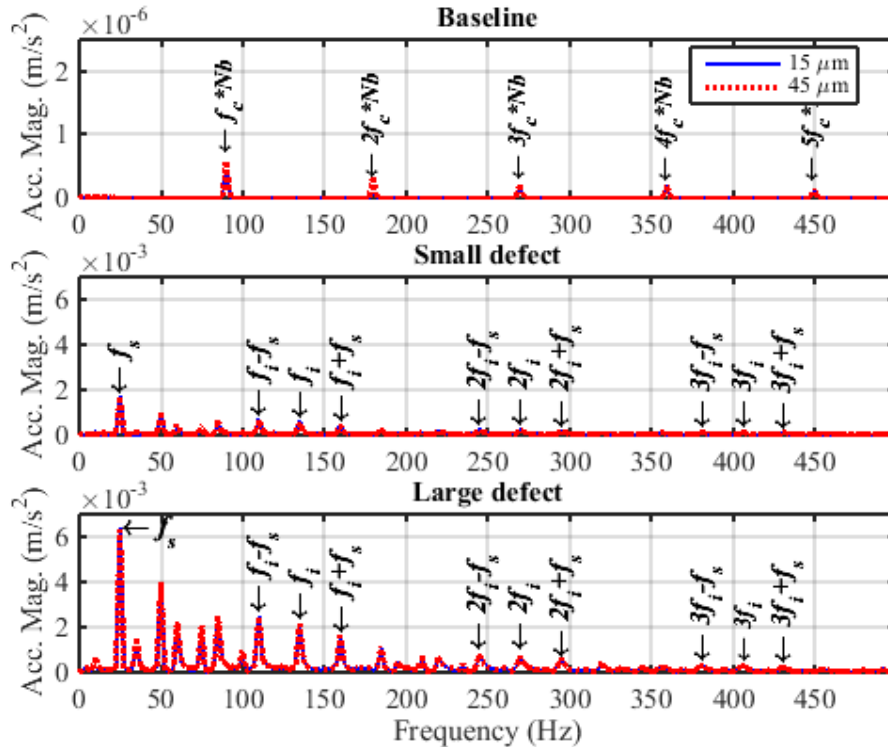
Figure 5-10 Envelope spectrum of baseline and small and lrage inner-race defects

The envelope spectra obtained for the baseline, small defect and the larger defect are presented in Figure 5-10. In this case, the ball-pass-frequency-inner-race (BPFI) is calculated at 135.198 Hz. Also, the fault feature-frequency, shaft's rotational frequency and their corresponding harmonics are clearly displayed. Since the inner-race defect rotates at the shaft's speed, the calculated BPFI is amplitude-modulated by the shaft rotational frequency. Therefore, peaks at frequencies of $BPFI \pm f_s$ with their corresponding harmonics can also be found.
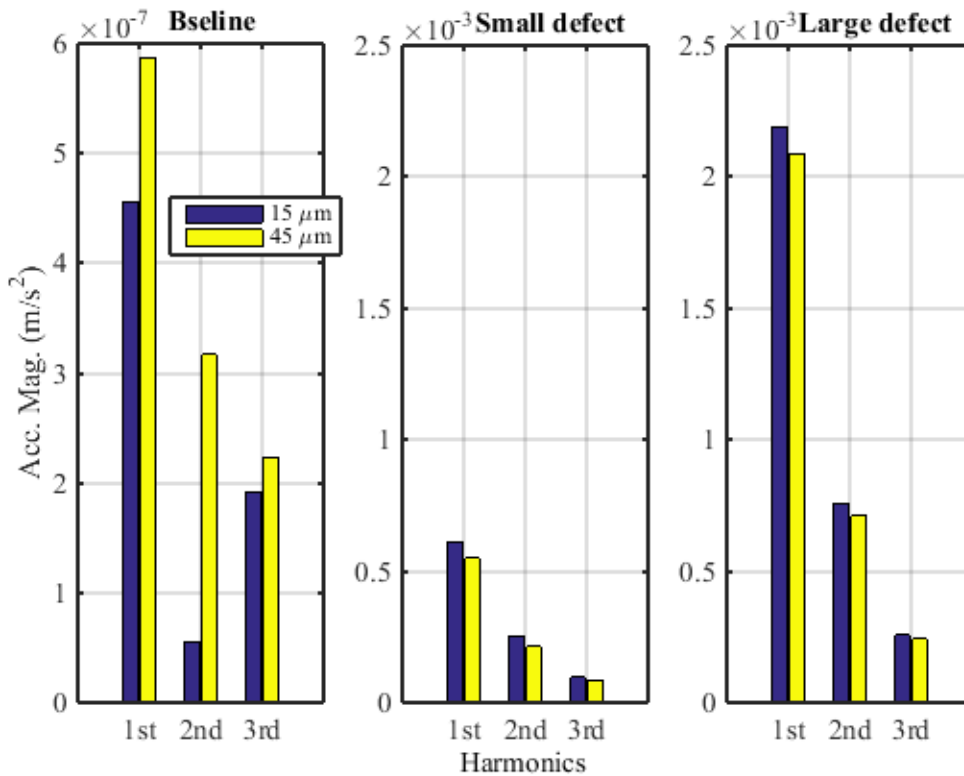
Figure 5-11 Baseline and inner-race acceleration amplitudes obtained for the fault characteristic-frequency

The envelope spectrum amplitude for the baseline, small and large inner-race defects are presented in Figure 5-11. As can be seen, for the baseline case, as the clearance value increases, so does the loading frequency amplitude. In contrast, for the defect cases, as the clearance value increases, the defect amplitude is slightly reduced.

5.2.2.2 Effect of Radial Load Variation

In order to study the effect of radial-load variation on the bearing acceleration amplitude, the radial load was allowed to vary from 0.8 to 2.4 kN, with a defect width of 0.2 mm on

the inner and outer raceways. Figure 5-12 presents the envelope spectrum amplitude of the different loading conditions. As observable, for both inner- and outer-race defects, a significant increase in the amplitude level occurs with increasing radial load. This is caused by the nonlinear deformation.
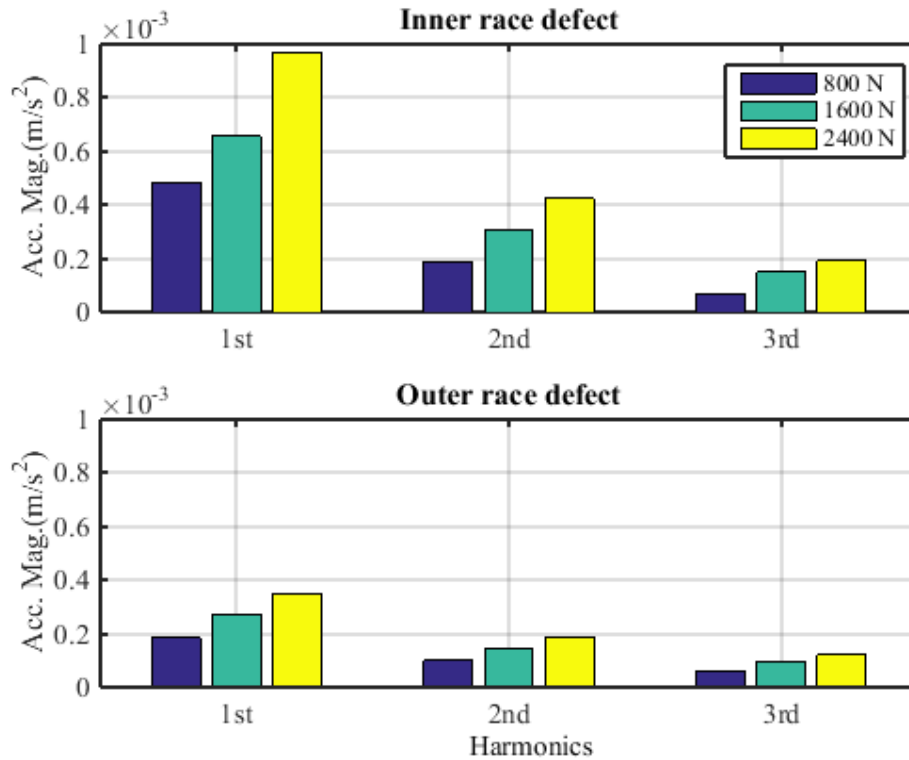
Figure 5-12 Envelope spectrum amplitudes of inner-race and outer-race faults under different radial loads

5.3   Summary

Numerical simulation results of the bearing dynamic model which are considered in the previous Chapter are presented in this Chapter. It starts by tuning the model parameters which include resonance frequencies and damping ratios (see Section 5.2.1).

For understanding the influence of internal clearance a comparison results of the nonlinear model are presented in Section 5.2.2 which are based on two different clearance values, constant speed and load, and two defect sizes in both inner-race and outer-race. The results exhibit the same signature for the fundamental frequency component and its harmonics. This demonstrates a good correlation between actual and simulated results.

From comparisons of results of the nonlinear dynamic model it can be observed that as the internal radial clearance grows the vibration amplitude of outer-race defect increases at the characteristic frequency and its harmonics. However, the amplitude shows decreases for the inner-race defect. Moreover, as expected as the radial load increases the vibration amplitude increases.

CHAPTER SIX

TEST RIG FACILITIES AND EXPERIMENTAL PROCEDURE

The chapter details the test rig construction and bearing fault simulation used to carry out this research. It starts by characterising the bearing test rigs and their key components. It then explains specifications of appropriate transducer and data acquisition system. Finally, fault simulations and the data collection procedures have been fully described for obtaining adequate data sets in validating the nonlinear dynamic model results shown in Chapter four and data processing methods in development.

6.1   Introduction

In order to validate the knowledge obtained in Chapters two, three and four, an experiment was conducted to measure the dynamic response of a bearing subjected to typical bearing defects. A ball bearing test system was developed to enable this, via measurements of the bearing vibration signal. The data was collected from a transducer mounted upon the bearing housing, while the test bearing was run for a short period of time under certain speed and load conditions. The test system was designed to be similar to the industrial equivalent, in which the vibration can be measured with sufficient accuracy while defects are introduced in a controlled, repeatable manner. In the present study, the test system is used to develop data analysis methods appropriate for extracting the useful information relevant to early detection and diagnosis of faults. The bearing test system is comprised of three subsystems:

1- A mechanical subsystem capable of simulating typical bearing operating conditions.
2- An electrical control subsystem to enable control of the mechanical subsystem under a range of test programs.
3- A measurement subsystem, which is responsible for recording the operating condition and dynamic response data of the bearing under test.

It is very important that faults are introduced into a practical system in a controlled manner in order to acquire data that is comparable to that produced by a real industrial application. The ball-type bearing was selected because it is commonly used in a large range of rotating machinery applications. A deep groove ball bearing (6206ZZ) was chosen for this experiment, because bearing faults are straightforward to introduce, and also because is typically used in many industrial rotating machines. The vibration signal generated in the bearing system was measured via a piezoelectric accelerometer attached to the bearing test rig. The equipment and instrumentation used was selected because it is accurate and reliable, and was obtainable at the University of Huddersfield.

The bearing test rig used is easy to assemble and disassemble, and enables simple connection of other experimental equipment. It can also be isolated from other sources of vibration.

6.2   Test Rigs Construction

To understand the vibration response of a ball bearing, and to improve the bearing condition monitoring (CM) techniques, experimental work was implemented using two bearing test rigs developed at the University of Huddersfield.

6.2.1   Bearing Test Rig

The experimental test rig was composed of two bearings that support a shaft which is driven by a variable speed motor (type Brook Crompton). The test bearing, a single-row deep groove ball bearing UC206 (6206ZZ) was situated at the drive end of the shaft, while a single-row self-aligning ball bearing was placed at the non-drive end of the shaft. A hydraulic loading arrangement was used to apply a radial load on the bearing. This consisted of a hand pump, pressure sensor, hydraulic ram frame, and hydraulic hose. A type IP65 pressure sensor with an operational range of 0 to 40 bar was placed into the hydraulic hose of the hydraulic cylinder that is used to control the radial load (see Figure 6-2 and Figure 6-1).
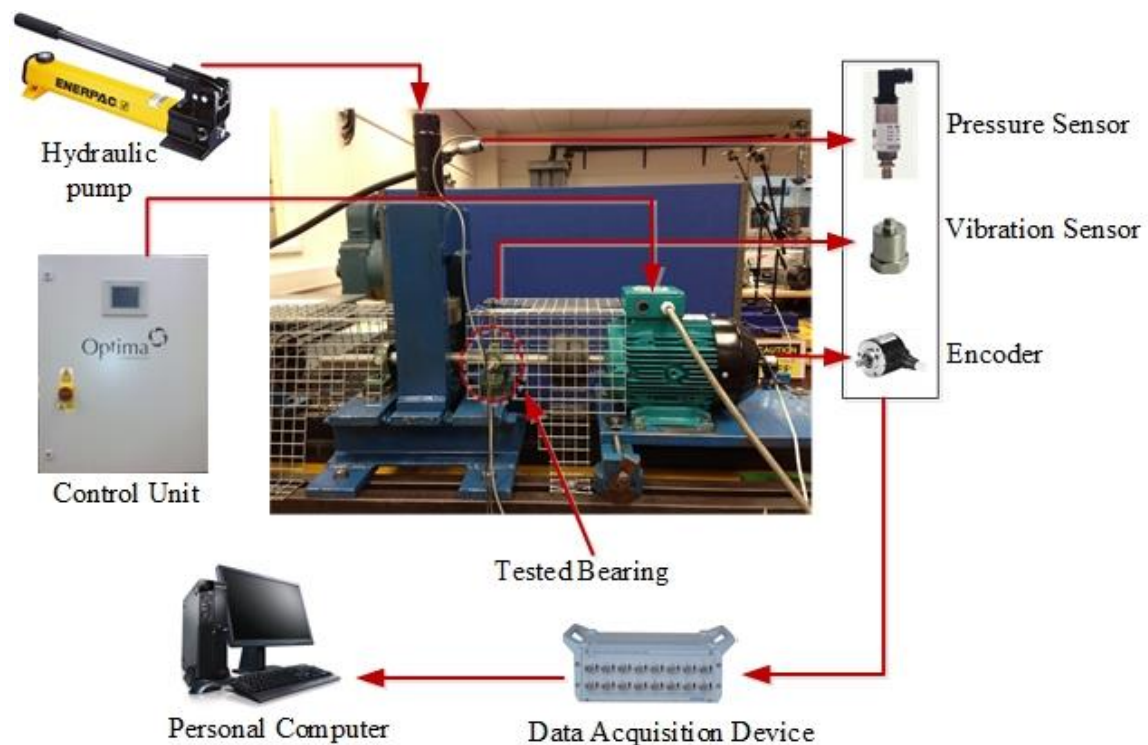
Figure 6-1 Bearing test rig construction process

A – AC Motor
B – Flexible Couplings
C – Hydraulic Ram Frame
D – Supporting Bearing

Sensor Position

Bearing Position

Encoder

Adjusting Bolts
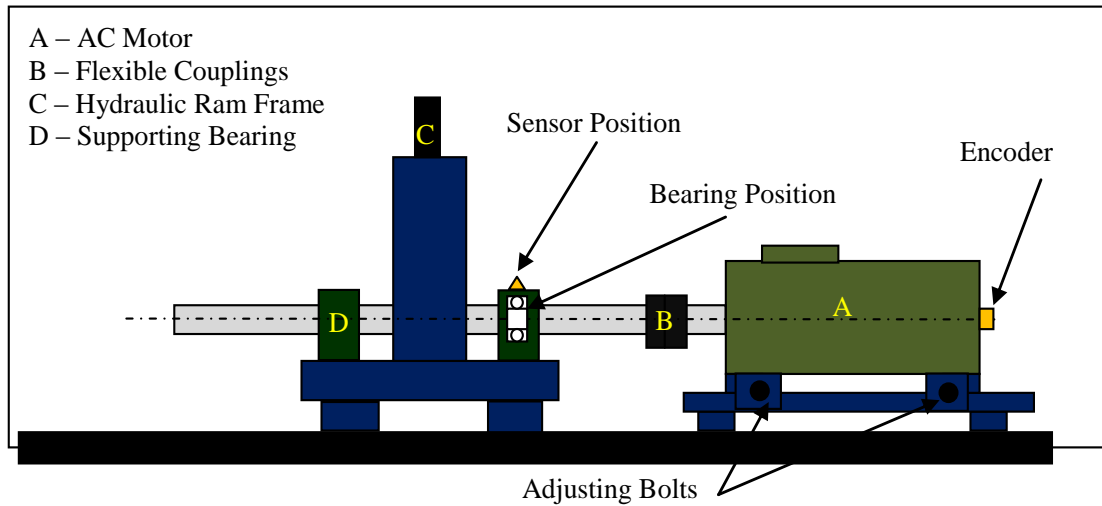
Figure 6-2 Schematic diagram of the bearing test rig construction

6.2.2 Motor Bearing Test Rig

The motor bearing test rig included of a 3-phase, 4 kW AC induction motor (Clarke type), which was coupled to the main shaft via a flexible coupling. A dynamic brake was connected to the motor via 2 intermediate shafts. These were connected by three pairs of matched spider flexible couplings. The two intermediate shafts were supported by two bearing housings. Deep grove ball bearing (type 6206ZZ) was used at the drive end of the motor, while the accelerometer was mounted onto the motor casing, oriented vertically as shown in Figure 6-4 and Figure 6-3.
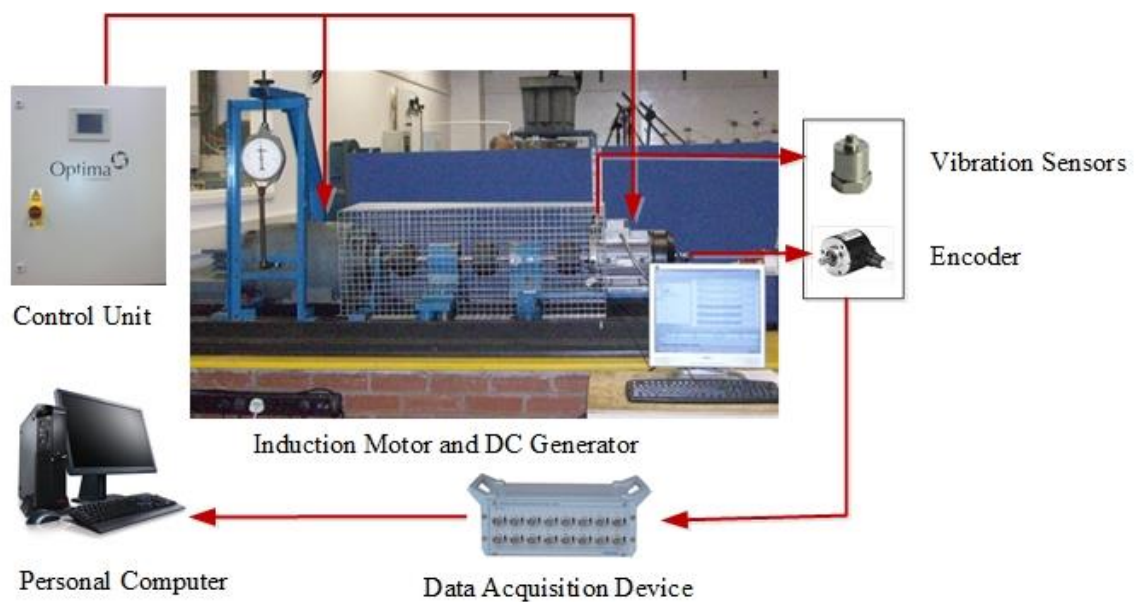
Figure 6-3 Motor bearing test rig

A Siemens Micro Master Controller was used to control the speed of the AC motor, which would in turn enable the drive shaft to turn at various speeds (to a maximum of 1460 rpm). This facilitates control over the torque of the dynamic brake, allowing various applied torque loads (up to a maximum of 4.0 kW). The construction of the test rig was designed to enable the whole test system to be constructed and deconstructed in such a way that the motor bearings could be replaced easily.
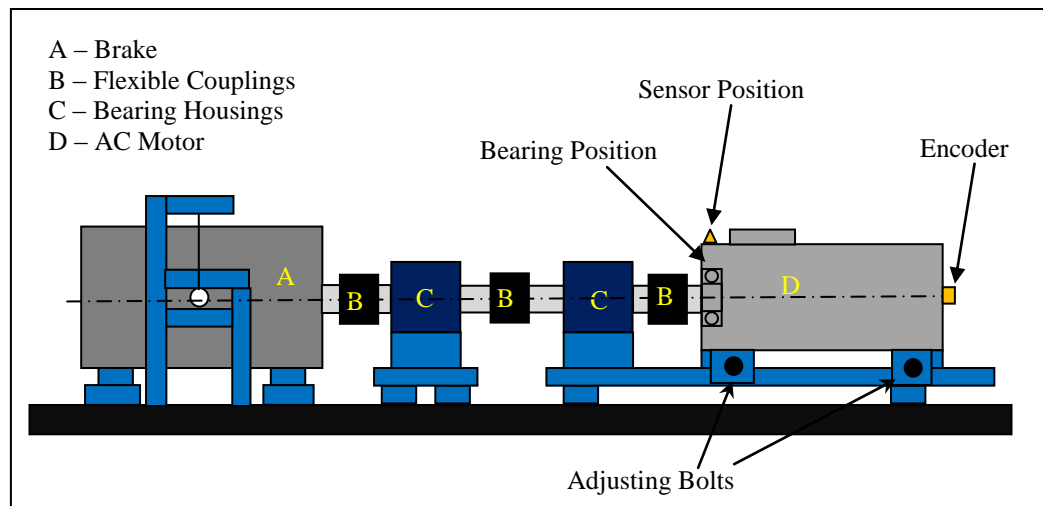
Figure 6-4 Schematic diagram of the construction of the motor bearing test rig

A piezoelectric accelerometer (type IEPE) was mounted on the bearing housing to measure the vibration signals. The transducer was oriented vertically, and had a frequency response in the range of 0.5 to 5000 Hz. The accelerometer was connected to the data acquisition device, which was in turn connected to the host computer. All necessary hardware and the software (data acquisition, storage, user interface, etc.) to display the time-domain signals were installed on the host computer. The signals were sampled at a rate of 96 kHz.

❖ AC Motor Type Brook Crompton

Most induction motors available for commercial or industrial applications require three-phase power to be supplied. The fundamental principle on which three phase induction motors operate is based on the production of a rotating magnetic field. This magnetic field is produced by a supply of current to a set of stationary windings. The magnetic field (or flux) is generated by the current carrying windings. Due to the interaction of the

three fluxes produced by the three phase supply, a resultant flux is generated, which has a constant magnitude and an axis that rotates in space, without physically rotating the winding [148]. Figure 6-5 shows a typical photograph of an AC induction motor (Brook Crompton type). The Motor manufacturer's specifications can be found in Table 6-1.

Figure 6-5 AC Induction motor (Brook Crompton type) [149]

Table 6-1 AC Induction motor specifications (Brook Crompton type) [149]

AC Motor	Measurements
Type of mounting	Foot mounting (B3)
Phase	3 phase
Pole number / rpm	2 pole / 2870 rpm
Rated voltage (Δ/Y)	400/690
Rated current (Δ/Y)	7.3-4.2 Amp
Shaft diameter	30 mm with standard keyway

The number of pole pairs is the main factor that governs the maximum speed of the motor. A theoretical formulation to explain the motor speed is illustrated in Equation (6-1) and Equation (6-2).

Rotor speed, $N_R = N_S(1 - S_l)$ (6-1)

Synchronous speed, $N_S = \dfrac{120 * f_{\text{sup}}}{P} - S_l$ (6-2)

where P is the number of motor poles, f_{sup} is the supply frequency, and S_l is the slip. The motor slip and number of poles are intrinsic properties of a motor that are fixed

during manufacture. Therefore, the motor speed may only be controlled by adjusting the supply frequency (f_{sup}).

❖ AC Motor Type Clarke Motor

Figure 6-6 shows a photograph of a Clarke type AC induction motor. Table 6-2 displays the motor specifications provided by the manufacturer [150].
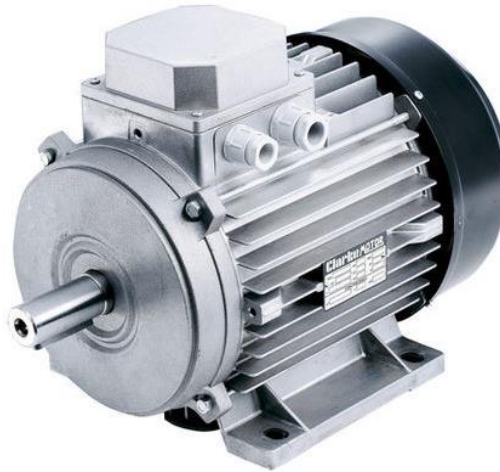
Figure 6-6 AC Induction motor (Clarke type) [150]

Table 6-2 AC induction motor specifications (Clarke type)

AC Motor	Measurements
Type of mounting	Foot mounting (B3)
Phase	3 phase
Pole number / rpm	4 pole / 1460 rpm
Rated voltage (Δ/Y)	230/400
Rated current (Δ/Y)	5.9-9.2 Amp
Shaft diameter	30 mm with standard keyway

❖ DC Dynamic Brake

The induction motor's rotational speed is controlled by supplying a DC voltage to the stator winding. A variable resistor may be included within the rotor (in the case of a slip ring induction motor) in order to dissipate the appropriate amount of power. Nowadays, a thyristor bridge is used to supply a D.C. voltage controlled by nature. This can enable dynamic braking to be achieved in a more effective manner.

❖ Hard Rubber Coupling

The hard rubber coupling (also known as a spider flexible coupling), illustrated in Figure 6-7, provided a flexible connection between the drive shaft of the AC motor and the supporting bearing shaft. A similar connection was made to connect the brake at the other end. The two main reasons for this are:

1. To enable the input torque to be transferred from one shaft to another at the same speed, causing both to rotate synchronously.
2. To compensate for the any small misalignments or random relative movements between the two shafts.

Figure 6-7 Hard rubber coupling

This type of compensation is essential, since a perfect alignment between two rotating shafts is incredibly difficult to achieve. Coupled rotating machines often shift from their primary position, leading to potential shaft misalignment, so the fixable coupling is used in order to compensate for the shaft's misalignment. This misalignment can inevitably cause wear that can in turn lead to early failure and renewal of machine components. The rubber couplings are also chosen in certain cases for additional benefits including [151]:

1. It can act as a fuse, breaking the connection between shafts if an overload torque is provided. This means that the easily replaceable coupling will fail before any other, more costly, parts of the machine.
2. It can dampen or even eliminate the transference of any natural torsional vibration within the driving and/or driven shafts.

This type of flexible coupling system generally consists of (i) two half couplings, (ii) an intermediate member that provides the flexibility, and in some specialised cases (iii) a cylindrical cover. The flexible member may take various forms, including: (i) splines and

sprockets, (ii) studs and rubber bushings, (iii) laminated disks, (iv) two sprockets joined by a single concentric double-studded chain, and many others. Each design of flexible member possesses its own strengths and weaknesses, which must be taken into account as they can significantly affect the performance of the coupling [152]. One such coupling is designated FRC130H. The specification for FRC130H is given in Table 6-3.

Table 6-3 Flexible coupling type FRC130H

Hard rubber coupling	Manufacturer SKF
Type	FRC130H
Size	130
Outer diameter	130 mm
Bore diameter	14-42 mm
Hub diameter	105 mm
Hub length	18 mm
Rubber width	36 mm
Taper lock bush size code	1610

❖ **Hydraulic Cylinder:**

The hydraulic cylinder system was used to apply the radial load on the bearing test rig described in Section 6.2.1. The hydraulic system includes a hydraulic ram, a hand hydraulic pump, pressure gage, pressure sensor and hydraulic hose. The specification of hydraulic ram is summarized in Table 6-6.

Table 6-4 Hydraulic ram geometric dimensions

Hydraulic Ram Parts	Measurement (mm)
Stroke	200
Rod diameter	42
Outside diameter	60
Piston diameter (D)	45

Figure 6-8 Photograph of the ENERPAC P391 hydraulic pump

Table 6-5 geometric dimensions of hydraulic pump

Hydraulic Pump	Measurement
Cylinder stroke	25.4 mm
Displacement per stroke 2nd stage	2.47 cm^3
Maximum handle effort	338.6 kg
Maximum operating pressure	700 bar
Single or two speed	Single
Usable oil capacity	901 cm^3
Weight	4.1 kg
Dimensions	533*120*177 mm

Theoretically, the force (F) provided by a hydraulic cylinder is calculated from the oil pressure and the usable projected piston area in contact with the oil. Thus:

$$F = pressure \times Area \tag{6-3}$$

$$Area = \frac{\pi \times D^2}{4} \tag{6-4}$$

The hydraulic system is illustrated via a schematic diagram in Figure 6-9.
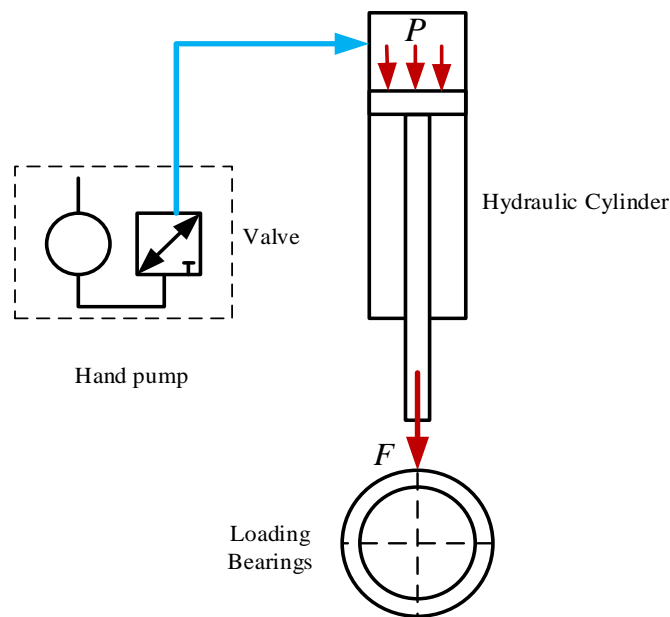
Figure 6-9 Schematic of hydraulic system

❖ **Bearing type 6206ZZ**

Figure 6-10 illustrates a type 6206ZZ motor bearing, which uses affordable metal-shielded deep-groove ball bearings. The geometric dimensions are listed in Table 6-6.

Table 6-6 Ball bearing geometric dimensions (6206ZZ)

Bearing Elements	Measurement
Diameter of outer housing	62 mm
Diameter of inner bore	30 mm
Bearing width	16 mm
Ball diameter	9.53 mm
Number of rows	1
Number of balls	9
Contact angle	0º
Pitch circle diameter	46.4 mm
Outer race diameter	55.93 mm
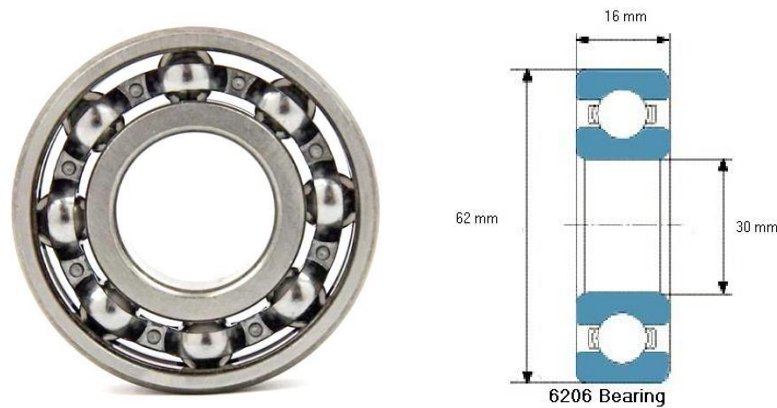
Figure 6-10 Schematic diagram and overview drawing of type 6206ZZ bearing [153]

❖ **Bearing type UC 206 (6206ZZ)**

Figure 6-11 shows a radial insert deep-groove ball bearing, of type UC206. Here, grub screws were used in the inner race and spherical outer ring. The measured dimensions along with the manufacturer's specifications are given in Table 6-7 and Table 6-8.
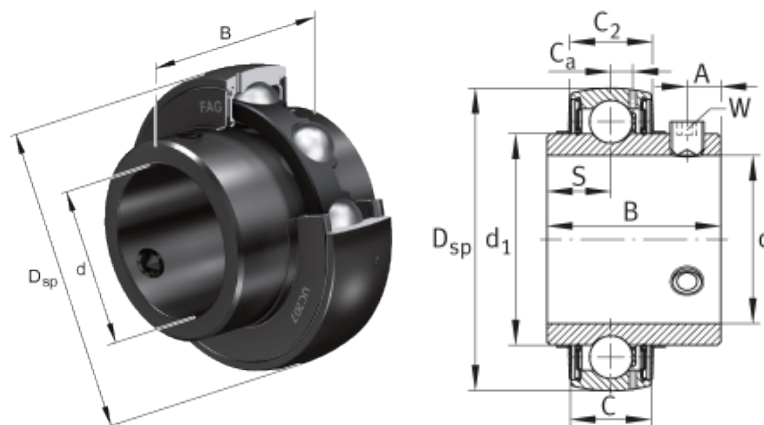
Figure 6-11 Schematic diagram and overview sketch of the radial insert ball bearing

Table 6-7 Measured diamensions of FSB type UC206 deep groove ball bearing

Bearing Elements	Measurement
Ball diameter	9.53 mm
Number of balls	9
Contact Angle	0°
Pitch Circle Diameter	46.4

Table 6-8 Manufacture specifications for FSB type UC206 deep groove ball bearing

Dimensions		Measurements (mm)
d		30
D_{sp}		62
C		19
C_2		19.6
C_a		5
B		38.1
S		15.9
d_1		40.2
A		5
Basic radial load ratings	Dynamic (N)	20700
	Static (N)	11300

❖ **Speed and Load Controller**

The test rig introduced in Section 6.2.2 was operated at a constant speed whilst under different torque loads. Therefore, a speed and torque controller was required. The Siemens Micro Master Controller was selected and connected to the rig in order to deliver the torque and speed accurately (see Figure 6-12).

Figure 6-12 Test rig control panel

Speed Control

A 3 phase induction motor (described earlier) was connected to the speed and load controller. The driver modified the supply frequency and speed set point in order to produce new supply voltages. The supplied voltage then drives the AC motor in order to operate the system at the chosen speed. The block diagram in Figure 6-13 presents the main features of the speed control system.
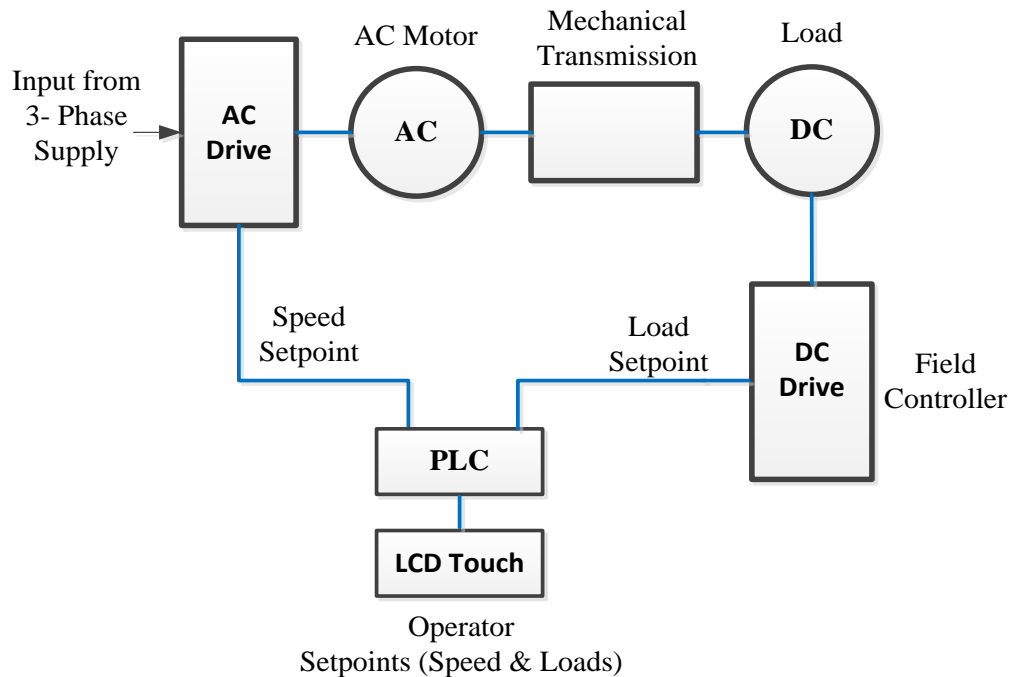
Figure 6-13 Block diagram representing of the experimental test rig control system

Load Control

The torque load presented by the DC motor was controlled via a DC drive. To allow the test rig to operate from 0 to 100 % motor load, the DC drive was connected to two supply phases configured to supply a current that was pre-set by a potentiometer. Figure 6-13 shows the main features of the load control system.

❖ Data Acquisition System

Data acquisition devices are designed to sample and record signals that typically represent real world physical phenomena. The signals being logged may be voltage, current, vibration, pressure, temperature, sound, etc. Data acquisition systems perform either (or both) of the following functions:

- Conversion of an input analog signal into a digital format using an ADC, with the data then being transferred to a computer for storage, analysis and display.

- Conversion of digital signals generated by a computer into an analog format using a DAC. The resulting analog signals are usually used for controlling a system or process.

The complete data acquisition system would consist of measurement sensors, data acquisition hardware (ADC/DAC), and a programmable control computer. Software on the computer may be used to enable the system to acquire, display, record, and analyse data [154]. In the present study, a Sinocera YE6232B dynamic data acquisition system was used to monitor and collect the vibration signal of the studied bearings. The system had 16 channels and high sampling rate of 96 kHz (see Figure 6-14).

Figure 6-14: YE6232B data acquisition system

Technical specifications for the data acquisition system are given in Table 6-9.

Table 6-9 Data acquisition system specifications (YE6232B)

Parameter	Performance
Number of channels	16 channels
A/D resolution	24 bit
IEPE power supply	4mA/+24VDC
Sampling rate (max.)	96 KHz/CH, 16 parallel
Signal input range	$\leq \pm 10$ VP
Signal frequency range	DC-30 KHz (-3dB±dB)
Accuracy	± 0.5 %
Software	YE7600 General Test & Analysis Software

A data acquisition programme was developed using Lab-windows. It mainly contains a parameters set-up board and a data inspection board. The software is able to perform on-line sampling of data and is operated via the Windows operating system. Within the

software, the filename, number of channels, sampling frequency, and sampling duration can all be set. These settings can also be stored on a separate set-up board of the data acquisition software package. In this research, three channels were used to collect the bearing vibration characteristics.

❖ **Pressure Transducer**

Pressure is generally expressed in units of force per unit area, and in fluids can be thought of as the force required to prevent the fluid from expanding. Pressure transducers are used to quantify fluid pressure in a wide range of industrial applications. They are typically used for pressure measurement in gases or liquids. They function by measuring the deflection of a flexible membrane, which is almost linearly related to the applied pressure. The mechanical deflection is converted to into a measurable electrical signal via a Piezoelectric ceramic sensor within stainless steel housing [155]. The manufacturer's specifications are given in Table 6-10.

Figure 6-15 Pressure sensor [155]

Table 6-10 Pressure sensor specifications [155]

Pressure Sensor	Measurements
Minimum pressure reading	0bar
Maximum pressure reading	40bar
Accuracy	±0.25 %
Supply voltage	3-12 V

❖ **Accelerometer**

An accelerometer is a sensing device that measures acceleration, but its data can also be used to determine force fall and shock, displacement, speed, and vibration. Accelerometers are therefore an essential component in condition monitoring

applications. Accelerometers primarily transform the physical characteristic of acceleration into an electrical quantity measurable by a data acquisition system [8]. Acceleration sensors must be selected based on the anticipated signal levels and also the frequency range of the phenomena of interest. They are suitable for high to low frequencies, with a good signal to noise ratio over a wide dynamic range. They are used for a variety of general purposes. Piezoelectric accelerometers are the most popular vibration sensor for the monitoring of machinery monitoring [156, 157]. The two primary parameters of a piezoelectric sensor are the sensitivity and the frequency range. Generally, low frequency sensors exhibit high sensitivity, while high frequency sensors have low sensitivity [156].
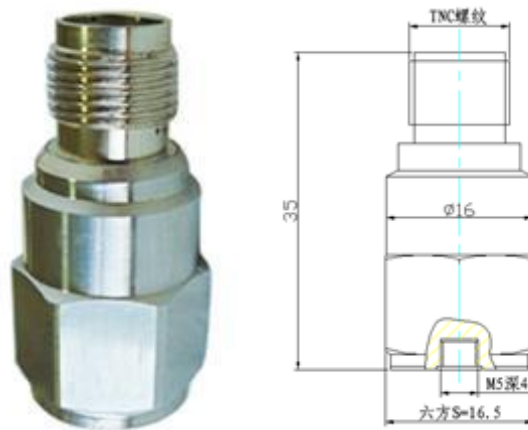
Figure 6-16 Piezoelectric accelerometer type CA-YD-185TNC [158]
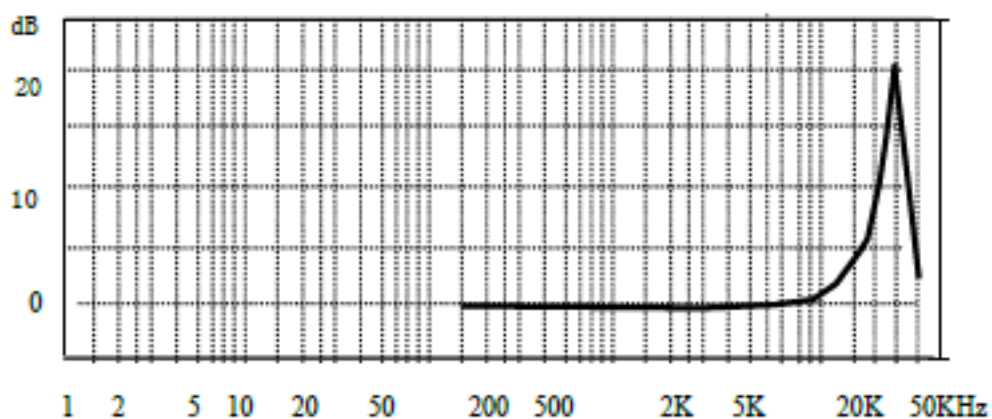
Figure 6-17 Frequency response curve [158]

YD-185TNC piezoelectric IEPE (Integrated electronic piezoelectric accelerometers) accelerometers were mounted in vertical direction of the bearing housing. YD-185TNC

sensors have a relatively uniform frequency response in the range 0.5 Hz to 5000 Hz. Additionally, the sensitivity of the sensor is 5.106 mV/ms^{-2} [158]. The specifications given by the manufacturer is listed in Table 6-11.

Table 6-11 Piezoelectric accelerometer specifications [158]

Axial sensitivity	~50mV/g
Frequency response (0.5dB)	0.5~5000 Hz ($f_0 \approx$20 KHz)
Sensitivity	5.106 mV/ms-2
Measurement range	100 g
Polarity	Positive
Operating voltage (constant current source)	12~24VDC(offset 6-8V)
Operating current	+2 to +10 mA
Noise	<2 mg
Shock limit	2000 g
Transient temperature	0.1g/^{o}C (0.3 Hz)
Weight	35 g
Mounting method	M5
Operating temp. range	-40 to +120 ^{o}C

❖ **Encoder**

An incremental shaft encoder (type RI32), was used to generate a series of pulses at equal angular intervals, as illustrated in Figure 6-18. This device was mounted to the fan cowl of the induction motors via flexible coupling. They are commonly used to measure the instantaneous angular speed (IAS) of an object or shaft. Two outputs are provided: (i) the first output 1000 electrical pulse train per revolution, and (ii) the second output one pulse per revolution.

Figure 6-18 Incremental shaft encoders type RI32

6.3   Fault Simulation

There are generally two approaches used by researchers for creating localised defects on bearings. The first approach is to intentionally cause a defect, measure the response of the bearing system, and compare it with the healthy bearing response. The second approach is to run the bearing until a defect forms naturally, recognised by monitoring for changes in sensor output [159, 160]. In this type of study, the defect generation is usually accelerated by overloading or shock loading the bearing under test. Even so, the approach is relatively time-consuming in the context of a research project, and can be very expensive to be implemented.

6.3.1   Ball Bearing Type UC206 (6206ZZ)

This experiment was conducted using eight different UC206 ball bearings. Two types of bearing clearance were examined.

Firstly, four bearings were chosen with CN clearance. Within this group, one bearing is healthy and used as a baseline for comparison. The second bearing is induced with an outer race fault 0.2mm width of the bearing raceway. In the same way, 0.2mm width inner race fault is induced of the bearing raceways. The fourth bearing is induced with an inner race fault 0.475 mm width of the bearing raceways.

The second group of four bearings was chosen to have C4 clearance. Again, one bearing is healthy and is used as a baseline. The C4 faults were induced in the same way as for the CN bearings, on the inner and outer raceways. The faults were simulated by Electrical Discharge Machining (EDM). The faults were artificially simulated and measured by Erodatools ltd. All the scratches induced in this research were rectangular slots of 0.2 mm depth. The width of the sparked groove, and the actual radial clearance, are given in Table 6-12. As it can be seen in the Figure 6-19 the defect slots are relatively small, compared with that simulated in [161].

Prepared test bearings may have artificially induced faults of specific size or location or geometrical errors of known form. Preferably, during a discrete test the state of the bearing should not change significantly, hence in some cases test brevity may be a priority. Discrete testing forms the bulk of the experimental work presented in this thesis.

Table 6-12 Deep groove UC206 ball bearing clearance value and defect size

measurements

CN (6-20 μm)		
Bearing condition	Clearance (μm)	Defect width (mm)
Outer race fault	6	0.2
Inner race fault	13	0.2
Healthy	8.334	-
C4 (28-46 μm)		
Bearing condition	Clearance (μm)	Defect width (mm)
Outer race fault	35.7143	0.2
Inner race fault	43.486	0.2
Healthy	40.8571	-

It can be observed that the single scratches with a uniform depth and width are not honestly representing the realistic bearing defects, but this method has a significant advantages: the localized faults are frequently reproducible across all the rolling element bearings, such a fault is anticipated to generate a clear periodic signal which will optimise the possible success of understanding the effect of clearance on the vibration signature; and it is more likely to control the severity of the fault. As known in Section 2.5 in Chapter two a real bearing faults are dependent on the nature of cause of that fault. Figure 6-19 gives out the photo of bearing defects with inner race fault and outer race fault, respectively.

0.2 mm inner race fault   0.475mm inner race fault   0.2mm outer race fault

Figure 6-19 Photographs of bearing faults
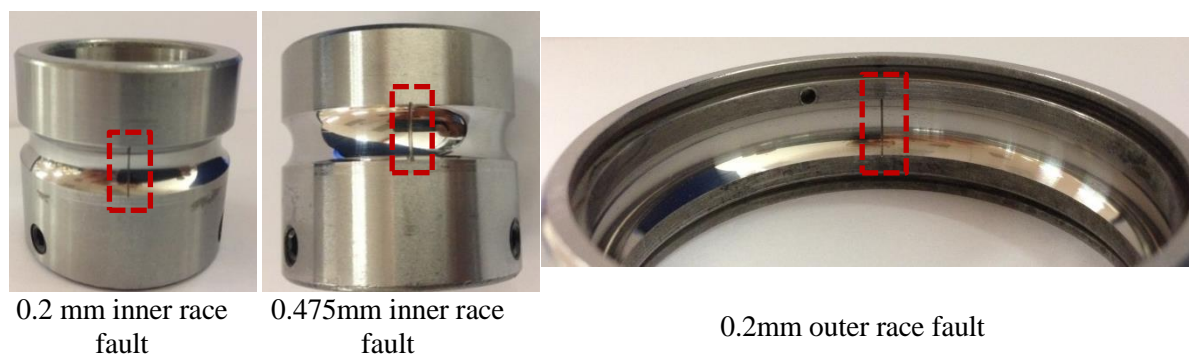
6.3.2 Motor Bearing Type 6206ZZ

The experiment was carried out based on three different ball bearings type 6206ZZ deep groove ball bearing which used to support the rotor of the AC motor. The bearing measurements are 30x62x16mm, with nine balls (Nb=9), ball diameter (D=9.52 mm) and pitch circuit diameter (dp=46.0 mm). Two types of typical localized bearing faults have

been introduced in this research. The faults have been introduced by the HB Bearings ltd as an abrasive wear in the same way on the inner and outer race; which models that caused by friction between ball and raceway surfaces due to lack of lubrication as shown in Figure 6-20.
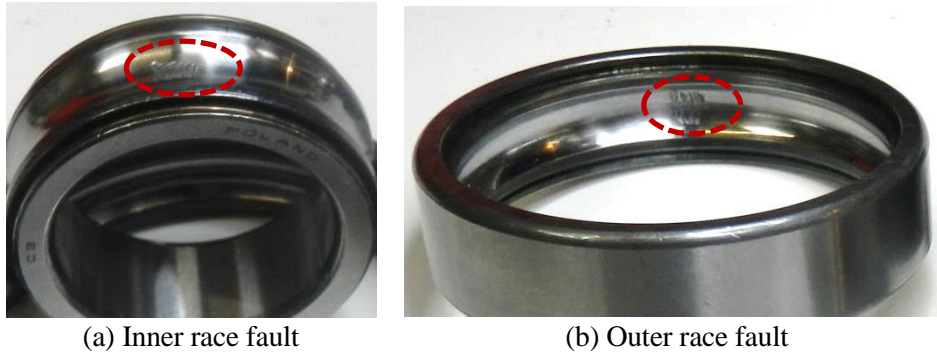

(a) Inner race fault   (b) Outer race fault

Figure 6-20 Photographs of motor bearing faults

6.4 Experimental and Data Collection Procedure

- All experiments for studying bearing fault detection and diagnosis were conducted in an equipped laboratory that maintains the same weather condition; therefore, all tests were supposedly carried out under the same conditions and also under shaft rotational speed of 1460 rpm to enhance the vibration produced by running on high speed.

- The data acquisition system recorded vibration signals from an accelerometer mounted vertically on the bearing housing as previously described.

- The output cable from the single pulse encoder was connected to the data acquisition channel, and the data was used to calculate the actual motor speed.

- A USB port was used to connect the data acquisition system (DAS) to the computer.

- YE7600 software was used to specify the sampling rate (96 kHz) and recording duration (20 seconds) to provide sample of 1920000 data points. It was also used to record the data via the data acquisition system.

- The motor control panel was used to select the desired speed and duration of each test step before switching the motor on.

- Around 15 minutes was allowed for the motor to warm up until the operating conditions (load and speed) reached a steady state. Then the data collection began.

- For the type UC206 ball bearing, four different radial loads of 0, 10, 20 and 30 bar (0, 0.8, 1.6 and 2.4 kN) were vertically applied to the shaft attached to the bearings. The

higher load is 2.4 kN, corresponding to 12% of the rated dynamic load, which allows the diagnostic capability to be evaluated under low load.

- For the motor bearing type 6206ZZ, four different torque loads of 0, 25, 50 and 75 % of the 4kW torsion load were applied.

- The experimental procedure was conducted in the following order: (i) healthy bearing, (ii) bearing with outer race fault, and (iii) bearing with inner race fault.

- For each bearing condition three sets of data were recorded, on the same day, each set of data containing two tests to ensure that the signals obtained were repeatable.

- The tests were conducted for the same motor speed, load conditions and sensor location, in order to avoid any unclear variation in the measurements.

- After data collection, the rig was stopped and turned off at the mains for safety.

- A set of MATLAB script was written by the researcher to enable processing and analysis of the recorded vibration signals with different techniques.

6.5   Summary

This chapter has explained in detail the developed test rigs, including all of the mechanical and electrical components, instrumentation and data acquisition software (Section 6.2). The type 6206ZZ deep groove ball bearing was introduced and specifications given. Finally, the fault simulations and test procedure used to carry out in this research were detailed (Section 6.3 and Section 6.4).

CHAPTER SEVEN

ROLLER-ELEMENT BEARING FAULT DETECTION AND DIAGNOSIS BASED ON AN OPTIMISED ENVELOPE ANALYSIS

This Chapter provides a comparative study on different techniques used in detection and diagnosis of incipient bearing faults. In particular, it examines the use of common signal processing techniques such as the time-domain, frequency-domain and envelope analysis. Furthermore, based on simulated signals, two methods based on spectral kurtosis (SK) analysis are examined in determining an optimal band filtration under typical noise cases: stationary noise and irregular pulses.

7.1   Introduction

Race surface indent results in the appearance of spalls on the inner race, outer race or the rolling elements. If one of the races encounters a spall defect, it will almost impact with the rolling elements periodically. In this case, the fault signature is represented by successive impulses, with a repetition rate that is strongly dependent on the faulty component, geometric dimensions and the rotational speed.

Defects in rolling element bearings produce signatory pulses of short duration, which are spread over a wide band of frequency. At the early stages of fault development, the generated impulse possesses low levels of energy with strong background noise. The resulting impulse excites the natural frequency of the bearing elements and the housing structures, which is quite different to those impulses caused by other machine components [34]. The excitation occurs every time when one of the rolling elements passes over the defect thus, the fundamental frequency of the response waveforms is the rate at which the element rolls over the defect. This is one of the characteristic frequencies described in Chapter three Section 3.2.3. Envelope analysis or high-frequency resonance technique is a well-known technique used to detect and diagnose rolling bearings (see Chapter three Section 3.4.4 for more details on envelope analysis). The envelope spectrum results are greatly influenced by the selection of the central frequency and the bandwidth of the band-pass filter. Therefore, knowledge of these two analysis parameters is necessary for any future research investigations to be conducted.

To accurately detect and diagnose bearing faults, the first part of this Chapter illustrates the collected bearing vibration signals from the motor bearing test rig described in Chapter six Section 6.2.2. The accelerometer was positioned vertically on the rear of the motor casing (drive-end side), closest to the studied bearing. Three bearing conditions were studied (healthy bearing as a baseline, an inner-race fault and a small outer-race fault). The study was carried out under full constant motor speed of 1460 rpm and four different torque loads of 0%, 25%, 50% and 75% (see Sections 6.3.2 and 6.4 in Chapter six for more details on the bearing fault simulation and test procedure). While the second part presents a simulated time impact signal where spectral contents is known (see Section 3.2.4 in Chapter three for more details) under different noise level to evaluate the performance of spectral kurtosis based STFT, kurtogram and fast kurtogram.

Finally, MATLAB was used to process the collected datasets to perform a clear comparison of time wave form signal, spectrum analysis, envelope spectrum based on fixed band-pass filter parameters, and then envelope spectrum based on optimal band-pass filter.

7.2   Motor Bearing Vibration Signals

7.2.1   Time Waveform Analysis

Time-domain waveform is the most obvious technique for visual inspection. Therefore, the time-domain waveform of the vibration signal, without any processing, presents clearly that no impacts can be located and it can be concluded that the system is running smoothly. Figure 7-1 and Figure 7-2 illustrate a 0.2 second excerpt of the vibration signal from two deep-groove ball bearings (6206ZZ), where the full shaft rotational speed was 1460 rpm and the sampling rate was 96 kHz.
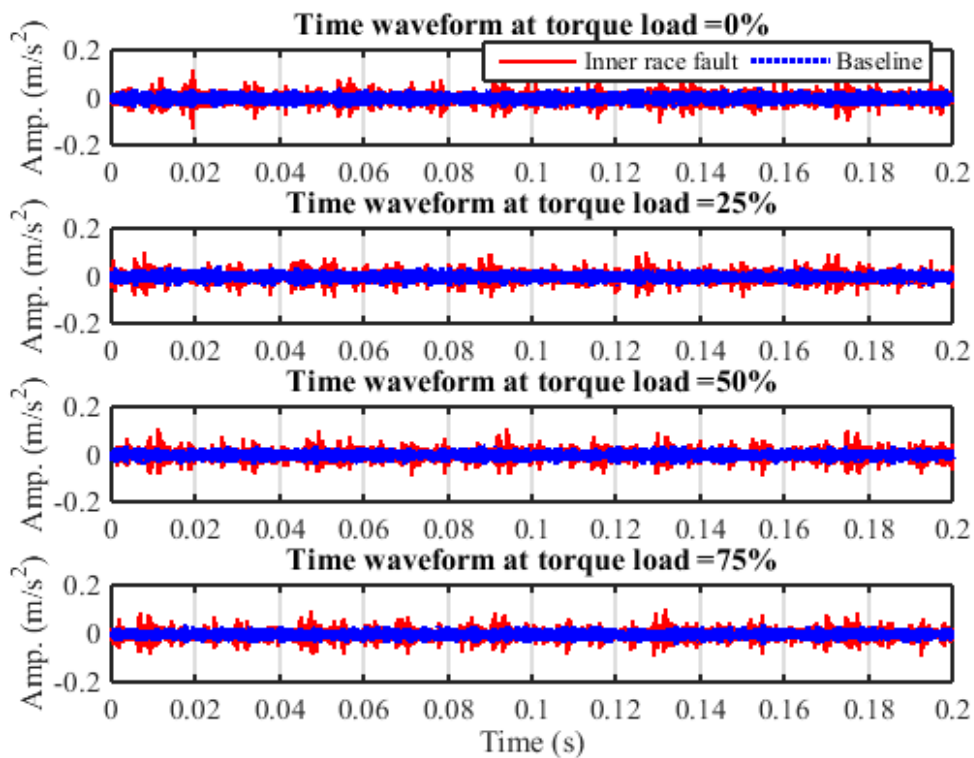

Figure 7-1 Time-domain signal for a healthy bearing as baseline and inner-race fault under different load conditions

Figure 7-1 shows two vibration signals; one is from a healthy bearing used as the baseline presented with blue solid line, and the other one is from a bearing with the inner-race

fault presented with a red dash line, at four different torque loads of 0%, 25%, 50% and 75% generated by a DC motor. It can be seen that the amplitude of the inner-race fault signal is significantly higher than that of the baseline signal. In addition, the repetitive impact signal of the inner-race fault, which is generated whenever the rolling elements pass over the defect on the raceway, is clearly visible. Furthermore, as the inner-race defect rotates, the rolling element passes over the defect in both the loaded zone and unloaded zone, which mainly influences the impact signal's amplitude as a result of amplitude modulation.
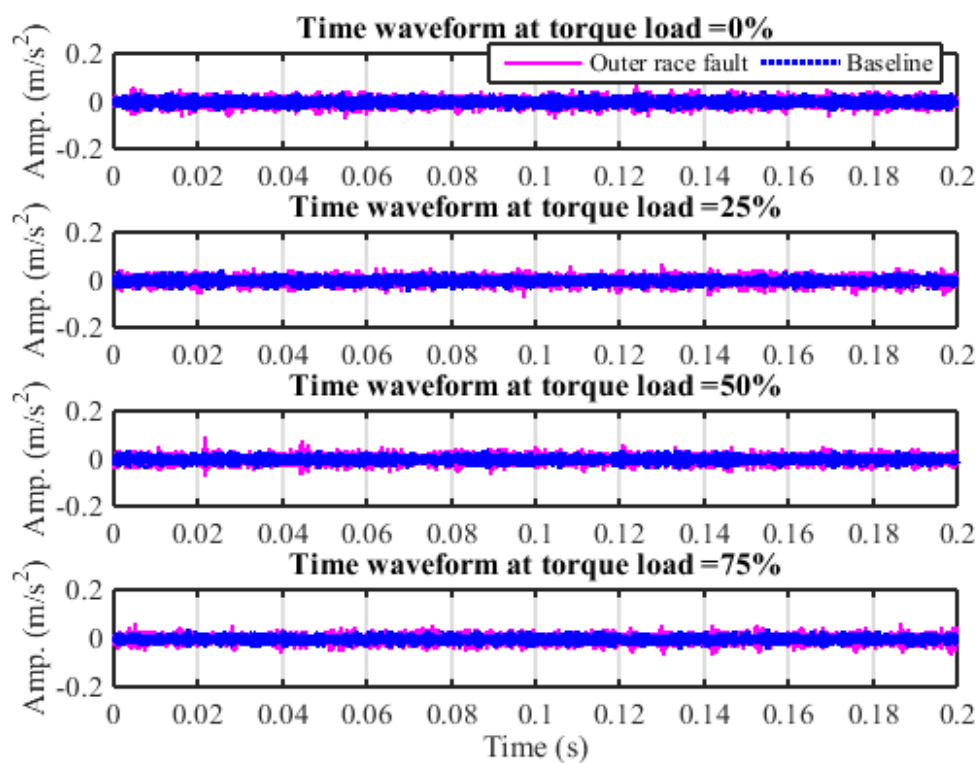
Figure 7-2 Time-domain waveforms for a healthy bearing as baseline and a bearing with an outer-race defect under different load conditions

Figure 7-2 shows two vibration signals; one from a healthy bearing as the baseline presented with solid blue line, and the other one from a bearing with an outer-race fault presented with a dash pink line at four different torque loads of 0%, 25%, 50% and 75% generated by a DC motor. It can be seen that the amplitude of the outer-race defect signal is slightly higher than that of the baseline signal. Moreover, as the outer-race defect remains stationary, the amplitude of the repetitive impact signal does not change.

Figure 7-3 RMS value, peak value and kurtosis of baseline, outer-race defect, and inner-race defect
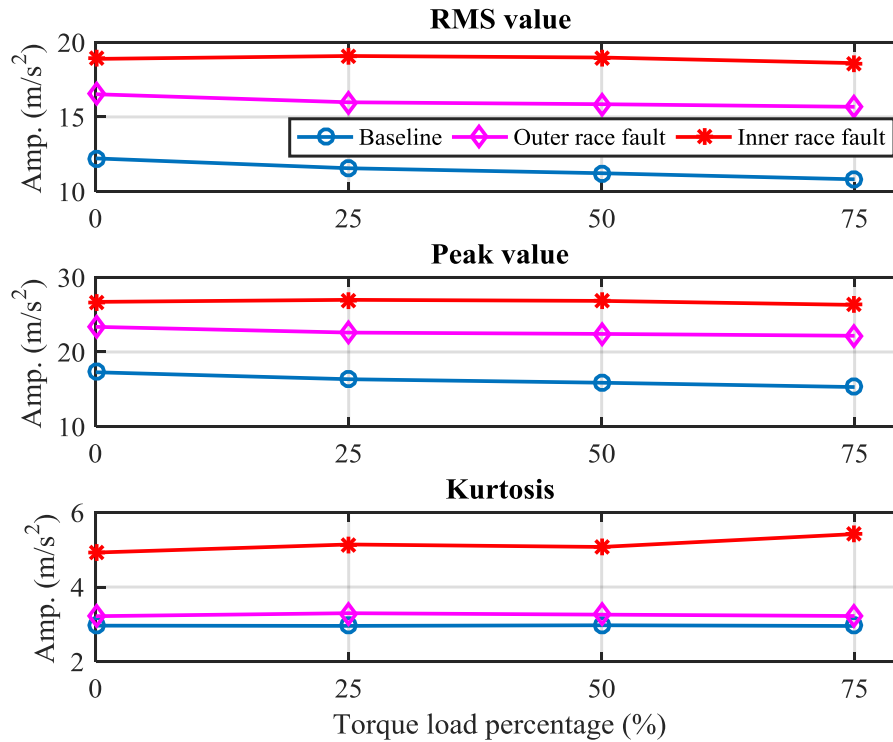
Typically, real bearing vibration signals are non-stationary. In this case, statistical parameters can be used to extract interesting features from the time-domain analysis, which can provide clear information on overall level and the spikiness of the signal associated with the defective bearing. Figure 7-3 shows the RMS, peak value and kurtosis of the studied bearings under four different torque loads. It can be clearly seen that the RMS, peak value and kurtosis of inner-race fault are significantly higher than that of the outer-race fault and the baseline. This is due to geometric deformation. Moreover, the torque loads do not make any significant changes to the aforementioned statistical values.

The resonance frequency of the bearing structure occurs whenever a rolling element passes over the defect in the raceways, which decays away rapidly. Therefore, vibration signals from bearings do not always produce a signal showing the impacts clearly. The vibration signal measured by a sensor is usually the sum of all the vibrations coming from many different machine components. It is unlikely to detect the fault by simply viewing the time-domain signal.

7.2.2   Raw Data Spectrum

By applying FFT and transforming the time-domain signal into the frequency domain, a clear image of the signal can be obtained from the raw data spectrum. The fault-feature frequencies of each bearing element can be calculated based on the geometric structure of the bearing (see Chapter three Section 3.2.3 for more details) as well as the shaft rotational frequency obtained from the encoder signal.

Table 7-1 Roller bearing elements fault frequencies

Load (%)	Shaft frequency (Hz)	Inner-race frequency (Hz)	Outer-race frequency (Hz)
0	24.9362	135.2601	89.1657
25	24.7353	134.1703	88.4474
50	24.5034	132.9125	87.6181
75	24.2394	131.4805	86.6741

The torque-load impact is inversely proportional to the shaft speed, which implies that a small change in the shaft frequency can affect the bearing elements' fault frequencies, as presented in Table 7-1. The interaction of defects in rolling-element bearings produces pulses of very short duration every time the rolling elements pass over the defect on the inner race or outer race of the bearing. These pulses excite the natural frequencies of bearing elements and housing structures, resulting in an increase in the vibrational energy generated at these high frequencies.

Figure 7-4 and Figure 7-5 show the vibration spectrum of a baseline as a normal bearing, a bearing with an inner-race fault, and a bearing with an outer-race fault, respectively. The initial dominant peak in the obtained spectra can be easily identified by the difference between the baseline and faulty spectrum. Moreover, it can be seen that the low-frequency phenomenon, that is, the impact of bearing defects associated with wide-band noise, makes the bearing fault frequencies and its harmonics less obvious in the spectrum. Finally, the bearing defect frequencies that are in the same range as the low-frequency vibrations induced by normal machine operation, including vibrations caused by misalignment and imbalance, as well as random vibrations, are more difficult to identify in the presence of high environmental noises.
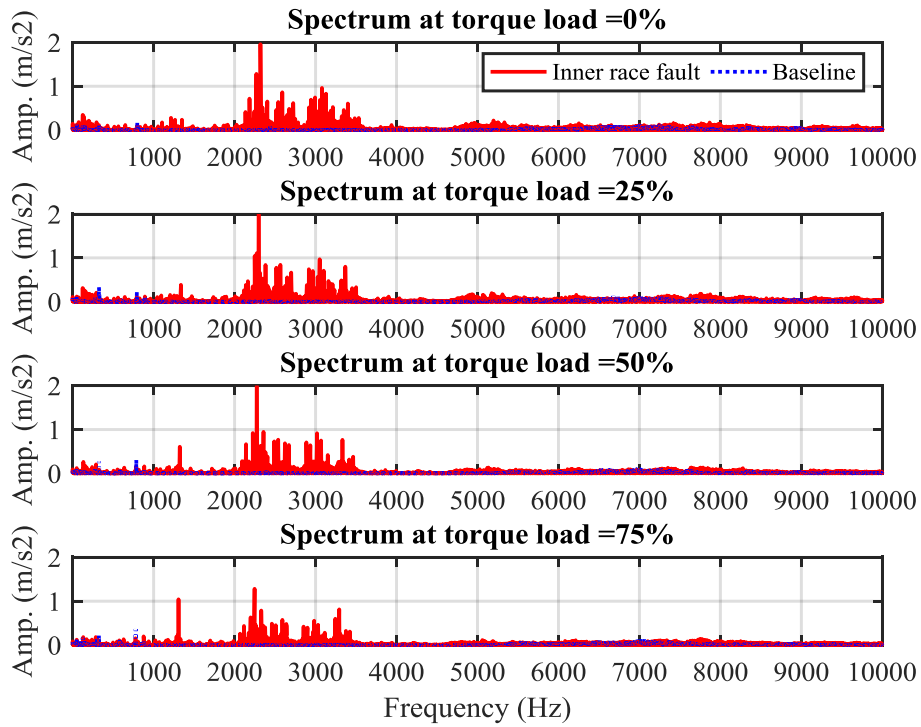
Figure 7-4 Spectrum of vibration signals of baseline and inner-race fault under different load conditions
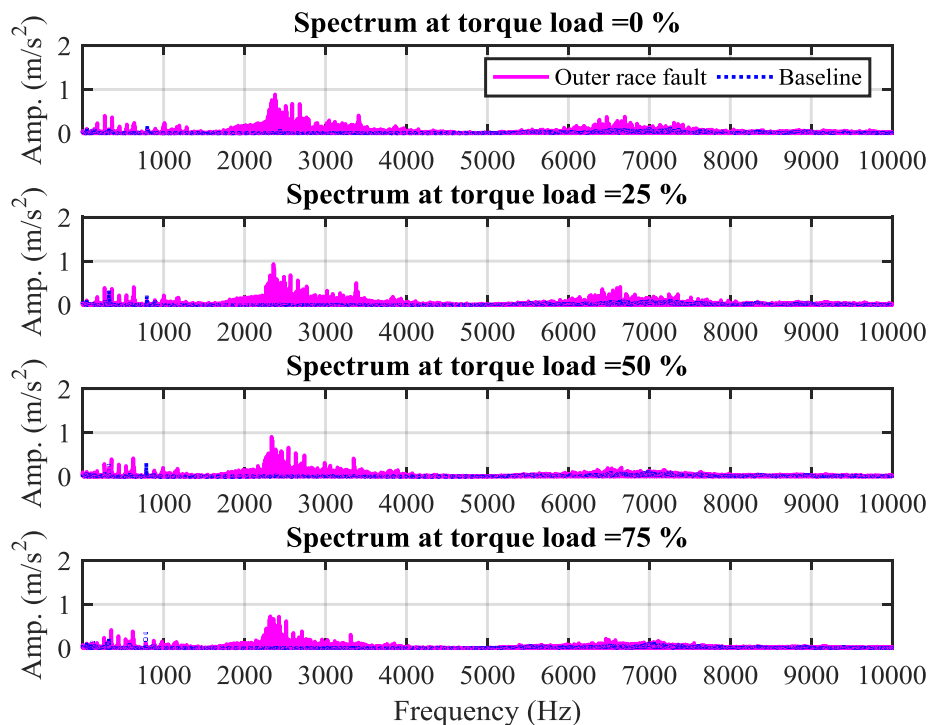

Figure 7-5 Spectrum of vibration signals of baseline and an outer-race fault under different load conditions

7.2.3 Envelope Spectrum of Conventional Band-Pass Filter

The envelope spectrum has been applied to remove the resonance frequency by using a band-pass filter, which is designed based on the raw data spectrum, followed by an FFT operation (see Chapter three Section 3.4.4 for more details).

Figure 7-6 and Figure 7-7 depict the envelope analysis results for a filter frequency range of 1.5 kHz to 4 kHz. This range was selected according to the power spectrum of vibration signals, in order to cover the whole resonance frequency band of the machine under study.
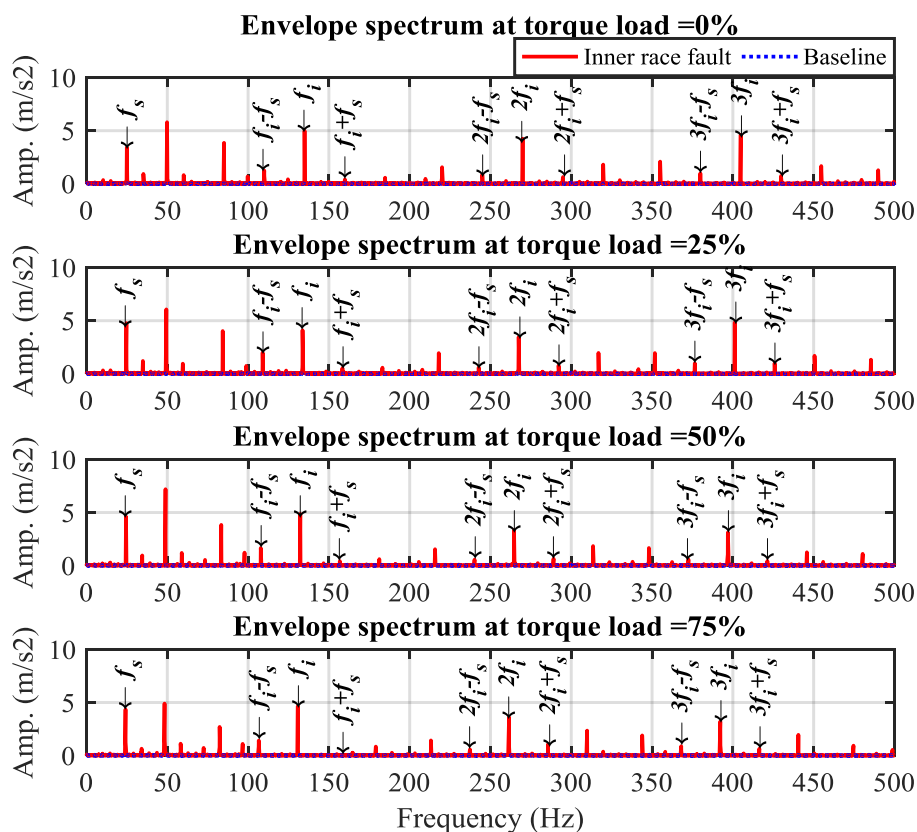

Figure 7-6 Envelope spectrum of baseline and an inner-race fault under different load conditions

Figure 7-6 illustrates the envelope spectrum of the baseline and the inner-race fault under four different torque loads. A clear indication for the presence of a fault can be seen. Moreover, the characteristic of the inner-race fault frequency and its harmonics are clearly indicated, as well as the pair of modulation sidebands. Similarly, in Figure 7-7, which compares the envelope spectrum of the baseline and the outer-race fault, a clear

indication for the presence of a fault is evident. The characteristic outer-race fault frequency and its harmonics are clearly indicated in this figure.
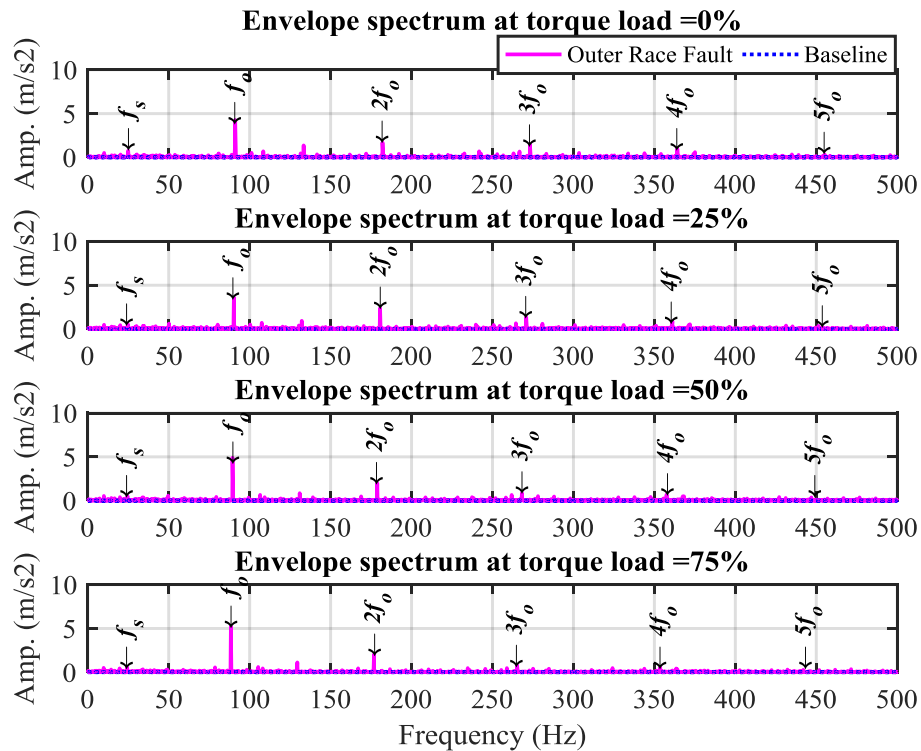

Figure 7-7 Envelope spectrum of baseline and an outer-race fault under different load conditions

Although, the characteristic frequencies and their corresponding harmonics for the outer- and inner-race faults can be extracted from Figure 7-6 and Figure 7-7 respectively, the presence of other frequency components in the presented spectra can cause uncertainties when making diagnostic decisions.

7.2.4 Envelope Spectrum of Optimal Band-pass Filter

7.2.4.1 Optimal Window based on Short-Time Fourier Transform

The Short-Time Fourier Transform (STFT) of a non-stationary signal from the time domain into the frequency domain can be achieved by performing an ordinary Fast Fourier Transform (FFT) on a moving window of the time-series signal, applies a moving window of a prescribed length along the recorded data to convert it into narrow-enough time intervals for the signal to be considered stationary. Figure 7-8 illustrates the STFT of the baseline, inner-race, and the outer-race faults at 0% torque load (see Appendix A,

Section A1, for the analysis of other torque load scenarios). The presence of high frequency clearly appears for the three cases. Additionally, the inner fault presents higher amplitude than outer race fault and baseline.
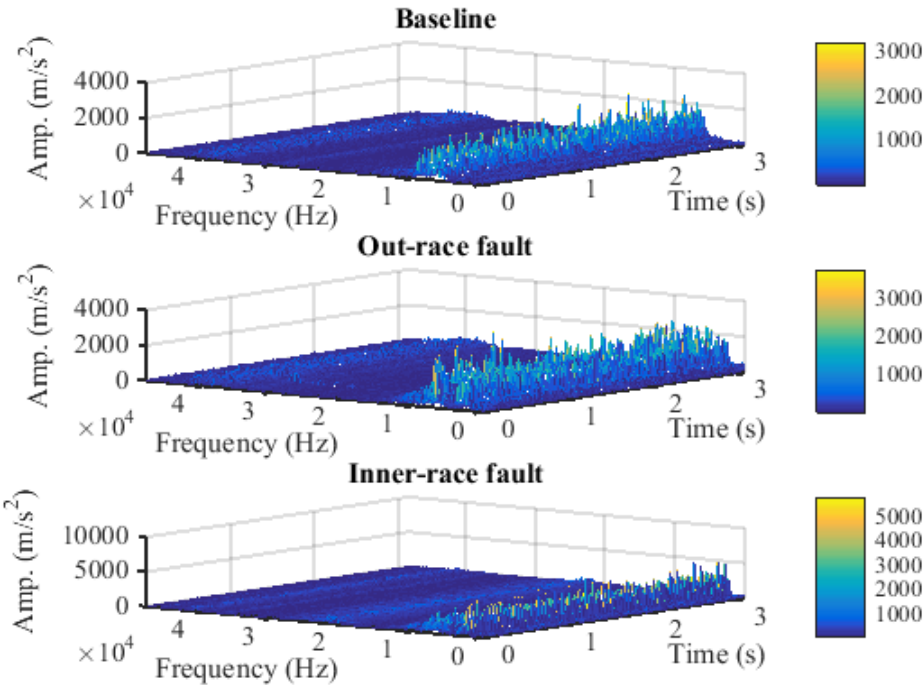

Figure 7-8 STFT of baseline, the outer-race and the inner-race faults at 0% torque load

In order to localise transients or hidden non-stationary signals, the STFT has been computed based on the spectral kurtosis, using eight different window durations of 16, 32, 64, 128, 256, 512, 1024 and 2048 corresponding to spectral resolutions of 6000, 3000, 1500, 750, 375, 187.5, 93.75 and 46.875 per line, respectively. The kurtosis was calculated for each spectrum window. The maximum obtained spectral kurtosis value was then used to determine the frequency band of interest, which serves useful for the identification of optimum band-pass filter parameters for envelope spectrum. Figure 7-9 exhibits the spectral kurtosis in the case of the inner-race fault under 0% torque load (for other torque load scenarios, see Appendix A Section A2), based on different window lengths. In all cases, the spectral kurtosis clearly discloses the existence of the signal in the frequency band from 12 kHz upwards. It is evident that the maximum values are achieved within the band of 15–25 kHz, where the signal-to-noise ratio is greatest. Moreover, it can be seen that the window lengths between 64 to 128 represent the highest spectral kurtosis values.
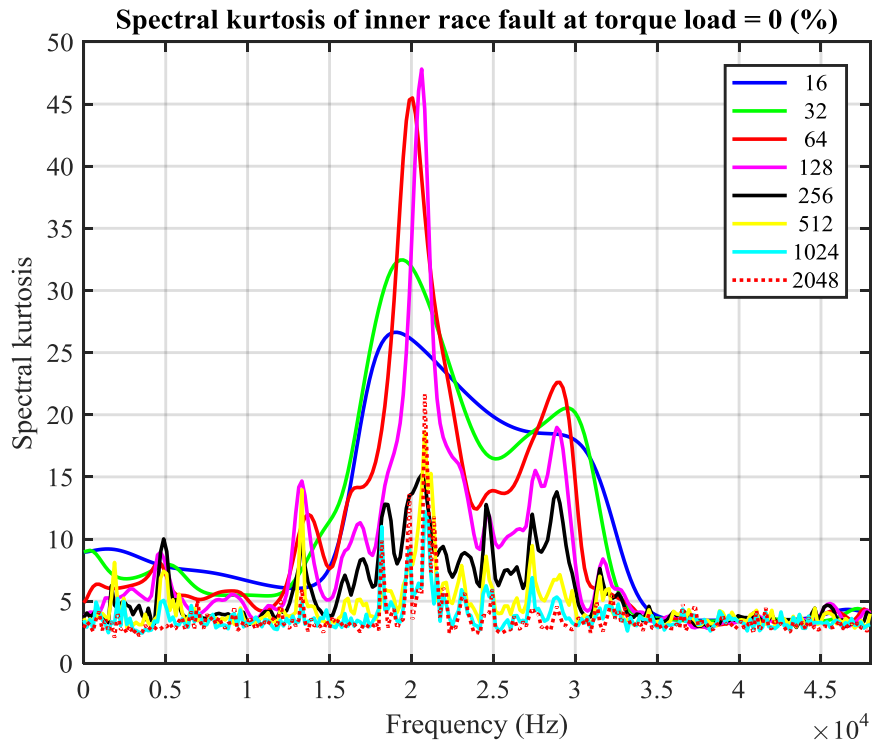
Figure 7-9 SK of inner-race fault computed for different frequency resolution at 0% torque load
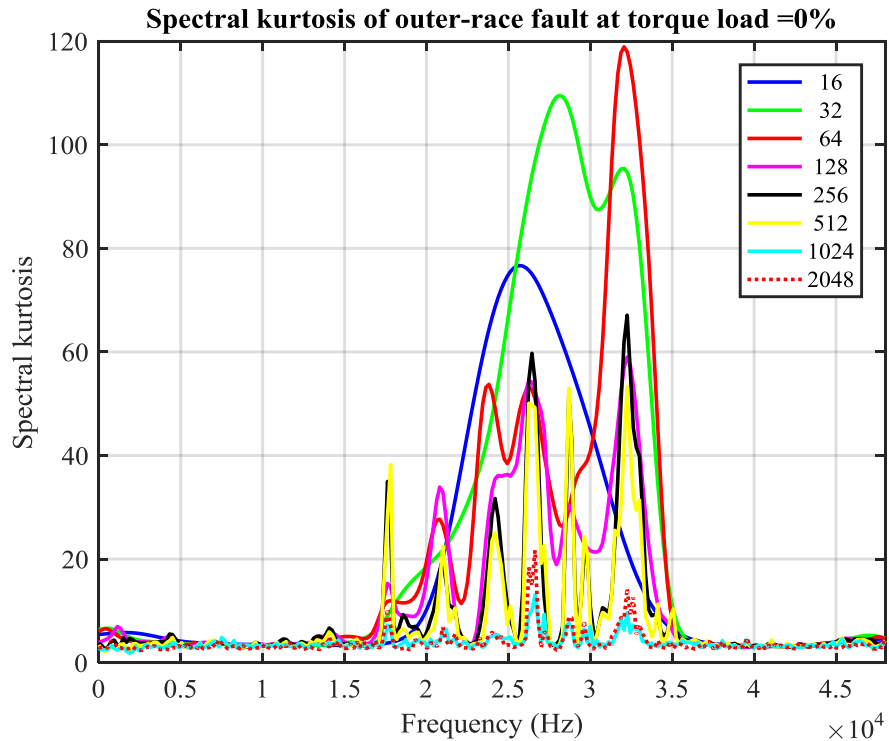

Figure 7-10 SK of outer-race fault computed for different frequency resolution at 0% torque load

Figure 7-10 displays similar analysis in the case of an outer-race fault under 0% torque load (for other torque load cases see Appendix A Section A2). Here, the spectral kurtosis discloses the existence of the signal in the frequency band from just over 15 kHz upwards and maximum values are reached in the band 25-35 kHz. Moreover, it can be seen that the window with value of 32-64 represents the highest spectral kurtosis.

From Figure 7-9 and Figure 7-10, it can be seen that the spectral kurtosis with a window length of 16 introduces unexpected results, while those window lengths from just over 128 promptly decrease to zero. Therefore, it can be concluded that the value of spectral kurtosis calculated based on STFT is largely affected by the window length. However, using this STFT-based method, it is possible to obtain the central frequency and window length over all possible conditions.

7.2.4.2   Optimal Window based on Kurtogram

Kurtogram is a map formed by STFT and is expressed as a function of central frequency and window length. Therefore, the maximum joint values of the kurtogram are found to be useful merit in the identification of the optimal central frequency and bandwidth of the band-pass filter [43].
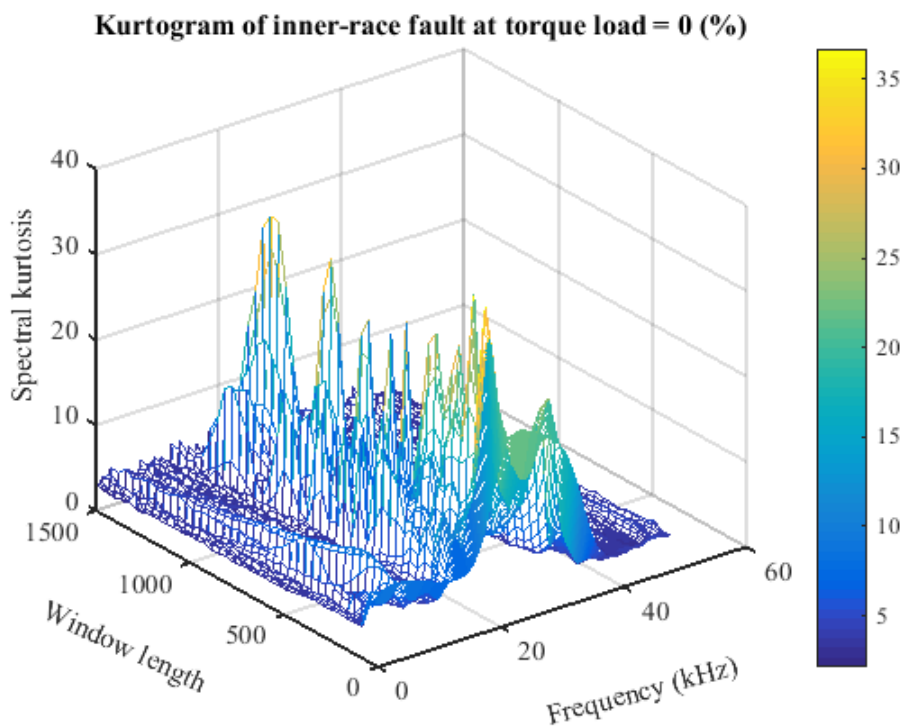

Figure 7-11 Kurtogram of the inner-race fault at 0% torque load

The kurtogram was computed for window lengths of 10 to 1500 samples, with a step of 40 samples between successive windows. Figure 7-11 illustrated the kurtogram of the inner-race fault signal under 0% torque load (for other torque load cases see Appendix A Section A3). It can be seen that the maximum kurtogram is achieved at a central frequency around 20 kHz, which matches the system's natural frequency.

Figure 7-12 illustrates the kurtogram of an outer-race fault signal under 0% torque load (for other torque load scenarios see Appendix A Section A3). It is observable that the maximum kurtogram is reached at a central frequency round 32 kHz.
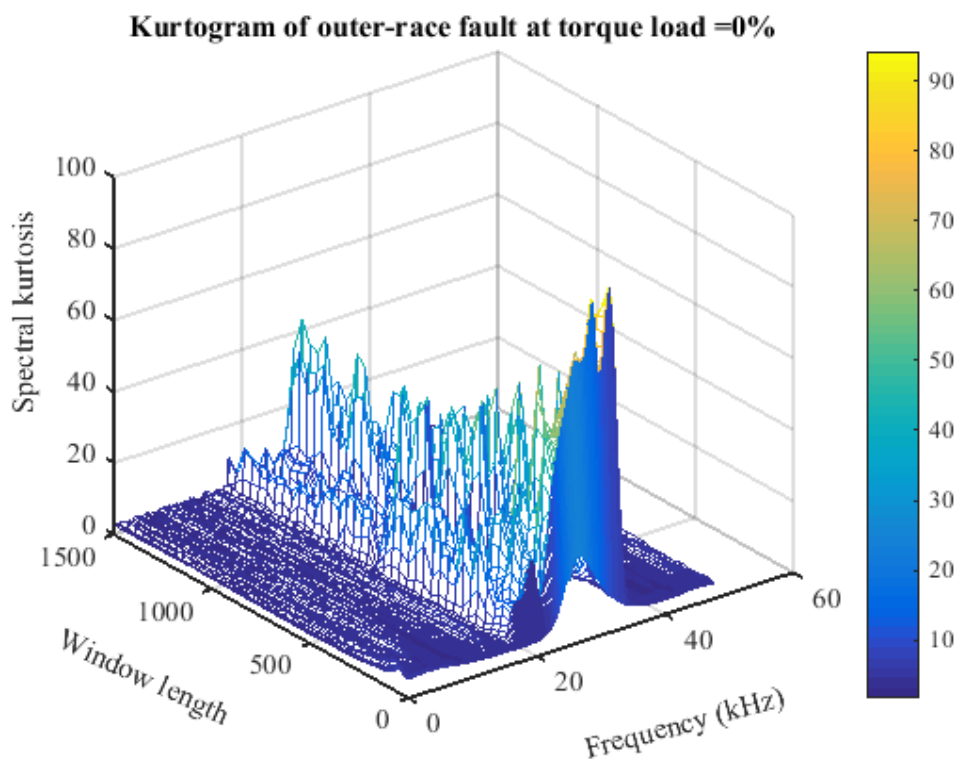
Figure 7-12 Kurtogram of an outer-race fault at 0% torque load

It should be noted that the band-pass filters are designed by using the finite impulse response (FIR) structure of 64th order, based on the obtained central frequency and window length values of the kurtogram for all the fault scenarios.

The envelope spectrum parameters have been determined based on the designed filters, which were identified from the maximum values of the kurtogram for the three studied bearing cases. Figure 7-13 depicts the optimised envelope spectrum of the baseline and the inner-race fault under four different torque loads. For the baseline with no fault

present, the envelope spectrum of the vibration signal shows a flat spectrum. On the other
hand, for the case with an inner-race fault, there is a clear indication for the presence of
the fault and its harmonics, which in turn verifies the validity of the band-pass filter
parameters. In addition, the characteristic frequencies, as well as the pair of modulation
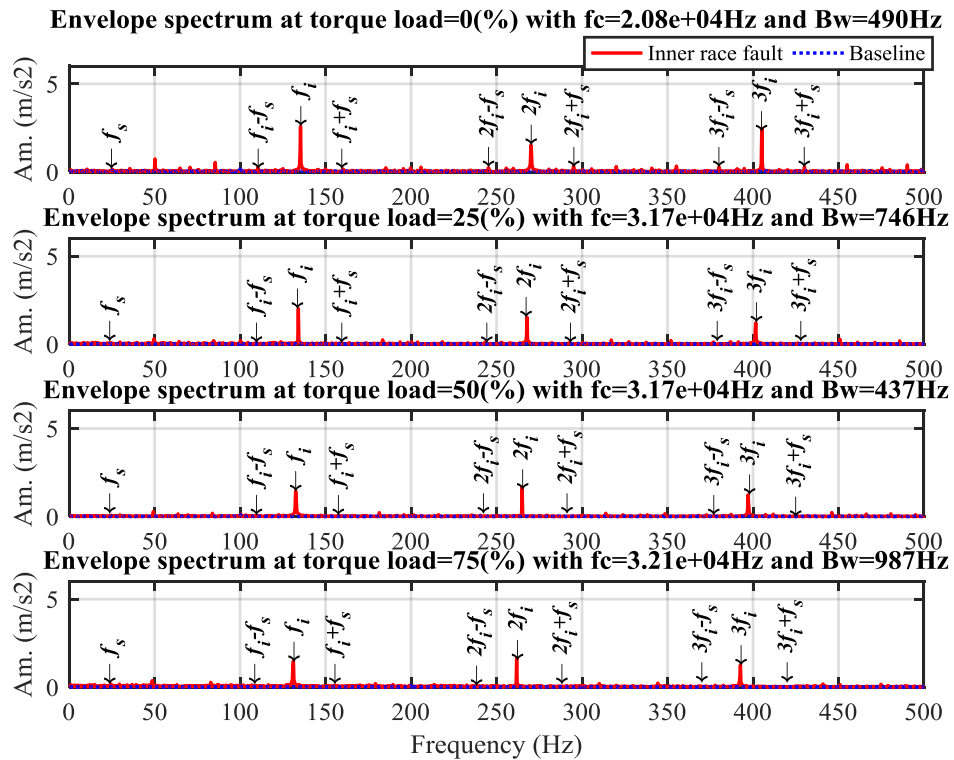sidebands, are clearly indicated.

Figure 7-13 Optimised envelope spectrum of baseline and an inner-race fault under
different load conditions

Figure 7-14 presents the optimised envelope spectrum of the baseline and the outer-race
fault using four different torque load scenarios. For the baseline, the envelope spectrum
of the vibration signal shows a flat spectrum. For the outer-race fault, there is a clear
indication of a fault existence, where the characteristic fault-frequencies and their
harmonics are also indicated. In contrary to the outer-race faults, the inner-race fault-
frequency amplitudes are greater. This is a result of geometric deformation.

Comparing the envelope spectrum results obtained for both the conventional (fixed) and
the optimal band-pass filter parameters, the envelope spectrum of conventional filter
illustrates some unknown spectral lines. This is due to the presence of random noise,
which is largely influenced by the selected central frequency. However, despite the

presence of random noise, the defect feature-frequencies for the inner- and outer-race faults, as well as their harmonic frequencies, are clearly visible without any traces of the random noise effects.
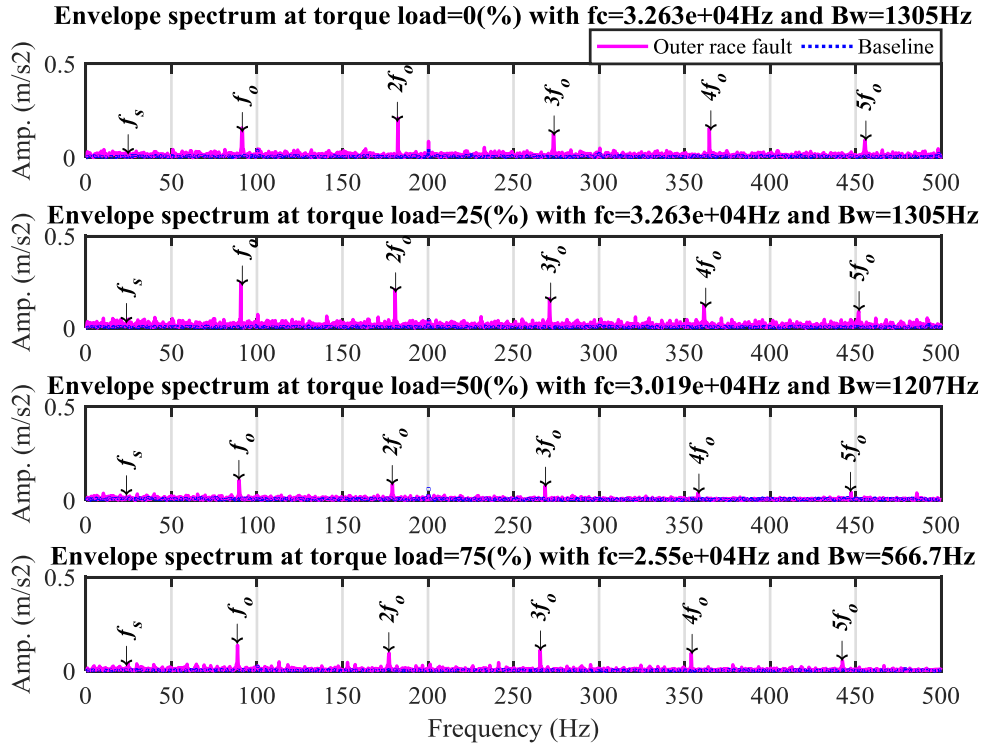
Figure 7-14 Optimised envelope spectrum of baseline and outer-race fault under different load conditions

7.3 Performance Evaluation based on Simulated Signals

To accurately evaluate the performance of kurtogram and fast kurtogram for selecting the optimal bandpass filter parameters, a simulated impact time signal was generated based on a study the influence of irregular noise pulses along with white noise on the simulated signal. A simulated impact time signal is used where spectral contents is known based on the principles described in Chapter three Section 3.4.6 using an exponentially damped cosine wave signal as the following:

$$x(t) = u(t) + \theta(t) + n(t) \tag{7-1}$$

where $x(t)$ denotes the vibration signal of the defective bearing, $u(t)$ is the transient component, $\theta(t)$ denotes the interference component, and $n(t)$ stands for the white

Gaussian noise component. The transient signature of the defective bearings can be modelled as:

$$u(t) = B \sum_n P(t - \frac{n}{f} + \tau_n) \qquad (7\text{-}2)$$

where B is the impulses amplitude which is considered as 1.0, n the number of the impulses which is considered as 100, f is the fault characteristic frequency which is considered as 89 Hz (outer race fault), τ_n is the random fluctuation due to slippage, and $P(.)$ the impulse response function that is given as [162]:

$$P(t) = \begin{cases} e^{-\alpha t} \cos(2\pi f_0 t) & ; \quad t > 0 \\ 0 & ; \quad otherwise \end{cases} \qquad (7\text{-}3)$$

where f_o is the structural resonance frequency, which is considered as 5 kHz and α is the damping ratio which is assumed to be 0.02. These are common parameters for motor drive below 10kW. In addition, the random fluctuation of the ball positions in a real rolling bearing system resulting from the nominal motion of the cage, which can be either backward or forward. It was introduced as a random number to the simulated impact signal when they are jointed one after each other.

What is more, to evaluate the influence of the Gaussian noise, signal-to-noise ratio (SNR) is used to restrict the noise, which is defined as

$$SNR = 20 \log_{10}(\frac{P_s}{P_n}) \qquad (7\text{-}4)$$

where P_s and P_n are the power of the noise free signal and the white noise respectively.

7.3.1 Initial Results

The time simulated signal of outer race fault under irregular pulses along with low noise level for SNR as low as -5dB with comparison with noise free signal are illustrated in Figure 7-15 (a), while the corresponding spectrum of simulated time signal is given out in Figure 7-15 (b). It can be seen that the simulated structural resonance region which naturally amplify bearing frequency harmonics are clearly visible. Moreover, the

envelope spectrum of simulated signal where the frequency range for fixed filtering is selected from 4 kHz to 6 kHz is illustrated in Figure 7-15 (c). It is selected according to the power spectrum of vibration signals to cover the whole resonance frequency band of the structural resonance region. A clear indication for the presence of the fault and its harmonics can be clearly seen.
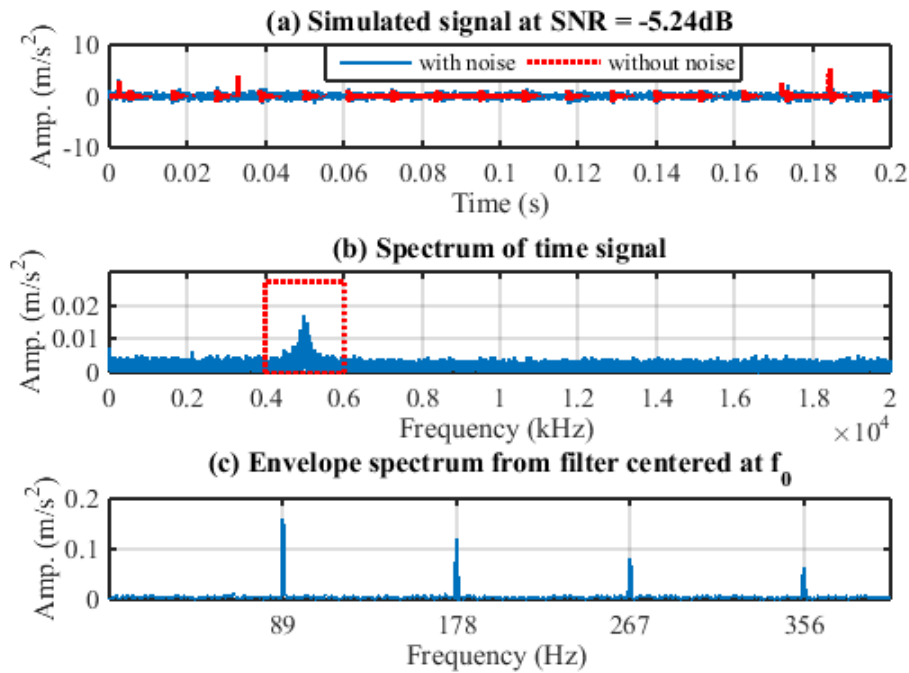

Figure 7-15 Simulated impact signal contains irregular pulses along with white background noise (a) time signal (b) spectrum analysis (c) envelope analysis

7.3.2   Optimal Window based on Kurtogram

Spectrogram of a non-stationary signal from the time domain into the frequency domain can be achieved by performing an ordinary Fast Fourier Transform (FFT) on a moving window along time-series signal, applies a moving window of a prescribed length along the recorded data to convert it into narrow-enough time intervals for the signal to be considered stationary. Figure 7-16 (a) illustrates the spectrogram of the simulated signal. . It can be seen that significant magnitudes appear at in a high band around 5 kHz throughout the time duration. While, Figure 7-16 (b) shows the mean value of the spectral kurtosis based on spectrogram results calculated using Equation (3-20). It can be seen that the maximum spectral kurtosis is achieved at 5 kHz, being consistent with that of the simulated components.
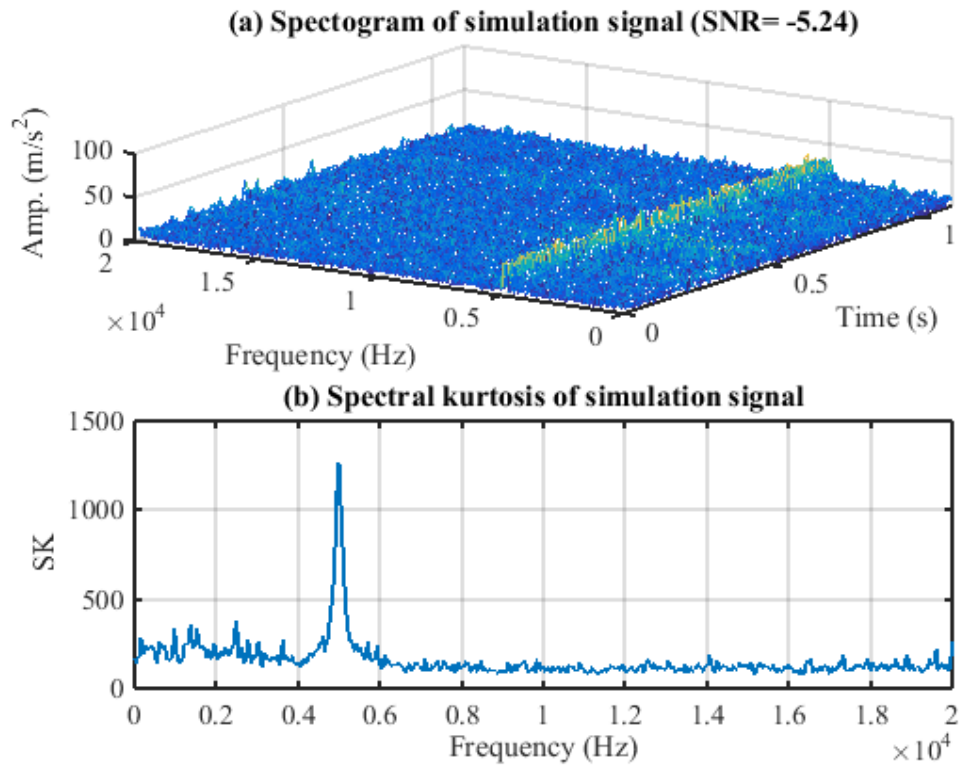
Figure 7-16 (a) Spectrogram of simulation signal (b) spectral kurtosis of simulation signal
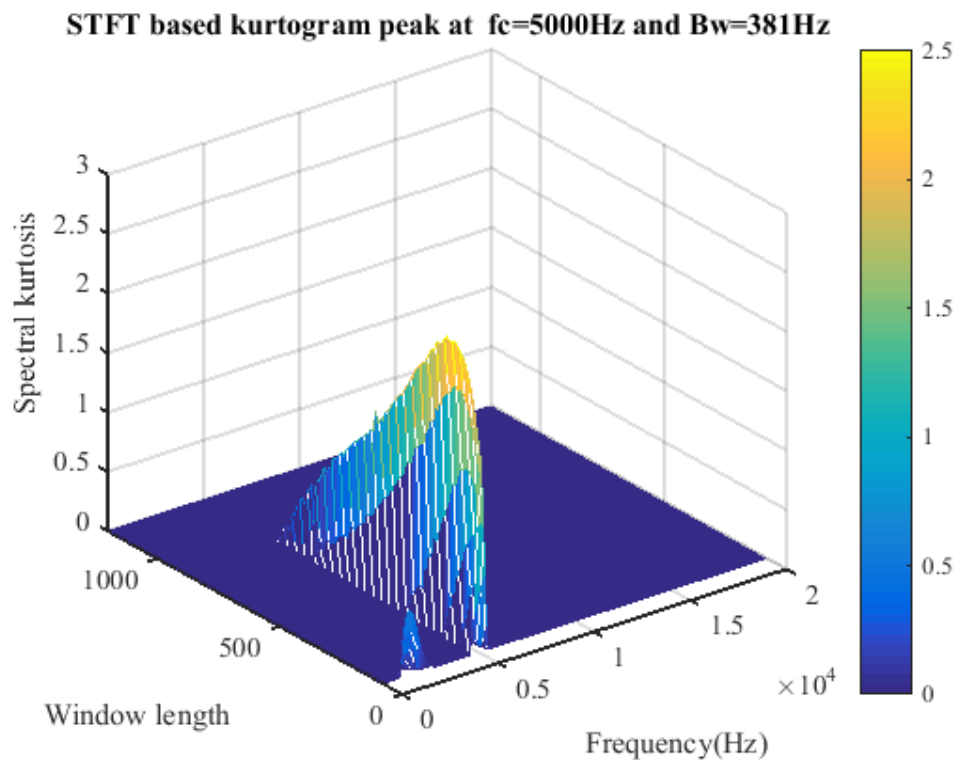

Figure 7-17 Kurtogram based STFT of simulation signal

By varying the window widths in calculating STFT over a large range, a kurtogram can be obtained as shown in Figure 7-17 . It can be seen that the kurtogram of simulated signal computed for window width from 80 to 1200 samples, with a step of 40 samples between successive windows, the maximum kurtogram value is achieved at a central frequency of 5 kHz and window width 381, which matches the simulated system's natural frequency.

The envelope filtered signal based on optimal filter parameters and its envelope spectrum are presented in Figure 7-18. From the envelope spectrum results it can be seen that a clear indication for the presence of the fault and its harmonics, which in turn verifies the validity of the band-pass filter parameters obtained.

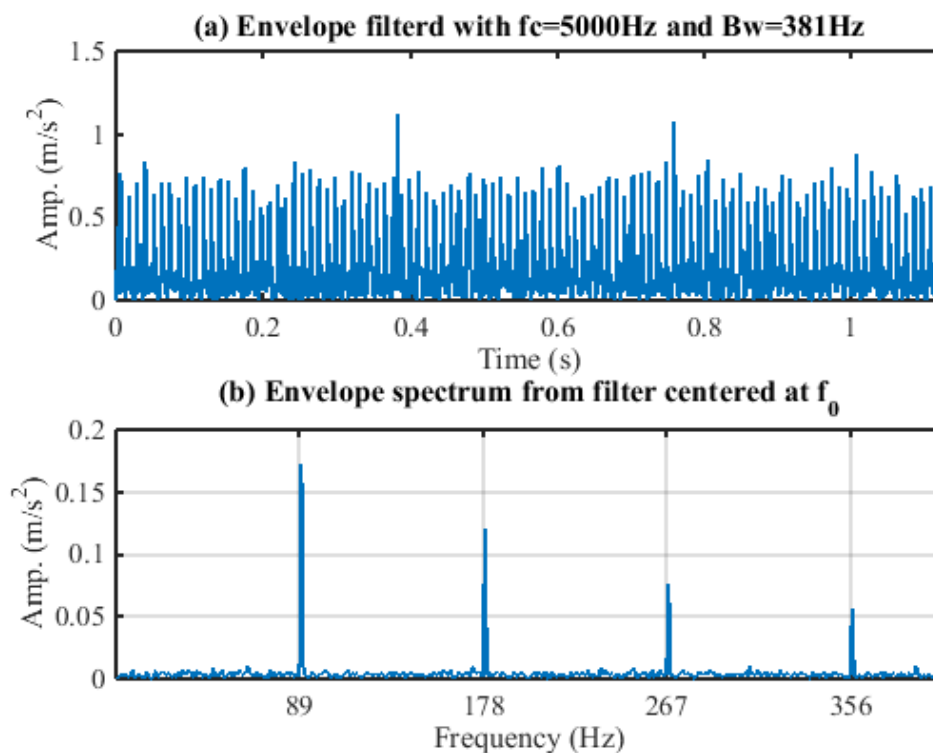Figure 7-18 (a) Envelop of filtered signal (b) envelope spectrum

7.3.3 Optimal Window based on Fast Kurtogram

The fast kurtogram is the state of the art in bearing monitoring research, which is reveals a colour map of thresholder Kurtosis across frequency, and hence it allows resonance regions to be identified and envelope filter edges to be selected. This method can be implemented in two different ways

7.3.3.1 Wavelet Based Fast Kurtogram

The envelope spectrum parameters have been determined based on the designed filters, which were identified from the maximum values of the fast kurtogram for the simulated signal. Figure 7-19 illustrates the wavelet based fast kurtogram (filter bank) for the simulated signal contains irregular pulses along with white background noise. The maximum kurtosis value of 0.4 where achieved at level 3 with the filter bandwidth is 2500 Hz and the central frequency is 1250 Hz.
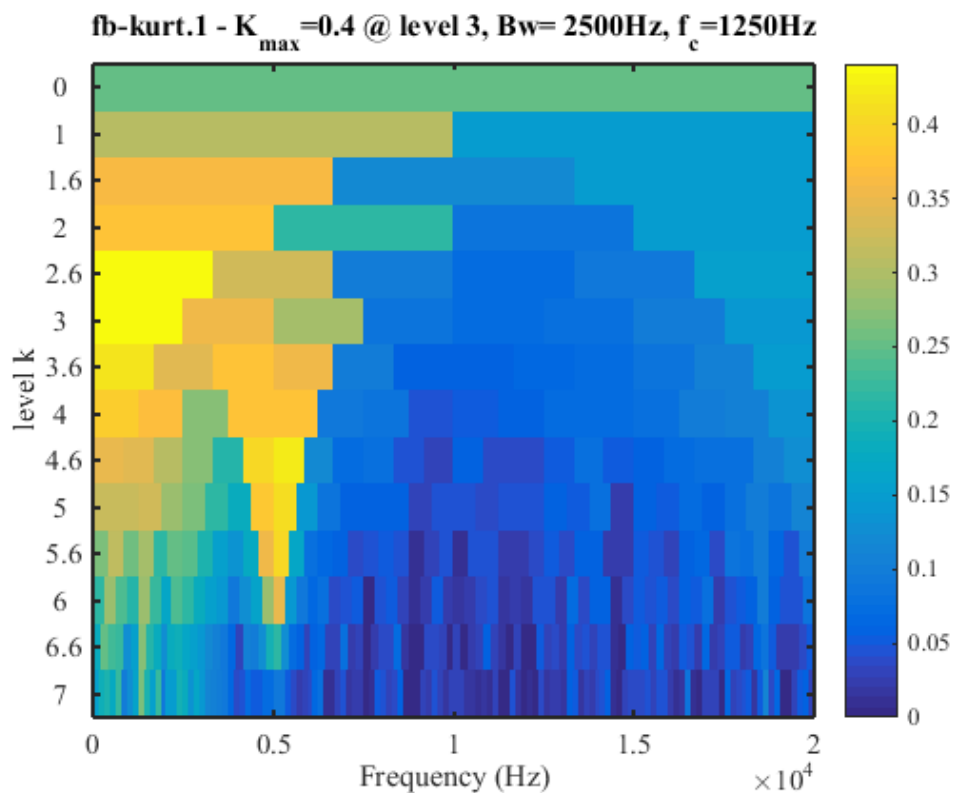
Figure 7-19 wavelet based fast kurtogram of simulation signal based filter bank

The simulation signal added with white noise, the filtered signal and its squared envelope spectrum are given in Figure 7-20 (a), (b) and (c), respectively. The envelope spectrum parameters have been determined based on the designed filters, which were identified from the maximum values of the wavelet based fast kurtogram for the simulated signal. From Figure 7-20 (c), it can be seen that no clear indication for the presence of the fault and its harmonics, which in turn clarify that the wavelet based fast kurtogram is not sufficiently robust because it is very sensitive to random noise and large aperiodic impulses which normally exist in practical application.

Figure 7-20 (a) Simulation signal (b) envelope of filtered signal (c) Fourier transform magnitude of the squared envelope

7.3.3.2 STFT based Fast Kurtogram

Figure 7-21 illustrates the STFT based fast kurtogram of the simulated impact signal contains irregular pulses along with white background noise. The maximum kurtosis value of 0.6 where achieved at level 4 with central frequency is 5000 Hz.

The simulation signal added with white noise, the filtered signal and its squared envelope spectrum are given in Figure 7-22 (a), (b) and (c), respectively. The envelope spectrum parameters have been determined based on the designed filters, which were identified from the maximum values of the STFT based fast kurtogram for the simulated signal. From Figure 7-22 (c), it can be seen that a clear indication for the presence of the fault and its harmonics, which in turn verifies the validity of the band-pass filter parameters. Moreover, the STFT based fast kurtogram does not influence by the irregular pulses.
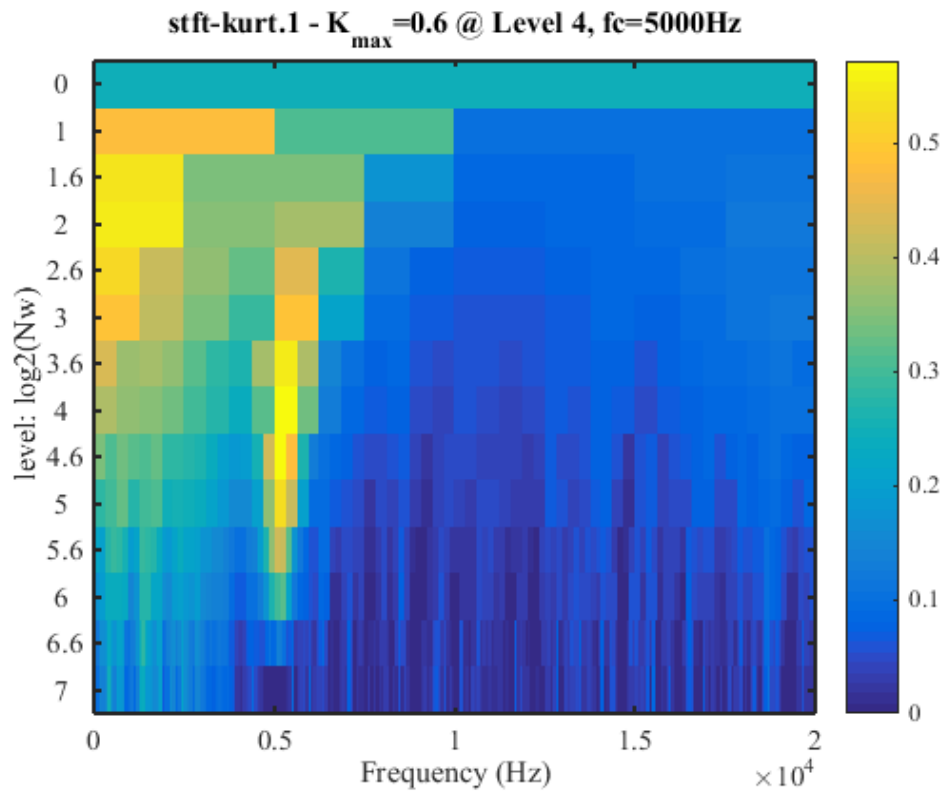
Figure 7-21 STFT based fast kurtogram of simulation signal based STFT
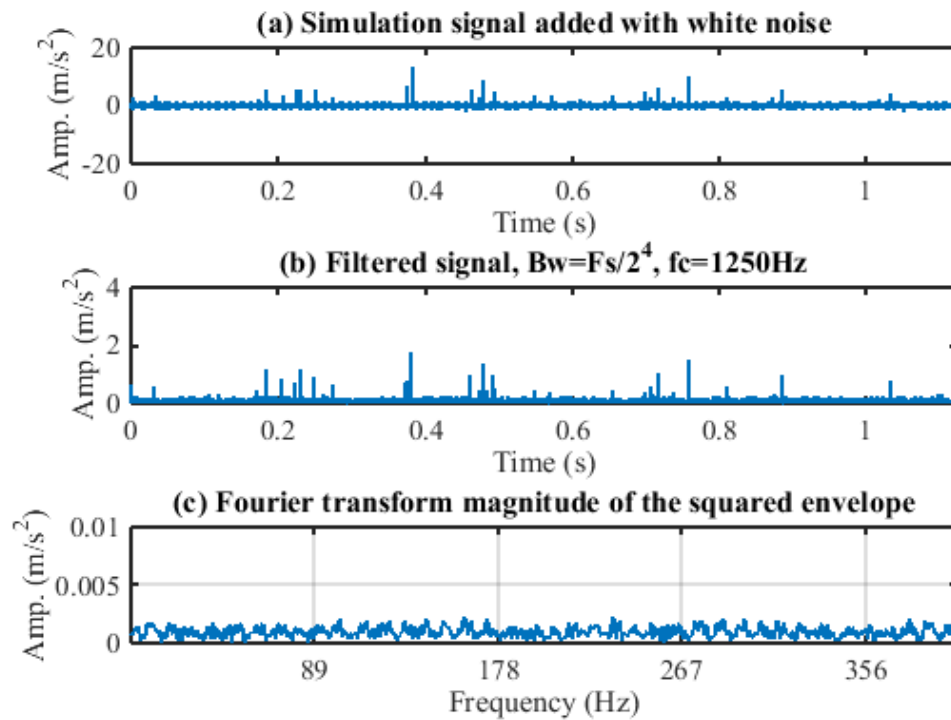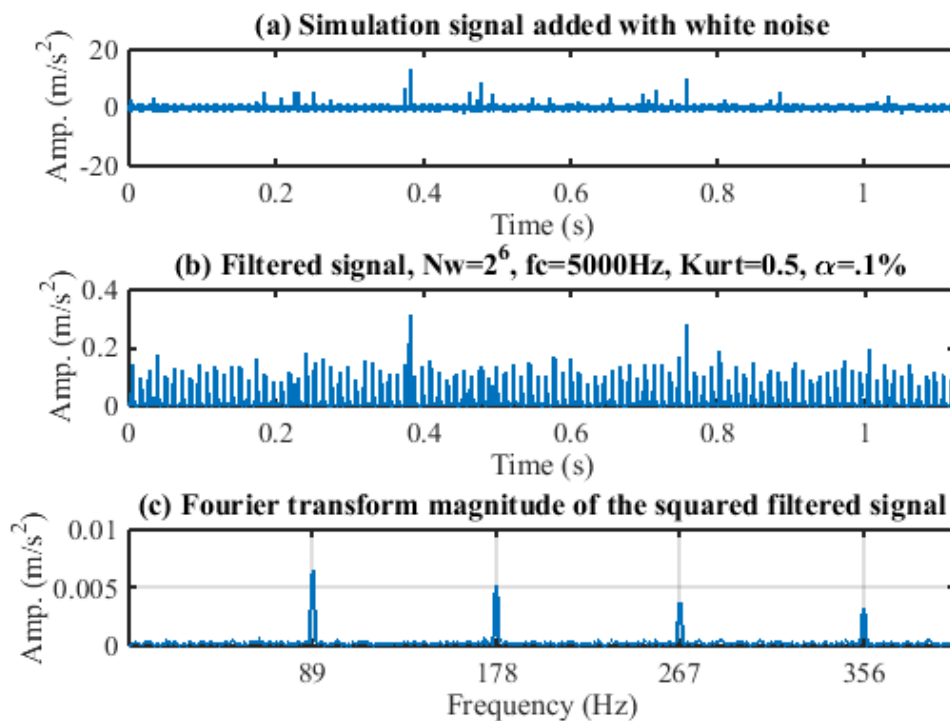

Figure 7-22 (a) Simulation signal (b) envelope of filtered signal (c) Fourier transform

magnitude of the squared envelope

7.4 Summary

In this Chapter, an optimised envelope analysis method is examined for roller element bearing fault detection and diagnosis. The parameters of band pass filters are optimised by spectral kurtosis because it is an effective technique to enhance impulse components. It is evaluated based on simulated impact signal using irregular pulses along with white background noise. It is found that the STFT based kurtogram is more effective to highlight the periodic components due to bearing faults and less influenced by irregular noise pulses than the wavelet based fast kurtogram. This is because STFT can suppress the noise to certain degrees due to its smoothness prosperity that is arisen from its limited time-frequency resolutions.

Moreover, both types of kurtogram have no noise suppression capability. As results it cannot be effective for high noise or small fault cases and the envelope spectrum is not so accurate to quantify fault severity adequately.

CHAPTER EIGHT

EXPERIMENTAL VERIFICATION OF THE DYNAMIC MODEL RESULTS

This chapter reports the experimental studies conducted based on deep-groove ball bearings in order to gain full understandings of the nonlinear dynamic response of the bearing system under different conditions and noise environments and also to verify the results of the nonlinear dynamic model presented in Chapter five. The vibration acceleration responses were obtained from the bearing rig for two types of common localised faults with two incremental severities and under two grades of internal radial clearances and four different radial loads, which are then analysed using the time-domain, frequency-domain, and envelope spectrum techniques to obtain the fundamental characteristics of the fault signatures under such conditions for providing both qualitative and quantitative knowledge for extracting the signatures marked by various noises.

8.1 Introduction

This Chapter further investigates the signal processing and bearing diagnosis techniques that were reviewed in Chapter three. These techniques include the time-domain, frequency-domain, and envelope spectrum analysis. The aim of this Chapter is to provide a comprehensive insight on such signal processing techniques when applied in bearing fault diagnosis, and to clarify the effect of various internal radial clearances on the resulting vibration signals for faulted bearings. To this end, two groups of bearing clearances, namely CN and C4, were chosen as subject of study in this work. Moreover, four sets of bearing conditions were tested for each bearing clearance; a healthy bearing as a reference baseline; 0.2 mm inner-race fault; 0.2 mm outer-race fault; and 0.475 mm inner-race fault. The fault size where chosen to quantify and understand the influence of the clearance on the rolling bearing vibration signature. The results are also used to investigate the performance of the nonlinear dynamic model discussed in Chapter five.

8.2 Experimental Results

The vibration signals are measured using the accelerometer, which is mounted vertically on the bearing housing case by threaded bronze studs. It should be noted that all the experiments were conducted at 1500 rpm (25 Hz) shaft rotational speed, with a sampling rate of 96 kHz. The reader is referred to Sections 6.2.1, 6.3.1 and 6.4 in Chapter six for more details.

8.3 Initial Experimental Results and Discussion

8.3.1 Time Waveform Analysis

Figure 8-1 and Figure 8-2 show the raw vibration signals obtained for the two test bearing clearance grades, CN and C4, under the four bearing conditions; baseline, 0.2mm inner race, 0.475mm inner race and 0.2mm outer race. Each bearing under the mentioned conditions is imposed to four different types of radial loads, that is, 0, 0.8, 1.6 and 2.4 kN, respectively. As can be seen, for the healthy bearings used as the baseline, a waveform covered in small spikes of high-frequency components is produced. On the other hand, for the faulted bearings, a more significant change in the waveform is observed. For example, for the fixed outer-race defect case, the impulse caused by the contact between the ball and the defect is repeated periodically at the same amplitude. Whilst, a rotating

inner-race defect results in a rather more complicated vibration waveform. This is due to the rotation of both defect and balls with respect to another, as the rolling ball can either approach the defect either in the loaded zone or the unloaded zone. The result is vibration amplitudes whose period is dependent on the operating conditions and can change accordingly. In addition, it is evident that the vibration amplitudes obtained for 0.2 mm outer-race defect are smaller than those measured for the same-size inner-race defect. This is also true for the 0.475 mm defect cases. The impulses resulting from the inner-race defects are more obvious than the outer-race ones. The repetitive impacts between the rolling elements and the defect points located either on the inner or outer race occur at a specific rate, at which the defect is struck. In addition, the impulses are amplitude-modulated with a similar pattern, repeated every revolution.
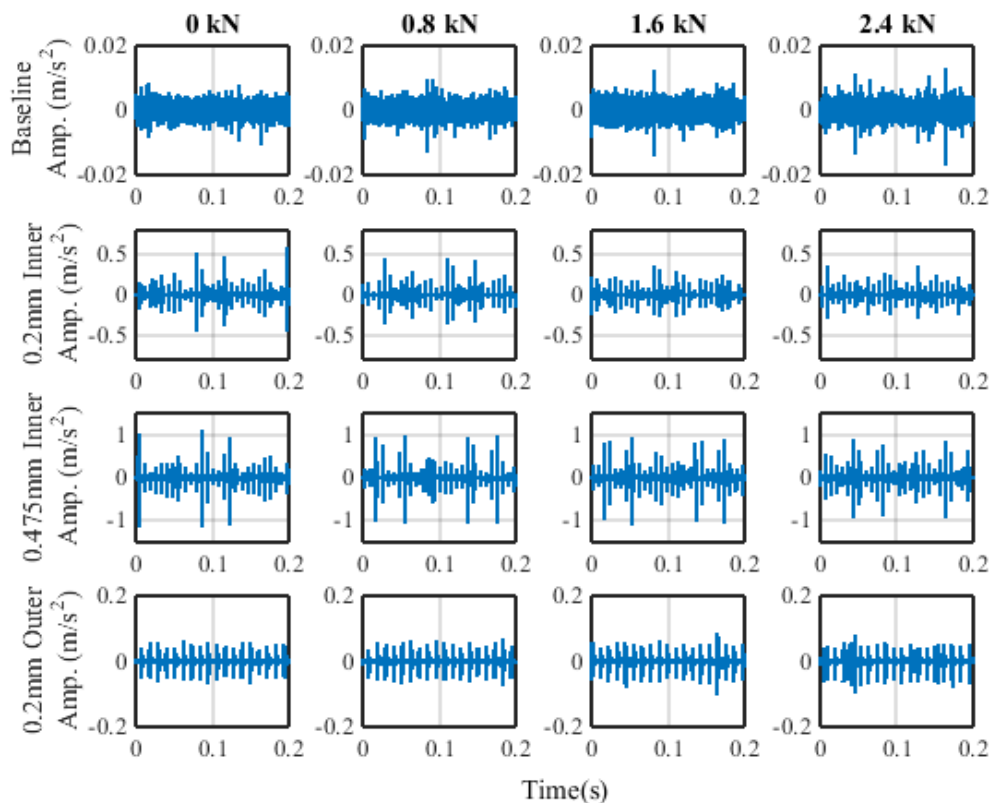

Figure 8-1 Waveform obtained in the time domain for CN bearings under four different radial loads

As discussed previously, the collected vibration signal by the accelerometer is the sum of all vibration components caused by different parts of the machine. As can be observed in Figure 8-1 and Figure 8-2, the measured signals can be quite noisy, due to electrical and

mechanical sources. This makes the detection of incipient faults an even harder task. Therefore, it is practically impossible to detect the presence of faults at their early stages of development by simply viewing the signals in the time domain.
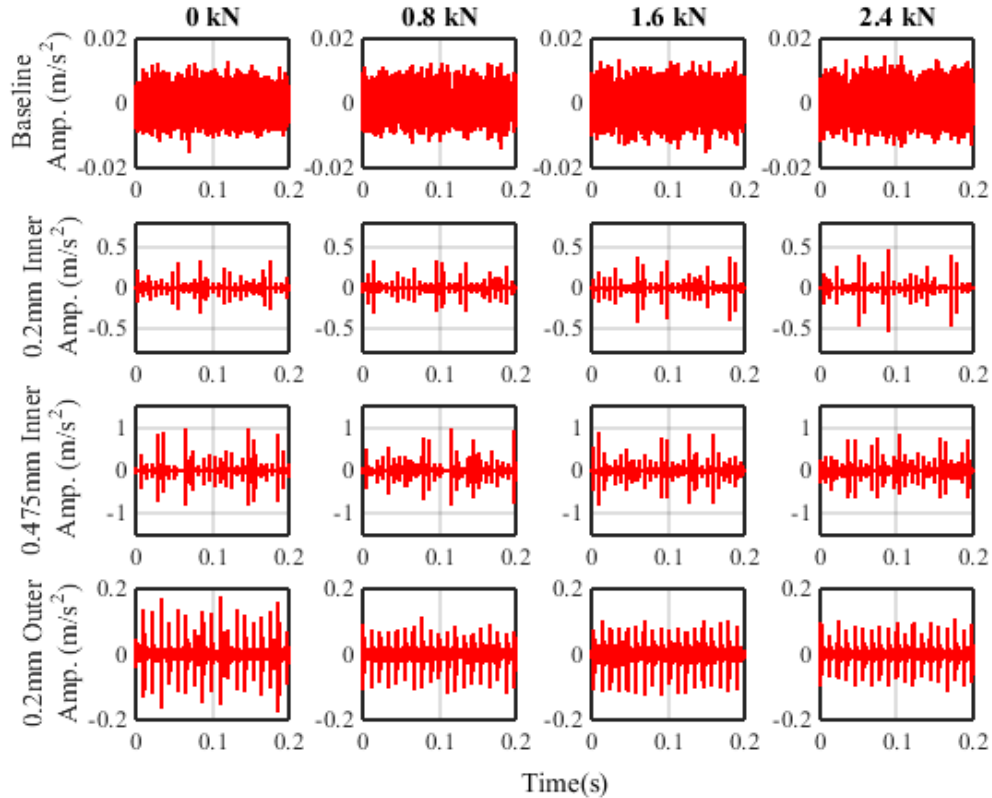
Figure 8-2 Waveform obtained in the time domain for C4 bearings under four different radial loads

Typically, vibration signals from real bearings are non-stationary and non-deterministic. Statistical parameters have proven effective in extracting the time-domain features, which provide useful information on the overall levels and the spikiness of the bearing vibration signals. In normal and defective bearings, the most frequently used time-domain statistical parameters are RMS, peak value, crest factor, kurtosis, and impulse factor.

In order to gather a deep understanding of the underlying concepts of RMS, kurtosis and crest factor, two signals S_1 and S_2 have been considered. It should be noted that, signal S_1 is less spiky, but has a high energy, whilst the signal S_2 is spikier with less energy. It can be observed that S_1 produces a higher RMS value, whereas S_2 produces a higher kurtosis and crest factor. Kurtosis and crest factor are commonly used to indicate bearing

premature spalling due to fatigue. As the defect progresses and becomes adequately severe, the values of kurtosis and crest factor return back to the values observed for normal bearing conditions. Consequently, sharp impulses of relatively low amplitude start to appear in the vibration signal as the incipient bearing fault is developed. Over time, the defect progression results in an increase in the observed signal energy levels.

Figure 8-3 demonstrates RMS, peak value and kurtosis of bearing clearance grades CN and C4 for baseline, 0.2 mm inner-race, 0.475 mm inner-race, and 0.2 mm outer-race defects at 0 kN radial load, respectively (for other radial load cases see Appendix B Section B1). It is evident that the RMS and peak values increase with fault severity. As the clearance value for the baseline and outer-race defect increases, so do the RMS and peak values, whilst, a decrease in these values is observed with inner-race defect. In contrary, the kurtosis value decreases with an increasing clearance value for the baseline and increases for the outer-race defect case, and increases for small and decreases larger inner-race defects.
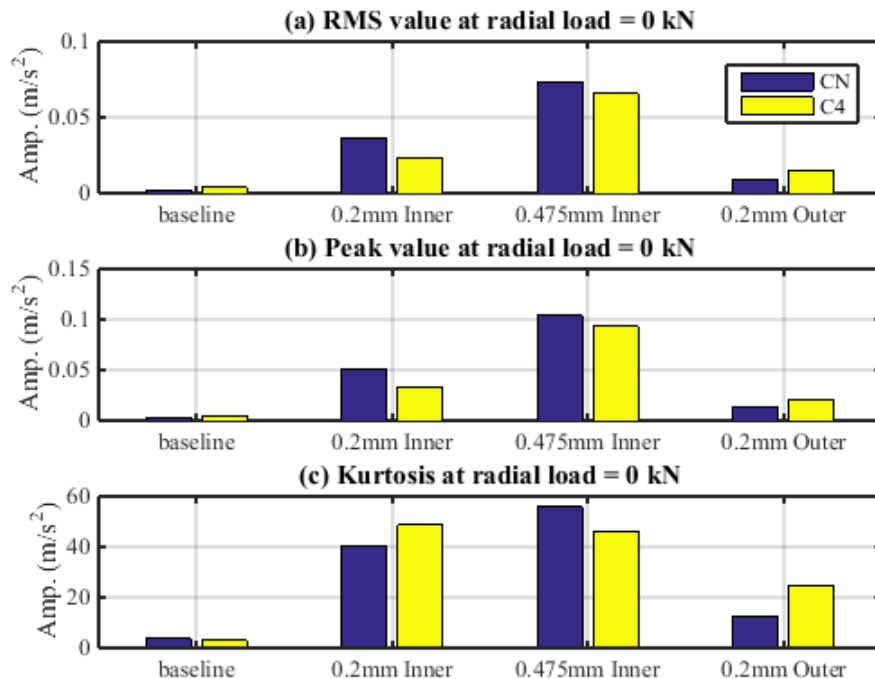

Figure 8-3 (a) RMS, (b) peak value and (c) kurtosis of raw data at 0 kN radial-load condition

In case of a similar size defect in both outer-race and inner-race cases, the resulting impulse amplitude for the outer-race defect is constant and generally less spiky, whilst the

inner-race fault occurs at a frequency that is modulated at the shaft frequency. Compared with the inner-race fault, a lower peakiness is observed in the impulse signal measured for an inner-race fault. This is clearly evident in the results presented in Figure 8-3. However, RMS is the better choice for fault diagnosis compared with kurtosis. Note that the RMS and kurtosis values obtained for small inner-race faults are higher than those for the outer-race fault with the same degree of fault severity. This is mainly due to the effect of defect geometries.

8.3.2 Raw Data Spectrum Analysis

The FFT algorithm is applied to convert the signal information from the time domain into the frequency domain in order to extract a clear image of the signal form the raw data spectrum. It is imperative to have an appreciation for the characteristic frequencies associated with specific faults, which are key to detection and diagnosis of bearing faults. It is possible to calculate the fault characteristic frequencies for each bearing element, based on the geometric structure of the bearing and the actual shaft rotational frequency measured using the encoder setup described in Section 3.2.3 in Chapter three.
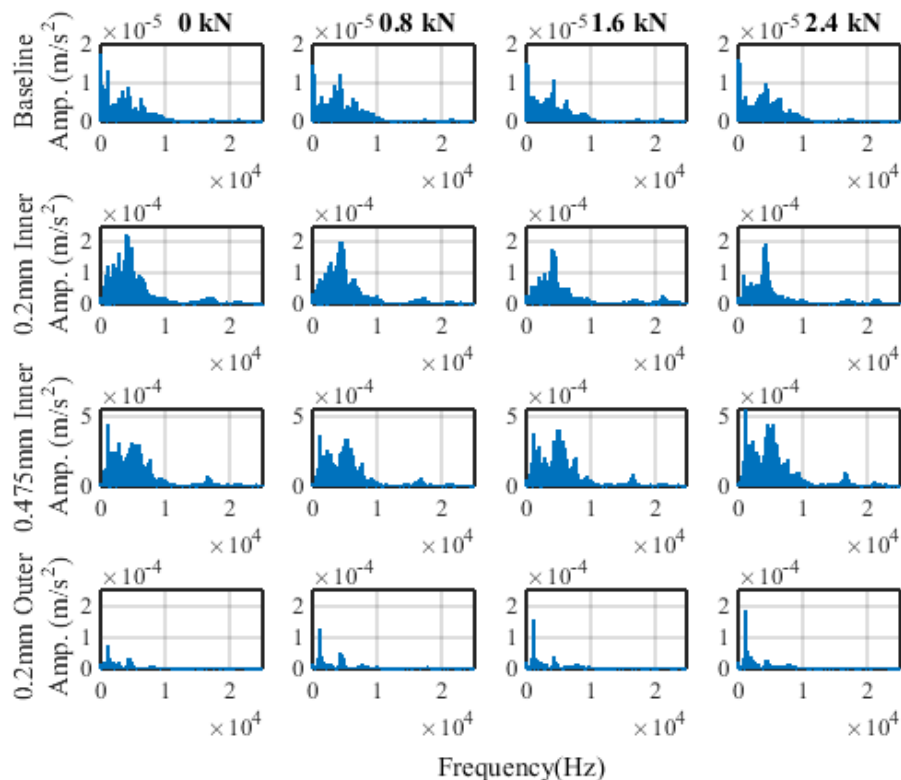

Figure 8-4 Vibration signal spectrum of CN bearings under four different radial loads

Figure 8-4 and Figure 8-5 present the vibration spectra obtained for two different types of bearing clearance grades, CN and C4, for a healthy bearing as the baseline, a 0.2 mm inner-race defect, a 0.475 mm inner-race defect, and a 0.2 mm outer-race defect at four radial load conditions of 0, 0.8, 1.6 and 2.4 kN. The first dominant peak can be easily identified by the subtracting the baseline away from the faulty spectrum. It can be seen that the low frequency component of the vibration signal is the impact of defects of bearing associated with wide band noise caused by the vibration energy of the defective bearing. Furthermore, the amplitudes of the spectra obtained for the inner-race defect is higher than those obtained for the outer-race defect with the same degree of fault severity. In addition, an increasing trend between the amplitude of the spectra and the fault severity can be observed.
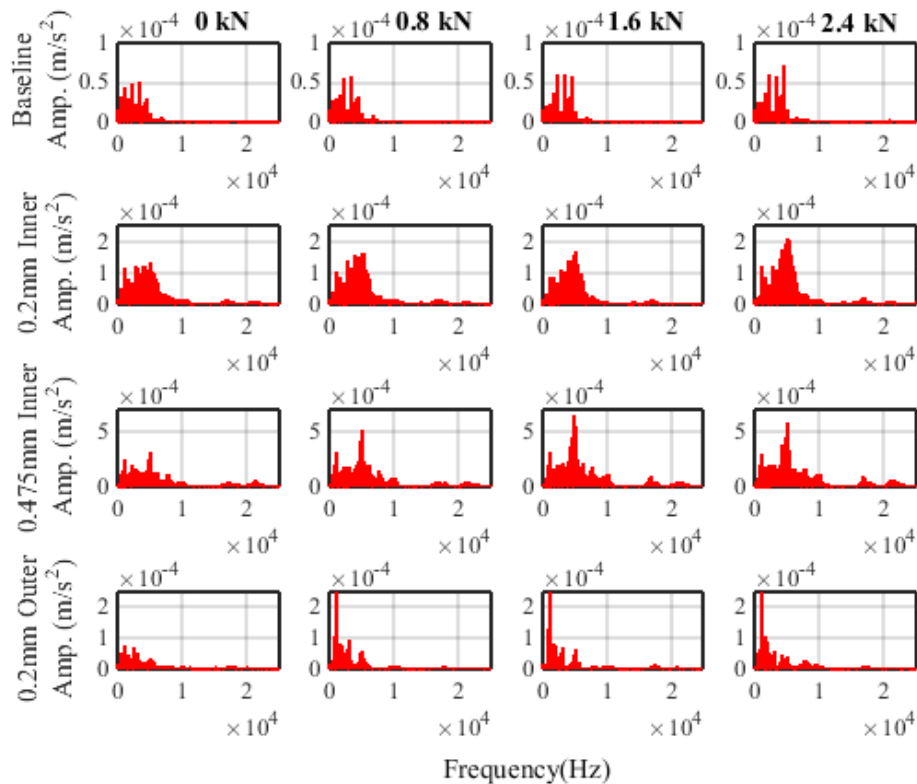
Figure 8-5 Vibration signal spectrum of C4 bearings under four different radial loads

The shaft's rotational frequency and its multiples can be easily extracted from the measured spectra, whereas the fault-characteristic frequencies and their corresponding harmonics are more difficult to identify. At the fault-characteristic frequencies, pulses of very short duration are generated, as a result of interaction between the rolling elements and the defect. These pulses excite the natural frequencies of bearing elements and

housing structures, resulting in an increase in the vibrational energy at these high frequencies. However, such characteristic frequencies are not automatically detected using the raw vibration data; it requires the spectrum to be analysed over specific frequency ranges, including their harmonics and sidebands [163]. It is often difficult to distinguish these peaks, because they can be masked by high environmental noise levels due to the wide-band noise generated by the bearing vibration. This can easily bury the fault-characteristic frequencies, as this wide-band noise excites the resonant frequencies in the bearing and surrounding structures [164].

8.4   Envelope Spectrum Analysis for Baselining Results

As explained in Chapter three Section 3.4.4, the envelope spectrum is a well-known and popular method that is employed in condition monitoring of rolling-element bearings. Herein, a common envelope procedure has been applied to find out if the vibration data contains any information on the different bearing faults, and if fault-characteristic frequencies exist.
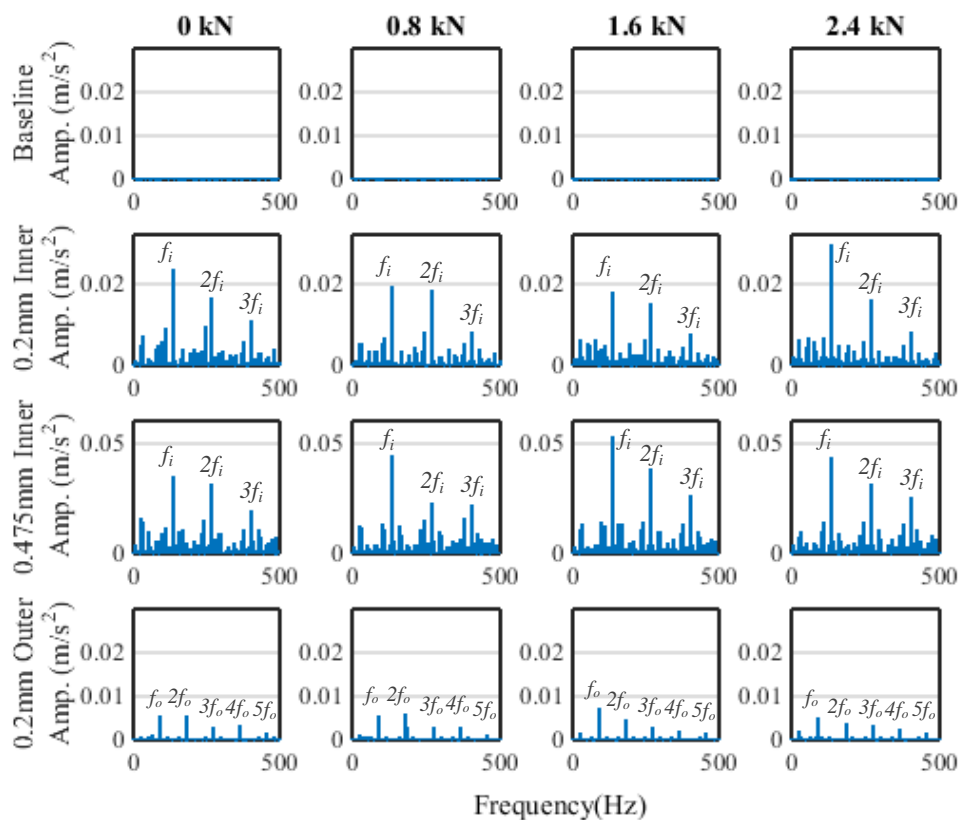

Figure 8-6 Envelope spectrum of CN bearings under four different radial loads

Figure 8-6 and Figure 8-7 illustrate the envelope spectra for two kinds of bearing clearance grades, CN and C4, for a normal bearing as baseline, a 0.2 mm inner-race defect, a 0.475 mm inner-race defect, and a 0.2 mm outer-race defect under four radial load conditions of 0, 0.8, 1.6 and 2.4 kN. The band-pass filter's central frequency is chosen according to the power spectrum measured for the vibration signals, in an effort to cover the whole resonance frequency-band of the machine, from 3 kHz to 10 kHz. In order to satisfy the condition for Nyquist-Shannon sampling theorem, the bandwidth is selected to be more than double the highest fault-characteristic frequency. This ensures the filter can pass the carrier frequency and at least one pair of the side bands. For the baseline, the envelope spectra shown in Figure 8-6 and Figure 8-7 is fairly flat, and no clear spectral lines can be found. However, in the faulted conditions, peaks at the fault-characteristic frequencies are clearly visible, as well as their harmonic frequencies. It is apparent that, as the fault severity increases, so does the amplitude of measured peaks. Nevertheless, there are some unexpected frequencies, as well as the background noise, which might affect the diagnostic results.
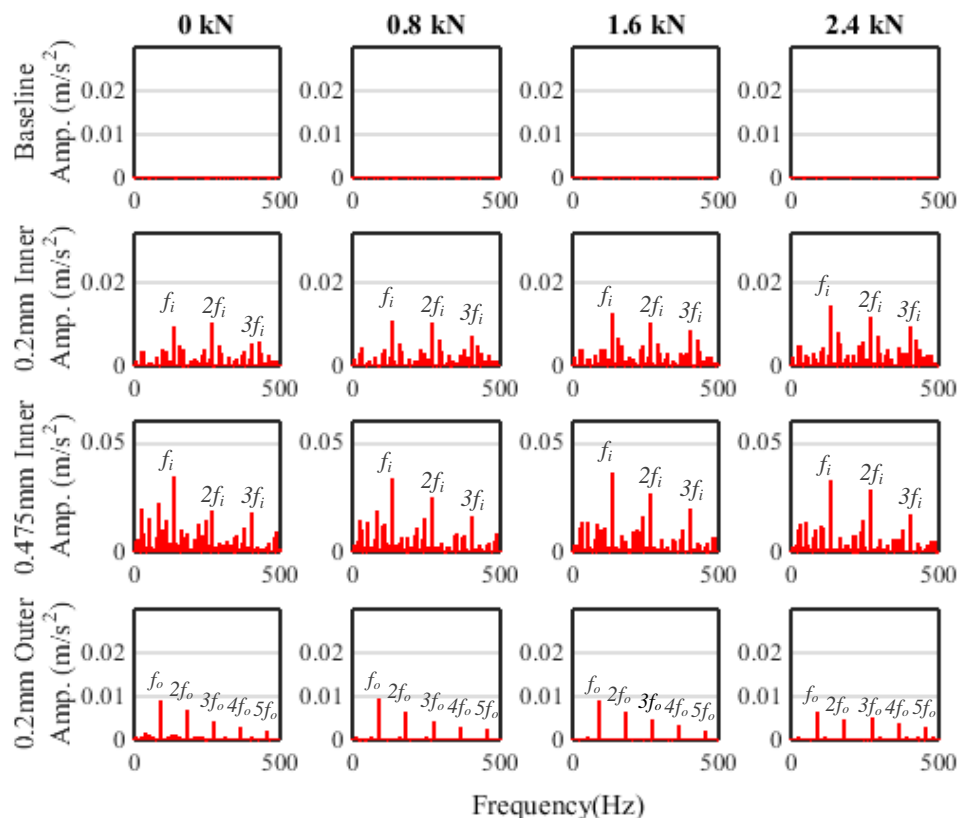

Figure 8-7 Envelope spectrum of C4 Bearings under four different radial loads

The envelope spectrum amplitude of the first three harmonics for two kinds of bearing clearance grades, CN and C4, for a normal bearing as baseline, a 0.2 mm inner-race defect, a 0.475 mm inner-race defect, and a 0.2 mm outer-race defect case under four different radial loads of 0, 0.8, 1.6 and 2.4 kN, are illustrated in Figure 8-8. For the inner-race defect, the fault-frequency amplitude drops slightly with increasing clearance value for the first three harmonics. In contrast, for the outer-race defect, the fault-frequency amplitude increases slightly with increasing clearance value. This is due to the change of the load-zone angle for the two defect conditions.
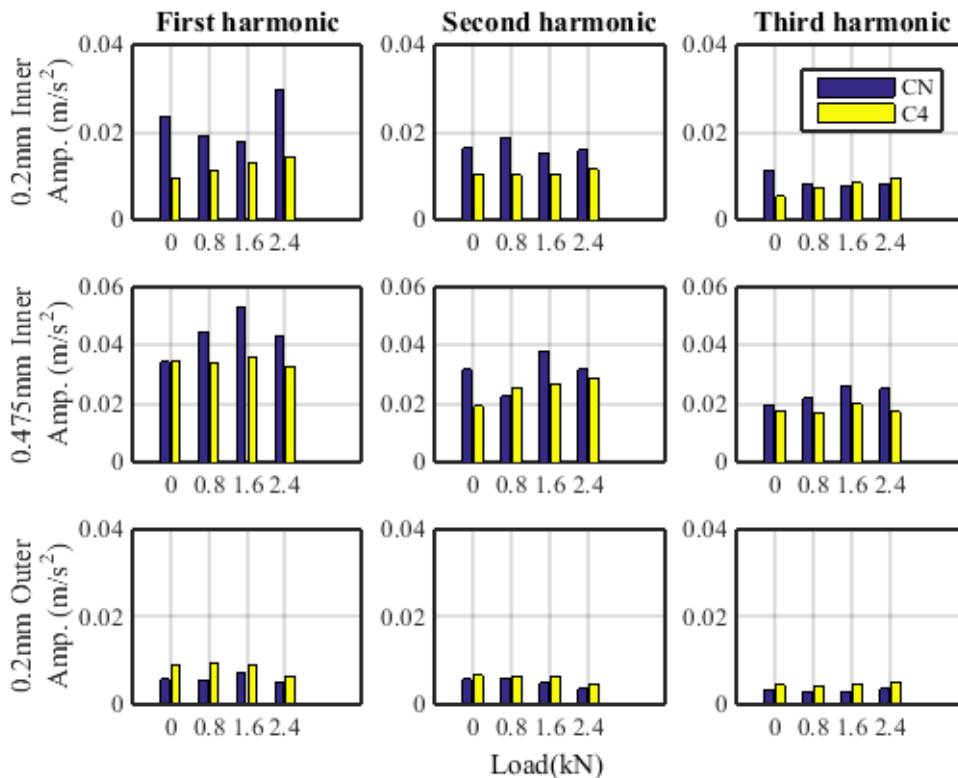
Figure 8-8 Envelope spectrum amplitude of the first three harmonics under four different radial loads

As the magnitude of the radial load becomes larger, a significant increase in the vibration signal's amplitude should be observable as a result of nonlinear deformation. However, this is not very clearly demonstrated in practice, and thus, in Figure 8-8. This can be related to the presence of large background noise. Therefore, further analysis needs to be performed in order to improve the signal-to-noise ratio, and to verify the concepts of radial load fault detection.

8.5 Summary

In this Chapter, two groups of bearing clearances, namely CN and C4, were chosen to clarify the effect of various internal radial clearances on the resulting vibration signals for faulted bearings and also used to verify the performance of the nonlinear dynamic model discussed in Chapter five. In addition, four sets of bearing conditions were tested for each bearing clearance; a healthy bearing as a reference baseline; a 0.2 mm inner-race fault; a 0.2 mm outer-race fault; and a 0.475 mm inner-race fault. The studied bearings were examined using the time-domain, frequency-domain, and envelope spectrum analysis.

The time domain analysis and frequency domain analysis provides limited information about the presence of the fault signals, whereas the envelope spectrum delivers a clear demonstration of the bearing faults frequencies. In addition, as expected, the larger the clearance, the higher amplitude of the diagnostic feature for the outer race defects. However, the large clearance reduces the amplitudes of the feature for inner race defects. Moreover, as the radial loads become large the fault feature frequency amplitude should be increased as result of nonlinear deformation (Hertzian contact theory), which it is not. This mainly results from high presence of background noise and further analysis needs to be implemented to verify this concept.

CHAPTER NINE

HIGHER ORDER SPECTRA ANALYSIS BASED ROLLING ELEMENT BEARING FAULT DETECTION AND DIAGNOSIS

This chapter presents the enhancement of diagnostic signatures using higher order spectra analysis. It suggests applying the bispectrum analysis to envelope signal to suppress noise influences and thereby provide an accurate estimation of fault signature magnitudes. It starts with verifying the performance of two typical higher order spectra methods: conventional bispectrum and modulation signal bispectrum in obtaining accurate spectral magnitudes for severity assessments through both a simulated signal and a noise measurement. Then, it presents the use of these evaluated methods to enhance the ball bearing vibration signals of different radial load and internal clearance increments when they are subjected to inventible noises.

9.1   Introduction

For an accurate diagnosis of the bearing fault, a number of techniques have been proposed to separate deterministic fault components from noisy bearing vibration. McFadden and Smith [165] reported that the envelope spectrum contain single, discrete components only in the very simplest examples of an axial bearing or a radial bearing with a defect in outer race and it is possible to detect the bearing condition. Randall [166] noted that the discrete random separation (DRS) technique is more successful in separating gear signals from the cyclostationary bearing signals compared to the self-adaptive noise cancellation (SANC) technique. Minimum entropy deconvolution (MED) was first proposed by Wiggins [167] to sharpen the reflections from different subterranean layers in seismic analysis. Spectral kurtosis (SK) provides a means of determining which frequency bands contain a signal of maximum impulsivity. It was first used in the 1980s for detecting impulsive events in sonar signals [168]. Sawalhi et al. [33] proposed an algorithm using a combination of autoregressive model and MED technique to enhance the defect recognition capability of the SK by sharpening the impulses originating from the defective bearings. However, in these studies, the authors have focused more on tracking the variations of vibration components at the characteristic fault frequency but with limited concentration on noise reduction and utilizing the modulation characteristics in extracting the diagnostic information.

Bispectrum analysis has been widely used in machinery diagnostics for various mechanical systems such as gears [169], bearings [170], rotating machines [171, 172] and induction machines [173]. Li [174] investigated the application of bispectrum diagonal slice to gear fault diagnostics. Yang [170] used both bispectrum diagonal slice and bicoherence diagonal slice $B(f, f)$ for bearing fault diagnostics. Rehab et al [76] applied MSB to extract the fault feature from envelope signals due to its capability to suppress noise for reliable bearing fault severity diagnosis. Tian et al [77] presented a unique method for diagnosing combination faults in planetary gearboxes using a modulation signal bispectrum based sideband estimator (MSB-SE). Furthermore, the authors [78] also proposed a robust MSB detector that allows the achievement of both optimal band selection and envelope analysis, which overcome the filter band optimisation problem in traditional narrowband envelope analysis, compared with optimal envelope analysis using fast Kurtogram.

9.2   Diagnostic Feature Enhancement

To accurately detect and diagnose bearing faults, bispectral analysis has received more attention recently because of its unique property of noise reduction and nonlinearity extraction. Based on the key properties of bispectrum analysis reviewed in Section 3.4.7, both conventional bispectrum (CB) and modulation signal bispectrum (MSB) can be used to suppress noise and irregular influences in vibration signals. Therefore, this chapter investigates the performance of both of them in estimating spectral magnitudes based on envelope signals that are obtained optimally based on Kurtogram.

The first component from the diagonal slice of CB results and that of the sub-diagonal slices of MSB results are taken as the diagnostic feature as they can include full diagnostic information and easy of computations. In the meantime, conventional spectrum magnitude is also calculated as the benchmark for these two bispectral features.

9.3   Performance of the Bispectral Features from Envelope Signals

To accurately estimate the performance of higher order spectrum analysis, power spectrum, conventional bispectrum and modulation signal bispectrum based on statistical significance of the estimated spectra are presented in two selected case studies: a simulated time signal where spectral contents is known (see Section 3.2.4 in Chapter three for more details) and then an estimation of the higher order spectrum amplitude using Mote Carlo estimator. In the next section vibration signal of tapered roller bearing fatigue test will be analysed using aforementioned methods.

9.3.1   Monte Carlo Estimator

Monte Carlo methods were first developed as a method for estimating integrals that could not be evaluated analytically. It is now a very important class of computational algorithms that depend on random sampling to achieve numerical results [175]. Monte Carlo methods are largely used in three distinctive problem classes: numerical integration, optimization, and generating draws from a probability distribution [176]. Monte Carlo estimator is essentially known as a numerical method for estimating the simulated signal components when subjected to the random noise.

9.3.2   Simulation Study

To evaluate the performance of MSB, CB and PS, for estimating the signal components contaminated with high level of white noise, a harmonic signal was generated with three components under pulsing a white noise for a SNR as low as -5dB as the following:

$$x(t) = A_1 \cos(2\pi f_1 t + \varphi_1) + A_2 \cos(2\pi f_2 t + \varphi_2) + A_3 \cos(2\pi f_3 t + \varphi_3) \tag{9-1}$$

where A_1, A_2 and A_3 are the amplitudes of each individual signal, which are considered as 0.1 (the same amplitude for the three harmonics to compare the estimation performance). The f_1, f_2 and f_3 are three frequency components, which are considered as 20 Hz, 40 Hz and 60 Hz, respectively. The φ_1, φ_2 and φ_3 are the initial phase angle of each individual signal, which are considered as 0.5, 1.0 and 1.5, respectively.

Figure 9-1 shows the results of MSB and CB of the simulated signal. It can be seen that the MSB results have a clear distinct peak at bifrequency $B_{MS}(f_F, 2f_F)$, while CB results presents also a clear distinct peak at bifrequency $B_{MS}(f_F, f_F)$. Moreover, the PS illustrates a clear peak at $B_{MS}(0, f_F)$.
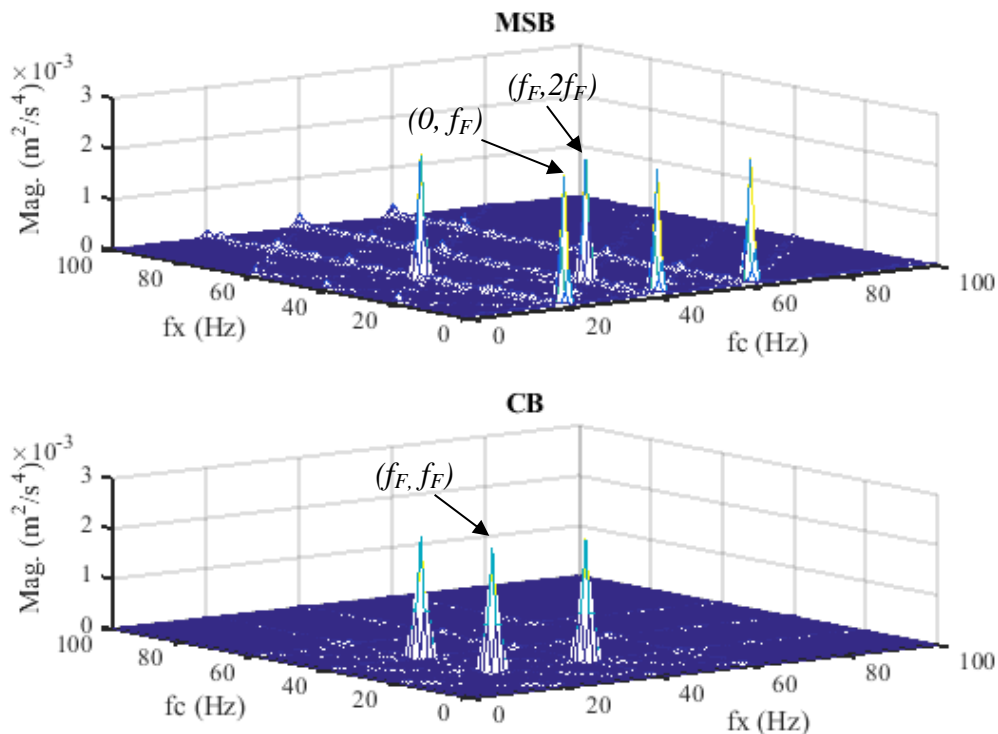

Figure 9-1 MSB and CB of simulated signals

Diagnostic feature magnitudes have been calculated for PS, CB and MSB along the diagonal slices from 20 Monte Carlo tests. In practice, these three features are obtained using following methods respectively.

$$D_{PS} = \left| B_{MS}(0, f_F) \right|^{2/4} \left| B_{MS}(0, 2f_F) \right|^{2/4} \tag{9-2}$$

$$D_{CB} = \left| B_{MS}(f_F, f_F) \right|^{2/3} \tag{9-3}$$

$$D_{MSB} = \left| B_{MS}(f_F, 2f_F) \right|^{2/4} \tag{9-4}$$

where f_F is the characteristic frequency. These components are usually more significant in an envelope signal and provide sufficient diagnostic information for both the fault components and severity. The results of comparative bispectrum analysis that have been obtained based on the basic of the diagonal slices for MSB, CB and PS are illustrated in Figure 9-2. It can be seen that the MSB, CB and PS detectors show a clear distinct peaks at bispectral frequency.
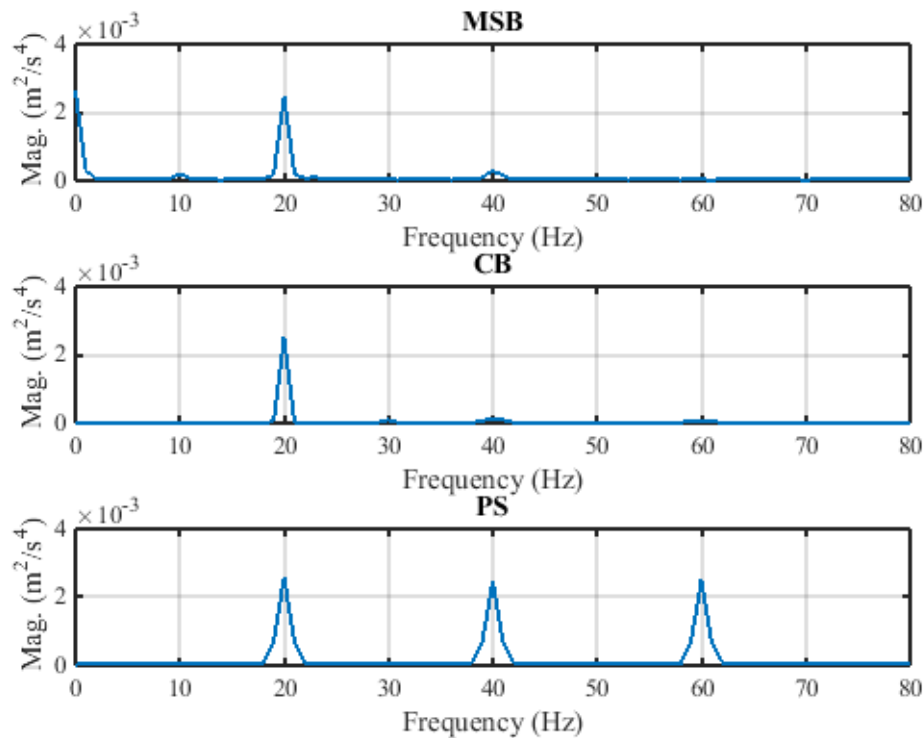

Figure 9-2 Diagonal slices for MSB, CB and PS of the simulated signal

Figure 9-3 illustrates the feature harmonic magnitude of aforementioned simulated signal with averages of PS, CB and MSB in blue dot lines whilst the expected magnitude with solid red line. The error has been calculated based on of the mean value of each harmonics magnitude to the expected magnitude, the MSB presents relatively lower deviation compared with CB and PS.

$$error = \frac{\text{mean value of each harmonics magnitude} - \exp ected\ magnitude}{\exp ected\ magnitude} \times 100 \qquad (9\text{-}5)$$
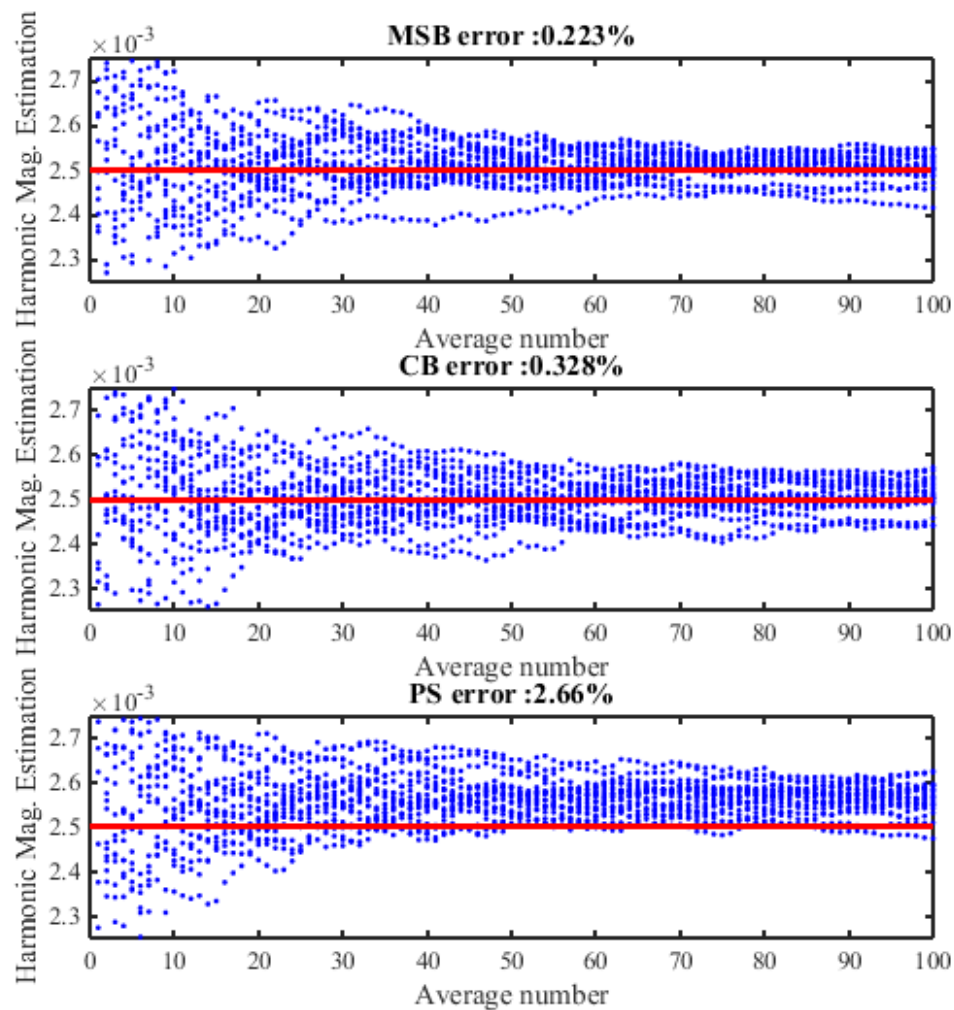

Figure 9-3 Monte Carlo tests for feature magnitude with averages

To evaluate the variability of the averaged tests, the average values of MSB, CB and PS of each Monte Carlo test were considered as estimator while the standard deviation of MSB, CB and PS were calculated based on calculated value and expected value of the

simulated signal. Figure 9-4 illustrates the estimation of variability vs averages of MSB, CB and PS. The MSB presents a clear converge than CB and PS for both the Estimator and SD calculation.
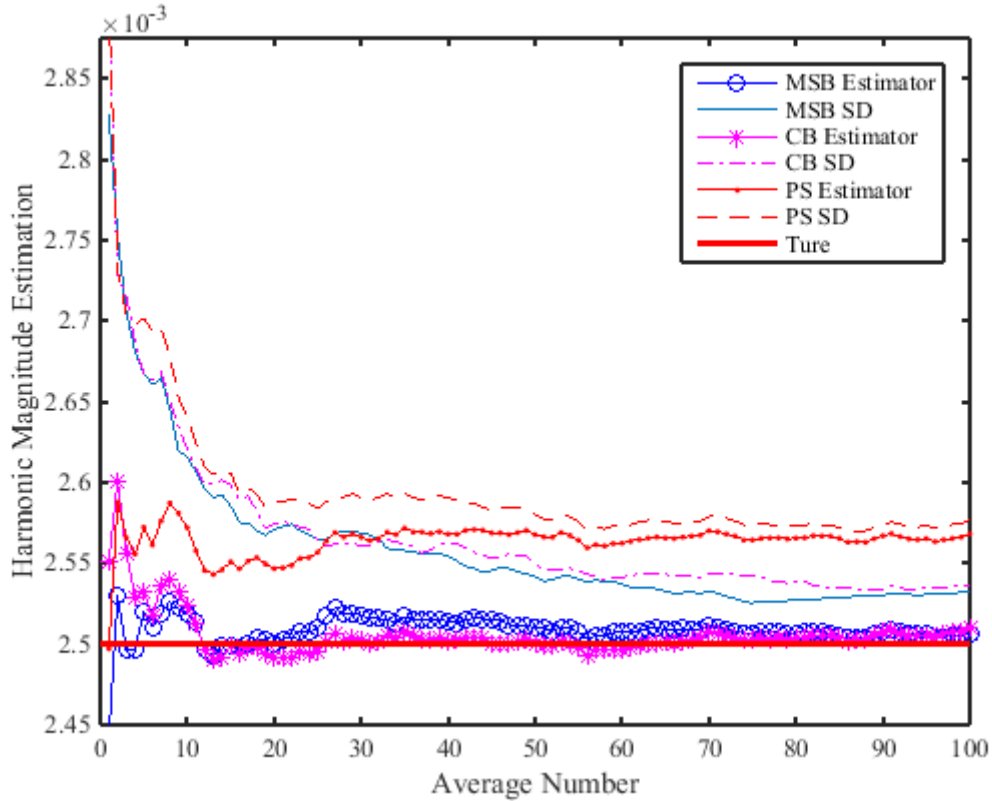

Figure 9-4 Estimation of variability vs averages

9.3.3 Experimental Verification

9.3.3.1 Test Rig Facility and Test Procedure

The bearing vibration data is from a gearbox test rig shown in Figure 9-5 (a). Vibration signals were acquired from an in-house gearbox test system. The maximum torque of gearbox is 1372 Nm, the large gear speed is 1122 rpm and the pinion gear speed is close to 1400 rpm. Figure 9-5 (b) shows the position of experiment studied bearing which mounted on the pinion gear whose rotation frequency is 23.33Hz. Moreover, the accelerometer mounted on the outer surface of the gearbox on the vertical direction.

In the experiment, the gearbox operates at constant speed and constant load condition. The vibration is measured by a general purpose accelerometer with a sensitivity of 31.9 mv/(m/s^2) and frequency response ranges from 1Hz to 10kHz. All the data were logged

by a multiple-channel, high-speed data acquisition system with 25.6 kHz sampling rate and 16-bit resolution. Tapered roller bearings geometric dimensions and bearing defect frequencies are listed in Table 9-1 and Table 9-2, respectively.
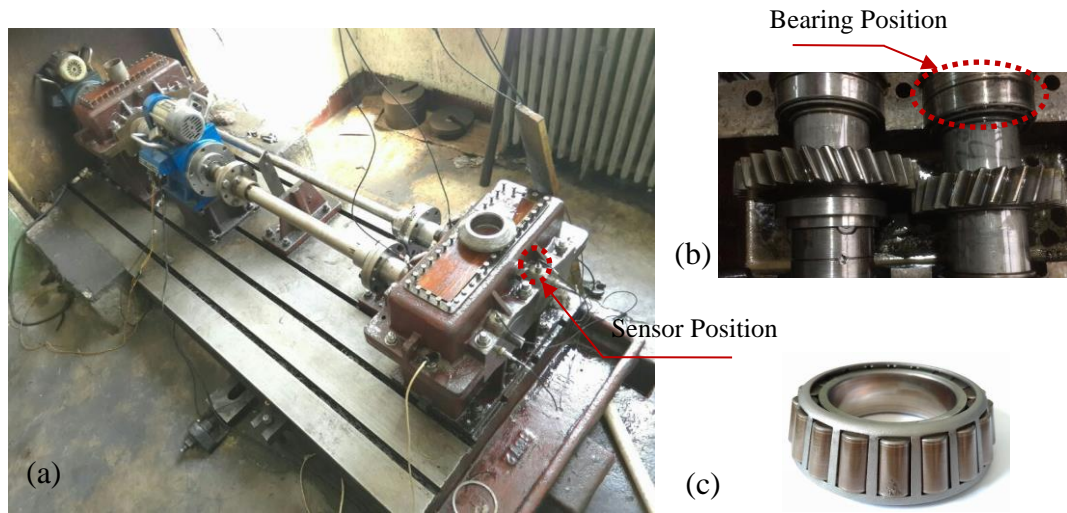

Figure 9-5 Experimental set-up, (a) test rig components, (b) bearing position and (c) bearing type

Table 9-1 Specification of tapered roller bearing type 32212

Parameter	Measurement
Outer diameter	110 mm
Inner diameter	60 mm
Pitch diameter	85 mm
Roller diameter	13 mm
Roller number	19
Contact angle	14.931^{o}

Table 9-2 Fault characteristic frequencies

Fault type	Defect frequency (Hz)
Inner race	254.39
Outer race	188.88
Rolling element	74.61
Cage	9.94

The test was carried out for 11h and 13min, at the beginning the data were collected once every 9min with a data collection interval of 1min. During the test an abnormal sound appeared at 60 time index of the data collection then the data collection intervals have been reduced to 4min. during the test the RMS and kurtosis have been calculated to monitor the change of the vibration signal.

badly fatigued inner race

one rolling element has a fatigue dent

little scratched outer race

Figure 9-6 Photos of fault bearing
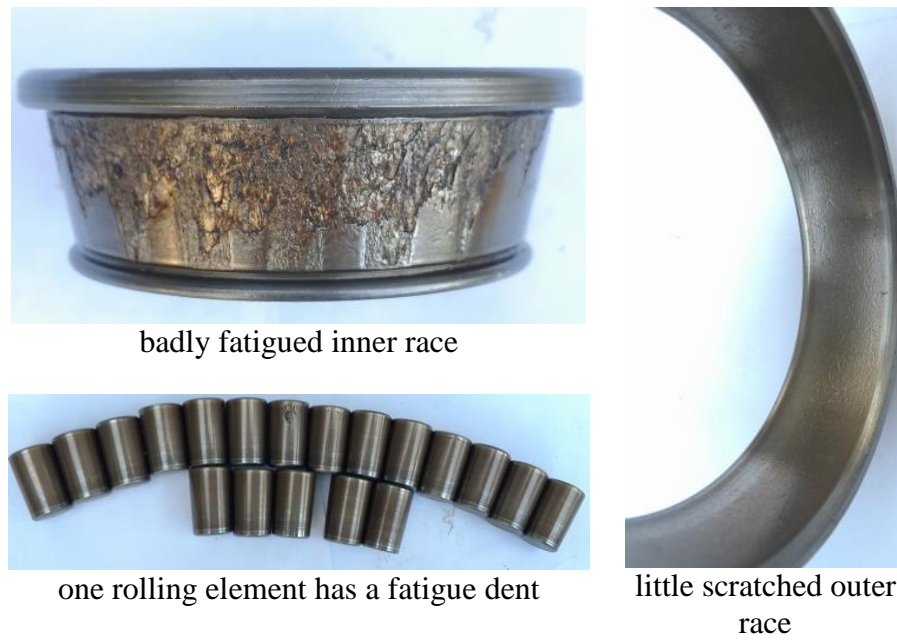
9.3.4 Signal Processing Results and Discussion

9.3.4.1 Online Results

Figure 9-7 shows the RMS and Kurtosis of the collected data, which were obtained online. The RMS values increase gradually for the initial 50 test time index then it increases rapidly as result of increse the surface fatigue which led to increase vibraion.
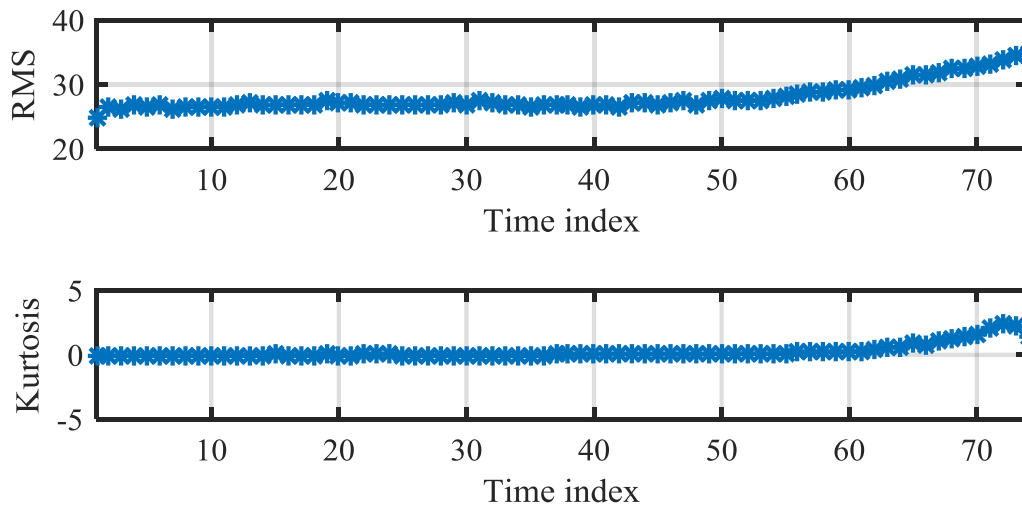

Figure 9-7 RMS and Kurtosis of the collected data

The kurtosis values increse gradually for the first 60 test time index then it increses rapidly up to 72 test time index after that it decreses as a result of the increse of the fatigue surface, at this time the test was stopped because the high levels of vibration. The offline inspection found that the bearing are damaged badly as show in Figure 9-6.

9.3.4.2 MSB and CB Results

To investigate the early signs of the bearing defects and evaluate the performance of two bisspctra analysis, vibration signal processing procedure is illustrated in Figure 9-8. Firstly, it calculates the envelope of vibration signal. Then, CB and MSB analysis are carried out to enhance the nonlinear components in the envelope signal. The next step is extracting features using the first component from the diagonal slice of CB results and that of the sub-diagonal slices of MSB results. Finally, the fault type and severity are examined using the features.
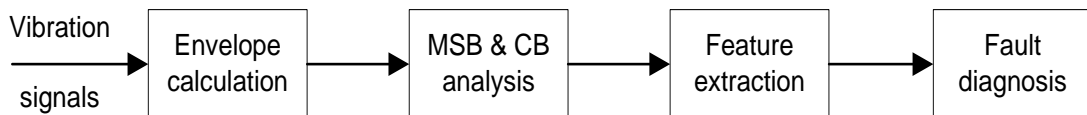

Figure 9-8 Signal processing procedure

MSB and CB of the bearing vibration signal of test time index 1 are illustrated in Figure 9-9. It shows that the bearing has faults on both inner race and cage at beginning of the test. For the inner race the magnitude of inner race fault frequency f_i as well as the both sidebands are clearly visible using MSB and nothing can be seen from CB. For the cage defect the second harmonic of the cage frequency $2*f_c$ is clearly visible from both MSB and CB and CB produces higher magnitude than MSB. Figure 9-10 shows the MSB and CB of bearing vibration data of test time indices 74. It can be seen that the increase magnitude of inner race fault and cage fault compared with Figure 9-9 based on the MSB detector. Whilst, from the CB detector the magnitude of cage defect at the second harmonics remains almost the same compared with Figure 9-9. Moreover, the magnitude of inner race defect is high using CB detector. Therefore, the MSB has a good noise reduction performance and it can be used to identify the fault type more accurately.
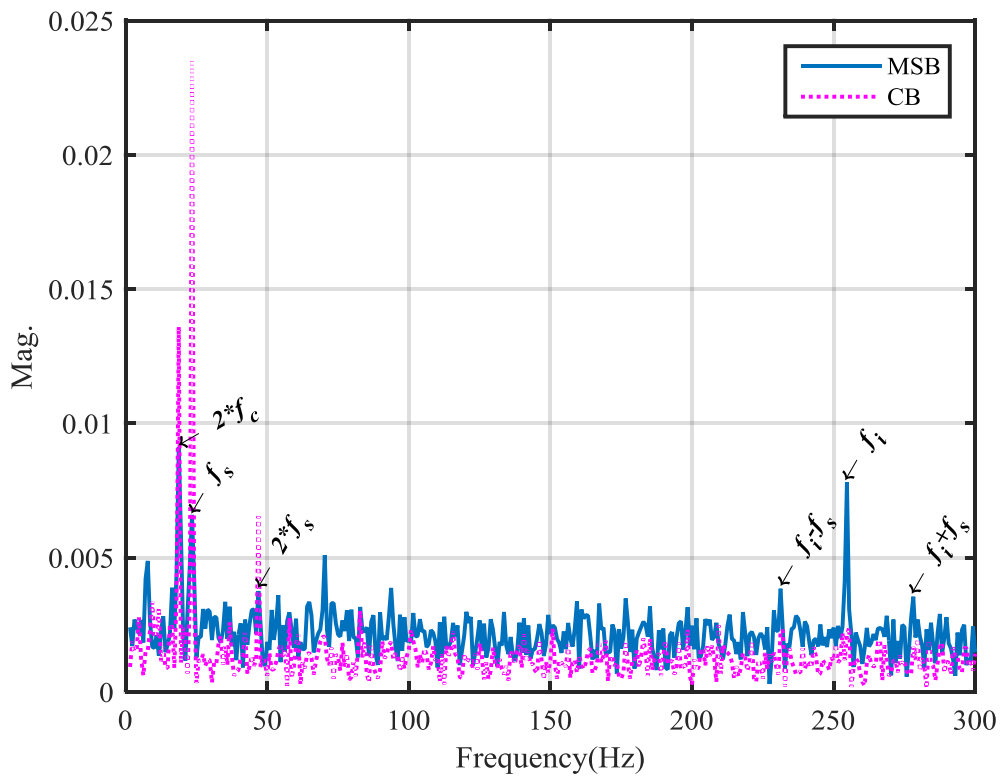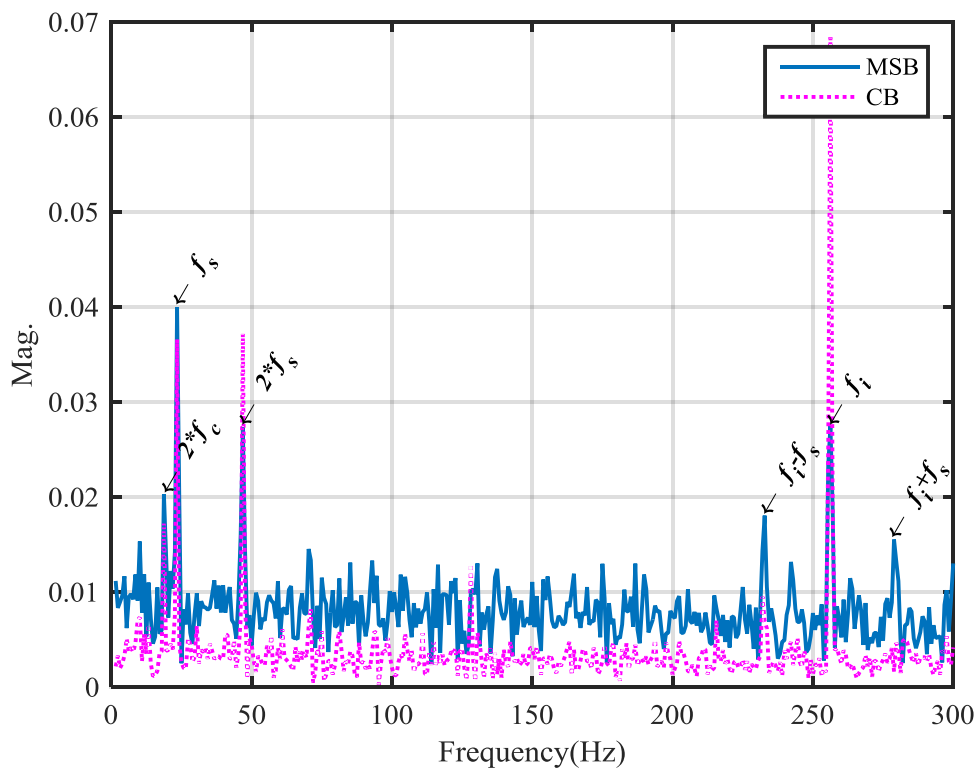
Figure 9-9 MSB and CB of the time index 1

Figure 9-10 MSB and CB of the time index 74

9.4   The Enhancement of the Deep Grove Ball Bearing Vibration Signal

The proposed method is used to enhance the vibration signal of deep groove ball bearing when it is subjected to different internal radial clearance and different radial loads achieved in Chapter eight in Section 8.4.

Figure 9-11 shows representative results of bispectra and corresponding bicoherences for the vibration signals of CN bearing with 0.2 mm inner race fault case under four different radial loads of 0, 0.8, 1.6 and 2.4 kN (for other bearing cases see Appendix C Section C1). The four graphs in the first row of Figure 9-11 give out CB magnitude results while the four graphs in the second row illustrate corresponding CBc results. From the CB results, it can be seen that there is a distinct peak at the bifrequency $B_{MS}(f_i, f_i)$, which can be used to quantify the nonlinear characteristics between the harmonic components f_i, $2f_i$ and $3f_i$, corresponding to the envelope spectra. Moreover, a number of small peaks, which may arise from the shaft frequency as well as the high background noise are also shown in Figure 9-11.
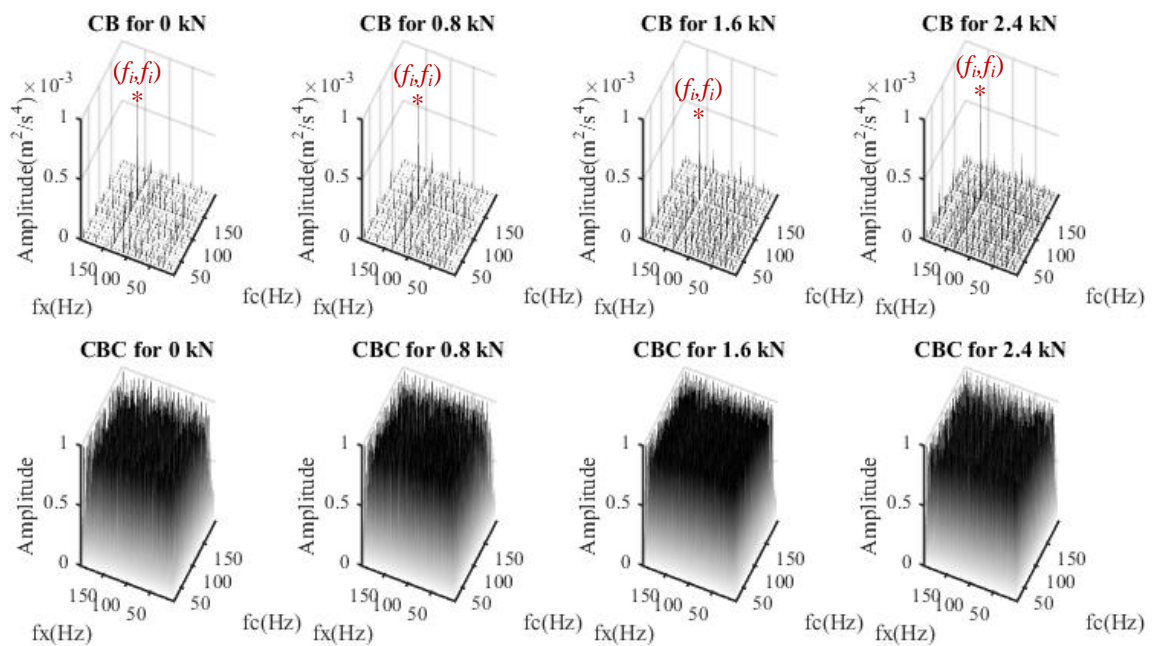

Figure 9-11 CB and CBc of 0.2mm inner race defect with CN clearance value under four different radial loads

Figure 9-12 shows representative results of MSB and MSBc for the vibration signals with 0.2 mm inner race fault case under four different radial loads as 0, 0.8, 1.6 and 2.4 kN

(for other bearing cases see Appendix C Section C2).. The four graphs in the first row of Figure 9-12 give out MSB magnitude results while the four graphs in the second row illustrate corresponding MSBc results. From the MSB results, it can be seen that there is a distinct peak at the bifrequency $B_{MS}(2f_i, f_i)$, which can be used to quantifying the nonlinear characteristics between the harmonic components f_i, $2f_i$ and $3f_i$, corresponding to the envelope spectra.
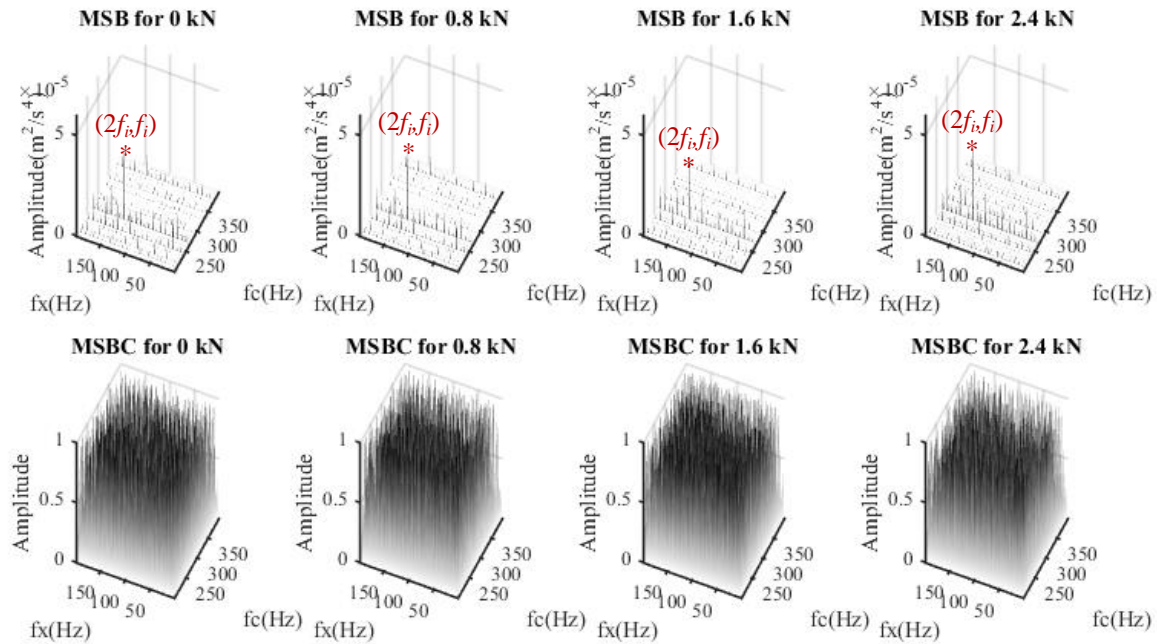
Figure 9-12 MSB and MSBc of 0.2mm inner race defect with CN clearance value under four different radial loads

It is assumed that the fault type is unknown in a signal measured. Therefore, feature values of each signal are calculated at all three potential fault frequencies predicted by Equations (3-2) to (3-4) as outer race f_o, inner race f_i and roller f_r. Then the fault type can be diagnosed by comparing between these three values and from a predefined threshold. Figure 9-13 shows the results of CB and CBc for all the tested signals. It can be seen in Figure 9-13 that the feature amplitudes for nearly all the cases are distinctively higher for the fault cases at the corresponding fault frequencies of the CB, compared with that of fault-free cases, allowing the fault types to be easily determined. Moreover, the corresponding conventional bicoherence amplitude is very high which means that the CB results are extremely reliable and it can be used for bearing fault detection and diagnosis.
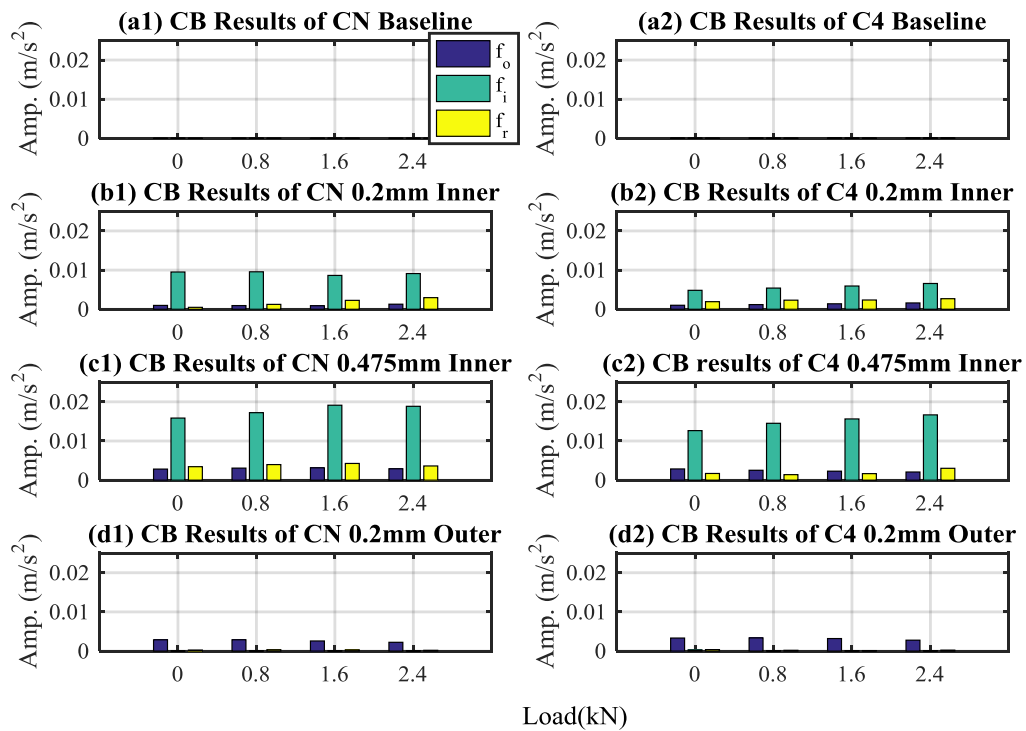
(a) CB Results
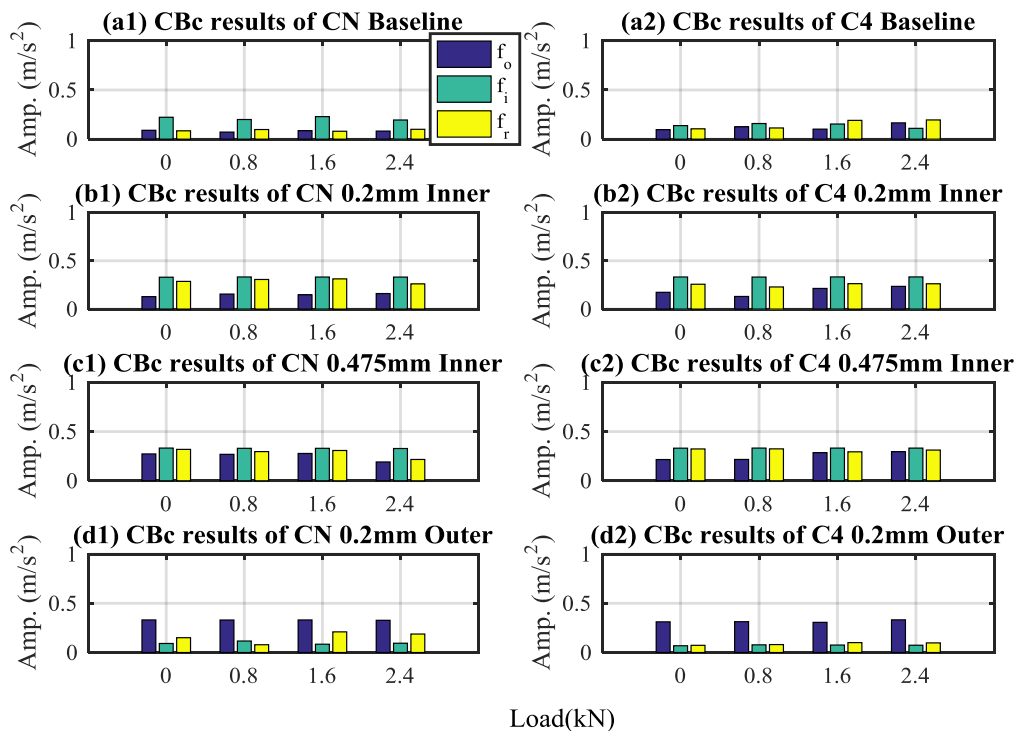
(b) CBc Results

Figure 9-13 Fault diagnosis results of (a) CB and (b) CBc of the bearing vibration signals

(a) MSB Results

(b) MSBc Results

Figure 9-14 Fault diagnosis results of (a) MSB and (b) MSBc of the bearing vibration signals

Figure 9-14 shows the results of MSB detector for all the tested signals. It can be seen in Figure 9-14 that the feature amplitudes for 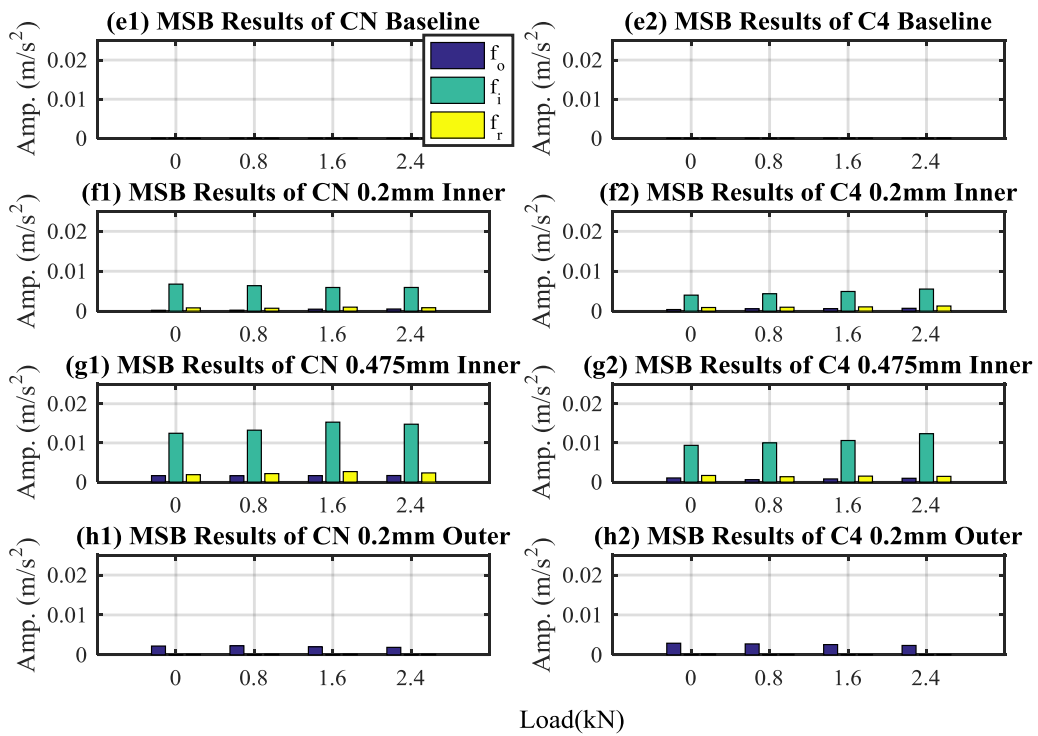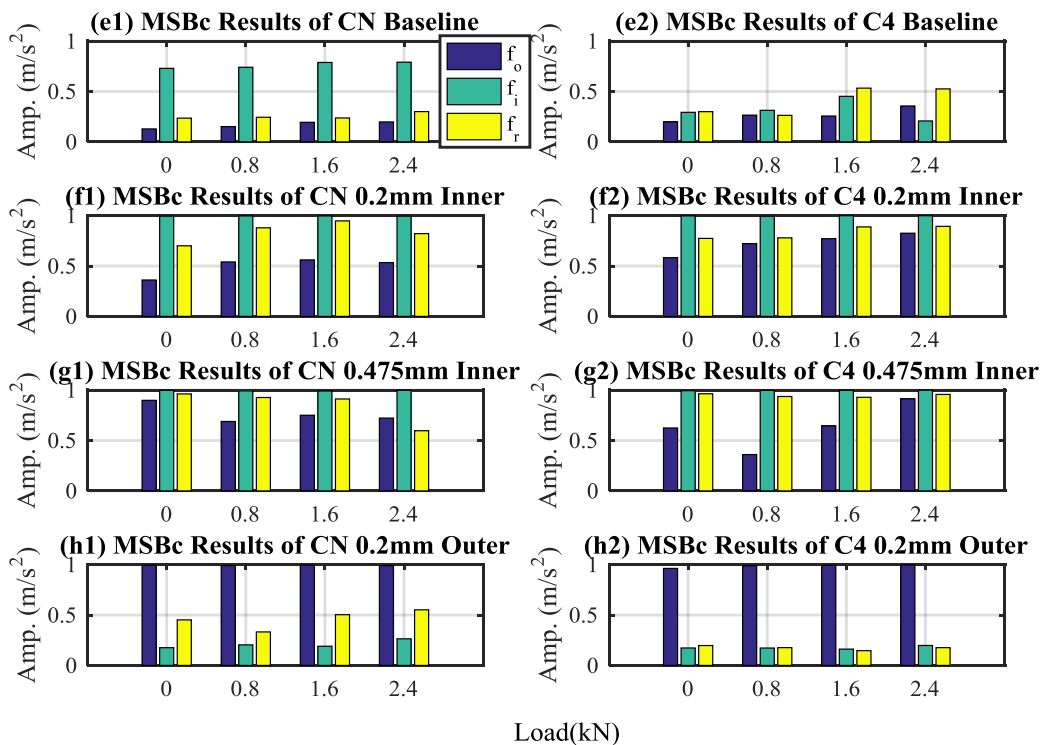nearly all the cases are distinctively higher for the fault cases at the corresponding fault frequencies of MSB, compared with that fault-free cases, allowing the fault types to be determined straightforwardly. In the meantime, it shows that random noise and non-relevant interferences are reduced effectively by MSB analysis. As a result, MSB analysis produces a result that has no confusion in differentiating different types of faults and it can produce better severity estimation. Furthermore, the corresponding conventional bicoherence amplitude is very high which means that the MSB results are very reliable and it can be used for bearing fault detection and diagnosis.
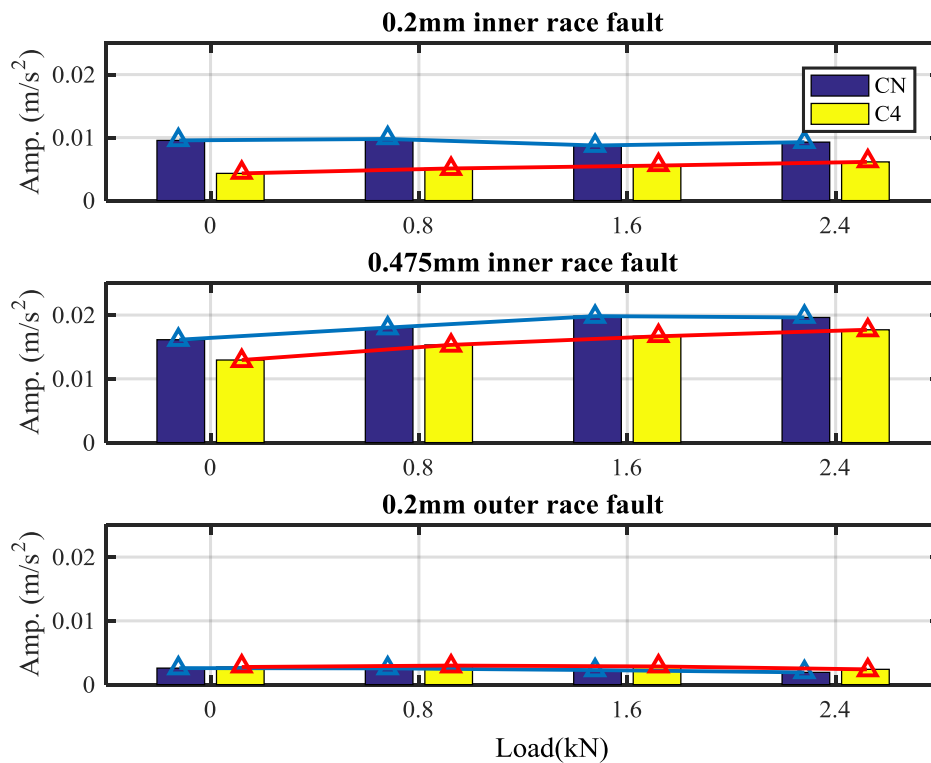
Figure 9-15 CB vibration amplitude of CN and C4 bearings

To study the influence of clearance, the fault features extracted from CB and MSB results of faulty bearing vibrations with two different clearance grades under four different radial loads from 0 kN to 2.4 kN are illustrated in Figure 9-15 and Figure 9-16, respectively. As expected, the fault frequency amplitude increases with the growth of radial clearance for the outer race defect. However, the amplitude exhibits a decrease for the inner race defect. This decrease is due to the changes in load zone angles. In addition, the outer race

fault frequency exhibits lower amplitude compared with the same size of inner race defect, which is caused by the geometric deformation. Moreover, the fault frequency amplitude of both CB and MSB are more stable in terms of radial load change than envelope spectrum, as described in Section 8.4 in Chapter seven, and it generally increases of with radial load increase
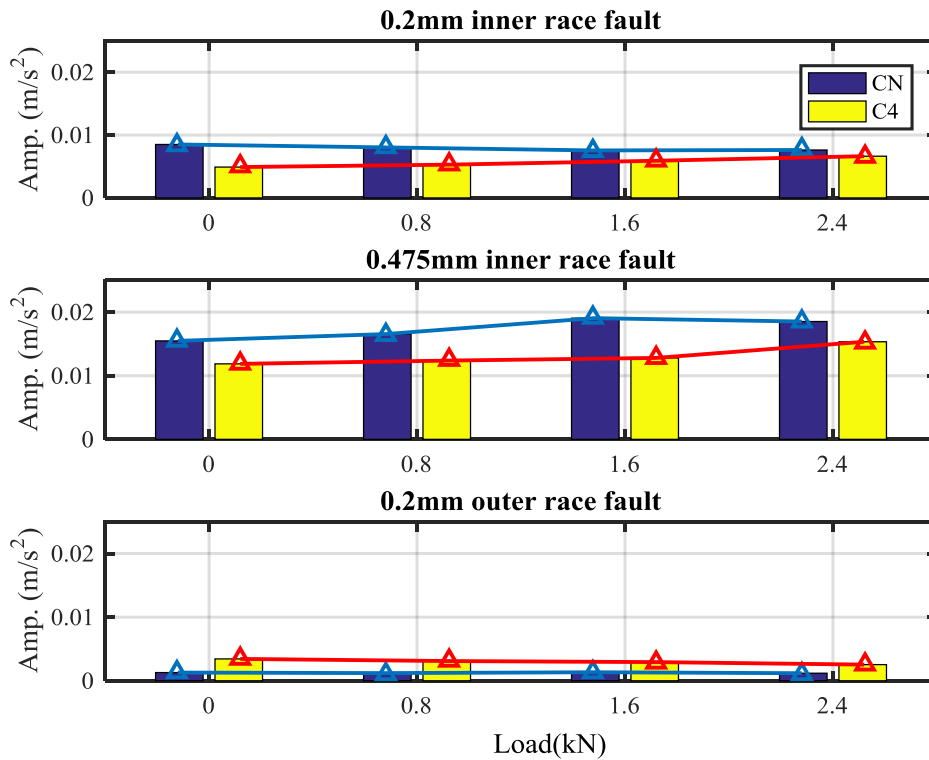
Figure 9-16 MSB vibration amplitude of CN and C4 bearings

From the results and discussion above, it can be concluded that MSB analysis have better performance than CB in both fault type diagnosis and severity estimation.

9.5   Summary

In this Chapter, a new method has been proposed by joining higher order spectra to envelope analysis, to enhance the nonlinear components in the envelope signal for more accurate and reliable results. The performance of the proposed method was accurately estimated using two case studies, a simulated time signal where spectral contents is known and vibration signal of tapered roller bearing fatigue test (Section 9.3). In addition, the first component from the diagonal slice of conventional bispectrum results and that of

the sub-diagonal slices of modulation signal bispectrum results are taken as the diagnostic features considering effective inclusion of information and easy of computations.

The proposed method was then used to enhance the deep grove ball bearing vibration signal when it was subject to different internal radial clearances and different radial loads to obtain reliable detection and diagnosis results. It is found that, as the internal clearance increase the amplitude of outer-race fault increase, but it decreases the amplitude of inner-race defect. Moreover, as the radial load becomes large the fault frequency amplitude increases, which verifies the concepts of Hertzian deformation theory.

CHAPTER TEN

CONCLUSIONS AND FUTURE WORK

This chapter presents a review of the project achievements in light of the original objectives. It begins by summarising each key research achievement individually in relation to the objectives presented in Chapter one. The novel elements are then summarised, and the contributions to knowledge that have been made by this research are then described. Finally, conclusions on the condition monitoring of rolling element bearings using vibration analysis, and recommendations for future work have been addressed.

10.1 Review of the Aim, Objectives and Achievements

This Chapter describes the main achievements and contributions to knowledge generated by this research work. This research aim was to study the influence of internal radial clearance on the vibration signal of rolling element bearings, particularly where the clearance is increased due to inevitable wear and bearing radial clearance grades. A nonlinear dynamic model was developed, and experimental studies were carried out to characterise the vibration signal characteristics of a rolling element bearing. A suite of signal processing methods were employed to investigate the effect of localised defects in the internal radial clearance.

The main aim of this research was:

To investigate bearing dynamics and develop a nonlinear dynamic model and advanced data analysis techniques for accurate and reliable fault severity diagnosis in bearing faults under a range of clearance grades due to inevitable wear.

The main objectives of this thesis and the corresponding key achievements are detailed below.

Objective 1: To research and describe machine condition monitoring techniques used for fault detection and diagnosis in rolling element bearings.

Achievement 1: The concept of condition monitoring and its relationship with predictive maintenance (condition-based maintenance) are defined and discussed in Section 1.1 and Section 1.2, along with the advantages of bearing condition monitoring techniques. Moreover, Chapter one describes the process of vibration measurement, as this is the most reliable method for machine condition monitoring, detection and diagnosis. It has been used in industry and is the technique used for rolling element bearings in this research project.

Objective 2: To carry out a comprehensive literature review covering the most commonly used vibration analysis techniques. This is to include fault detection methods for simple/premature rolling element bearings, such as (i) time domain, (ii) frequency domain and (iii) envelope analysis, (iv) kurtogram based short time Fourier transform, as well as advanced signal processing techniques such as higher order spectra.

Achievement 2: Relevant techniques for condition monitoring of rolling element bearing are primarily introduced and discussed in Section 1.4 to assist in the understanding of results presented in the subsequent Chapters. Vibration signals originating from rolling element bearings were expected to be nonlinear and non-stationary. They were processed using traditional signal processing methods (time domain, frequency domain and envelope analysis) as well as more advanced signal processing methods such as higher order statistics. Comprehensive details of the reviewed condition monitoring techniques are presented in Chapter three.

Objective 3: To carry out an extensive literature review on topics related to the model based technique used for rolling element bearing.

Achievement 3: A literature review was conducted covering model-based methods for rolling element bearing fault detection and diagnosis. This is discussed in Section 1.4.3. The bearing model focuses on the bearing vibration response under different radial clearances.

Objective 4: To review the rolling element bearing fundamentals, theory, types, components, failure modes, friction and wear.

Achievement 4: Fundamental theory of rolling element bearings was expansively described in Sections 2.2, 2.3, 2.4, 2.5 and 2.6. This includes bearing theory, rolling element bearing type, components, mode of bearing failure, and friction and wear.

Objective 5: To review several conventional vibration analysis techniques that could be applied to the detection and diagnosis of rolling element bearing faults.

Achievement 5: The vibration response in the case of bearing defects is explained in Section 3.2. This includes the dynamic response caused by bearing defects, characteristic frequencies of bearing faults, rolling element bearing vibration, amplitude modulation and resonant frequency. The most common condition monitoring techniques for rolling bearing fault detection and diagnosis were fully detailed in 3.4.2, 3.4.3and 3.4.4. These include time domain analysis, frequency domain analysis and envelope analysis respectively. In addition, Section 3.4.6 described the use of spectral kurtosis to optimise the bandpass filter parameters. Moreover, the higher order spectra were explained in

section 3.4.7, including power spectra, conventional bispectra, and modulation signal bispectra.

Objective 6: To develop an accurate dynamic nonlinear model that will provide a better understanding of the vibrations induced by rolling element bearing systems. Examine different fault types under different clearance values. Use this to characterise changes in the vibration signature arising from clearance increases, enabling more reliable diagnostic results.

Achievement 6: A five-degrees-of-freedom nonlinear dynamic model has been developed to predict vibration signal of a rolling element bearing subjected to localised defects and changes in internal radial clearance. The model represents the inner race-shaft, the outer race-housing and the sensor as a three masses, as described in Sections 4.2.1 and 4.2.2. The model accounts for the load deflection relationship (Hertzian contact). This arises from the nonlinear force between different bearing elements, the time-varying stiffness (load transmission dependency on the positioning of the supporting elements) and the clearance between the rolling elements and the bearing races, as detailed in Section 4.2.3.3. It also models the influence of defect size and location (see Section 4.2.4).

Objective 7: To evaluate and discuss the outputs of the nonlinear model using time domain analysis, frequency domain analysis and envelope analysis for three different bearing conditions under two different clearance values.

Achievement 7: A computer simulation program has been generated using MATLAB for the simulated model. Firstly the model parameters, including resonance frequencies and damping ratios, were calibrated using the state space method described in Section 5.2.1. Secondly the equations of motion (second order differential equations) are solved by converting each of which into two first order differential equations and using the ordinary differential equation solver (ode15s) to solve the first differential equation as described in Section 5.2.2. Two internal radial clearances and local defects of two sizes on the inner and outer raceways were used to study the model vibration response as described in Section 5.2.2.1. The effect of varying the radial load is also included a described in Section 5.2.2.2.

Objective 8: To design and build an appropriate bearing test rig facility in which to allow the localised faults to be introduced into rolling element bearings, enabling the subsequent system behaviour to be characterised.

Achievement 8: Two test rigs have been developed to examine the rolling element bearing vibration signal as detailed in Chapter six. The bearing test rig described in Section 6.2.1 was used to verify the nonlinear dynamic model for different bearing clearance grades under four different radial loads. The fault simulation and testing procedure is fully explained in Sections 6.3.1 and 6.4 respectively. The other test rig, described in Section 6.2.2, was used to test the motor bearing vibration signal using a kurtogram when subjected to localised defects and four different torque loads. Detail of the fault simulation and testing procedure is given in Sections 6.3.2 and 6.4 respectively. Full details about the test rig components and data acquisition software are also included in Chapter six.

Objective 9: To study the influence of the envelope analysis parameters on resulting vibration signal of the motor bearing based on fixed bandpass and optimal bandpass filters parameters.

Achievement 9: Two motor bearing faults under four different torque loads (0%, 25%, 50% and 75%) were studied to identify the performance of the optimal bandpass filter based on the kurtogram. Firstly, the vibration signals were processed to produce a time waveform signal and frequency domain analysis was applied as described in Sections 7.2.1 and 7.2.2 respectively. Envelope spectrum analysis was then applied to the vibration signals using a fixed bandpass filter designed based on the power spectrum. This is fully discussed in Section 7.2.3. In order to localise transients or hidden nonstationary signals, the short time Fourier transform was computed based on spectral kurtosis using different window lengths, as detailed in Section 7.2.4.1. The optimal bandpass filter was calculated using the kurtogram as described in Section 7.2.4.2 to enable more reliable fault detection and diagnosis.

Objective 10: To accurately evaluate the performance of the kurtogram and fast kurtogram based on a simulated impact signal.

Achievement 10: A simulated impact time signal with known spectral content, containing irregular noise pulses along with white background noise, was used to

accurately examine the capability of the kurtogram and fast kurtogram to capture the optimal bandpass filter parameters. More details are given in section 7.3.

Objective 11: to analyse and discuss the bearing vibration signals recorded from the accelerometer when the bearing is subjected to localised defects and varying clearance values using the time domain, frequency domain and envelope analysis.

Achievement 11: The vibration signals for four different bearing conditions (baseline, 0.2 mm inner race defect, 0.475 mm inner race defect, and 0.2 mm outer race defect) as well as two different clearance grades (CN and C4) were examined under four different radial loads (0, 0.8, 1.6 and 2.4 kN). It was found that the signal waveforms were very complex and a significant amount of information remained unknown. Different amplitudes were generated depending on the fault location and severity, as detailed in Section 8.3.1. Initially some statistical parameters (RMS, peak value and kurtosis) were extracted from the time waveform signals characterise the bearing vibration signal as discussed in Section 8.3.1. Frequency domain analysis is usually more reliable than time waveform analysis for fault detection and diagnosis in rotating machinery, but unfortunately it cannot be used for bearing vibration signals as the signal is masked by high background noise (see Section 8.3.2). Nevertheless, envelope analysis is more reliable in identifying the bearing faults, as detailed in Section 8.4.

Objective 12: To accurately estimate the performance of higher order spectrum analysis (power spectrum, conventional bispectrum and modulation signal bispectrum) based on the statistical significance of the estimated spectra when combined with envelope analysis for different bearing conditions.

Achievement 12: Two case studies were used to accurately estimate the performance of the higher order spectrum analysis when combined with envelope analysis: (i) a simulated time signal with white background noise was used to estimate the higher order spectrum amplitude using Mote Carlo estimation as described in Section 9.3.2; (ii) the vibration signal of a tapered roller bearing fatigue test was analysed using the aforementioned methods described in Section 9.3.3.

Objective 13: To apply the higher order spectrum analysis techniques to the envelopes of bearing vibration signals when the bearings are subjected to the different clearance values.

Achievement 13: The envelope signals for four different bearing conditions (baseline, 0.2 mm inner race defect, 0.475 mm inner race defect, and 0.2 mm outer race defect) as well as for two different clearance grades (CN and C4), and under four different radial loads (0, 0.8, 1.6 and 2.4 kN) were examined using combined envelope analysis with the conventional bispectrum and the modulation signal bispectrum, as described in Section 9.4.

10.2 Conclusions

This study has enabled a number of key conclusions to be drawn. These fall broadly in the areas of (i) envelope analysis, (ii) radial clearance simulations, and (iii) radial clearance measurements. The main conclusions under each of these areas will be described in the following sub-sections.

10.2.1 The Optimal and Accurate Envelope Analysis

In this research, an optimal bandpass filter technique has been examined by combining spectral kurtosis with envelope analysis for fault detection and diagnosis in deep groove ball bearings.

1- Three bearings conditions (baseline/healthy bearing, an inner-race fault, and an outer-race fault) were used to detect and diagnose the bearing faults. Vibration signals obtained from the aforementioned bearings were processed and analysed via time domain, frequency domain and envelope spectrum approaches. The time domain parameters included the RMS, peak value and kurtosis. These statistics provided limited information about the vibration signals. The frequency domain highlights significant frequency content that may be associated with the characteristic frequencies of specific bearing defects. The envelope spectrum of the filtered data presents a clear indication of the bearing faults.

2- The optimal filter is used to select signal frequency bands with high SNR. The filter parameters (band width and central frequency) are optimised by a maximal spectral kurtosis criterion. The filtered vibration signal is then analysed using envelope analysis to extract fault features. The effectiveness of the proposed method has been evaluated by comparison with experimental data sets from two types of faults. The diagnostic results show that the types of fault can be identified correctly.

3- The performance of the kurtogram and fast kurtogram has been examined using a simulated impact signal composed of white background noise and irregular pulses. It was found that the STFT-based kurtogram is more effective at identifying periodic components due to bearing faults, and is less influenced by irregular noise pulses than the wavelet based fast kurtogram. This is because STFT can suppress the noise to a certain degree.

10.2.2 The Influence of Internal Radial Clearance on Deep Groove Ball Bearings

10.2.2.1 Simulation Results of the Nonlinear Dynamic Model

In this study, a dynamic model for deep groove ball bearings was developed, which can account for the effect of internal radial clearance on localised defects of the inner and outer races. The proposed model can be used to obtain the vibration responses for accurate bearing diagnosis.

1- Five degrees of freedom (DOF) were studied: vibration of the shaft, housing in the X and Y directions, and the sensor in X direction. The number of DOFs was selected as the optimum choice in terms of both accuracy and complexity. This resulted in a model structure that is sufficiently accurate to reflect the diagnostic features comprehensively, whilst being computationally efficient.

2- The modal parameters, including resonance frequencies and damping ratios, have been conveniently identified using the standard eigen method.

3- The governing equations of motion are second order nonlinear differential equations, each of which has been converted into two first order differential equations. The ordinary differential equation solver (ode15s) has then been used to solve the first differential equation set in the MATLAB environment

4- The simulation study has shown that the overall vibration response increases with increased internal radial clearance. This occurs due to inevitable wear during the bearing's service life.

5- Based on the envelope spectrum analysis for an outer-race defect, it was determined that the larger the radial clearance, the higher the amplitude of the diagnostic feature. In addition, a defect at the loading zone produced a higher amplitude. In contrast to the outer-race defect, an inner-race defect caused only a subtle reduction in the observed amplitude for the diagnostic feature for the large clearance bearing.

6- The study also proved that, for the same defect size, the feature amplitudes for the inner-race defects were larger than those of the outer-race defects.

10.2.2.2 Experimental Validation of Results

In this research the effect of internal radial clearance, which inevitably grows due to wear over the bearing service period, has been studied to enable the accurate detection and diagnosis of roller bearings faults.

1. Two fault locations on the inner race and outer race, under two grades of internal clearance, have been used to detect and diagnose bearing faults. Vibration signals obtained from the studied bearings were processed and analysed through the time domain, frequency domain and envelope spectrum. The time domain parameters included the RMS value, peak value and kurtosis. These can provide limited information about the vibration signals, which can be relied on to predict the change of bearing clearance value. The frequency domain highlights significant frequency components that may be associated with the characteristic frequencies of bearing defects. Envelope analysis is a very reliable method to detect bearing faults. It can provide a clear identification of the bearing fault frequencies. Consequently, for the inner race defect, the fault frequency amplitude drops slightly with increasing clearance for the first three harmonics. For the outer race defect, the fault frequency amplitude increases slightly with increasing clearance. This is due to the change of load zone angle. Moreover, as the radial loads become large, the vibration signal amplitude was expected to increase as a result of a rise in the nonlinear deformation. This is not very clearly achieved due to the influence of the background noise

2. A new method has been developed by combining the higher order spectra with envelope analysis to allow significant suppression of noise content in the envelope signal, leading to more accurate diagnostic features.

3. The higher order spectra based noise suppression method was developed to refine the envelope signals so that the irregular impulsive and stationary noise are minimised. This enables more accurate and robust detection results.

   The performance of higher order spectrum analysis has been accurately estimated in two selected case studies: (i) a simulated time signal where spectral contents are known, and then the higher order spectrum amplitude is estimated using a Monte

Carlo estimator. (ii) the vibration signal of a tapered roller bearing during a fatigue test was analysed using the aforementioned methods.

Monte Carlo tests show that the MSB features exhibit less deviation and lower variation between different tests compared with that of PS and CB. This shows that MSB performs better in extracting the diagnostic information, as its first component combines the first three harmonics in the original spectrum. It also has a higher SNR compared with CB and PS, which includes only the first two harmonics. As a result, MSB provides more sensitive detection of the incipient faults occurring in the tapered roller bearing of the gearbox.

4. To obtain reliable detection and diagnosis results for deep groove ball bearing vibration signals, MSB and CB were applied to supress the random noise and extract the harmonic features from the envelope signals more accurately. From the signal processing results, it can be seen that MSB has better noise reduction performance compared with CB. Moreover, it can be concluded that the fault frequency amplitudes not only change with the fault severity but also with the change in radial clearance. This is a result of the load zone angle change, which validates the model results. Therefore, during the diagnosis of bearing fault severity, it is necessary to take into account the bearing service duration and bearing clearance grades.

10.3 Novelties and Contribution to Knowledge

The main aspects of novelty that have been demonstrated during the research project and within this report are summarised in this section. They are focussed on the phenomena being researched, methodologies used and results obtained.

Novelty One:

Rolling bearings encounter various types of wear during their lifetime, which can lead to large radial clearances and high vibration levels. The changes in clearance have been proven in this thesis to significantly affect the fault diagnosis. For the first time, this thesis has addressed the issue comprehensively.

Novelty Two:

The author believes that the nonlinear dynamic model and the method for calculating the

vibration responses under different radial clearances to be effective and novel.

Novelty Three:

A new method has been developed by combining the conventional bispectrum and modulation bispectrum with envelope analysis for noise and interference suppression. This enables more accurate detection and diagnosis of roller bearings faults. The innovative method has not been used before in the field of advancing monitoring, diagnosis, prognosis, and health management.

Novelty Four:

Both the simulation and the experimental study showed that the overall vibration levels increased with increasing internal radial clearances, which occurs due to inevitable wear during a bearing's service life. Based on the signal processing results for an outer-race defect, it was determined that the larger the radial clearance, the higher the amplitude of the diagnostic feature. In contrast to the changes of outer-race defect, a fault on the inner-race causes a reduction in the observed amplitude of the diagnostic feature for larger clearances. This is particularly novel in terms of both the findings and the methodologies employed reach them.

10.4 Recommendations for Future Work on Rolling Element Bearing Fault Detection and Diagnosis

Recommendation 1:

The mass of the rolling elements needs to be included in the nonlinear dynamic model to make the model more comprehensive.

Recommendation 2:

The influence of (i) the moment of inertia, (ii) centrifugal force and (iii) damping due to the lubricant film needs to be included in the nonlinear model.

Recommendation 3:

The effect of slippage and skidding needs to be included in the nonlinear dynamic model to enable study of the influence of the frequency change, especially when radial clearances change.

Recommendation 4:

Fatigue tests should be conducted to quantify the typical wear ratio and normal changes in internal clearance.

REFERENCES

1.   Rai, A. and S.H. Upadhyay, *A review on signal processing techniques utilized in the fault diagnosis of rolling element bearings.* Tribology International, 2016. **96**: p. 289-306.

2.   Han, Y. and Y.H. Song, *Condition monitoring techniques for electrical equipment- a literature survey.* Power Delivery, IEEE Transactions on, 2003. **18**(1): p. 4-13.

3.   J.H. Williams, A.D., P.R. Drake, *Condition-based maintenance and machine diagnostics*. 1994: Chapman & Hall, 2-6 Boundary Row, London Se1 8HN, UK.

4.   Davies, A., *Handbook of condition monitoring 'technique and methodology'*. 1st ed. 1998: chapman & Hall, an imprint of Thomsin science, 2-6 Boundary Row, London SE1 8HN, UK.

5.   Jardine, A.K.S., D. Lin, and D. Banjevic, *A review on machinery diagnostics and prognostics implementing condition-based maintenance.* Mechanical Systems and Signal Processing, 2006. **20**(7): p. 1483-1510.

6.   Brändlein, J., *Ball and roller bearings: theory, design, and application*. 3rd ed. 1999: Chichester : Wiley. 630.

7.   Vachtsevanos, G.J., *Intelligent fault diagnosis and prognosis for engineering systems*. 2006, Hoboken, N.J.: John Wiley & Sons.

8.   Randall, R.B., *Vibration-Based Condition Monitoring : Industrial, Automotive and Aerospace Applications*. 2010, Hoboken, NJ, USA: Wiley.

9.   Kim, Y.-H., et al., *Condition Monitoring of Low Speed Bearings: A Comparative Study of the Ultrasound Technique Versus Vibration Measurements*, in *Engineering Asset Management*, J. Mathew, et al., Editors. 2006, Springer London. p. 182-191.

10.   Meyer, L., F. Ahlgren, and B. Weichbrodt, *An analytic model for ball bearing vibrations to predict vibration response to distributed defects.* Journal of Mechanical Design, 1980. **102**(2): p. 205-210.

11. McFadden, P. and J. Smith, *Model for the vibration produced by a single point defect in a rolling element bearing.* Journal of Sound and Vibration, 1984. **96**(1): p. 69-82.

12. Patil, M., et al., *A theoretical model to predict the effect of localized defect on vibrations associated with ball bearing.* International Journal of Mechanical Sciences, 2010. **52**(9): p. 1193-1201.

13. Patel, V., N. Tandon, and R. Pandey, *A dynamic model for vibration studies of deep groove ball bearings considering single and multiple defects in races.* Journal of Tribology, 2010. **132**(4): p. 041101.

14. Harris, T.A.K., Michael N., *Rolling bearing analysis : advanced concepts of bearing technology.* 2007, Boca Raton, FL: CRC/Taylor & Francis.

15. Tandon, N. and A. Choudhury, *A review of vibration and acoustic measurement methods for the detection of defects in rolling element bearings.* Tribology International, 1999. **32**(8): p. 469-480.

16. Proulx, T., *Rotating Machinery, Structural Health Monitoring, Shock and Vibration.* Vol. Volume 5. 2011: Society for Experimental Machanies, Inc, 7 School Street Bethel, CT 06801-1405, USA.

17. Samanta, B. and K. Al-Balushi, *Artificial neural network based fault diagnostics of rolling element bearings using time-domain features.* Mechanical systems and signal processing, 2003. **17**(2): p. 317-328.

18. McInerny, S.A. and Y. Dai, *Basic vibration signal processing for bearing fault detection.* Education, IEEE Transactions on, 2003. **46**(1): p. 149-156.

19. Xu, P. and A.K. Chan. *Fast and robust neural network based wheel bearing fault detection with optimal wavelet features.* in *Neural Networks, 2002. IJCNN'02. Proceedings of the 2002 International Joint Conference on.* 2002. IEEE.

20. Williams, T., et al., *Rolling element bearing diagnostics in run-to-failure lifetime testing.* Mechanical Systems and Signal Processing, 2001. **15**(5): p. 979-993.

21. Ocak, H., K.A. Loparo, and F.M. Discenzo, *Online tracking of bearing wear using wavelet packet decomposition and probabilistic modeling: A method for bearing prognostics.* Journal of Sound and Vibration, 2007. **302**(4–5): p. 951-961.

22. Heng, R.B.W. and M.J.M. Nor, *Statistical analysis of sound and vibration signals for monitoring rolling element bearing condition.* Applied Acoustics, 1998. **53**(1–3): p. 211-226.

23.   Su, Y.T. and S.J. Lin, *On initial fault detection of a tapered roller bearing: Frequency domain analysis.* Journal of Sound and Vibration, 1992. **155**(1): p. 75-84.

24.   Yacamini, R. and S.C. Chang, *Noise and vibration from induction machines fed from harmonic sources.* Energy Conversion, IEEE Transactions on, 1995. **10**(2): p. 286-292.

25.   Stack, J.R., R.G. Harley, and T.G. Habetler, *An amplitude Modulation detector for fault diagnosis in rolling element bearings.* Industrial Electronics, IEEE Transactions on, 2004. **51**(5): p. 1097-1102.

26.   Stack, J.R., T.G. Habetler, and R.G. Harley. *Fault classification and fault signature production for rolling element bearings in electric machines*. in *Diagnostics for Electric Machines, Power Electronics and Drives, 2003. SDEMPED 2003. 4th IEEE International Symposium on*. 2003.

27.   Barber, A., *handbook of noise and vibration control*. 6th ed. 1992: Oxford : Elsevier Advanced Technology.

28.   Li, B., G. Goddu, and M.-Y. Chow. *Detection of common motor bearing faults using frequency-domain vibration signals and a neural network based approach*. in *American Control Conference, 1998. Proceedings of the 1998*. 1998. IEEE.

29.   Goddu, G., et al. *Motor bearing fault diagnosis by a fundamental frequency amplitude based fuzzy decision system*. in *Industrial Electronics Society, 1998. IECON'98. Proceedings of the 24th Annual Conference of the IEEE*. 1998. IEEE.

30.   Li, B., et al., *Neural-network-based motor rolling bearing fault diagnosis.* Industrial Electronics, IEEE Transactions on, 2000. **47**(5): p. 1060-1069.

31.   Wang, C. and R.X. Gao, *A virtual instrumentation system for integrated bearing condition monitoring.* Instrumentation and Measurement, IEEE Transactions on, 2000. **49**(2): p. 325-332.

32.   Blair, J. and A. Shirkhodaie. *Diagnosis and prognosis of bearings using data mining and numerical visualization techniques*. in *System Theory, 2001. Proceedings of the 33rd Southeastern Symposium on*. 2001. IEEE.

33.   Sawalhi, N., R.B. Randall, and H. Endo, *The enhancement of fault detection and diagnosis in rolling element bearings using minimum entropy deconvolution combined with spectral kurtosis.* Mechanical Systems and Signal Processing, 2007. **21**(6): p. 2616-2633.

34. Molitor, M. and M. Moldzio. *Acoustic roller bearing diagnosis in a closed-loop quality control system.* in *Instrumentation and Measurement Technology Conference, 1996. IMTC-96. Conference Proceedings. Quality Measurements: The Indispensable Bridge between Theory and Reality., IEEE.* 1996. IEEE.

35. Cline, J.E., J.R. Bilodeau, and R.L. Smith. *Acoustic wayside identification of freight car roller bearing defects.* in *Railroad Conference, 1998. Proceedings of the 1998 ASME/IEEE Joint.* 1998. IEEE.

36. Peter, W.T., Y. Peng, and R. Yam, *Wavelet analysis and envelope detection for rolling element bearing fault diagnosis—their effectiveness and flexibilities.* Journal of vibration and acoustics, 2001. **123**(3): p. 303-310.

37. Yang, W.-X. and X.-M. Ren, *Detecting impulses in mechanical signals by wavelets.* EURASIP Journal on Applied Signal Processing, 2004. **2004**: p. 1156-1162.

38. Nikolaou, N. and I. Antoniadis, *Demodulation of vibration signals generated by defects in rolling element bearings using complex shifted Morlet wavelets.* Mechanical Systems and Signal Processing, 2002. **16**(4): p. 677-694.

39. Rubini, R. and U. Meneghetti, *Application of the envelope and wavelet transform analyses for the diagnosis of incipient faults in ball bearings.* Mechanical systems and signal processing, 2001. **15**(2): p. 287-302.

40. Ocak, H. and K.A. Loparo. *A new bearing fault detection and diagnosis scheme based on hidden Markov modeling of vibration signals.* in *Acoustics, Speech, and Signal Processing, 2001. Proceedings.(ICASSP'01). 2001 IEEE International Conference on.* 2001. IEEE.

41. Sawalhi, N. and R.B. Randall. *Spectral kurtosis optimization for rolling element bearings.* in *Signal Processing and Its Applications, 2005. Proceedings of the Eighth International Symposium on.* 2005.

42. Yu, D., J. Cheng, and Y. Yang, *Application of EMD method and Hilbert spectrum to the fault diagnosis of roller bearings.* Mechanical Systems and Signal Processing, 2005. **19**(2): p. 259-270.

43. Antoni, J. and R.B. Randall, *The spectral kurtosis: application to the vibratory surveillance and diagnostics of rotating machines.* Mechanical Systems and Signal Processing, 2006. **20**(2): p. 308-331.

44. Polikar, R. *Fundamental Concepts & an Overview of the Wavelet Theory.* 2006; Second:[

45.   Li, C.J. and J. Ma, *Wavelet decomposition of vibrations for detection of bearing-localized defects.* Ndt & E International, 1997. **30**(3): p. 143-149.

46.   Yen, G.G. and K.-C. Lin, *Wavelet packet feature extraction for vibration monitoring.* Industrial Electronics, IEEE Transactions on, 2000. **47**(3): p. 650-667.

47.   Staszewski, W.J., K. Worden, and G.R. Tomlinson, *TIME–FREQUENCY ANALYSIS IN GEARBOX FAULT DETECTION USING THE WIGNER–VILLE DISTRIBUTION AND PATTERN RECOGNITION.* Mechanical Systems and Signal Processing, 1997. **11**(5): p. 673-692.

48.   Padovese, L., *Hybrid time–frequency methods for non-stationary mechanical signal analysis.* Mechanical Systems and Signal Processing, 2004. **18**(5): p. 1047-1064.

49.   Allen, J.C. *Advanced beamforming concepts: source localization using the bispectrum, Gabor transform, Wigner-Ville distribution, and nonstationary signal representations*. in *Signals, Systems and Computers, 1991. 1991 Conference Record of the Twenty-Fifth Asilomar Conference on*. 1991. IEEE.

50.   Chen, P., M. Taniguchi, and T. Toyota. *Intelligent diagnosis method of multi-fault state for plant machinery using wavelet analysis, genetic programming and possibility theory*. in *Robotics and Automation, 2003. Proceedings. ICRA'03. IEEE International Conference on*. 2003. IEEE.

51.   Altmann, J. and J. Mathew, *Multiple band-pass autoregressive demodulation for rolling-element bearing fault diagnosis.* Mechanical systems and signal processing, 2001. **15**(5): p. 963-977.

52.   Lin, J. and L. Qu, *Feature extraction based on Morlet wavelet and its application for mechanical fault diagnosis.* Journal of sound and vibration, 2000. **234**(1): p. 135-148.

53.   Lin, J., M.J. Zuo, and K.R. Fyfe, *Mechanical fault detection based on the wavelet de-noising technique.* Journal of vibration and acoustics, 2004. **126**(1): p. 9-16.

54.   Vafaei, S. and H. Rahnejat, *Indicated repeatable runout with wavelet decomposition (IRR-WD) for effective determination of bearing-induced vibration.* Journal of sound and vibration, 2003. **260**(1): p. 67-82.

55.   Pineyro, J., A. Klempnow, and V. Lescano, *Effectiveness of new spectral tools in the anomaly detection of rolling element bearings.* Journal of alloys and compounds, 2000. **310**(1): p. 276-279.

56. Vachtsevanos, G. and P. Wang. *Fault prognosis using dynamic wavelet neural networks*. in *AUTOTESTCON Proceedings, 2001. IEEE Systems Readiness Technology Conference*. 2001. IEEE.

57. Sun, Q. and Y. Tang, *Singularity analysis using continuous wavelet transform for bearing fault diagnosis.* Mechanical systems and signal processing, 2002. **16**(6): p. 1025-1041.

58. Immovilli, F., et al., *Detection of Generalized-Roughness Bearing Fault by Spectral-Kurtosis Energy of Vibration or Current Signals.* Industrial Electronics, IEEE Transactions on, 2009. **56**(11): p. 4710-4717.

59. Antoni, J., *The spectral kurtosis: a useful tool for characterising non-stationary signals.* Mechanical Systems and Signal Processing, 2006. **20**(2): p. 282-307.

60. Zhang, Y. and R.B. Randall, *Rolling element bearing fault diagnosis based on the combination of genetic algorithms and fast kurtogram.* Mechanical Systems and Signal Processing, 2009. **23**(5): p. 1509-1517.

61. Antoni, J., *Fast computation of the kurtogram for the detection of transient faults.* Mechanical Systems and Signal Processing, 2007. **21**(1): p. 108-124.

62. Alwodai, A., et al., *A Study of Motor Bearing Fault Diagnosis using Modulation Signal Bispectrum Analysis of Motor Current Signals.* Journal of Signal and Information Processing, 2013. **4**: p. 72.

63. Barszcz, T. and A. JabŁoński, *A novel method for the optimal band selection for vibration signal demodulation and comparison with the Kurtogram.* Mechanical Systems and Signal Processing, 2011. **25**(1): p. 431-451.

64. Wang, Y. and M. Liang, *An adaptive SK technique and its application for fault detection of rolling element bearings.* Mechanical Systems and Signal Processing, 2011. **25**(5): p. 1750-1764.

65. Huang, F. and S. Gu. *Application of higher order cumulants to structure fault diagnosis*. in *the 11 th International Modal Analysis Conference*. 1993.

66. Gelle, G., M. Colas, and G. Delaunay. *Higher order statistics for detection and classification of faulty fanbelts using acoustical analysis*. in *Higher-Order Statistics, 1997., Proceedings of the IEEE Signal Processing Workshop on*. 1997. IEEE.

67. Howard, I., *Higher-order spectral techniques for machine vibration condition monitoring.* Proceedings of the Institution of Mechanical Engineers, Part G: Journal of Aerospace Engineering, 1997. **211**(4): p. 211-219.

68. Arthur, N. and J. Penman, *Induction machine condition monitoring with higher order spectra.* Industrial Electronics, IEEE Transactions on, 2000. **47**(5): p. 1031-1041.

69. McCormick, A.C. and A.K. Nandi, *Bispectral and trispectral features for machine condition diagnosis.* Vision, Image and Signal Processing, IEE Proceedings -, 1999. **146**(5): p. 229-234.

70. McCormick, A. and A.K. Nandi, *Bispectral and trispectral features for machine condition diagnosis.* IEE Proceedings-Vision, Image and Signal Processing, 1999. **146**(5): p. 229-234.

71. Li, C.J., J. Ma, and B. Hwang, *Bearing localized defect detection by bicoherence analysis of vibrations.* Journal of Manufacturing Science and Engineering, 1995. **117**(4): p. 625-629.

72. Gu, F., et al., *Electrical motor current signal analysis using a modified bispectrum for fault diagnosis of downstream mechanical equipment.* Mechanical Systems and Signal Processing, 2011. **25**(1): p. 360-372.

73. Alwodai, A., F. Gu, and A. Ball. *A comparison of different techniques for induction motor rotor fault diagnosis.* in *Journal of Physics: Conference Series.* 2012. IOP Publishing.

74. Alwodai, A., et al., *A Study of Motor Bearing Fault Diagnosis using Modulation Signal Bispectrum Analysis of Motor Current Signals.* Journal of Signal and Information Processing, 2013. **4**(03): p. 72.

75. Haram, M., et al. *An Investigation of the electrical response of a variable speed motor drive for mechanical fault diagnosis.* 2011. COMADEM.

76. Rehab, I., et al., *The fault detection and severity diagnosis of rolling element bearings using modulation signal bispectrum.* 2014.

77. Tian, X., et al. *Diagnosis of combination faults in a planetary gearbox using a modulation signal bispectrum based sideband estimator.* in *Automation and Computing (ICAC), 2015 21st International Conference on.* 2015. IEEE.

78. Tian, X., et al., *A robust fault detection method of rolling bearings using modulation signal bispectrum analysis*, in *28th International Congress of Condition Monitoring and Diagnostic Engineering Management (COMADEM 2015).* 2015: Buenos Aires, Argentina p. 1-7.

79. Purohit, R. and K. Purohit, *Dynamic analysis of ball bearings with effect of preload and number of balls.* International journal of applied mechanics and engineering, 2006. **11**(1): p. 77-91.

80. Culita, J., D. Stefanoiu, and F. Ionescu, *Simulation models of defect encoding vibrations.* Journal of Control Engineering and Applied Informatics, 2007. **9**(2): p. 59-67.

81. Sassi, S., B. Badri, and M. Thomas, *A numerical model to predict damaged bearing vibrations.* Journal of Vibration and Control, 2007. **13**(11): p. 1603-1628.

82. Upadhyay, S., S. Harsha, and S. Jain, *Analysis of nonlinear phenomena in high speed ball bearings due to radial clearance and unbalanced rotor effects.* Journal of Vibration and Control, 2010. **16**(1): p. 65-88.

83. Patil, M.S., et al., *A theoretical model to predict the effect of localized defect on vibrations associated with ball bearing.* International Journal of Mechanical Sciences, 2010. **52**(9): p. 1193-1201.

84. Dougdag, M., et al., *An experimental testing of a simplified model of a ball bearing: stiffness calculation and defect simulation.* Meccanica, 2012. **47**(2): p. 335-354.

85. Patel, V.N., N. Tandon, and R.K. Pandey, *Vibration Studies of Dynamically Loaded Deep Groove Ball Bearings in Presence of Local Defects on Races.* Procedia Engineering, 2013. **64**(0): p. 1582-1591.

86. Halme, J. and P. Andersson, *Rolling contact fatigue and wear fundamentals for rolling bearing diagnostics-state of the art.* Proceedings of the Institution of Mechanical Engineers, Part J: Journal of Engineering Tribology, 2010. **224**(4): p. 377-393.

87. Hwang, S.Y., N.R. Lee, and N. Kim, *Experiment and Numerical Study of Wear in Cross Roller Thrust Bearings.* Lubricants, 2015. **3**(2): p. 447-458.

88. Khonsari, M.M. and E.R. Booser, *Applied tribology: bearing design and lubrication.* Vol. 12. 2008: John Wiley & Sons.

89. Harris, T.A. and M.N. Kotzalas, *Rolling Bearing Analysis, Fifth Edition - 2 Volume Set.* 2006: Taylor & Francis.

90. Oswald, F.B., E.V. Zaretsky, and J.V. Poplawski, *Effect of Internal Clearance on Load Distribution and Life of Radially Loaded Ball and Roller Bearings.* Tribology Transactions, 2012. **55**(2): p. 245-265.

91. Howard, I., *A Review of Rolling Element Bearing Vibration'Detection, Diagnosis and Prognosis'*. 1994, DTIC Document.

92. Kuhnell, B.T., *Wear in rolling element bearings and gears- How age and contamination affect them.* Machinery Lubrication, 2004: p. 62-64.

93. Shigley, J.E. and C.R. Mischke, *Mechanical Engineering Design*. 2003: McGraw-Hill.

94. Lundberg, G. and A. Palmgren, *Dynamic Capacity of Rolling Bearings*. 1947: Generalstabens Litografiska Anstalts Förl.

95. Weibull, W., *A Statistical Theory of the Strength of Materials*. 1939: Generalstabens litografiska anstalts förlag.

96. Zaretsky, E.V., J.V. Poplawski, and C. Miller, *Rolling bearing life prediction-past, present, and future.* 2000.

97. Zaretsky, E.V., J.V. Poplawski, and C. Miller, *Rolling Bearing Life Prediction: Past, Present, and Future*. Vol. 210529. 2000: National Aeronautics and Space Administration, Glenn Research Center.

98. Mobley, R.K., *An Introduction To Predictive Maintenance*. Second ed. 2002: Library of Congress Cataloging-. 459.

99. Hindhede, U., *Machine design fundamentals : a practical approach*. 1983, New York [etc.]: John Wiley & Sons.

100. Peter Tavner, L.R., Jim Penman and Howard Sedding, *Condition Monitoring of Rotating Electrical Machines*. 2008: London : Institution of Engineering and Technology.

101. SKF. *Bearing Installation and Maintenance Guide,* . Inc., February 2012; Available from: http://www.skf.com/binary/tcm:12-114679/140-710%20BIMG%2011_2012_tcm_12-114679.pdf.

102. Australia, F.A.G., *Rolling bearing damage : recognition of damage and bearing inspection*. 1996, Frenchs Forest, N.S.W.: FAG Australia.

103. Group, S., *Roller Bearing Damage : Recognition of damage and bearing inspection*. 2010, Schaeffler Technolgies GmbH@co.KG: Germany.

104. Goddard, K.N. and B.D. MacIsaac, *The use of oil borne debris as a failure criterion of rolling element bearings.* Lubrication engineering, 1995. **51**(6): p. 481-487.

105. Limited, F.A.G.B., *Rolling bearing damage : recognition of damage and bearing inspection*. 2003, Mississauga, Ont.: FAG Bearings Limited.

106.   Miller, J.L. and D. Kitaljevich. *In-line oil debris monitor for aircraft engine condition assessment*. in *Aerospace Conference Proceedings, 2000 IEEE*. 2000.

107.   Cotporation, J. *Ball and Roller Bearings: Failures, Causes and Countermeasures*. Cat.   No.   B3001E   1992;   Available   from: http://www.koyousa.com/brochures/pdfs/catb3001e.pdf.

108.   Torrington, C., *Bearing failure prevention guide*. 1989, Torrington, Conn.: Torrington Co.

109.   SKF. *Bearing failure and their causes*. 1994; Available from: http://www.mana-omerzu.si/files/Bearing_Failures_and_Their_Causes.pdf.

110.   Calvin, J., *Maintenance and troubleshooting are keys to longer bearing life.* Plant Engineer, October, 1995. **9**.

111.   Company, E.B. *Bearing Failure Analysis*. 2015; Available from: http://info.emersonbearing.com/thank-you-bearing-failure-analysis?submissionGuid=e3852a03-062f-41af-af72-1d24e7d1785c.

112.   Williams, J.A. and A.M. Hyncica, *Mechanisms of abrasive wear in lubricated contacts.* Wear, 1992. **152**(1): p. 57-74.

113.   Hamrock, B.J. and W.J. Anderson, *Rolling-element bearings.* 1983.

114.   Yang, H., *Automatic Fault Diagnosis of Rolling Element Bearings Using Wavelet Based Pursuit Features*, in *School of Mechanical, Manufacturing and Medical Engineering*. 2004, Dalian University of Technology: China. p. 220.

115.   Sawalhi, N. and R. Randall, *Simulating gear and bearing interactions in the presence of faults: Part I. The combined gear bearing dynamic model and the simulation of localised bearing faults.* Mechanical Systems and Signal Processing, 2008. **22**(8): p. 1924-1951.

116.   Choudhury, A. and N. Tandon, *Vibration response of rolling element bearings in a rotor bearing system to a local defect under radial load.* Journal of Tribology, 2006. **128**(2): p. 252-261.

117.   Tandon, N. and A. Choudhury, *An analytical model for the prediction of the vibration response of rolling element bearings due to a localized defect.* Journal of sound and vibration, 1997. **205**(3): p. 275-292.

118.   Randall, R.B. and J. Antoni, *Rolling element bearing diagnostics—A tutorial.* Mechanical Systems and Signal Processing, 2011. **25**(2): p. 485-520.

119. Ho, D. and R.B. Randall, *OPTIMISATION OF BEARING DIAGNOSTIC TECHNIQUES USING SIMULATED AND ACTUAL BEARING FAULT SIGNALS.* Mechanical Systems and Signal Processing, 2000. **14**(5): p. 763-788.

120. Kıral, Z. and H. Karagülle, *Vibration analysis of rolling element bearings with various defects under the action of an unbalanced force.* Mechanical Systems and Signal Processing, 2006. **20**(8): p. 1967-1991.

121. Braun, S.G., *The Signature Analysis of Sonic Bearing Vibrations.* Sonics and Ultrasonics, IEEE Transactions on, 1980. **27**(6): p. 317-327.

122. Gustafsson, O.G. and T. Tallian, *Detection of damage in assembled rolling element bearings.* ASLE TRANSACTIONS, 1962. **5**(1): p. 197-209.

123. Sun, Q., F. Xi, and G. Krishnappa. *'Signature Analysis of Rolling Element Bearing Defects*. in *Proceedings of CSME Forum*. 1998.

124. McFadden, P., *Condition monitoring of rolling element bearings by vibration analysis.* Proceedings of Institution of Mechanical Engineers, 1990: p. 49-54.

125. Al Kazzaz, S.a.A.S. and G.K. Singh, *Experimental investigations on induction machine condition monitoring and fault diagnosis using digital signal processing techniques.* Electric Power Systems Research, 2003. **65**(3): p. 197-221.

126. Alfredson, R. and J. Mathew, *Time domain methods for monitoring the condition of rolling element bearings.* NASA STI/Recon Technical Report A, 1985. **86**: p. 22166.

127. Kim, Y.-H., et al., *Condition Monitoring of Low Speed Bearings: A Comparative Study of the Ultrasound Technique Versus Vibration Measurements Engineering Asset Management.*, J. Mathew, et al., Editors. 2006, Springer London, 2006. p. 182-191.

128. Dyer, D. and R. Stewart, *Detection of rolling element bearing damage by statistical vibration analysis.* Journal of mechanical design, 1978. **100**(2): p. 229-235.

129. Randall, R.B., J. Antoni, and S. Chobsaard. *A comparison of cyclostationary and envelope analysis in the diagnostics of rolling element bearings*. in *Acoustics, Speech, and Signal Processing, 2000. ICASSP '00. Proceedings. 2000 IEEE International Conference on*. 2000.

130. Bechhoefer, E., P. Menon, and M. Kingsley. *Bearing envelope analysis window selection Using spectral kurtosis techniques*. in *Prognostics and Health Management (PHM), 2011 IEEE Conference on*. 2011.

131. Patel, R.K., S. Agrawal, and N.C. Joshi. *Induction motor bearing fault identification using vibration measurement*. in *Engineering and Systems (SCES), 2012 Students Conference on*. 2012.

132. Yuriy, S., *Continuous-Time Signal*, ed. S.a.C. Technology. 2006: Dordrecht : Springer, c2006.

133. Dwyer, R. *Detection of non-Gaussian signals by frequency domain Kurtosis estimation*. in *Acoustics, Speech, and Signal Processing, IEEE International Conference on ICASSP '83*. 1983.

134. Cocconcelli, M., et al., *Kurtosis over Energy Distribution Approach for STFT Enhancement in Ball Bearing Diagnostics*, in *Condition Monitoring of Machinery in Non-Stationary Operations*, T. Fakhfakh, et al., Editors. 2012, Springer Berlin Heidelberg. p. 51-59.

135. Cong, F., J. Chen, and G. Dong, *Spectral kurtosis based on AR model for fault diagnosis and condition monitoring of rolling bearing*. Journal of Mechanical Science and Technology, 2012. **26**(2): p. 301-306.

136. Wang, Y., et al., *Spectral kurtosis for fault detection, diagnosis and prognostics of rotating machines: A review with applications*. Mechanical Systems and Signal Processing, 2016. **66**: p. 679-698.

137. Collis, W., P. White, and J. Hammond, *Higher-order spectra: the bispectrum and trispectrum*. Mechanical systems and signal processing, 1998. **12**(3): p. 375-394.

138. Xinxin, L., et al. *Feature Extraction of Underwater Signals Based on Bispectrum Estimation*. in *Wireless Communications, Networking and Mobile Computing (WiCOM), 2011 7th International Conference on*. 2011. IEEE.

139. Naid, A., et al. *Bispectrum Analysis of Motor Current Signals for Fault Diagnosis of Reciprocating Compressors*. in *Key Engineering Materials*. 2009. Trans Tech Publ.

140. Zhang, G., et al., *Bispectral analysis for on-line monitoring of stamping operation*. Engineering Applications of Artificial Intelligence, 2002. **15**(1): p. 97-104.

141. Kim, Y.C. and E.J. Powers, *Digital Bispectral Analysis and Its Applications to Nonlinear Wave Interactions*. Plasma Science, IEEE Transactions on, 1979. **7**(2): p. 120-131.

142. Rai, A. and S. Upadhyay, *A review on signal processing techniques utilized in the fault diagnosis of rolling element bearings.* Tribology International, 2016. **96**: p. 289-306.

143. Harris, T.A., *Rolling bearing analysis*. 4th ed. 2001, New York: Wiley. 1105.

144. Arslan, H. and N. Aktürk, *An investigation of rolling element vibrations caused by local defects.* Journal of Tribology, 2008. **130**(4): p. 041101.

145. Karacay, T. and N. Akturk, *Vibrations of a grinding spindle supported by angular contact ball bearings.* Proceedings of the Institution of Mechanical Engineers, Part K: Journal of Multi-body Dynamics, 2008. **222**(1): p. 61-75.

146. Schmid, S.R., B.J. Hamrock, and B.O. Jacobson, *Fundamentals of Machine Elements: SI Version*. 2014: CRC Press.

147. Igarashi, T. and H. Hamada, *Studies on the vibration and sound of defective rolling bearings: First report: Vibration of ball bearings with one defect.* Bulletin of JSME, 1982. **25**(204): p. 994-1001.

148. Haydock, L., P.J. Wyles, and J.E.C. Bean, *Alternating current machines*. 2001, Google Patents.

149. Crompton, B. *AC Motors*. Available from: http://www.brookcrompton.com/index.html.

150. Mart, M. *Clarke 5.5 Hp, 400V Electric Motor*. Available from: https://www.machinemart.co.uk/p/motor-28/.

151. Cochran, P., *Polyphase Induction Motors, Analysis: Design, and Application*. 1989: CRC Press.

152. Stanley, R. and P. Sognate, *Alignment of critical and noncritical machines.* orbit, 1995.

153. Bearings, V.B., *6206 Bearing Deep Groove 6206.*

154. Park, J. and S. Mackay, *Data acquisition for instrumentation and control system.* 2003, Newnes.

155. RS. *Gauge Pressure Sensor*. Available from: http://uk.rs-online.com/web/p/products/797-4977/.

156. Monitoring, S.C., *Vibration Sensors* 2005, SKF USA Inc. p. 44.

157. Shieh, J., et al., *The selection of sensors.* Progress in Materials Science, 2001. **46**(3–4): p. 461-504.

158. SINOCERA PIEZOTRONICS, I. *CA-YD-185TNC Piezoelectric Accelerometer*. Available from: http://en.china-yec.com/products_detail1/&productId=128.html.

159. Nishio, K., et al. *An investigation of the early detection of defects in ball bearings by the vibration monitoring*. in *American Society of Mechanical Engineers, Design Engineering Technical Conference, St. Louis, Mo*. 1979.

160. Lai, M.S., *Detection of developing bearing failures by means of vibration analysis*. ASME, Design Engineering Division, , 1996. **18**(1): p. 231-236.

161. Lei, Y., Z. He, and Y. Zi, *A new approach to intelligent fault diagnosis of rotating machinery*. Expert Systems with Applications, 2008. **35**(4): p. 1593-1600.

162. Li, C., et al., *Multi-scale autocorrelation via morphological wavelet slices for rolling element bearing fault diagnosis*. Mechanical Systems and Signal Processing, 2012. **31**: p. 428-446.

163. Phipps, T. and R. King. *A Speaker Verification Biometric In 40 Bytes*. in *CardTech/SecurTech*. 1997.

164. Mechefske, C.K. and L. Liu, *Fault detection and diagnosis in variable speed machines*. International Journal of COMADEM(1363-7681), 2002. **5**(2): p. 29-39.

165. McFadden, P.D. and J.D. Smith, *Vibration monitoring of rolling element bearings by the high-frequency resonance technique — a review*. Tribology International, 1984. **17**(1): p. 3-10.

166. Randall, R.B., *Detection and diagnosis of incipient bearing failure in helicopter gearboxes*. Engineering Failure Analysis, 2004. **11**(2): p. 177-190.

167. Wiggins, R.A., *Minimum entropy deconvolution*. Geoexploration, 1978. **16**(1): p. 21-35.

168. Dwyer, R.F. *Detection of non-Gaussian signals by frequency domain kurtosis estimation*. in *Acoustics, Speech, and Signal Processing, IEEE International Conference on ICASSP'83*. 1983. IEEE.

169. Liangcai, X., et al., *A novel application of wavelet-based bispectrum analysis to diagnose faults in gears*. International Journal of COMADEM, vol. 5, iss. No. 3, p. 31-38, 2002. **5**: p. 31-38.

170. Yang, D.-M., et al., *Third-order spectral techniques for the diagnosis of motor bearing condition using artificial neural networks*. Mechanical systems and signal processing, 2002. **16**(2): p. 391-411.

171. Chow, T. and G. Fei, *Three phase induction machines asymmetrical faults identification using bispectrum*. IEEE Transactions on Energy Conversion, 1995. **10**(4): p. 688-693.

172. Arthur, N. and J. Penman. *Inverter fed induction machine condition monitoring using the bispectrum.* in *Higher-Order Statistics, 1997., Proceedings of the IEEE Signal Processing Workshop on.* 1997. IEEE.

173. Parker, B.E., et al., *Fault diagnostics using statistical change detection in the bispectral domain.* Mechanical systems and signal processing, 2000. **14**(4): p. 561-570.

174. Tielin, L.W.Z.G.S. and Y. Shuzi, *GEAR CRACK EARLY DIAGNOSIS USING BISPECTRUM DIAGONAL SLICE.*

175. Newman, M.E., G.T. Barkema, and M. Newman, *Monte Carlo methods in statistical physics.* Vol. 13. 1999: Clarendon Press Oxford.

176. Kroese, D.P., et al., *Why the Monte Carlo method is so important today.* Wiley Interdisciplinary Reviews: Computational Statistics, 2014. **6**(6): p. 386-392.

APPENDICES

The following section contains the appendices of the additional results.

APPENDIX A

A1: Spectrogram

The spectrogram is applied using a moving window of a prescribed length along the recorded data to convert it into narrow-enough time intervals for the signal to be considered stationary. Figure A-0-1, Figure A-0-2 and Figure A-0-3 show the STFT of the baseline, inner-race, and the outer-race faults at 25%, 50% and 75% torque loads (see Chapter seven, Section 7.2.4.1, for more details).
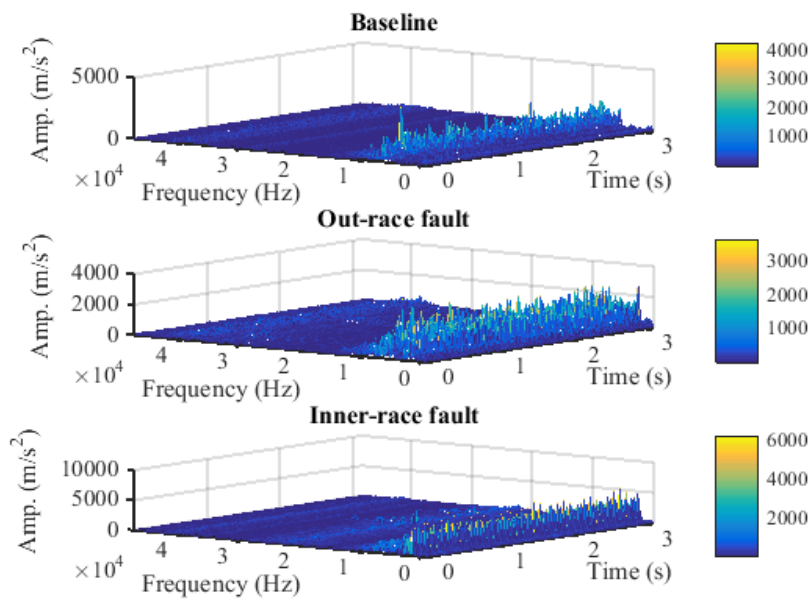
Figure A-0-1 Spectrogram of baseline, outer-race and inner-race under 25% torque load
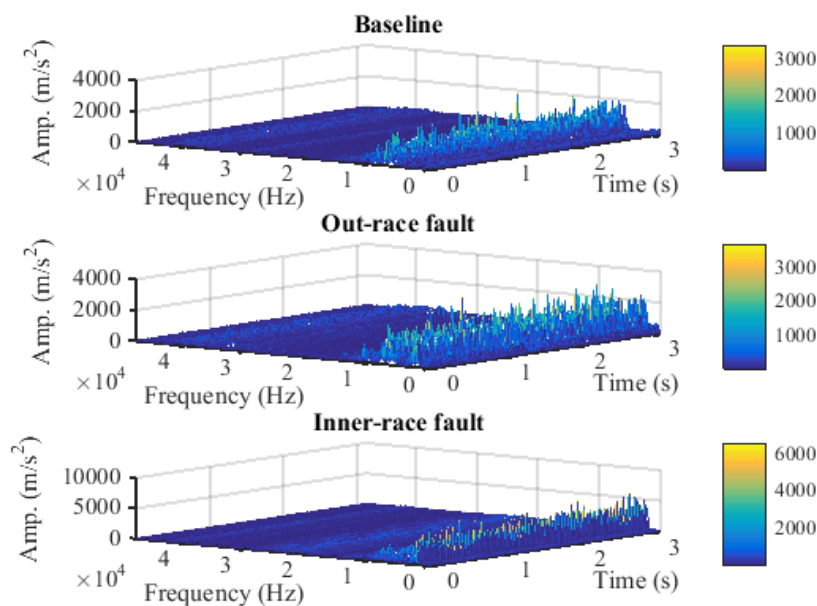
Figure A-0-2 Spectrogram of baseline, outer-race and inner-race under 50% torque load
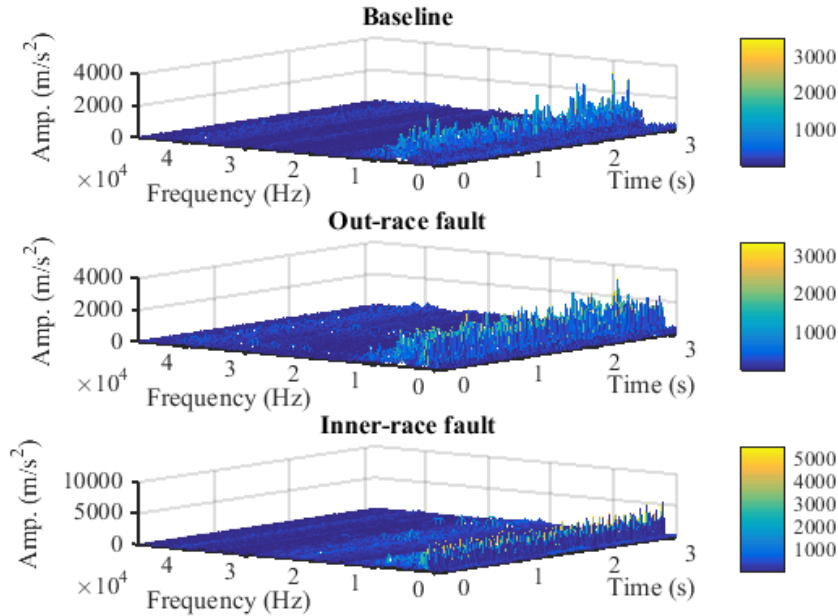
Figure A-0-3 Spectrogram of baseline, outer-race and inner-race under 75% torque load

A2: Spectral Kurtosis

The STFT has been computed based on the spectral kurtosis, using eight different window durations of 16, 32, 64, 128, 256, 512, 1024 and 2048 for the collected data under 25%, 50% and 75% (for more details, see Chapter seven, Section 7.2.4.1).

1- Inner Race Fault
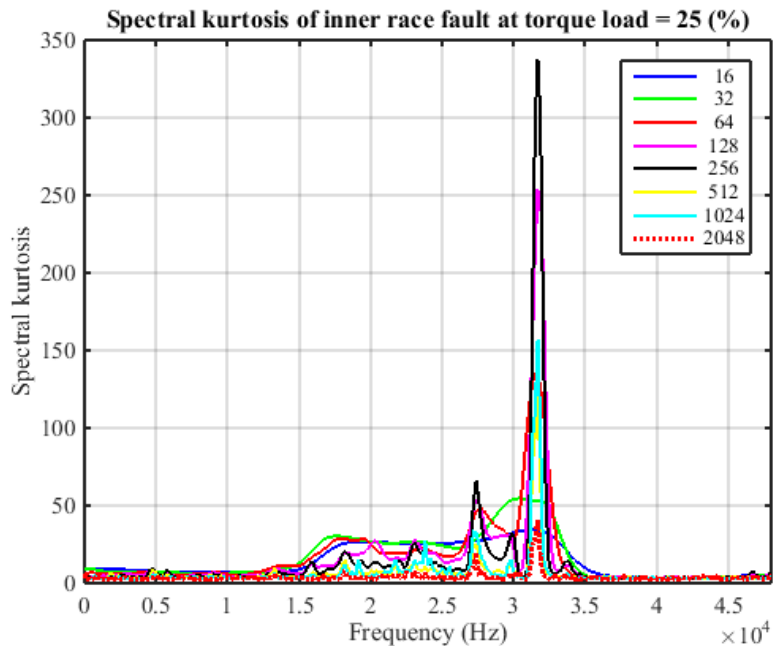
Figure A-0-4 Spectral kurtosis of inner-race fault computed for different frequency

resolution under 25% torque load
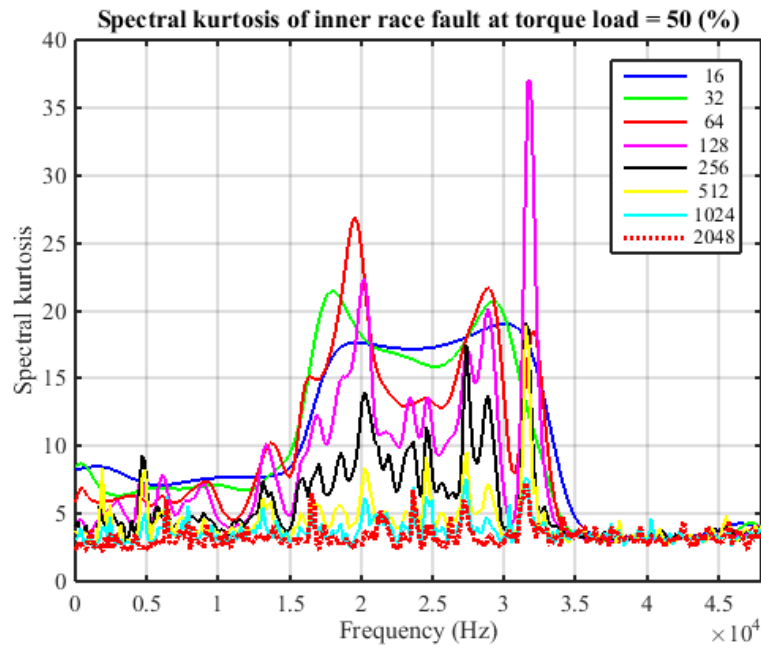
Figure A-0-5 Spectral kurtosis of inner-race fault computed for different frequency resolution under 50% torque load
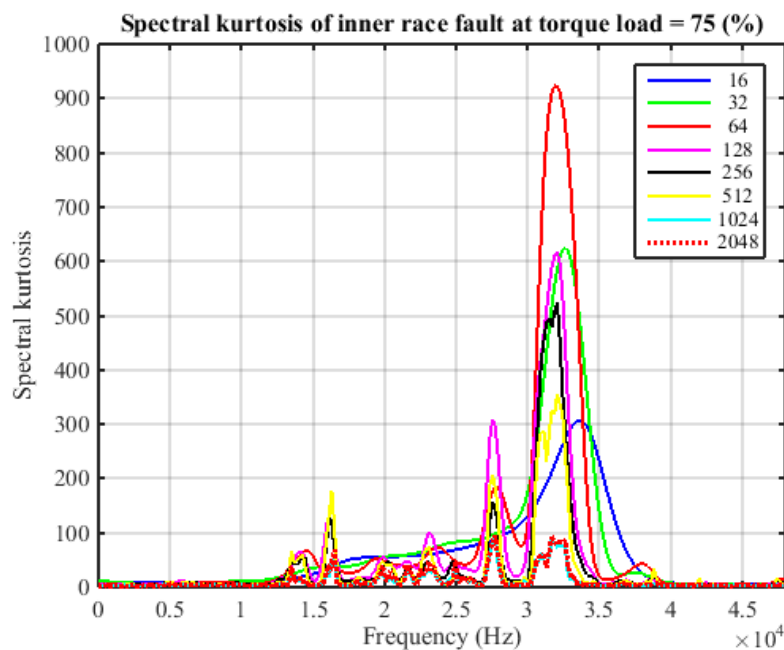
Figure A-0-6 Spectral kurtosis of inner-race fault computed for different frequency resolution under 75% torque load
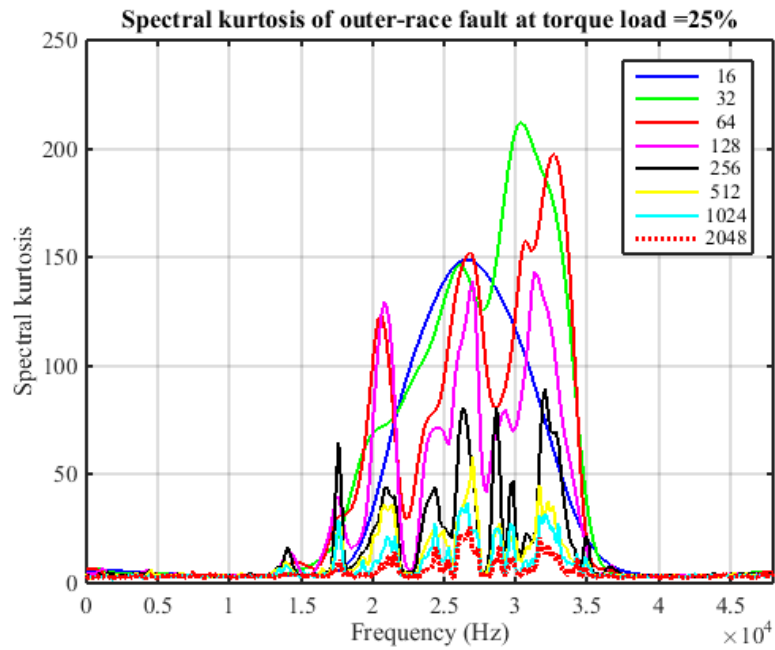
2- Outer Race Fault

Figure A-0-7 Spectral kurtosis of outer-race fault computed for different frequency resolution under 25% torque load
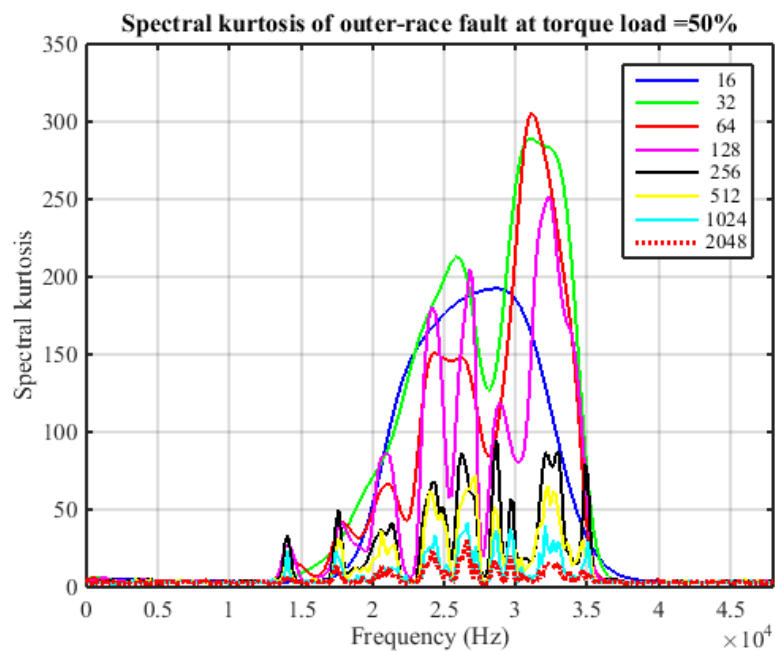
Figure A-0-8 Spectral kurtosis of outer-race fault computed for different frequency resolution under 50% torque load
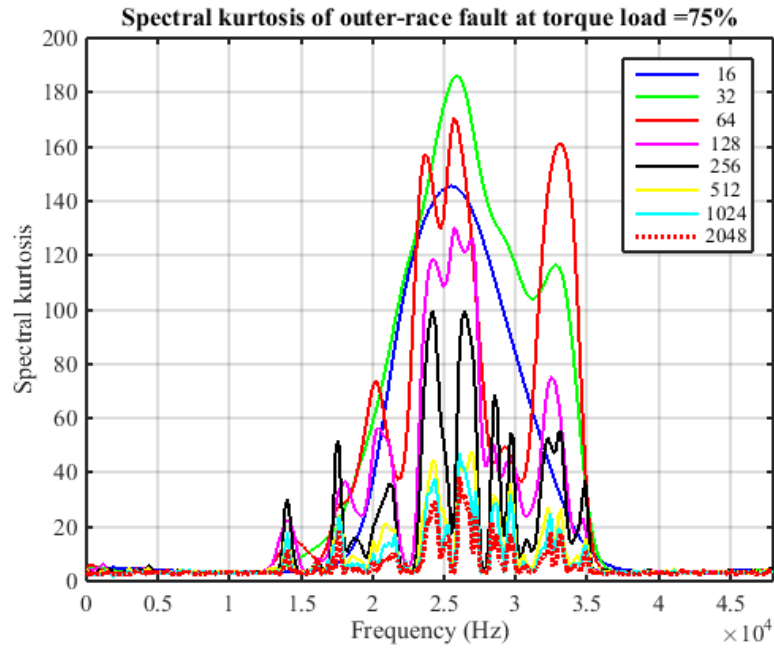
Figure A-0-9 Spectral kurtosis of outer-race fault computed for different frequency resolution under 75% torque load

A3: Kurtogram

Kurtogram is a map formed by STFT and is expressed as a function of central frequency and window length for the collected data under four different torque loads (see Chapter seven, Section 7.2.4.2, for more details).

1- Inner Race Fault
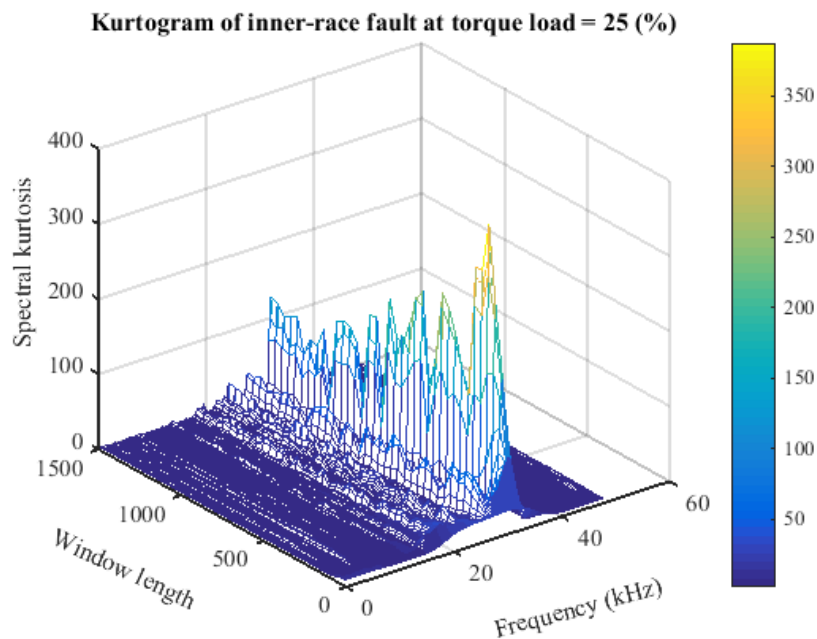
Figure A-0-10 Kurtogram of inner-race fault under 25% torque load
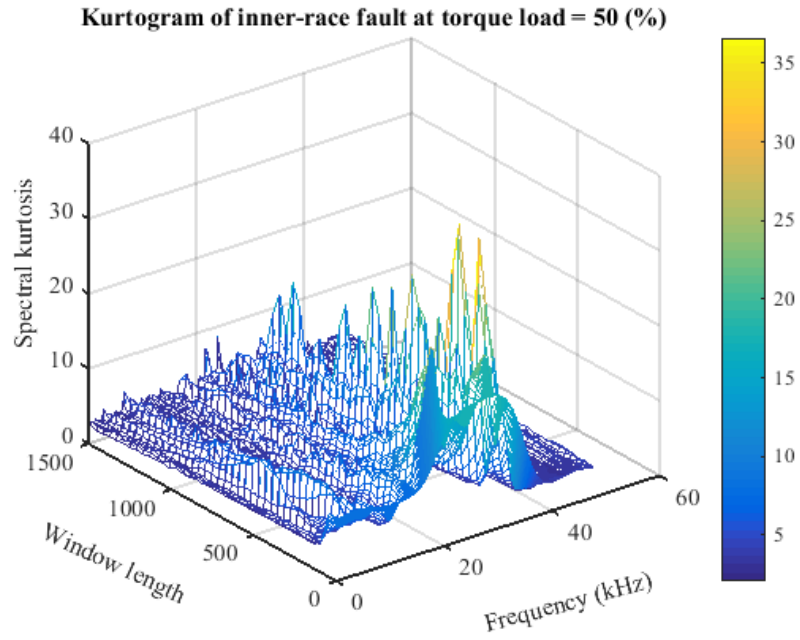
Figure A-0-11 Kurtogram of inner-race fault under 50% torque load
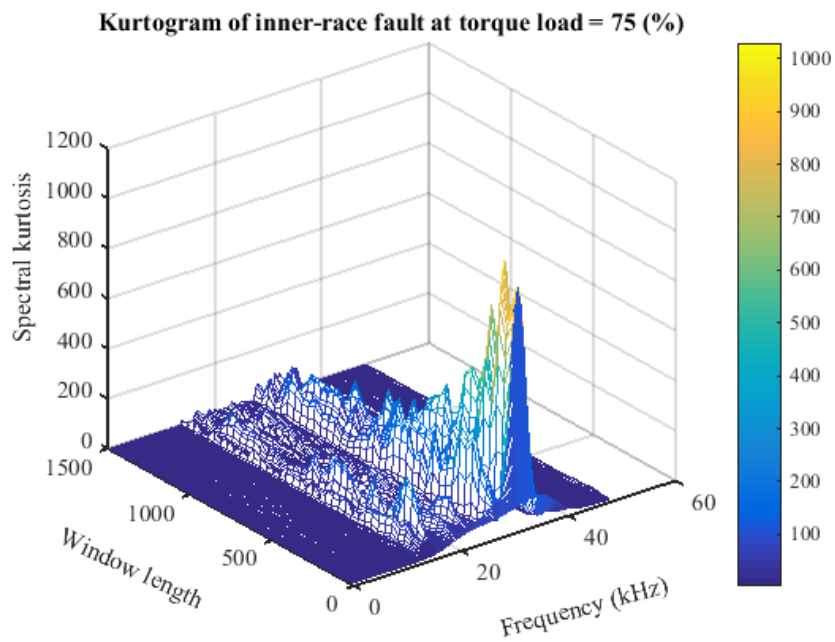
Figure A-0-12 Kurtogram of inner-race fault under 75% torque load
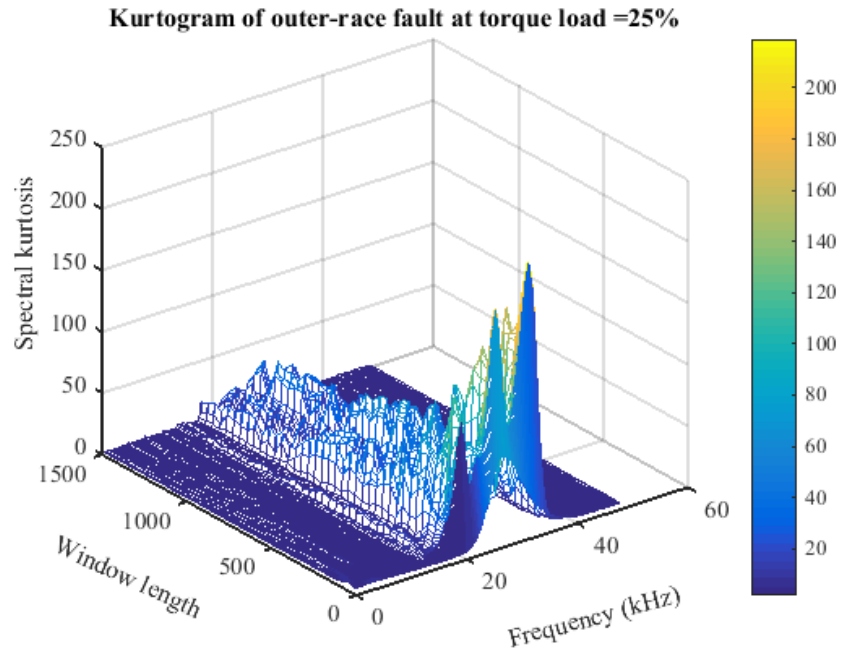
2- Outer Race Fault

Figure A-0-13 Kurtogram of outer-race fault under 25% torque load
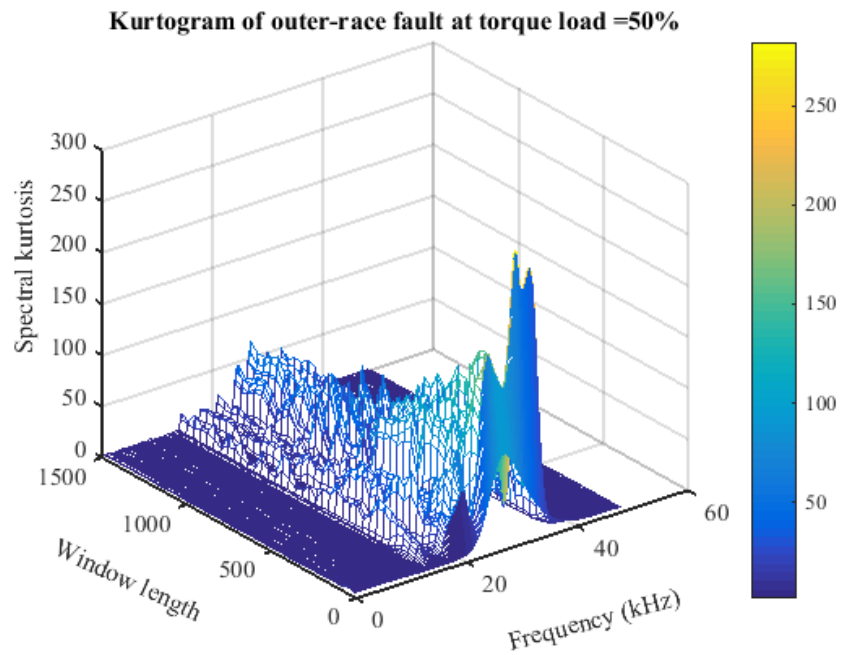
Figure A-0-14 Kurtogram of outer-race fault under 50% torque load
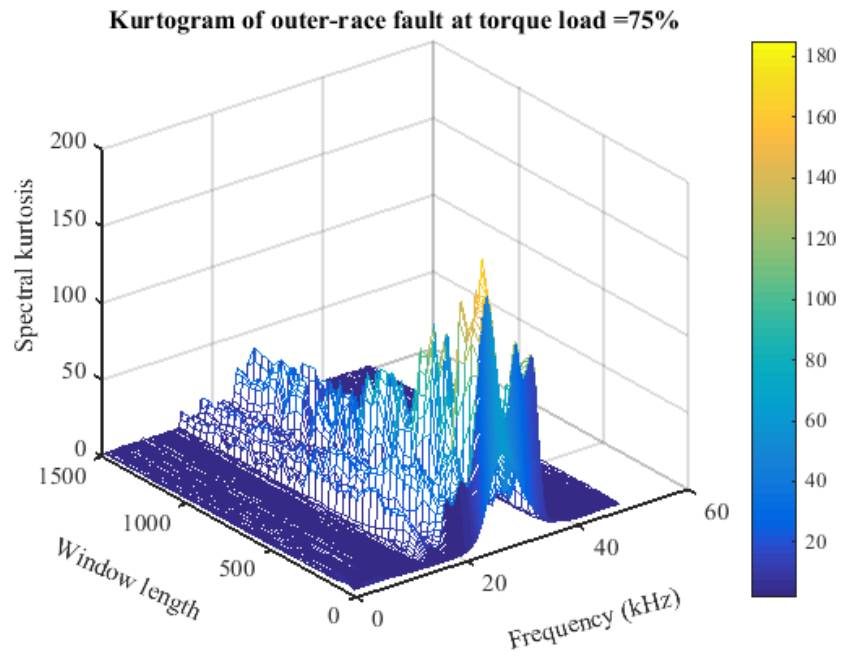
Figure A-0-15 Kurtogram of outer-race fault under 75% torque load

APPENDIX B

B1: RMS, PV and Kurtosis of the vibration signal under different radial loads

Figure B-0-1, Figure B-0-2 and Figure B-0-3 exhibit RMS, peak value and kurtosis of bearing clearance grades CN and C4 for baseline, 0.2 mm inner-race, 0.475 mm inner-race, and 0.2 mm outer-race defects at 0.8, 1.6 and 2.4 kN radial loads, respectively (for more details see Chapter eight Section 8.3.1).
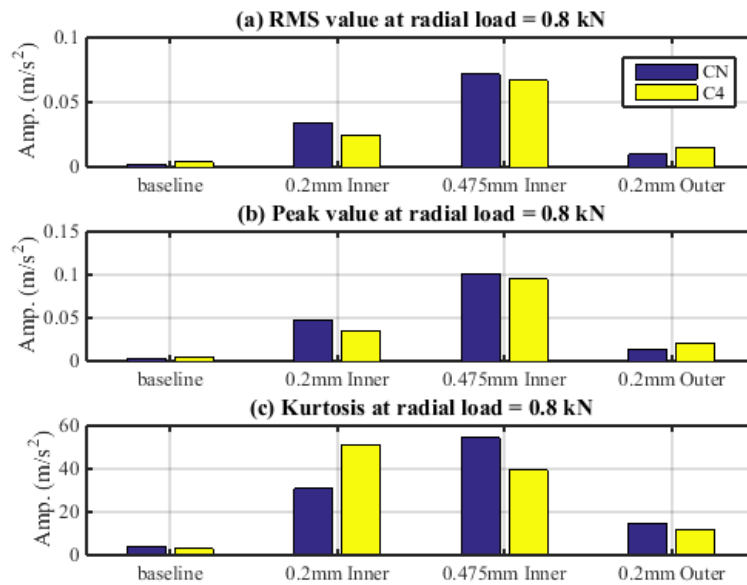
Figure B-0-1 (a) RMS, (b) peak value and (c) kurtosis of raw data at 0.8 kN radial-load condition
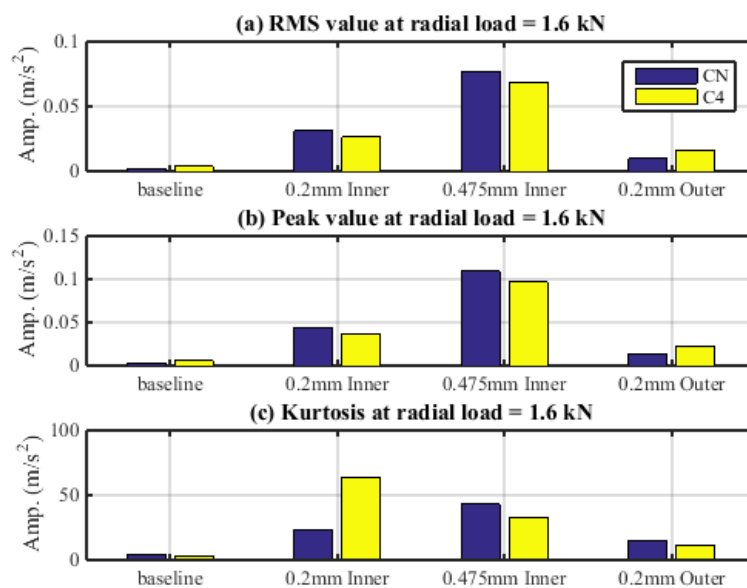
Figure B-0-2 (a) RMS, (b) peak value and (c) kurtosis of raw data at 1.6 kN radial-load condition
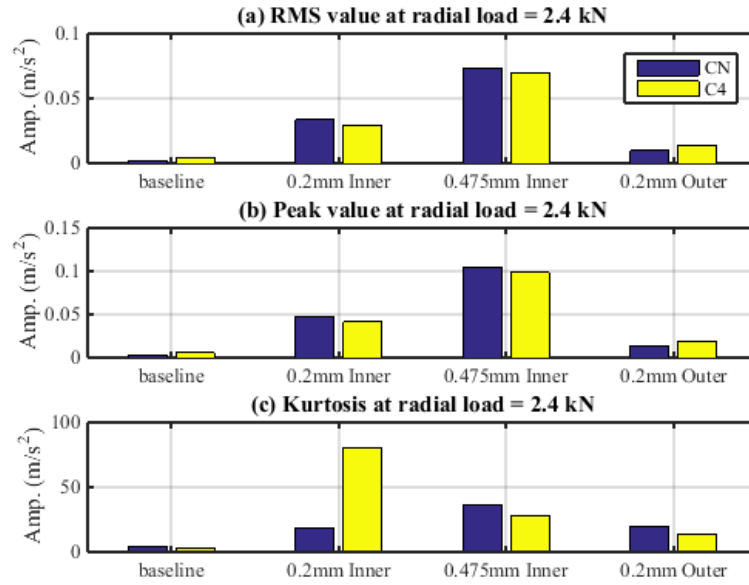
Figure B-0-3 (a) RMS, (b) peak value and (c) kurtosis of raw data at 2.4 kN radial-load condition

APPENDIX C

C1: Conventional Bispectrum Results

The following Figures show representative results of bispectra and corresponding bicoherences for the vibration signals of CN and C4 bearings with 0.2mm inner-race fault, 0.475mm inner-race fault and 0.2mm outer-race fault cases under four different radial loads of 0, 0.8, 1.6 and 2.4 kN (see Chapter nine, Section 9.4, for more details). The four graphs in the first row of each Figure give out CB magnitude results while the four graphs in the second row illustrate corresponding CBc results. From the CB results, it can be seen that there is a distinct peak at the bifrequency $B_{MS}(f,f)$, which can be used to quantify the nonlinear characteristics between the harmonic components f , $2f$ and $3f$, corresponding to the envelope spectra.

1- CB of Bearings with CN Internal Radial Clearance
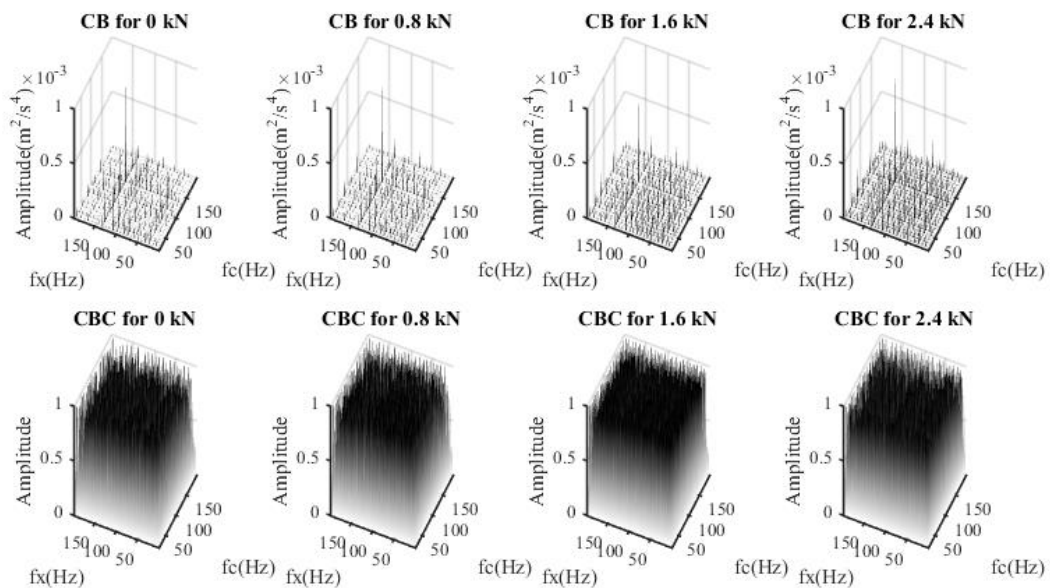
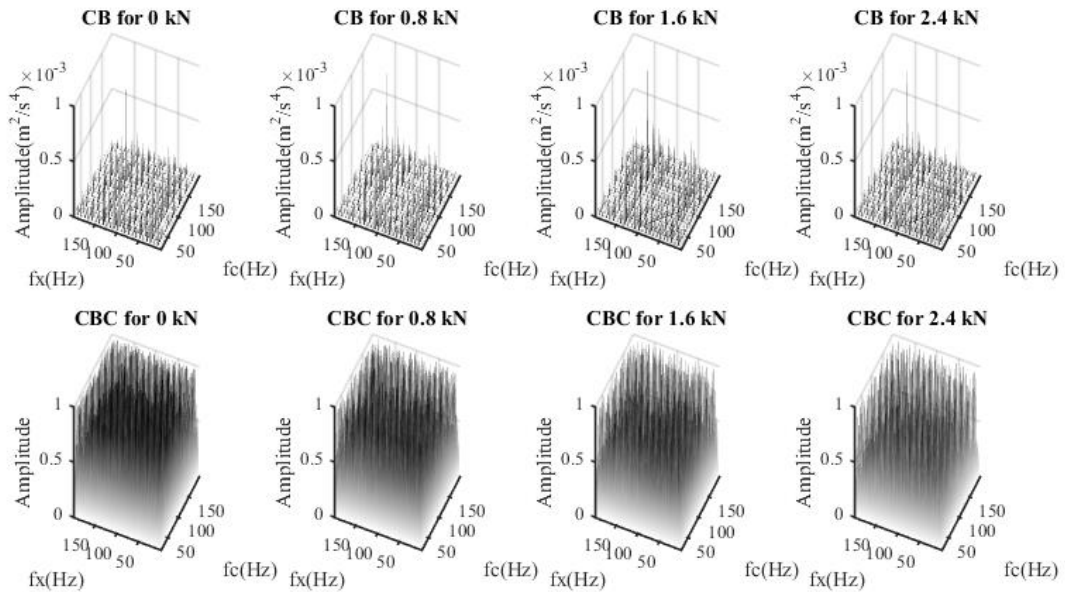Figure C-0-1 CB of CN bearing with 0.2mm inner-race defect under different radial load conditions
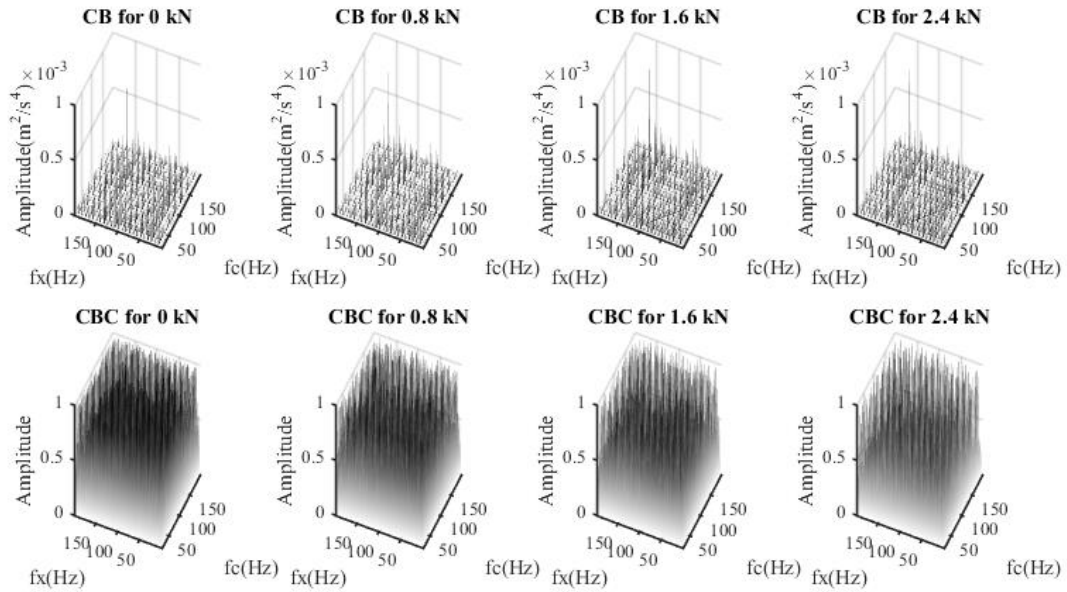
Figure C-0-2 CB of CN bearing with 0.475mm inner-race defect under different radial load
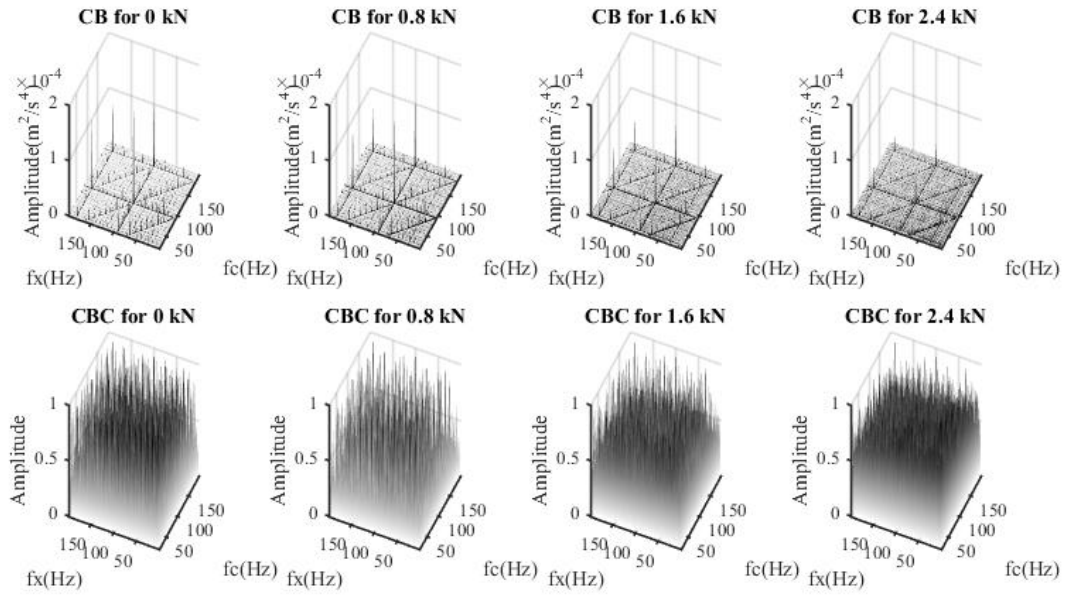conditions
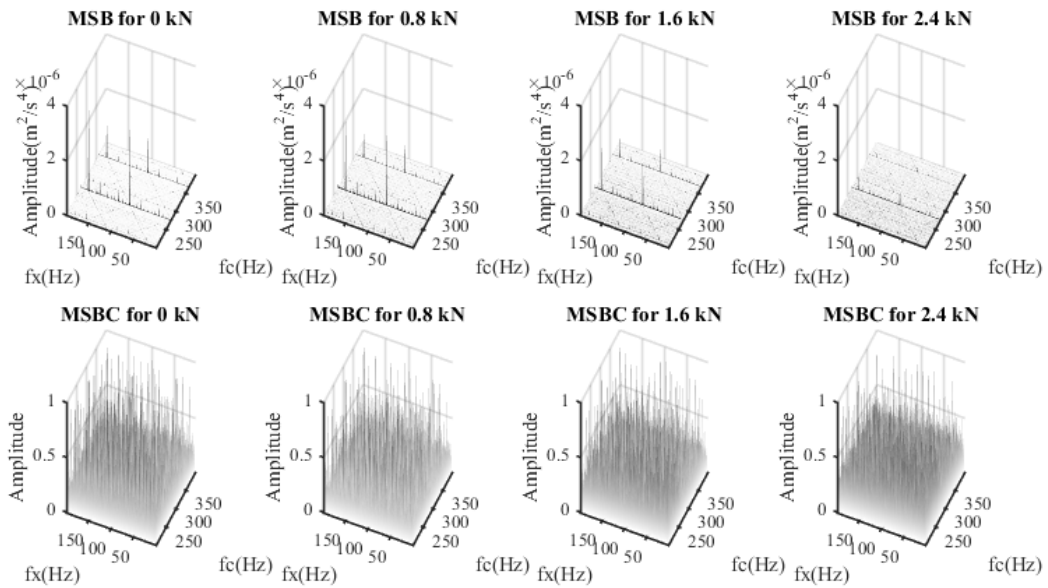
Figure C-0-3 CB of CN bearing with 0.2mm outer-race defect under different radial load
conditions
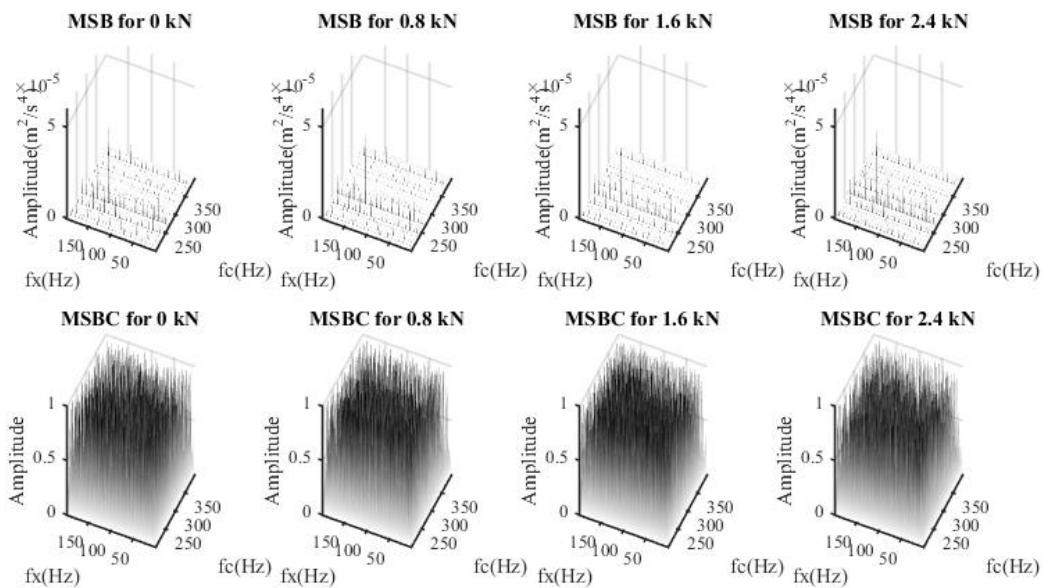
2- CB of Bearings with C4 Internal Radial Clearance
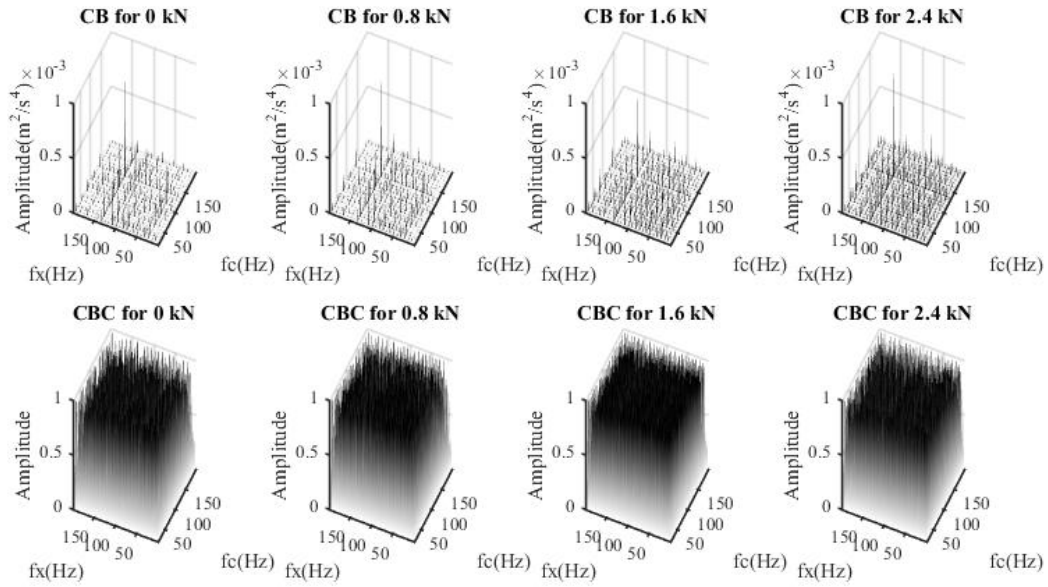
Figure C-0-4 CB of C4 bearing with 0.2mm inner-race defect under different radial load conditions

Figure C-0-5 CB of C4 bearing with 0.475mm inner-race defect under different radial load conditions

Figure C-0-6 CB of C4 bearing with 0.2mm outer-race defect under different radial load
conditions

C2: Modulation Signal Bispectrum Results

The following Figures show representative results of MSB and corresponding MSBc for the vibration signals of CN and C4 bearings with 0.2mm inner-race fault, 0.475mm inner-race fault and 0.2mm outer-race fault cases under four different radial loads of 0, 0.8, 1.6 and 2.4 kN (see Chapter nine, Section 9.4, for more details). The four graphs in the first row of each Figure give out CB magnitude results while the four graphs in the second row illustrate corresponding CBc results. From the CB results, it can be seen that there is a distinct peak at the bifrequency $B_{MS}(2f, f)$, which can be used to quantify the nonlinear characteristics between the harmonic components f, $2f$ and $3f$, corresponding to the envelope spectra.

1- MSB of Bearing with CN Internal Radial clearance

Figure C-0-7 MSB of CN bearing with 0.2mm inner-race defect under different radial load conditions
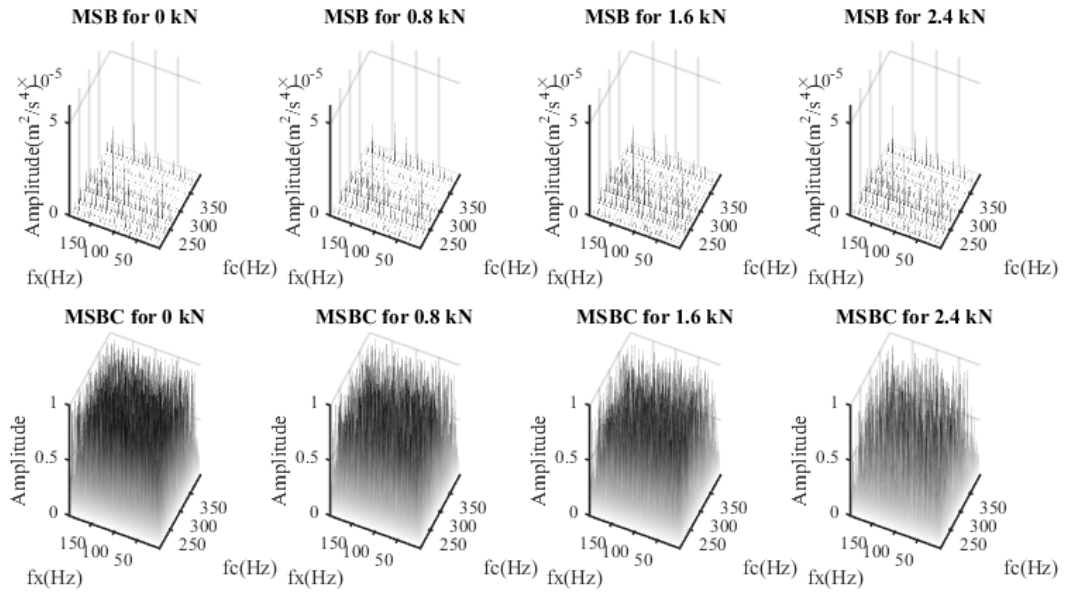
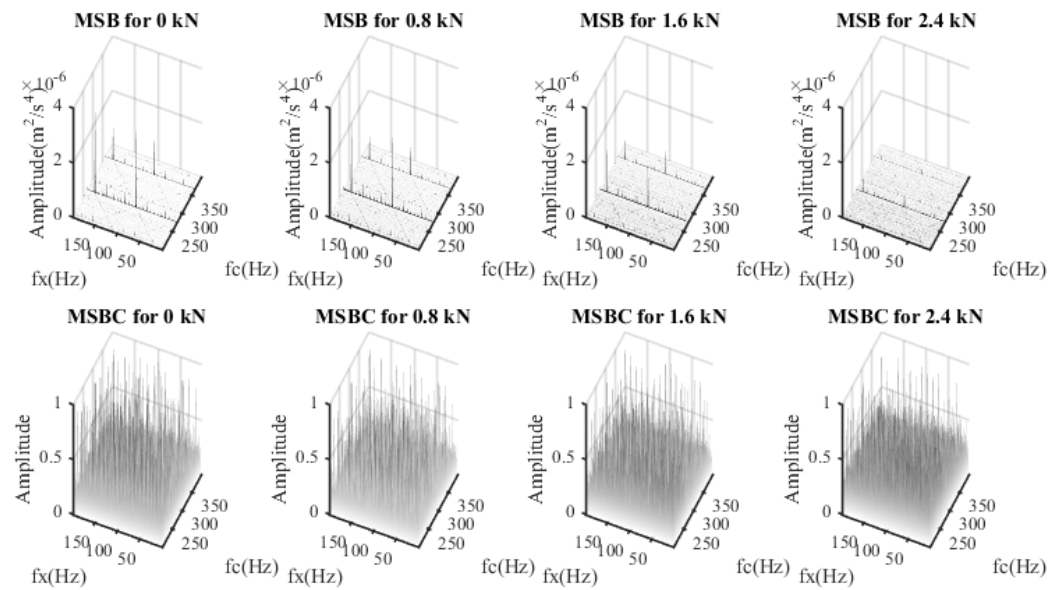Figure C-0-8 MSB of CN bearing with 0.475mm inner-race defect under different radial load conditions

Figure C-0-9 MSB of CN bearing with 0.2mm outer-race defect under different radial load conditions

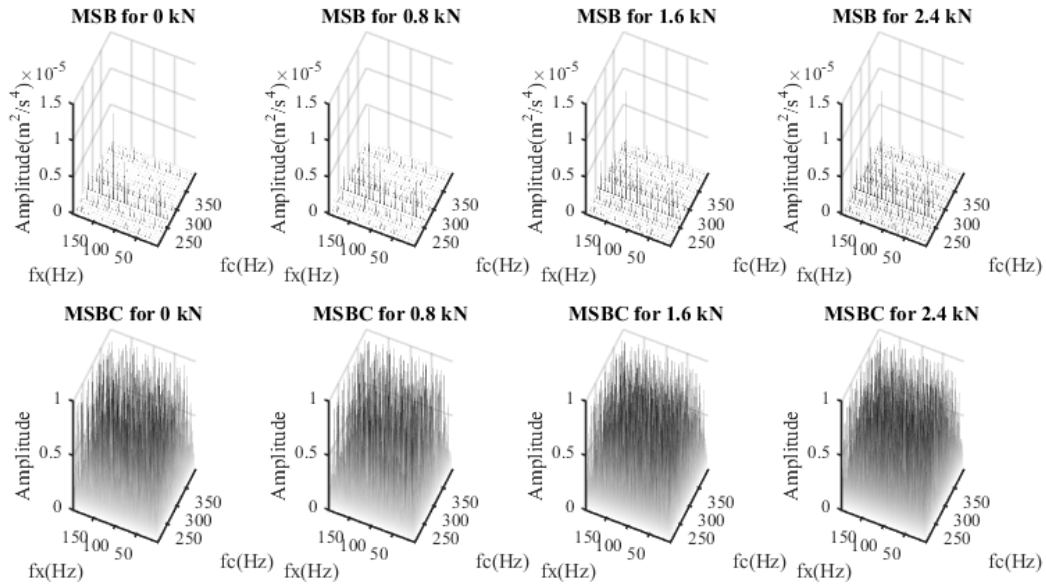## 2- MSB of Bearing with C4 Internal Radial clearance

Figure C-0-10 MSB of C4 bearing with 0.2mm inner-race defect under different radial load conditions
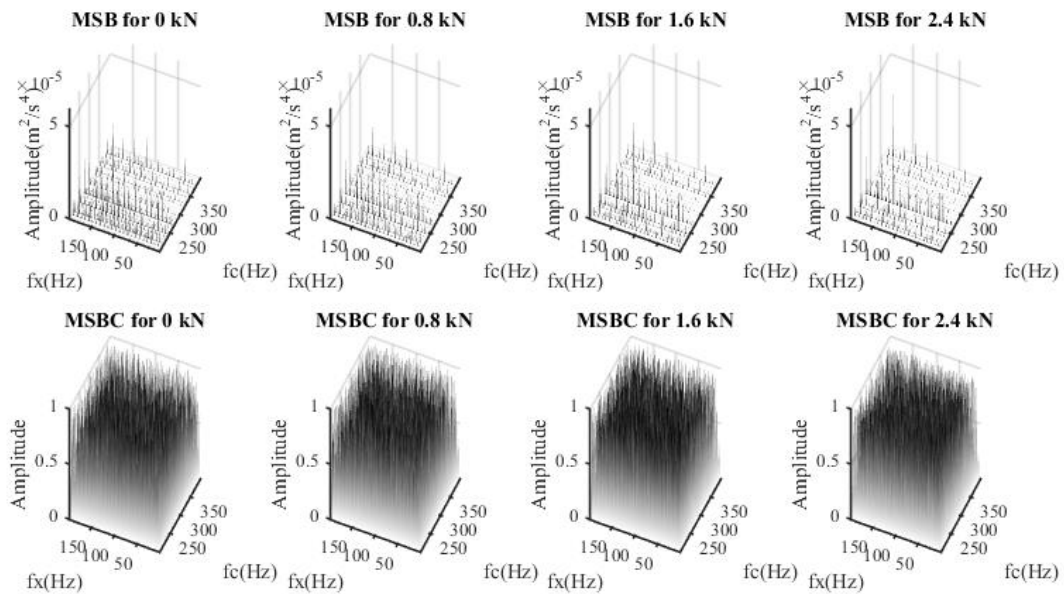

Figure C-0-11 MSB of C4 bearing with 0.475mm inner-race defect under different radial load conditions
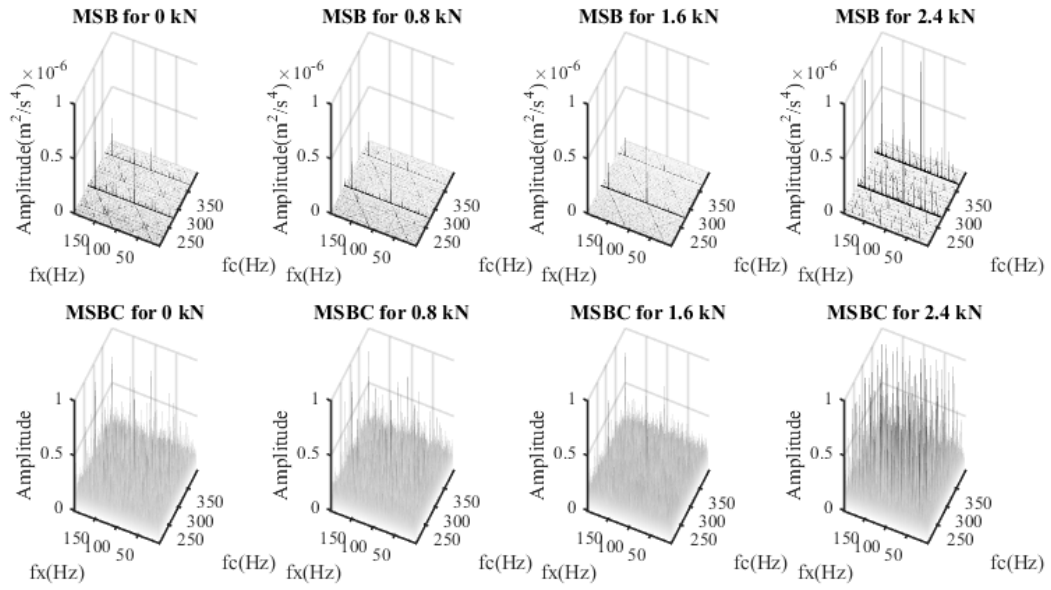
Figure C-0-12 MSB of C4 bearing with 0.2mm outer-race defect under different radial load
conditions